Institute of Experimental Pharmacology and Toxicology
Center for Experimental Medicine
University Medical Center Hamburg-Eppendorf

Establishment of a multi-cell-type *in vitro* model to study pathological cardiac hypertrophy

---

Dissertation
Submitted to the Department of Chemistry
Faculty of Mathematics, Informatics, and Natural Sciences
University of Hamburg
For the degree of
Doctor of Natural Sciences
(Dr. rer. nat.)

By

Kinga Maria Wrona

Hamburg, 2024

Reviewer 1: Prof. Dr. Elke Oetjen
Reviewer 2: Prof. Dr. Thomas Eschenhagen

Disputation committee:
Prof. Dr. Elke Oetjen
Prof. Dr. Wolfram Brune
Prof. Dr. Friederike Cuello

Date of disputation: 06.12.2024

Approved for printing: 14.02.2025

This thesis was carried out at the Institute of Experimental Pharmacology and Toxicology, University Medical Center Hamburg-Eppendorf from August 2020 to October 2024.

Supervisor: Prof. Dr. Elke Oetjen
Co-supervisor: Prof. Dr. Thomas Eschenhagen
Practical supervisor: Priv.-Doz. Dr. Dr. Marc N. Hirt

I. List of publications

Raabe J, Wittig I, Laurette P, Stathopoulou K, Brand T, Cabrera-Orefice A, Meisterknecht J, Thiemann E, Laufer SD, Shibamiya A, Reinsch M, Schulze T, Klampe B, Fuchs S, Kaiser J, Yang J, Zehr S, **Wrona KM**, Lorenz K, Lukowski R, Hansen A, Gilsbach R, Brandes RP, Ulmer BM, Eschenhagen T, Cuello F (2024) **NDUFA4L2 is a master regulator of hypoxia-mediated mitochondrial complex composition protecting stem cell viability**. Redox Biol. 77:103352. https://10.1016/j.redox.2024.103352

Albert AM, Balamurali D, Beslika E, Fernandez ID, Genedy HH, Babaei Khorzoughi R, Lauta FC, Peppas P, Ragone I, Rizzari G, Sansonetti M, Silva J, Spanò G, **Wrona KM** (2024) **Harnessing the power of RNA therapeutics in treating ischemic heart failure: the TRAIN-HEART story**. Front Cardiovasc Med. 10:1228160. https://doi.org/10.3389/fcvm.2023.1228160

Balamurali D, **Wrona KM**, Eich L, Witten A, Albert AM, Hirt MN, Eschenhagen T, Stoll M (2023) **GONE in 360 seconds: gentleMACS Octo Dissociator-based Nuclei Extraction**. Protocols.io. https://dx.doi.org/10.17504/protocols.io.dm6gp3bo8vzp/v1

Stenzig J, Lemoine MD, Stoter AMS**, Wrona KM**, Lemme M, Mulla W, Etzion Y, Eschenhagen T, Hirt MN (2022) **Recapitulation of dyssynchrony-associated contractile impairment in asymmetrically paced engineered heart tissue**. J Mol Cell Cardiol. 163:97-105. https://doi.org/10.1016/j.yjmcc.2021.10.001

Congress abstracts:

03/2023	Tissue Engineering & Regenerative Medicine International Society, Manchester, England; Poster presentation: “Modeling the cellular diversity of the human heart in engineered heart tissue”

I. List of publications

11/2022	American Heart Association Scientific Sessions, Chicago, USA; Oral presentation: “Human iPSC-derived multi-cell-type engineered heart tissues as an in vitro model to study pathological cardiac hypertrophy”
06/2022	XXIV World Congress International Society for Heart Research, Berlin, Germany; Poster presentation: “Human iPSC-derived multi-cell-type engineered heart tissues as an advanced model for pathological cardiac hypertrophy”
11/2021	American Heart Association Scientific Sessions, on-line; Oral presentation: “Characterization of multi-cell-type engineered heart tissues containing human iPSC-derived cardiomyocytes, endothelial cells, fibroblasts, smooth muscle cells and macrophages”

II. Table of content

III. List of abbreviations

A	
A	Atria
ActA	Activin A
ACTA1	Actin alpha 1
ACTA2	Actin alpha 2
AE	Afterload enhancement
Ang II	Angiotensin II
ANGPTL8	Angiopoietin-like protein 8
ANOVA	Analysis of variance
ANP	Atrial natriuretic peptide
AP	Action potential
APC	Allophycocyanin
APD$_{50}$	Action potential duration at 50% of repolarization
APD$_{90}$	Action potential duration at 90% of repolarization
Arg1	Arginase 1
ATP2A2	ATPase sarcoplasmic/endoplasmic reticulum Ca^{2+} transporting 2
AVN	Atrioventricular node
B	
BDM	Butanedione monoxime
BMP4	Bone morphogenetic protein 4
BNP	Brain natriuretic peptide
BSA	Bovine serum albumin
BTS	N-benzyl-p-toluene sulfonamide
C	
CaMKII	Ca^{2+} activate Ca^{2+}/calmodulin dependent kinase II
cAMP	Cyclic adenosine monophosphate
CASQ2	Calsequestrin 2
CBFHH	Calcium- and bicarbonate-free Hanks' solution with HEPES
CCN2	Cellular communication network factor 2
CCR2	Chemokine receptor type 2
CD14	Cluster of differentiation 14
CD31	Cluster of differentiation 31

CD34	Cluster of differentiation 34
CD36	Cluster of differentiation 36
CD45	Cluster of differentiation 45
CD68	Cluster of differentiation 68
CD80	Cluster of differentiation 80
CD86	Cluster of differentiation 86
CD90	Cluster of differentiation 90
CD144	Cluster of differentiation 144
CD206	Cluster of differentiation 206
CD309	Cluster of differentiation 309
cECs	Cardiac endothelial cells
CFs	Cardiac fibroblasts
cGMP	Cyclic guanosine monophosphate
CMs	Cardiomyocytes
c-Myc	MYC proto-oncogene
CNN-1	Calponin 1
CO	Carbon monoxide
CO_2	Carbon dioxide
Col1a1	Collagen type 1 alpha 1 chain
CTGF	Connective tissue growth factor
cTnI	Cardiac troponin I
cTnT	Cardiac troponin T
CVS	Cardiovascular system
Cx40	Connexin 40
Cx43	Connexin 43
D	
DAG	Diacylglycerol
DAPI	4',6-diamidyno-2-fenyloindol
DDR2	Discoidin domain receptor tyrosine kinase 2
DEGs	Differentially expressed genes
DMEM	Dulbecco’s modified Eagle medium
DMSO	Dimethyl sulfoxide
DNA	Deoxyribonucleic acid
dNTPs	Deoxynucleoside triphosphate

DPBS	Dulbecco's phosphate buffered saline
E	
EB	Embryoid body
ECM	Extracellular matrix
ECM1	Extracellular matrix protein 1
ECs	Endothelial cells
EDTA	Ethylenediaminetetraacetic acid
EGFR	Epidermal growth factor receptor
EGM	Endothelial Cell Growth Medium
EHM	Engineered human myocardium
EHT	Engineered heart tissue
EMT	Epithelial-mesenchymal transition
ET-1	Endothelin-1
F	
F	Forward
FACS	Fluorescence-activated cell sorting
FCS	Fetal calf serum
FDR	False discovery rate
FGF	Fibroblast growth factor
FITC	Fluorescein isothiocyanate
FSC	Forward scatter
FSC-A	Forward scatter area
G	
GA	Glutaraldehyde
GAPDH	Glyceraldehyde 3-phosphate dehydrogenase
GATA4	Transcription factor GATA4
GFP	Green fluorescent protein
GFR	Growth factor reduced
GM-CSF	Granulocyte macrophage colony-stimulating factor
GPCR	G protein coupled receptor
GSK-3β	Glycogen synthase kinase-3β
GUSB	β-Glucuronidase
H	
H_2O_2	Hydrogen peroxide

HBSS	Hanks' balanced salt solution
HE	Hemogenic endothelium
HEPES	4-(2-hydroxyethyl)-1-piperazineethanesulfonic acid
HF	Heart failure
HFF	Human foreskin fibroblasts
HIER	Heat induced epitope retrieval method
hiPSCs	Human induced pluripotent stem cells
HLA-DR	Human leukocyte antigen – DR isotype
HRT1	Hairy-related transcription factor 1
HRT2	Hairy-related transcription factor 2
I	
ICAM-1	Intercellular adhesion molecule 1
IEPT	Institute of Experimental Pharmacology and Toxicology
IF	Immunofluorescence
IFNγ	Interferon gamma
IL-1α	Interleukin 1α
IL-1β	Interleukin 1β
IL-3	Interleukin 3
IL-4	Interleukin 4
IL-6	Interleukin 6
IL-10	Interleukin 10
IL-12	Interleukin 12
iNOS	Inducible nitric oxide synthase
IP$_3$	Inositol trisphosphate
iPSCs	Induced pluripotent stem cells
IRX4	Iroquois homeobox gene 4
K	
Ki67	Antigen Kiel 67
Klf4	Kruppel-like transcription factor 4
KO	Knock out
L	
LIF	Leukemia inhibitory factor
LPS	Lipopolysaccharide
LV	Left ventricle

LYVE1	Lymphatic vessel endothelial hyaluronan receptor 1
M	
M	Molar
µM	Micromolar
Mφs	Macrophages
MACS	Magnetic-activated cell sorting
MCP-1	Monocyte chemoattractant protein-1
MCs	Mural cells
M-CSF	Macrophage colony-stimulating factor
MEF2A	Myocyte-specific enhancer factor 2A
Mertk	MER proto-oncogene, tyrosine kinase
MHC	Myosin heavy chain
MICS	MACSima Imaging Cyclic Staining
MIP-1α	Macrophage inflammatory protein 1α
MIP-2	Macrophage inflammatory protein 2
miRNA	MicroRNA
MLC2	Myosin light chain 2
MLC2a	Myosin light chain 2 (atrial)
MLC2v	Myosin light chain 2 (ventricular)
mM	Millimolar
MMPs	Matrix metalloproteinases
MMP-9	Matrix metalloproteinase-9
mN	Millinewton
MRC1	Mannose receptor C-type 1
mRNA	Messenger RNA
MTG	1-Thioglycerol
mTORC1	Mammalian target of rapamycin complex 1
MYH6	Myosin heavy chain 6
MYH7	Myosin heavy chain 7
MYH10	Myosin heavy chain 10
MYH11	Myosin heavy chain 11
N	
N_2	Nitrogen
Na_2HPO_4	Disodium hydrogen phosphate

NaCl	Sodium chloride
$NaHCO_3$	Sodium hydrogen carbonate
NFAT	Nuclear factor of activated T-cells
NGR-1	Neuregulin-1
NKM	Non-cardiomyocyte medium
nM	Nanomolar
NO	Nitric oxide
NPPA	Natriuretic peptide A
NPPB	Natriuretic peptide B
ns	Not significant
NT-proBNP	N-terminal pro–B-type natriuretic peptide
O	
O_2	Oxygen
Oct3/4	Octamer binding transcription factor 3/4
P	
PCA	Principal component analysis
PCR	Polymerase chain reaction
PDGF	Platelet-derived growth factor
PDGF-AA	Platelet-derived growth factor AA
PDGF-B	Platelet-derived growth factor B
PDGF-BB	Platelet-derived growth factor BB
PDGF-C	Platelet-derived growth factor C
PDMS	Polydimethylsiloxane
PE	Phenylephrine
PECAM-1	Platelet endothelial cell adhesion molecule-1
PFA	Paraformaldehyde
PGE_2	Prostaglandin E_2
PGI_2	Prostaglandin I_2
PI3K	Phosphoinositide 3-kinase
PIP_2	Phosphatidylinositol bisphosphate
PKA	Protein kinase A
$PKC\alpha$	Protein kinase $C\alpha$
PKG	cGMP-dependent protein kinase
PLC	Phospholipase C

PLN	Phospholamban
POSTN	Periostin
pp	Percentage point
PP2B	Protein phosphatase 2B
PTFE	Polytetrafluorethylene
PTPRC	Protein tyrosine phosphatase receptor type C
Q	
qPCR	Quantitative polymerase chain reaction
R	
R	Reverse
rEHT	Rat EHTs
RGS4	Regulator of G protein signaling 4
RMCs	Resident mesenchymal cells
RNA	Ribonucleic acid
RNA-seq	RNA sequencing
ROI	Region of interest
ROS	Reactive oxygen species
RPM	Revolutions per minute
RPMI	Roswell Park Memorial Institute
RT	Room temperature
$RT_{80\%}$	Relaxation time at 80% of peak height
RT-qPCR	Reverse transcription-quantative polymerase chain reaction
RYR2	Ryanodine receptor 2
S	
S100A4	S100 calcium binding protein A4
SA	Sinoatrial node
SALL1	Spalt-like transcription factor 1
SCF	Stem cell factor
scRNA-seq	Single-cell RNA-sequencing
SD	Standard deviation
SEM	Standard error of the mean
SERCA2a	Sarcoplasmic/endoplasmic reticulum Ca^{2+}-ATPase 2a
SHR	Spontaneously hypertensive rat
SIGLEC1	Sialic acid binding Ig like lectin 1

SIOP	Superparamagnetic iron oxide particles
Sox2	SRY (Sex determining region Y)-box 2
SM22-α	Smooth muscle protein 22-α
SMA	Smooth muscle actin
SMCs	Smooth muscle cells
snRNA-seq	Single nucleus RNA-sequencing
SSEA-3	Stage-specific embryonic antigen 3
T	
T_3	Triiodothyronine
TAC	Transverse aortic constriction
TAGLN	Transgelin
TBS	Tris-buffered saline
TBXT	T-box transcription factor T
TEM	Transmission electron microscopy
TGFβ1	Transforming growth factor beta-1
TIMP	Tissue inhibitors of metalloproteinases
TNF-α	Tumor necrosis factor alpha
TNNT2	Troponin T2, cardiac type
$TTP_{80\%}$	Time to peak at 80% peak height
U	
UKE	University Medical Center Hamburg-Eppendorf
V	
V	Ventricles
vECs	Vascular endothelial cells
VEGF	Vascular endothelial growth factor
VIM	Vimentin
VSMCs	Vascular smooth muscle cells
W	
WCB	Working cell bank
WNT	Wingless-related integration site
2D	Two-dimensional
3D	Three-dimensional
α-SMA	Alpha-Smooth Muscle Actin

1 Zusammenfassung

Die pathologische Hypertrophie des Herzens ist Folge von langanhaltendem kardialem Stress oder chronischer Herzerkrankungen. Sie geht mit einer verringerten Herzleistung einher und gilt als der beste Prädiktor für die Entstehung einer Herzinsuffizienz. Es besteht ein ungedeckter Bedarf an Modellen, welche die Veränderungen bei pathologischer Hypertrophie *in vitro* reproduzieren, um an diesen Modellen sowohl molekulare Mechanismen untersuchen als auch neuartige antihypertrophe Therapien evaluieren zu können. Die meisten aktuell verfügbaren Modelle besitzen jedoch Einschränkungen, z. B. die Verwendung von nur einem Zelltyp und meist die Nachbildung nur weniger der vielen Aspekte der pathologischen Hypertrophie. Angesichts der Bedeutung von Nicht-Kardiomyozyten für die Pathophysiologie der Herzhypertrophie wird in dieser Arbeit die Hypothese untersucht, dass Nicht-Kardiomyozyten unentbehrlich sind, um einen vollständigeren pathologischen Phänotyp im *In vitro*-Format nachzubilden. Der Fokus der vorliegenden Arbeit war somit die Etablierung verschiedener Multi-Zelltyp-i*n vitro*-Modelle auf der Grundlage von künstlichem Herzgewebe (EHT) und die Bewertung ihrer Reaktion auf pro-hypertrophe Stimuli.

Im ersten Teil des Projekts wurde ein Hybrid-EHT-Modell durch die Kombination humaner induzierter Stammzell-abgeleiteter Kardiomyozyten (hiPSC-CMs) mit Nicht-Kardiomyozyten aus Herzen neugeborener Ratten etabliert. Im Gegensatz zu hiPSC-CM-EHTs entwickelten Hybrid-EHTs schneller kontraktile Aktivität und zeigten ausgeprägtere Gewebeumbauprozesse. Die Kontraktionskräfte und Schlagfrequenzen der Hybrid-EHTs waren dagegen geringer. Um eine pathologische Hypertrophie zu induzieren, wurden bei beiden Arten von EHTs die Nachlast erhöht (*Afterload Enhancement* = AE). Eine 7-tägige AE provozierte jedoch in keinem der beiden EHT-Modelle Hypertrophie, sodass als nächster Schritt EHTs etabliert wurden, die auch humane Nicht-Kardiomyozyten enthielten. Infolgedessen wurde die Hypertrophieinduktion unter Anwendung verschiedener experimenteller Ansätze an vollständig humanen EHTs untersucht.

Somit wurde im zweiten Teil des Projekts ein hiPSC-basiertes Multi-Zelltyp-EHT-Modell etabliert. Vier kardiale nicht-kardiomyozytäre Zelltypen (Endothelzellen, Makrophagen, glatte Muskelzellen und kardiale Fibroblasten) wurden aus einer hiPSC-Zelllinie mittels

Zelltyp-spezifischer Protokolle differenziert. Nach erfolgreicher und verifizierter Differenzierung dieser Zelltypen wurden die Zellen zusammen mit hiPSC-CMs in Multi-Zelltyp-EHTs gegossen. In der Etablierungsphase des Multi-Zelltyp-Systems wurden die Zellzusammensetzung der EHTs sowie verschiedene Modifikationen des Zellkulturmediums untersucht. Im dann gewählten Kulturmedium (Standardmedium mit VEGF supplementiert) wurden Multi-Zelltyp-EHTs mit Uni-Zelltyp-EHTs (nur Kardiomyozyten) verglichen. Ähnlich wie in den Hybrid-EHTs führte das Hinzufügen von Nicht-Kardiomyozyten zu verstärktem Gewebeumbau und einem früheren Beginn der kontraktilen Aktivität. In den ersten drei Kulturwochen waren die Kräfte der Multi-Zelltyp-EHTs größer als die der Uni-Zelltyp-EHTs. Darüber hinaus waren deren Schlagfrequenzen höher und die Relaxationszeiten länger. In diesem Teil wurden zwei Methoden zur Induktion von Hypertrophie untersucht, pharmakologisch durch die prohypertrophe Substanzkombination PE+ET-1 (Phenylephrin und Endothelin-1) sowie durch AE. In beiden EHT-Modellen führte die PE+ET-1-Behandlung zu typischen Hypertrophie-begleitenden Phänomenen wie verringerten Kontraktionskräften oder einem Anstieg der NT-proBNP-Sekretion. Demgegenüber konnten andere Phänomene wie eine Hochregulation fetaler (*NPPA*, *NPPB*) oder Fibrose-assoziierter Gene nur in Multi-Zelltyp-EHTs beobachtet werden. Von entscheidender Bedeutung war zudem die weitere Beobachtung, dass eine Kardiomyozytenhypertrophie nur in Multi-Zelltyp-EHTs hervorgerufen werden konnte.

Die zweite Methode (AE) war hinsichtlich der Hypertrophieinduktion weniger wirksam als PE+ET-1. In Uni-Zelltyp-EHTs kam es lediglich zu verringerter Kraftentwicklung, während in Multi-Zelltyp-EHTs nur ein Anstieg der NT-proBNP-Sekretion hervorgerufen werden konnte. Diese unzureichende hypertrophe Antwort der EHTs, die AE ausgesetzt waren, konnte im Wesentlichen durch technische Limitationen dieser Methode und daraus resultierenden zu geringen EHT-Replikatzahlen erklärt werden.

Zusammenfassend wird in dieser Arbeit die erfolgreiche *in vitro*-Nachbildung des myokardialen Multi-Zelltyp-Aufbaus durch die Implementation von Nicht-Kardiomyozyten-Zelltypen in das EHT-System beschrieben. Neu etablierte Modelle wie Hybrid- sowie humane Multi-Zelltyp-EHTs zeigten im Vergleich zu Uni-Zelltyp-EHTs eine schnellere Entwicklung und einen beschleunigten Gewebeumbau. Die Eignung dieser EHT-Systeme zur Modellierung kardialer Hypertrophie durch PE+ET-1-Behandlung und AE wurde anschließend untersucht.

Letztlich konnten PE+ET-1-behandelte Multi-Zelltyp-EHTs die typischen Hypertrophie-Phänomene am besten nachbilden. Von großer Bedeutung ist, dass das zentrale Element der Hypertrophie, eine Vergrößerung der Kardiomyozyten, nur in EHTs hervorgerufen werden konnte, die humane Nicht-Kardiomyozyten enthielten, was die Bedeutung dieser Zellen für humane *in vitro*-Hypertrophie-Modelle unterstreicht. Darüber hinaus wurde eine Plattform zur Untersuchung der Pathophysiologie der kardialen Hypertrophie sowie zum *Drug-Screening* von antihypertrophen Substanzen *in vitro* geschaffen.

2 Summary

Pathological cardiac hypertrophy is a maladaptive response of the heart to chronic stress or disease. It is accompanied by reduced cardiac performance, and is considered to be the most important predictor of heart failure (HF). Thus, it is of clinical relevance to establish *in vitro* models that recapitulate the features of cardiac hypertrophy to study its molecular mechanisms and to test novel anti-hypertrophic therapeutics. However, the majority of currently utilized human models share common limitations, specifically, lack of cellular diversity and only partial demonstration of hypertrophic phenotype. Given the implications of non-cardiomyocytes (non-CMs) in the pathophysiology of cardiac hypertrophy, this thesis investigates the hypothesis of non-CM indispensability to recapitulate a more complete pathological phenotype in the *in vitro* format. For this purpose, the study presented here focused on the establishment of various multi-cell-type *in vitro* models based on engineered heart tissue (EHT) and evaluation of their response to pro-hypertrophic stimuli.

In the first part of the project, a hybrid EHT model was established by combining human induced pluripotent stem cell-derived cardiomyocytes (hiPSC-CMs) with non-CMs isolated from neonatal rat hearts. In comparison to hiPSC-CM EHTs, hybrid EHTs displayed more rapid development of contractile activity and more extensive tissue remodeling. Moreover, the hybrid EHTs generated lower contractile forces and beating frequencies than the hiPSC-CM EHTs. To induce pathological hypertrophy, both types of EHTs were subjected to increased afterload (AE: afterload enhancement). A 7-day-long AE failed to recapitulate hypertrophic features in both EHT models. Consequently, this result prompted experiments aiming to create EHTs containing non-CMs of human origin and evaluate different experimental procedures of hypertrophy induction in the EHT system generated entirely from human cells.

Therefore, in the second part of the project, a hiPSC-based multi-cell-type EHT model was established. Four non-CM populations, i.e., endothelial cells, macrophages, smooth muscle cells and cardiac fibroblasts were differentiated from one hiPSC line by application of cell-type-specific differentiation protocols. Following confirmation of the correct hiPSC-derivatives' phenotype, the non-CMs were cast together with hiPSC-CMs into

multi-cell-type EHTs. The establishment phase of the multi-cell-type system included evaluation of different cell densities in the EHTs as well as investigation of various modifications of the cell culture medium. In the chosen culture conditions (medium supplemented with VEGF), multi-cell-type EHTs were compared to CM-only EHTs. Similar to the results obtained in the hybrid EHT experiments, the presence of non-CMs in the tissues resulted in accelerated remodeling of the EHTs and earlier initiation of contractile activity. In the first three weeks of culture, the forces generated by the multi-cell-type EHTs were greater than the ones of CM-only EHTs. Moreover, multi-cell-type EHTs displayed higher beating frequencies and a longer relaxation time than their CM-only counterparts. In this part of the project, two methods to induce hypertrophy were evaluated, namely, pharmacological treatment with pro-hypertrophic compounds (PE+ET-1; PE: phenylephrine, ET-1: endothelin-1) and AE. In both EHT models, the PE+ET-1 treatment resulted in recapitulation of hypertrophic features such as decrease of contractile force and elevation of NT-proBNP secretion. However, other hypertrophic hallmarks, in particular, upregulation of fetal genes (*NPPA*, *NPPB*), increased expression of fibrosis-related genes and, importantly, CM enlargement could only be recapitulated in the multi-cell-type EHTs. The second method, AE, demonstrated lower efficiency in hypertrophy induction compared to PE+ET-1 treatment. In CM-only EHTs, the observed effect was limited to force reduction, whereas in multi-cell-type tissues only the elevation of NT-proBNP secretion could be recapitulated. The lack of hypertrophic characteristics in the tissues that underwent AE was mainly attributed to the technical restrictions of the method leading to low number of EHTs completing the experiments.

In summary, this thesis describes successful recapitulation of myocardial hetero-cellularity in the *in vitro* setting through implementation of non-CM populations into the EHT system. Newly established models, that is, hybrid EHTs and human multi-cell-type EHTs displayed accelerated development and remodeling in comparison to tissues solely composed of hiPSC-CMs. The ability of these EHT systems to reproduce the hypertrophic phenotype *in vitro* was evaluated via PE+ET-1 exposure or AE. The final results demonstrated the highest degree of recapitulation of the hypertrophic phenotype in the hiPSC-derived multi-cell-type EHTs stimulated with the PE+ET-1. More importantly, the hallmark of hypertrophy, i.e., CM enlargement, was recorded for the first time in the human EHT system and was found

exclusively in tissues containing hiPSC-derived non-CMs. This study demonstrates the importance of the non-CMs in the human cardiac *in vitro* models of pathological hypertrophy. Moreover, it provides a platform for further studies on the pathophysiology of cardiac hypertrophy and for drug screening of anti-hypertrophic compounds in the *in vitro* setting.

3 Introduction

3.1 Structure and function of the heart

The cardiovascular system (CVS) consists of the heart, blood vessels and blood. The CVS fulfills many important functions, the major one being transportation of nutrients, gases, hormones and enzymes throughout the body, alongside the removal of CO_2 and other waste products. The heart serves as a pump to circulate the blood with an average cardiac output at-rest of 5 – 6 L/min (King and Lowery 2023). It is composed of four chambers: right atrium, right ventricle, left atrium and left ventricle (Figure 1). The right atrium receives de-oxygenated blood from the body via the superior and inferior vena cava. The blood passes from the right atrium into the right ventricle through the tricuspid valve and is pumped out via the pulmonary artery to the lungs for O_2 and CO_2 exchange. The oxygen-rich blood is transported by pulmonary veins to the left atrium. Subsequently, the blood passes through the mitral valve into the left ventricle, which propels it through the systemic aorta to all the other tissues and organs.

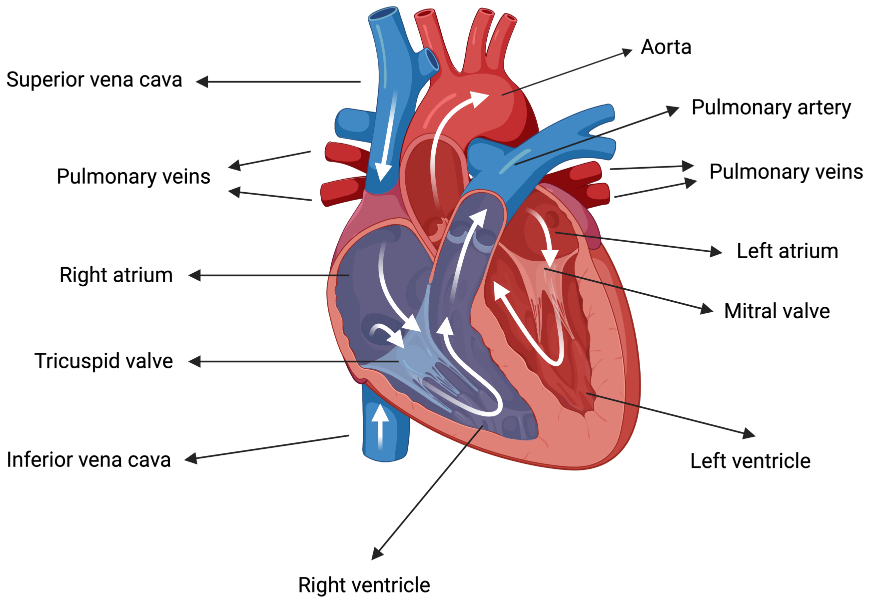

Figure 1 Anatomical structure of a human heart with representation of a blood flow through the chambers. Created with BioRender.com.

3.2 Cellular composition of the heart

3.2.1 Rat heart

Initial strategies to determine the cellular composition of the rat heart were based on morphometric and stereological methodologies. These approaches were adapted by Dämmrich and Pfeifer (1983) to investigate the cellular heterogeneity of adult rat heart. In these analyses, the highest volume of the subepicardial region of left ventricle (LV) was occupied by cardiomyocytes (CMs) (78.5% – 83.7%), followed by endothelial cells (ECs) (3.5% – 5.3%) and interstitial cells (1.2% – 1.7%) (Dämmrich & Pfeifer 1983). Although CMs were observed to cover a majority of the total cell volume, in further investigations performed on adult rat ventricular tissue with electron microscopy and gradient centrifugation, CMs were found to account for only 30% – 40% of all cardiac cells, whereas 60% – 70% were identified as non-cardiomyocytes (non-CMs) (Zak 1974; Nag 1980). Similar results were obtained when rat hearts at developmental day 15 were analyzed by flow cytometry with cell-type-specific antibodies. The analyzed tissues were found to comprise up to 64% of cardiac fibroblasts (CFs), 30% of CMs and the remaining 6% was assigned to a non-CF/non-CM fraction. Interestingly, at postnatal day 1, rat hearts were analyzed by flow cytometry and showed a distinct composition, with 30% being identified as CFs, 62% as CMs, and the remaining 8% were lacking the expression of CFs or CMs markers (Banerjee et al. 2007). These results demonstrate the significant changes in the cellular composition of the heart over the course of its development. The summary of above-described studies is presented in Table 1.

3.2.2 Human heart

Stereological analyses carried out on the LV of human hearts yielded results that were comparable to those obtained in the rat model. In particular, it was found that the CMs occupied approximately 70% of the LV volume (Tang et al. 2009). Further stereological studies on the LV showed dynamic changes of cellular composition during development. In the postnatal period, CMs were found to be the most abundant cell type in the LV tissue (66% ± 1.7%). Over the course of development, an increase of EC and resident mesenchymal cell (RMC) number was observed (by a factor of 6.5 and 8.2, respectively), whereas the number of CMs remained constant. These alternations were reflected in the analysis of the adult heart where 58% ± 5.6% of all cells were identified as RMCs, 24% ± 4.7% as ECs and only 18% ± 3.0% belonged to CM population (Bergmann et al. 2015). The lower frequency of CMs in the adult heart was further corroborated by the immunohistochemical analysis published by Pinto et al. (2016). The examination of a ventricular tissue revealed a cellular composition comprising of 31.2% ± 5.6% CMs, 53.8% ± 6.4% ECs and 2.8% ± 1.2% leukocytes. In this study, the number of RMCs could not be identified due to low antibody specificity (Pinto et al. 2016).

Another experimental method used to determine the frequencies of different cell types in the cardiac tissue is flow cytometry of enzymatically dispersed cells. The analysis performed on a fetal human heart demonstrated the highest prevalence of CMs (75% – 80%), followed by smooth muscle cells (SMCs)/CFs (10% – 15%), and ECs (10%). Moreover, 11% of the analyzed cells co-expressed CF and SMC markers, which could represent a mixed population of these two cell types or a myofibroblast population (Dewing et al. 2022). The flow cytometry analysis of an adult human heart, performed by Bergmann and colleagues (2015), demonstrated a decrease in CM content, previously shown by application of stereological methods. In this study, 43% ± 10% of isolated nuclei belonged to RMCs, whereas the 33% ± 15% and 24% ± 9.5% were assigned to CMs and ECs, respectively (Bergmann et al. 2015).

The advances in sequencing technologies allowed for the analysis of the heart at a single cell resolution by utilizing single-cell RNA-sequencing (scRNA-seq) technology. Cui and colleagues performed analyses of fetal human hearts at three different time points of the development: early (5 weeks – 7 weeks), mid-stage (9 weeks – 17 weeks) and late (20 weeks – 25 weeks). The results showed a decrease in CM content over time and an increase in fibroblast-like cells and immune cells, confirming the results obtained with stereological and flow cytometry methods (Cui et al. 2019). The analysis of an adult healthy human heart by single nucleus RNA-sequencing (snRNA-seq) revealed differences in cellular composition between distinct regions of the heart. In a study performed by Litviňuková and colleagues, the ventricular tissue (LV, RV, intraventricular septum and apex) was found to contain more CMs and mural cells (SMCs and pericytes) than atrial tissue. On the other hand, the atria were more abundant in CFs, ECs and immune cells. The comparison of female and male cardiac tissue showed no significant differences between the analyzed samples, which was further corroborated by studies of Koenig and colleagues (Litviňuková et al. 2020; Koenig et al. 2022). These studies suggest that the spatial distribution and specialization of different regions of the heart, rather than the sex of the tissue donor, is associated with differences in cellular composition in the human heart.

Table 1 Overview of the cellular composition of the rat heart

Species	Developmental stage	Material	Method	Estimated composition	Reference
Rat	Day 1	Whole heart	Flow cytometry	62% CMs, 30% CFs, 8% non-CMs/non-CFs	Banerjee et al. 2007
Rat	Day 15	Whole heart	Flow cytometry	30% CMs, 64% CFs, 6% non-CMs/non-CFs	Banerjee et al. 2007
Rat	Adult	LV	SEM, TEM, morphometric	30% – 35% CMs, 65% – 70% non-CMs	Zak 1974; Nag 1980
Rat	Adult	LV	Morphometric, stereological	78.5% – 83.7% CMs, 3.5% – 5.3% ECs, 1.2% – 1.7% interstitial cells	Dämmrich & Pfeifer 1983

CFs: cardiac fibroblasts, CMs: cardiomyocytes, ECs: endothelial cells, SEM: scanning electron microscopy, TEM: transmission electron microscopy

Table 2 Overview of the cellular composition of the human heart

Species	Developmental stage	Material	Method	Estimated cellular composition	Reference
Human	Adult	LV	Stereological	70% CMs, 30% non-CMs	Tang et al. 2009
Human	Adult	LV	Stereological	18% ± 3.0% CMs, 24% ± 4.7% ECs, 58% ± 5.6% RMCs	Bergmann et al. 2015
Human	Adult	V	Immunohisto-chemistry	31.2% ± 5.6 % CMs, 53.8% ± 6.4% ECs, 2.8% ± 1.2% leukocytes, RMCs N/A	Pinto et al. 2016
Human	Fetal (8w – 12w)	A + V	Flow cytometry	75% – 80% CMs, 10% – 15% SMCs/CFs, 10% ECs	Dewing et al. 2022
Human	Adult	LV	Flow cytometry	33% ± 15% CMs, 24% ± 9.5% ECs, 43% ± 10% RMCs	Bergmann et al. 2015

Human	Fetal (5w – 7w)	A + V	scRNA-seq	60.1% CMs, 14.6% CFs, 16.1% ECs, 6.4% pro-epicardial cells, 2.5% Mφs, 0.2% mast cells, 0.1% valvular cells, 0.1% T/B cells	Cui et al. 2019
Human	Fetal (9w – 17w)	A + V	scRNA-seq	52.1% CMs, 26.6% CFs, 12% ECs, 6.1% Mφs, 0.6% epicardial cells, 0.5% mast cells, 0.2% valvular cells, 2% T/B cells	Cui et al. 2019
Human	Fetal (20w – 25w)	A + V	scRNA-seq	38.4% CMs, 25.2% CFs, 10.8% ECs, 4.9% epicardial cells, 16.4% Mφs, 0.6% mast cells, 0.1% pro-epicardial cells, 3.6% T/B cells	Cui et al. 2019
Human	Adult	A	snRNA-seq	30.1% CMs, 24.3% CFs, 17.1% mural cells, 12.2% ECs, 10.4% immune cells	Litviňuková et al. 2020
Human	Adult	V	snRNA-seq	49.2% CMs, 15.5% CFs, 21.2% mural cells, 7.8% ECs, 5.3% immune cells	Litviňuková et al. 2020
Human (female)	Adult	LV	snRNA-seq	25.7% ± 14% CMs, 2.2% ± 0.7% SMCs, 16.8% ± 5.1% CFs, 18.3% ± 5.5% endothelium, 1.0% ± 0.9% lymphatic, 0.8% ± 0.4% neural, 0.7% ± 1.2% epicardium, 0.7% ± 0.6% mast cells, 0.1% ± 0.1% B cells, 0.5% ± 1.1% adipocytes, 12.2% ± 5.1% myeloid, 12.6% ± 4.6% pericytes, 6.5% ± 4.6% endocardium, 1.8% ± 1.2% T/NK cells	Koenig et al. 2022
Human (male)	Adult	LV	snRNA-seq	25.6% ± 13% CMs, 2.1% ± 0.7% SMCs, 19.8% ± 3.0% CFs, 14.6% ± 5.3% endothelium, 0.7% ± 0.5% lymphatic, 0.7% ± 0.4% neural, 0.8% ± 0.1% epicardium, 0.8% ± 0.5% mast cells, 0.1% ± 0.1% B cells, 0.5% ± 0.5% adipocytes, 13.4% ± 3.4% myeloid, 13.7% ± 6.5% pericytes, 5.8% ± 4.9% endocardium, 1.4% ± 1.1% T/NK cells	Koenig et al. 2022

A: atria, CFs: cardiac fibroblasts, CMs: cardiomyocytes, ECs: endothelial cells, LV: left ventricle, Mφs: macrophages, RMCs: resident mesenchymal cells, SMCs: smooth muscle cells, V: ventricles, w: week

3.3 Characterization of cardiac cell types

3.3.1 Cardiomyocytes

CMs are specialized muscle cells, which are responsible for the generation of the contractile force in the heart. They occupy around 70% of the ventricular volume and are exclusively found in the myocardial layer of the heart (Tang et al. 2009). The broad classification of CMs is based on their division into two groups: "working CMs", i.e., CMs belonging to the contractile myocardium and therefore responsible for contraction and relaxation of the heart, and the "non-working" CMs involved in generation and propagation of the electric signals in the heart (Grassam-Rowe et al. 2020). In the group of working CMs, depending on the location within the heart, two populations of CMs are identified: ventricular and atrial CMs. Ventricular CMs are larger and have higher numbers and more prominent T tubules compared to their atrial counterparts (Kane et al. 2017; Richards et al. 2011). Apart from location, size and structural differences, these two groups of CMs differ in their molecular profile. For instance, the expression of the hairy-related transcription factor 2 (HRT2) and iroquois homeobox gene 4 (IRX4) is associated with ventricular CMs, whereas hairy-related transcription factor 1 (HRT1), connexin 40 (Cx40) and sarcolipin are expressed predominantly in atrial CMs (Gaborit et al. 2007; Minamisawa et al. 2003; Ng et al. 2010). Most commonly the determination of the CM phenotype is based on the chamber-specific expression of myosin light chain 2 (MLC2), with MLC2a (MYL7) being uniquely expressed in the atria and MLC2v (MYL2) found exclusively in the ventricles (De Sousa Lopes et al. 2006; Ng et al. 2010).

The "not-working CMs" can be further subdivided into pacemaking cells and conductive cells. Pacemaker cells are located in the sinoatrial and the atrioventricular node (AVN). These cells appear small in size, with low abundance of sarcomere structures, no intercalated disks and less abundant sarcoplasmic reticulum (James et al. 1966). The most relevant feature of pacemaking cells is the presence of spontaneous depolarization which triggers rhythmic action potentials (APs) (Kane & Terracciano 2017). The conductive CMs, also referred as Purkinje cells, are located in the conduction system of the heart. These cells are characterized as large-sized and cylindrical-shaped with well-developed intercalated disks. Similarly to pacemaking cells, Purkinje cells lack organized sarcomere and myofibrillar structures (Ono et al. 2009). The main function of Purkinje cells is the conduction and propagation of electrical impulses to the ventricular myocardium (Dun & Boyden 2008). Compared to the cells of the ventricles, Purkinje cells display a distinct expression pattern of genes associated with calcium handling, e.g., low expression of *ATP2A2*, *CASQ2* or *RYR2* (Gaborit et al. 2007).

3.3.2 Endothelial cells

The high metabolic activity of CMs in the heart requires constant supply of nutrients and oxygen and removal of metabolic waste. This demand is met through a network of blood vessels with ECs forming their inner lining. The ECs can be divided into two groups: 1) the coronary vascular endothelial cells (vECs), which are found in epicardial and intramyocardial coronary arteries and veins, 2) cardiac endothelial cells (cECs), which contribute to myocardial capillaries and endocardial endothelium. Both of these endothelial cell populations demonstrate distinct effects on the cardiac functions. The vECs are in direct contact with the components of the blood and regulate vascular constriction and relaxation, hence they control the coronary myocardial blood supply (Brutsaert 2003; Krüger-Genge et al. 2019). In contrast, cECs that build the myocardial capillaries and endocardial endothelium are located in close proximity to CMs and facilitate direct cell-to-cell communication (Brutsaert 2003). The cECs secrete paracrine factors that can regulate cardiac development. For instance, neuregulin-1 (NRG-1) secreted by endocardial endothelium is required for the formation of myocardial trabeculae and cardiac cushions, and the combination of NRG-1 and insulin growth factor 1 (IGF-1) promotes the expansion of the ventricular compact zone and the atrioventricular cushion tissue (Hertig et al. 1999; Hsieh et al. 2006). Alongside the well-described effect of cECs in the embryonic cardiogenesis, cECs are known to play an important role in regulation of cardiac contraction and survival in mature myocardium. One of the most studied cEC-derived factors is nitric oxide (NO). The effect of NO on cardiac contractility is strongly dependent on the NO concentration. In low concentrations, NO exhibits a positive inotropic effect, in contrast to high concentrations, which were shown to decrease the contractile force (Mohan et al. 1996).

Cardiac contractility can also be affected by cEC-derived endothelin-1 (ET-1). The effect of ET-1 on contractility varies across different species and their developmental stage. The positive inotropic effect was observed in neonatal mice expressing high levels of ET-1 receptors, however in the adult mice with low expression of ET-1 receptors, this effect was reversed. Moreover, a long-term stimulation with ET-1 was shown to induce hypertrophic phenotype (Drawnel et al. 2012; Moravec et al. 1989).

In addition to regulating cardiac contractility, the endothelial proteins can affect CM survival. For instance, platelet derived growth factor-B (PDGF-B) demonstrated an anti-apoptotic effect on CMs through phosphatidylinositol-3-kinase-Akt signaling, whereas angiopoietin-1, exhibited a cardioprotective effect by limiting the ischemia-induced cardiac injury in rats (Hsieh et al. 2006; Takahashi et al. 2003).

3.3.3 Macrophages

Macrophages (Mφs) are the most abundant immune cells identified in the resting heart. Morphologically, Mφs appear as spindle-shaped cells found mostly in myocardial interstitial spaces in close proximity to ECs and CMs (Pinto et al. 2012). Based on the expression of C-C chemokine receptor type 2 (CCR2), two distinct Mφ sub-populations can be identified. $CCR2^-$ Mφs originate from the embryonic yolk sack and are maintained in the tissue through self-renewal (Bajpai et al. 2018). The second identified subtype is the $CCR2^+$ Mφs. This Mφ subpopulation arises from definitive hematopoiesis progenitors and is maintained through the monocyte recruitment and proliferation (Bajpai et al. 2018). Given the distinct origins and maintenance forms, the $CCR2^-$ Mφs are often referred to as “resident” macrophages, whereas the $CCR2^+$ Mφs are designated as the “non-resident” population (Sansonetti et al. 2020). In the non-diseased heart, the resident Mφs outnumber the monocyte-derived fraction. However, as the heart ages, resident population of Mφs declines and is progressively replaced by the monocyte-derived Mφs (Molawi et al. 2014). Interestingly, the distinct Mφs subtypes are also associated with different functions in the heart. The resident Mφs play an important role in coronary development and the remodeling of the primitive coronary plexus (Leid et al. 2016). Furthermore, they have been shown to express various growth factors (IGF1, PDGF-C), extracellular matrix (ECM) components (SLYT3, ECM1) and tissue macrophage markers (LYVE1). In contrast, the monocyte-derived Mφs display high expression of pro-fibrotic and hypertrophic factors as well as the genes encoding for the ECM degradation machinery, e.g., matrix metalloproteinase-9 (MMP9). Overall, the phenotype associated with resident Mφs has been described as reparative, promoting tissue repair, whereas the monocyte-derived Mφs show pro-inflammatory characteristics (Bajpai et al. 2018; Epelman et al. 2014).

An intrinsic feature of Mφs is their ability to change the phenotype in response to external stimuli. An *in vitro* stimulation with lipopolysaccharide (LPS) and interferon γ (IFNγ) leads to induction of a pro-inflammatory phenotype, also referred to as M1 phenotype or classically activated Mφs. This polarization state is characterized by increased expression of co-stimulatory molecules like CD80, CD86 and an upregulation of pro-inflammatory cytokines/chemokines such as IL-1α, IL-1β, IL-6, TNFα and IL-12. Moreover, classically activated Mφs produce reactive oxygen species (ROS) and NO. The M1 phenotype is involved in antigen presentation and microbial and tumoral clearing (Orecchioni et al. 2019; Viola et al. 2019). Conversely, the stimulation of Mφs with IL-4 results in the transition to an anti-inflammatory phenotype, commonly named M2 or alternatively activated Mφs. The signature markers of M2-Mφs include CD36, MRC1, TGFβ, IL-10 and Arg1 (Orecchioni et al. 2019). The cytokines produced by alternatively activated Mφs are involved in resolution of inflammation and phagocytosis of apoptotic cells. Additionally, alternatively activated Mφs are associated with fibrotic events, through production of pro-fibrotic factors, namely TGFβ and PDGF, that can induce the transition of fibroblasts into myofibroblast. Mφs were shown to modulate the ECM content by secretion of MMPs and tissue inhibitors of matrix metalloproteinases (TIMPs) as well as directly by collagen production at the site of injury (Simões et al. 2020; Wynn & Barron 2010).

The canonical role of Mφs is phagocytosis, a process in which particles between 0.5 μm – 10 μm are taken up and eliminated. The nature of the ingested material can range from external particles, microorganisms (e.g., bacteria, yeast) to apoptotic and necrotic cells (Uribe-Querol & Rosales 2020) and even CM-derived debris (Nicolás-Ávila et al. 2020). Phagocytosis removes excessive tissue/cell during development or eliminates cells that were no longer functional due to damage or apoptosis (Li et al. 2021). The studies on heart development showed that endocardial Mφ phagocytic activity is required for normal valvular remodeling, and inefficient clearing of apoptotic cells led to activation of mesenchymal cells and abnormal valvular phenotypes (Shigeta et al. 2019). In the adult heart, due to cellular turnover, Mφs are responsible for elimination of apoptotic and necrotic cells in order to maintain homeostasis. Dysregulation of this process results in accumulation of cellular debris and induction of an inflammatory response. Macrophage phagocytic activity is specifically important after cardiac injury, when impaired removal of necrotic CMs could lead to maladaptive tissue remodeling and functional defects (Li et al. 2021). Absence of Mφs or a deficiency in the phagocytic reporter Mertk was shown to activate the inflammasome and ultimately result in impaired ventricular function (Nicolás-Ávila et al. 2020).

Moreover, cardiac Mφs are involved in facilitation of electrical conduction in the heart. High abundance of Mφs was identified in the AVN, where Mφs were in direct contact with CMs through gap junctions. When co-cultured, Mφs modulated the properties of CMs by elevating their resting membrane potential and shortening the action potential duration at 90% repolarization (APD_{90}). Additional experiments with macrophage-specific knockout (KO) of connexin 43 (Cx43) corroborated direct contribution of Mφs to facilitate the conduction in the heart (Hulsmans et al. 2017).

3.3.4 Cardiac fibroblasts

CFs are one of the main cellular components of the heart. They are characterized as flat and spindle shaped cells with well-defined Golgi apparatus and high level of granular content in the cytoplasm. The specific feature of CFs is the lack of basal membrane and presence of multiple processes or sheet-like extensions. CFs are found in the endomysial collagen network surrounding the muscle fibers or individual CMs. The structural organization of CFs allows them to contract the endomysial collagen and employ mechanical force on the CMs (Baudino et al. 2006). The primary functions of CFs include the maintenance of the structural integrity of the heart by regulation of ECM turnover and direct cellular and ECM interactions. CFs are responsible for synthesis of the ECM components, such as collagen types I, III, IV, V, VI, elastin, laminin and fibronectin. In addition to the direct contribution to ECM generation, CFs regulate the ECM turnover by production of ECM-modifying proteins, i.e., MMPs and TIMPs. MMPs degrade the components of ECM, whereas TIMPs inhibit the activity of MMPs. The CF-controlled balance between the activity of MMPs and TIMPs ensures the ECM homeostasis in the heart (Moore et al. 2012).

Following an injury, CFs transition into an activated state and undertake a phenotypic and functional change into myofibroblasts. Morphologically, myofibroblast are characterized by increased cytoplasmic content, serrated nuclei and abundant stress fibers (Gabbiani et al. 1972). Moreover, myofibroblasts demonstrate altered functional features such as increased proliferation and elevated production of ECM components. On the molecular level, myofibroblast were shown to express the markers of SMCs, for instance α-myosin smooth muscle actin (α-SMA) and transgelin (TAGLN). The presence of α-SMA allows for the constriction of myofibroblast enabling them to apply contractile force on the ECM (Gabbiani 2003). Additionally, myofibroblasts produce and secrete a variety of factors such as chemokines (e.g., IL-1α and β, IL-6, IL-10, TNF-α), cytokines (e.g., MCP-1, MIP-1α, MIP-2), growth factors (e.g., M-CSF, FGF-2, GM-CSF, PDGF-AA, PDGF-BB, SCF, TGFβ) and inflammatory mediators (e.g., CO, H_2O_2, NO, PGE_2, prostacyclin) (Baum & Duffy 2011). The transformation of CFs into myofibroblasts is mediated by various paracrine factors including TGFβ, angiotensin II (Ang II), ET-1 and IL-6. However, it has been shown that mechanical stimuli, e.g., increased stiffness of the environment or application of static tensile forces can also lead to CF activation (Hall et al. 2021; Kawano et al. 2000; Schmitt-Gräff et al. 1994; Wang et al. 2003). In the heart, the transformation of CFs into myofibroblasts occurs in response to injury. The reparative actions of myofibroblasts include the production of ECM in formation of a scar, preventing the rupture of the heart wall. After resolution of the injury, myofibroblasts are cleared out by apoptosis. However, a number of studies suggests a possible dedifferentiation or reversal of the myofibroblast phenotype towards non-activated CFs (Hecker et al. 2011). Nevertheless, prolonged myofibroblast activation and proliferation leads to a fibrotic state and impairs the contractile functions of the heart.

Except the immanent role of CFs in maintaining the ECM homeostasis and involvement in reparative responses, CFs regulate the properties of CMs via direct cell-to-cell contacts. The cellular interactions between CMs and CFs are facilitated through gap junctions and nanotubes. It was shown, that in a state of cardiac injury, CFs can couple to each other and to CMs providing the electrical conductivity of the scar (Vasquez et al. 2010). On the other hand, the connection of these two cell types through nanotubes allows for direct exchange of organelles (mitochondria) and Ca^{2+} between CMs and CFs (He et al. 2011). The CFs were also shown to interact with the other non-CM populations in the heart. In case of ECs, the

CF-produced fibroblast growth factors (FGFs) exhibit strong pro-angiogenic effects, whereas the ECM provides stabilization of capillaries. Moreover, CF-derived chemokines and cytokines regulate chemotaxis and migration of inflammatory cells, e.g., granulocyte macrophage-colony stimulating factor (GM-CSF) produced by myofibroblasts instructs Mφs to recruit neutrophils and monocytes to the injury site (Anzai et al. 2017).

3.3.5 Vascular smooth muscle cells

Vascular smooth muscle cells (VSMCs, hereinafter referred to as SMCs) are the main component building the middle part of the blood vessels. The SMCs are arranged around the vascular lumen and can form up to 60 layers in large vessels (Bacakova et al. 2018). The main function of the SMCs is modulation of blood flow and pressure through vascular resistance (Hafen & Burns 2023). The properties of SMCs can be regulated by endothelial-derived factors. For instance, NO secreted by ECs promotes vasodilation via cyclic guanosine monophosphate (cGMP) pathway and activation of cGMP-dependent protein kinase (PKG), which subsequently causes a decrease in intracellular calcium concentration and relaxation (Lincoln et al. 1996). Similar actions have been described for another factor produced by ECs, prostaglandin I_2 (PGI_2). PGI_2 generates cyclic adenosine monophosphate (cAMP) and activates protein kinase A (PKA). This leads to a decrease in intracellular calcium levels, and resuts in vasodilation (Mitchell et al. 2008). Under physiological conditions, the majority of SMCs display a non-proliferative, contractile phenotype responsible for modulation of vasoconstriction and vasodilation. However, in response to stress, injury or inflammation SMCs undergo phenotypic changes, acquiring more proliferative, dedifferentiated state, referred to as a synthetic phenotype (Zhuge et al. 2020). The contractile phenotype is characterized by the elongated, spindle-shape morphology, high expression of contractile proteins and limited proliferation and migration properties (Owens 1995; Rensen et al. 2007). The commonly used markers of contractile SMCs are myosin heavy chain 11 (MYH11), α-SMA, smoothelin and calponin-1 (CNN-1). In contrast, the synthetic SMCs have less elongated and cobble stone morphology. Moreover, they display high proliferative and migratory activity as well as increased production of ECM components such as collagen and elastin (Cao et al. 2022; Rensen et al. 2007). The synthetic SMCs do not express the contractile proteins and are associated with the expression of tumor necrosis factor-alpha (TNF-α), S100A4 and monocyte chemoattractant protein-1 (MCP-1) (Jaminon et al. 2019). The phenotype switching can be modulated by a variety of different factors. For instance, TGFβ has been shown to promote the contractile phenotype by increasing the expression of contractile proteins, specifically α-SMA, MHC and CNN-1 (Hao et al. 2002; Hautmann et al. 1997; Jaminon et al. 2019). In contrast, stimulation of SMCs with platelet-derived growth factor (PDGF) downregulates the expression of α-SMA and induces the proliferation of the cells, therefore leading to a switch towards the synthetic phenotype (Hao et al., 2002; X. Li et al., 1997). In addition to biochemical factors, phenotype transition can be affected by the components of ECM, biophysical factors, transcriptional regulators and microRNAs (miRNAs) (Zhuge et al. 2020).

3.4 Cardiac hypertrophy

3.4.1 Characterization of cardiac hypertrophy

Increased workload, caused by physiological or pathological stimuli, results in adaptive changes in the heart leading to an increase in its size and mass referred to as hypertrophy. The increase of ventricular wall thickness decreases the wall tension and therefore increases the contractile performance that allows for maintaining cardiac functions (Maillet et al. 2013). Depending on the nature of the stimuli, two types of hypertrophies are identified: physiological and pathological. Physiological hypertrophy occurs during postnatal growth, pregnancy or as a result of prolonged/intensive exercise. On the contrary, the cause of pathological hypertrophy lays in abnormal conditions such as hypertension, aortic stenosis (pressure overload), mitral and atrial regurgitation (volume overload), myocardial hypoxia or inherited diseases (e.g., hypertrophic cardiomyopathy) and progresses into maladaptive remodeling and heart failure (HF) (Bernardo et al. 2010). The common feature of pathological and physiological hypertrophy is the increase of CM size due to addition of sarcomere units. However, depending on the type of hypertrophy and triggering stimuli, two forms of geometries in the heart and CMs are described. The first one, concentric hypertrophy, typically observed in the pathological type of hypertrophy, is characterized by promotion of CM thickening over lengthening, leading to an increase in ventricular wall thickness and contribution to a reduction of the chamber dimensions. The second one, eccentric hypertrophy, can be associated with physiological as well as pathological hypertrophy. In the physiological type, the eccentric growth results in increase in CM width and length, leading to coordinated thickening of ventricular wall and septa. Conversely, the eccentric growth in pathological hypertrophy contribute to CM lengthening and promotion of chamber dilation (Maillet et al. 2013; Nakamura & Sadoshima 2018).

One of the features discriminating between physiological and pathological type of hypertrophy is the effect on cardiac function. In case of physiological hypertrophy, its state is reversible and contractility of the myocardium is preserved or increased, whereas the pathological phenotype is irreversible and is associated with decreased contractile performance of the heart (Bazgir et al. 2023). Moreover, pathological hypertrophy is marked by presence of fibrotic changes and apoptosis of the CMs, which impairs the systolic and diastolic properties of the myocardium. Another feature typical for the pathological type of hypertrophy is an activation of the fetal gene program, for instance, upregulation of *NPPA*, *NPPB*, *ACTA1* and *MYH7*, which were found to be unchanged or downregulated in physiological hypertrophy (Iemitsu et al. 2001; Takahashi et al. 1992). Also, the secretion of *NPPB*-encoded N-terminal pro-BNP (NT-proBNP) was identified to be exclusively elevated in the pathological hypertrophy (Dunn et al. 2017; Scharhag et al. 2004). Lastly, only the pathological type of hypertrophy is associated with dysregulation of calcium homeostasis in CMs, manifested by alterations of genes encoding for calcium handling proteins (Maillet et al. 2013).

Table 3 Comparison of physiological and pathological hypertrophy

Type / Feature	Physiological hypertrophy	Pathological hypertrophy
Triggering stimuli	Postnatal growth, pregnancy, exercise	Hypertension, aortic stenosis, mitral and atrial regurgitation, myocardial hypoxia, inherited diseases
Increase in CM size	Yes	Yes
Cardiac function	Normal/improved	Impaired
Phenotype	Reversible	Irreversible
Fibrosis	No	Yes
Activation of fetal gene program	No	Yes
Calcium homeostasis	Unchanged	Impaired
Elevation of NT-proBNP	No	Yes

It is important to note that presented characterization demonstrates a simplified correlation of certain features to only one hypertrophy type. However, phenotypes observed in clinical settings occasionally demonstrate mixed phenotypes displaying a combination of the traits associated with both hypertrophy types, e.g., cardiac fibrosis in athletes or partial regression of pathological hypertrophy (van de Schoor et al. 2016; Hou & Kang 2012).

3.4.2 Role of non-CMs in cardiac hypertrophy

Although CMs are the main focus of cardiovascular research, increasing evidence of the contribution of non-CMs on the development and pathophysiology of cardiac hypertrophy is described in the literature. The most relevant aspects are further presented in the following sections.

3.4.2.1 Endothelial cells

In response to hypertrophic stimuli, ECs exhibit the capacity for activation and regulation of hypertrophic signaling. One of the most studied endothelium-derived molecules is NO. The canonical effect of NO in CMs includes production of cGMP and subsequent activation of PKG, which inhibits the calcineurin-NFAT signaling, therefore attenuates the pathological hypertrophic response (Wollert et al. 2002). Furthermore, in a study performed by Jaba and colleagues, the induction of myocardial angiogenesis elevated the levels of released NO, and led to NO-dependent CM growth. The identified signaling pathway demonstrated NO-induced degradation of regulator 4 of G protein signaling (RGS4) leading to activation of Gβγ/PI3Kγ/Akt/mTORC1. Although NO was associated with an increase in CM size, no further features of pathological hypertrophy, e.g., reduced contractility, reactivation of fetal genes or fibrosis were detected in mice with elevated capillary density. Therefore, the observed phenotype was rather resembling the physiological type of hypertrophy (Jaba et al. 2013). Apart from NO, ECs are a source of another hypertrophy-regulating factor, i.e., ET-1. ET-1 can be also secreted by CFs and CMs, therefore acting in an autocrine and paracrine manner (Bazgir et al. 2023). A short-term treatment with ET-1 elicits a positive inotropic effect on CM contractility. However long-term stimulation demonstrated activation of hypertrophic signaling (Drawnel et al. 2012; Moravec et al. 1989; Yamazaki et al. 1996). Other endothelium-derived factors exhibiting pro-hypertrophic effects include Ang II, IL-6, IL-1β, and leukemia inhibitory factor (LIF) (Segers et al. 2018).

In addition to the secretion of proteins involved in development of hypertrophy, ECs contribute to a pathological phenotype by regulating fibrosis. The impact of ECs on fibrotic events lies in the promotion of inflammation (recruitment of immune cells through expression of chemokines and adhesion molecules), secretion of pro-fibrotic factors (e.g., ET-1, TGFβ, CTGF, FGF) and direct contribution to myofibroblast population by endothelial-to-mesenchymal transition (Kuwahara et al. 2003; Salvador et al. 2015; X. Yang et al. 2023; Zeisberg et al. 2007).

3.4.2.2 Macrophages

As described in section 3.3.3, Mφs are a heterogenous cell population within which numerous phenotypes can be identified. Distinct populations of Mφs have been shown to be activated in different stages of hypertrophy. In the model of pressure overload, the expansion of $CCR2^-$ Mφs was most prominent during the first week of hypertrophy (compensated phase) and was followed by infiltration of the myocardium by monocytes in the late phases (decompensated phase). The depletion of resident Mφs before TAC resulted in acute HF and high post-operational mortality. Thus, it demonstrates beneficial effects of resident Mφs in the early stages of hypertrophy (Liao et al. 2018). Further depletion effects included increased fibrosis and reduced microvascular density in TAC-operated hearts at 1 week after surgery, showing antifibrotic and pro-angiogenic potential of resident Mφs. Mφs isolated from TAC-operated mice produced high levels of pro-inflammatory cytokines, such as TNF-α, IL-6, IL-1β and MCP-1 (Revelo et al. 2021). In the pressure overload model, intercellular adhesion molecule 1 (ICAM-1) expressed by ECs of the intramyocardial arteries was found to mediate recruitment of Mφs (Kuwahara et al. 2003). Mφs were shown to accumulate in the perivascular spaces, where they colocalize with CFs and produce pro-fibrotic factors, including IL-10 and TGFβ, and promote transformation of CFs into myofibroblasts (Hinglais et al. 1994; Kuwahara et al. 2004). Additionally, microRNA-155 (miRNA-155), preferentially produced by Mφs stimulated with pro-inflammatory factors such as LPS or IFNγ, was found to promote further inflammation and induce hypertrophy in a model of pressure overload (Heymans et al. 2013).

3.4.2.3 Cardiac fibroblasts

Under mechanical stress, CFs become activated and transition into myofibroblasts. The myofibroblasts overproduce ECM components, which in turn cause increased stiffness of the myocardium and diastolic dysfunctions (Chaturvedi et al. 2010). Progressive fibrosis might lead to a disruption of electrical coupling between CMs and to increase of the oxygen diffusion distance in the myocardium promoting hypoxic conditions and functional impairments of CMs (Sabbah et al. 1995; Spach & Boineau 1997). Furthermore, CFs are a source of various pro-hypertrophic factors, e.g., TGFβ, FGF-2 and connective tissue growth factor (CTGF) (Cartledge et al. 2015; Chen et al. 2000; Parker et al. 1990). The regulation of hypertrophic responses by CFs is not only limited to ECM production and growth factor secretion. It has been shown that CFs can communicate with CMs through secretion of exosomes. Bang et al. identified fibroblast-derived exosomes loaded with passenger strands of miRNA. MicroRNA profiling identified miRNA-21-3p as the most enriched miRNA in these exosomes. Incubation of CMs with miRNA-21-3p led to a hypertrophic response, demonstrated by a significant increase in CM size. Moreover, inhibition of miRNA-21-3p in CMs treated with Ang II prevented the establishment of a hypertrophic phenotype (Bang et al. 2014).

3.4.2.4 Smooth muscle cells

Smooth muscle cell dysregulation and vascular remodeling is associated with pathogenesis of a major hypertrophy risk factor, i.e., hypertension. SMCs respond to pro-hypertensive stimuli, e.g., activation of renin-angiotensin-aldosterone system or oxidative stress, by sustained constriction resulting in elevation of blood pressure. Additionally, it was demonstrated that in hypertension, SMCs can undergo dedifferentiation and adapt a proliferative/migratory phenotype. This causes ECM overproduction, accumulation of SMCs in the vascular wall and elevated vascular stiffness (Touyz et al. 2018). Further studies on the relation of SMCs to hypertrophy were based on KO models of genes expressed by SMC and their effect on hypertrophy. For instance, it was shown that deletion of a gene encoding angiopoietin-like protein 8 (*ANGPTL8*) in SMCs attenuated the effect of Ang II on induction of hypertension and cardiac hypertrophy (Jiao et al. 2023).

3.4.3 Experimental models to study cardiac hypertrophy

3.4.3.1 Animal models

Pathological cardiac hypertrophy is a common widespread risk factor for the development of HF. Several experimental models have been developed to study this condition in the laboratory environment. The most commonly used small animal models to investigate cardiac hypertrophy are rats and mice. The use of rats in the research on cardiac hypertrophy and its transition into HF dates back to 1963 and the establishment of spontaneously hypertensive rat (SHR) (Okamoto & Aoki 1963). Due to elevated blood pressure over long period of time, the SHR develop progressive LV hypertrophy, alongside contractile dysfunction, fibrosis and upregulation of hypertrophic genes (Conrad et al. 1995; Iemitsu et al. 2001). However, it has been shown that a minimum of 12 months is required to establish a full manifestation of pathological hypertrophic phenotype with systolic dysfunction, and “clinical” HF can only be observed in animals that reached 18 – 24 months of age (Boluyt et al. 1995). The time- and cost-consuming experiments utilizing the SHR led to establishment of new approaches demonstrating more rapid development of pathological hypertrophic phenotype. One prominent example is transverse aortic constriction (TAC) model. TAC is commonly performed in rodents and it is based on application of a permanent constriction on the aortic arch leading to pressure increase in the LV. The pressure-overload causes pathological remodeling and cardiac hypertrophy that ultimately progresses into HF (Rockman et al. 1991). The manifestation of a hypertrophic phenotype is typically observed within 1 – 2 weeks post-surgery. However, the onset of a pathological phenotype also depends on the level of constriction (deAlmeida et al. 2010). The utilization of rodents to study pathological hypertrophy has many advantages including low maintenance cost, higher availability of biological material and ability to generate genetic models. However, major differences between human and rodent cardiovascular physiology were identified in terms of heart architecture, beating frequencies or expression of cardiac proteins (Milani-Nejad & Janssen 2014). Large animals such as sheep, dogs, cats, and pigs better recapitulate the human physiology and therefore are considered more accurate models to study human pathologies, including pressure overload-induced hypertrophy. The surgical procedures adapted in order to induce pressure-overload hypertrophy in large animals are mainly based on aortic banding placed on the aorta (the ascending aorta, the descending aorta or the aortic arch) (Beslika et al. 2024). Large animal models offer the advantage of physiological similarity to humans. However, their use is limited by high maintenance costs and labor-intensive nature.

Despite all the benefits of utilizing animal models to study cardiovascular diseases, the prevailing approach is to minimize animal use in scientific research, aligning with the principles of 3R: Replacement, Reduction and Refinement (Russell et al. 1959). Therefore, increasing efforts are undertaken in order to recapitulate the aspects of pathological hypertrophy in the *in vitro* settings with the use of cell culture techniques and tissue engineering.

3.4.3.2 *In vitro* models based on primary cells

First *in vitro* studies on cardiac hypertrophy were established in rodent cells. Most of the research utilized 2D culture of neonatal and adult rat CMs stimulated with pro-hypertrophic compounds, for instance PE or Ang II. The treatment was shown to induce CM enlargement and reactivation of fetal genes, such as *NPPA* and *NPPB* (Liu et al. 1998; Miller et al. 2009; Sadoshima & Izumo 1993; Watkins et al. 2012). However, uni-cell-type cultures and 2D format do not resemble the complexity of native cardiac environment, hence further effort on establishing a 3D multi-cell-type model of pathological hypertrophy was exerted.

One of the examples of a 3D cardiac tissue is engineered heart tissue (EHT). EHT is a form of lab-generated tissue enabling long-term culture of cardiac cells in a 3D format (Eschenhagen et al. 1997). Over the years, numerous modifications of the original model have been introduced (Weinberger et al. 2017). In the most commonly used form, EHTs consist of a fibrin scaffold and cells dispersed throughout the construct. Tissues are anchored to two silicone pillars. Once EHTs start to spontaneously beat, they exert the force on the posts, causing them to phasically bend toward each other. The extent of the post deflection can then be recalculated to the force generated by the EHTs. By using a video-optical device with regulated temperature and gases, the functional performance of the tissues can be monitored throughout the time of culture (Hansen et al. 2010). The EHT format provides long-term cultivation of cardiac tissues with higher structural complexity and higher grade of recapitulation of the native cardiac tissue. Among many applications, EHTs allow for testing the effects of pharmacological compounds not only on the molecular level but also to determine their effects on the functionality of the cardiac tissues.

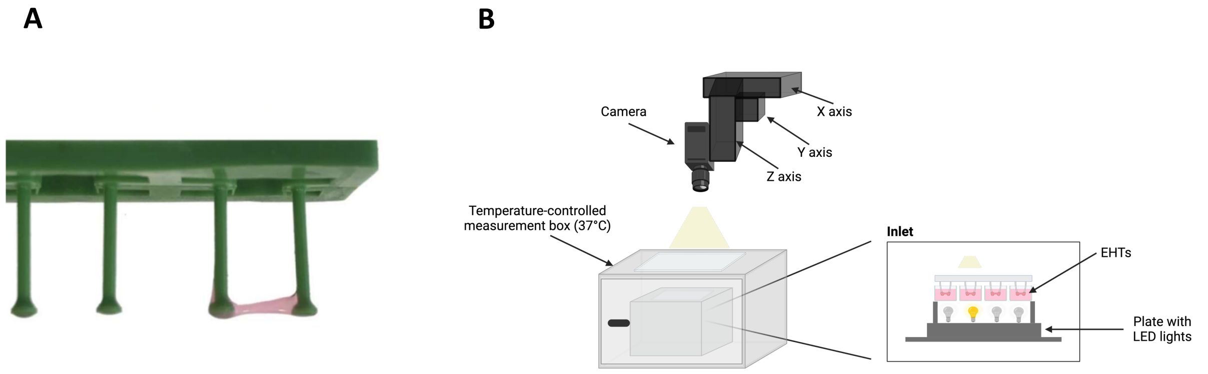

Figure 2 (A) Image of an engineered heart tissue (EHT). Adapted from Becker B. (2022). **(B)** The schematic representation of a video-optical device used to measure the contractile properties of the EHTs. Modified from Hansen et al. 2010. Created with BioRender.com

A study published by Hirt et al. (2012) presented a successful induction of pathological hypertrophic phenotype in EHTs containing neonatal rat cardiac cells. The EHTs underwent pharmacological stimulation with hypertrophy-inducing compounds (ET-1, PE) or were mechanically challenged by increasing the afterload (AE: afterload enhancement). The results of this study demonstrated a pathological phenotype in all treated groups on the functional and molecular level. The CMs in the hypertrophic groups showed increased cell size (+40.6% ET-1, +23.6% PE, +28.4% AE) and an elevated content of collagen I. Additionally, a hypertrophic phenotype was manifested by reactivation of fetal genes and an increased glucose consumption. On the functional level, all three types of intervention demonstrated a decrease in contractile force and an increase in relaxation time of the tissues (Hirt et al. 2012).

3.4.3.3 Human induced pluripotent stem cell-based models

The first description of induced pluripotent stem cells (iPSCs) comes from the year 2006, when Takahashi and Yamanaka published a protocol for reprogramming mouse embryonic and adult fibroblasts into a pluripotent state through forced expression of four transcription factors (Oct3/4, Sox2, c-Myc and Klf4) involved in maintaining the pluripotency in embryonic stem cells (ESC) (Takahashi & Yamanaka 2006). One year later, two independent groups were able to generate human iPSCs (hiPSCs) by reprogramming human fibroblasts through viral transduction of pluripotency-associated factors: Oct3/4, Sox2, c-Myc and Klf4 or Oct4, Sox2, Nanog and LIN28 (Takahashi et al. 2007; Yu et al. 2007). The hiPSCs very closely recapitulate the features of ESC, including the morphology, surface marker expression, proliferation and *in vitro* differentiation capabilities (Takahashi et al. 2007). The breakthrough of generating hiPSCs and the ability to redirect their faith to obtain cells of all three germ layers opened many possibilities in clinical and basic research. In cardiovascular sciences, hiPSCs are commonly used as a source for CM differentiation, which can be further utilized for replacement therapies, disease modeling and *in vitro* drug testing. The progress in stem cell technologies and differentiation protocols of various cell types gives the opportunity to study cardiac pathologies in human models.

The majority of the studies on pathological hypertrophy with hiPSC-derivatives is based on hiPSC-CMs cultured in 2D environment (Johansson et al. 2020; Li et al. 2023; Pohjolainen et al. 2022). The typically used method to induce hypertrophic response in hiPSC-CMs is stimulation with pro-hypertrophic compounds such as Ang II, ET-1 or combination of ET-1 and PE. Another approach is cell exposure to mechanical loading. In this set-up, hiPSC-CMs are plated onto flexible-bottomed culture plates and are subjected to cyclic stretch by applying vacuum suction. It has been shown that both of these methods similarly lead to recapitulation of selected aspects of hypertrophy, for instance, increase of hiPSC-CMs size and reactivation of fetal genes. However, these studies lack the possibility to investigate the contractile dysfunctions and fibrotic changes, which are observed in pathological hypertrophy. The recapitulation of the above-mentioned features was attempted with EHTs consisting of hiPSC-CMs or a combination of hiPSC-CMs and hiPSC-derived cardiac fibroblasts (hiPSC-CFs) (Madsen et al. 2021; Werner 2018). In these studies, two different methods of hypertrophy induction were evaluated, namely, pharmacological stimulation with ET-1/PE+ET-1 or mechanical challenge by increasing the afterload. The exposure of the EHTs containing hiPSC-CMs to PE+ET-1 led to a decrease in contractile force and reactivation of fetal genes (Madsen et al. 2021). However, no further analysis of hypertrophic features was performed in this study. Interestingly, in the work of Werner (2018), the AE or stimulation with ET-1 alone did not induce a similar EHT phenotype. No contractile impairment was detected in ET-1 treated EHTs, whereas the effect of AE varied depending on the cell line used for hiPSC-CM generation. More importantly, the addition of 5% CFs to the constructs did not improve the induction of a pathological phenotype (Werner 2018). This result suggested the need for implementation of other non-CM populations in order to evoke the hypertrophic phenotype in the EHT format. Tissues containing multiple cardiac cell populations (multi-cell-type EHTs) better recapitulate the cellular diversity observed in native cardiac tissue. Thus, this modification could enhance the pathological response to hypertrophic stimuli, similar to the one observed in rat EHTs.

3.4.3.3.1 Differentiation of major cardiac cell populations

The advancements in stem cell technologies enable the generation of different cell populations from hiPSCs. The specific differentiation protocols are based on recapitulation of the major stages that have been identified in the *in vivo* development of these cell types. In the *in vitro* settings it is achieved by sequential modulation of signaling pathways under chemically defined conditions. All the cardiac cell populations used in this study are of mesodermal origin, therefore mesoderm induction was a first step in their differentiation process. Subsequently, mesodermal progenitors underwent cell-type-specific stimulations in order to generate five major cardiac cell types, i.e, CMs, ECs, Mφs, SMCs and CFs. The schematic representation of the main differentiations stages is shown below. Detailed descriptions of differentiation procedures can be found in the material and method part of this thesis.

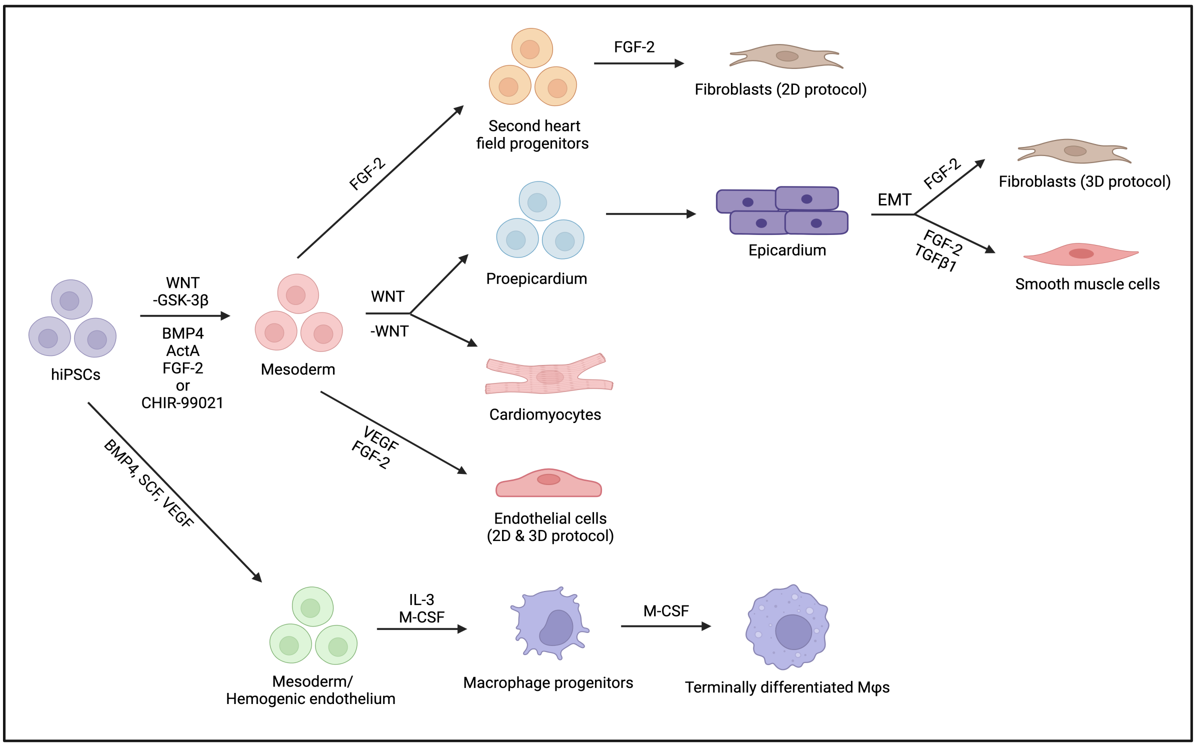

Figure 3 Schematic representation of differentiation protocols used in the study. Modified from Werner (2018). Created with BioRender.com. ActA: Activin A, BMP4: bone morphogenic protein 4, EMT: epithelial-mesenchymal transition, FGF-2: fibroblast growth factor 2, GSK-3β: glycogen synthase kinase-3β, hiPSCs: human induced pluripotent stem cells, IL-3: interleukin 3, M-CSF: macrophage-colony stimulating factor, SCF: stem cell factor, TGFβ1: transforming growth factor β1, VEGF: vascular endothelial growth factor, WNT: wingless-related integration site.

4 Aim of the study

The main aim of this dissertation was to establish a human *in vitro* model of pathological cardiac hypertrophy based on the EHT system. This project originated from a previously described hypertrophic model, i.e., neonatal rat engineered heart tissues (in short: rat EHTs; rEHTs). The induction of a hypertrophic phenotype was successfully achieved through treatment with PE and ET-1, as well as through the mechanical enhancement of afterload (Hirt et al. 2012). However, to date, attempts to recapitulate a complete hypertrophic phenotype in EHTs containing hiPSC-derived CMs were not successful. In contrast to rEHTs, the human iPSC-derived EHT system is a single-cell-type model consisting of only CMs. As a consequence, the unicellularity and the lack of interactions between CMs and non-CMs was hypothesized to be the major limitation of the human iPSC-derived EHT system. To investigate this hypothesis, one primary goal was set, i.e., to establish a multi-cell-type system by incorporating non-CM components into human EHTs and to evaluate its potential to recapitulate pathological hypertrophic phenotype. Three strategies were employed in order to challenge the realization of this hypothesis under laboratory conditions:

1) Combination of hiPSC-CMs and neonatal rat non-CMs in a form of hybrid EHTs
2) Differentiation of four hiPSC-derived non-CM populations and co-culture with hiPSC-CMs in a form of human multi-cell-type EHTs
3) Utilization of different methods to evoke hypertrophy (e.g., pharmacological or mechanical induction)

Different parameters were analyzed to assess the pathological phenotype in the EHTs. Functional assays were employed to evaluate the contractile performance of the tissues and transcriptomic analyses were used to examine the activation of the fetal gene program and expression of fibrosis-related genes. Furthermore, additional features such as CM size and production of NT-proBNP were characterized in order to understand the extent of the hypertrophic phenotype induction.

5 Materials and methods

A comprehensive list of media, buffers, reagents, solutions and devices used in this project can be found in the appendix (chapter 9).

5.1 Isolation of cardiac cells from neonatal rat heart

5.1.1 Dissociation of neonatal rat heart

All procedures have been conducted in compliance with the Hamburg Ethics Commission. The dissociation of neonatal rat heart was carried out based on a previously described protocol with modifications (Webster et al. 1993). In brief, the ventricles isolated from Wistar rats on postnatal days 0 – 3 were manually fragmented in CBFHH buffer. Afterwards, tissue pieces were subjected to repetitive enzymatic digestion with DNase II, type V and trypsin at room temperature (RT). After complete digestion of the tissue, cell suspension was filtered and the cell number was determined by manual cell counting with a Neubauer Chamber. The above-described work was kindly performed by June Uebeler (IEPT, UKE, Hamburg).

5.1.2 Cell separation by pre-plating

Pre-plating is a method that is widely used to separate the neonatal rat CMs from the non-CMs present in the cellular preparation. It is based on the differential attachment properties of the cells. Non-CMs (e.g., CFs, ECs) tend to attach rapidly whereas CMs need more time to adhere to cell culture dishes. To separate these two cellular fractions, cells were seeded onto non-coated cell culture dishes in NKM medium and were incubated for 1.5 hours at 37 °C. Afterwards, the medium containing CMs was collected into the conical tubes, whereas the attached cells (non-CMs) were washed once with DPBS and dissociated from the cell culture vessel with Accutase (5 minutes, 37 °C). Both fractions were centrifuged at 800 rpm for 8 minutes. Around 500,000 cells were collected for RNA isolation. For this purpose, cell pellet was resuspended in TRIzol (Thermo Fisher Scientific) and stored at -20 °C until further processing. Remaining cells were used for generation of hybrid EHTs.

5.1.3 Magnetic cell separation – neonatal rat heart

Another method utilized in this project to separate the non-CM and CM fractions of the neonatal rat heart was the magnetic-activated cell sorting (MACS). This technique utilizes a diverse mixture of monoclonal antibodies recognizing the surface markers expressed by the non-CM populations. These antibodies are directly conjugated to magnetic beads and are combined with the cell suspension. In the next step, the cell-antibody mix is transferred onto a column placed in a magnetic field which allows the non-CMs to be magnetically separated from the unlabeled CMs by being retained in the column. The CMs are found in the flow-through. In order to experimentally execute this protocol, isolated cardiac cells were centrifuged at 300×g for 5 min and the pellet was resuspended in MACS buffer. Next, the Neonatal Cardiomyocyte Isolation Cocktail (Miltenyi Biotec) and Anti-Red Blood Cell Microbeads (Miltenyi Biotec) were added to the cell suspension and incubated for 15 mins at 4 °C. The isolation was performed with LS columns and a MultiMACS (Miltenyi Biotec) separator. After placing the columns into the MACS separator, a maximum of 20 million cells was applied on a single MACS LS column and washed twice with 1 mL MACS buffer. The flow-through contained the unlabeled cells (CMs). The non-CMs were isolated by removing the column from the magnetic field and washing off the cells retained in the column matrix by applying 3 mL of NKM medium onto the column and eluting them into a separate conical tube.

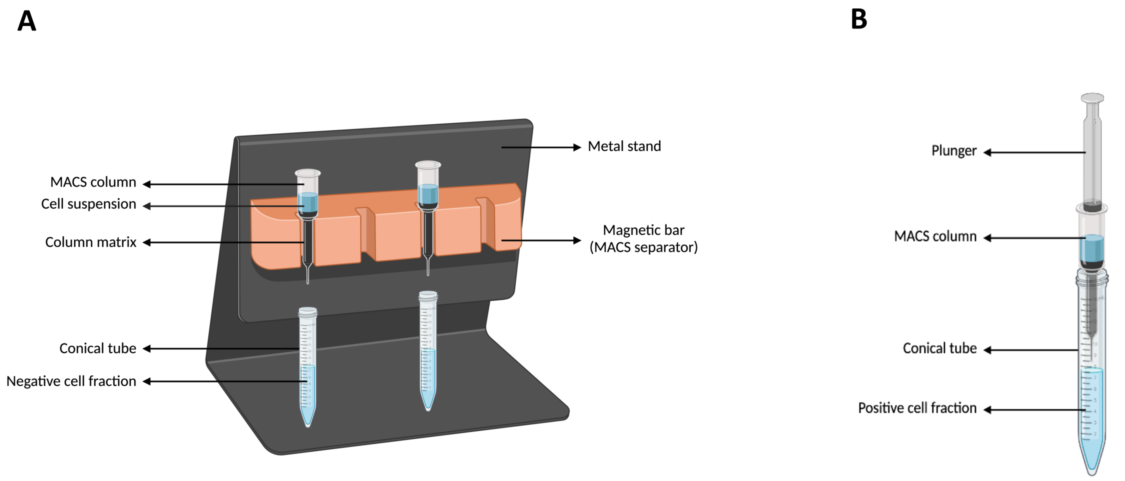

Figure 4 The set-up of MACS-based cell separation. **(A)** Isolation of negative cell fraction (CMs). **(B)** Elution of positive cell fraction (non-CMs). Created with BioRender.com.

Table 4 Reagents used for the separation of neonatal rat CMs and non-CMs with MACS

Component	Volume (for 20 million cells)
MACS buffer DPBS 0.5% bovine serum albumin (BSA) 2 mM EDTA	60 µL
Neonatal Cardiomyocyte Isolation Cocktail	20 µL
Anti-Red Blood Cells Microbeads	20 µL

5.2 Human induced pluripotent stem cells

5.2.1 Stem cell culture

The procedures of hiPSC generation and analysis were performed in compliance with the Hamburg Ethics Commission (Az PV4798). In the presented study, an in-house developed hiPSC line (ERC001) was a starting point to all differentiations. The process of ERC001 generation was based on the reprogramming of dermal fibroblasts from a skin biopsy of a healthy female donor (60 – 64 years old) with the CytoTune^{TM}-iPS 2.0 Sendai Reprogramming Kit (Life Technologies). This work was performed by Dr. Aya Domke-Shibamiya and Dr. Sandra Laufer (IEPT, UKE, Hamburg, Germany). The ERC001 line expressing green fluorescent protein (GFP) (ERC001 GFP; utilized for EC differentiation) was generated and provided by Dr. Tim Stüdemann (IEPT, UKE, Hamburg, Germany).

Basic stem cell culture was performed according to previously established protocols (Breckwoldt et al. 2017; Shibamiya et al. 2020). In short, a working cell bank (WCB) on passage 24 – 27 was expanded in FTDA medium in Geltrex^{TM}-coated vessels under hypoxic conditions (5% O_2 saturation). The cells were passaged twice a week with 3 – 4-day interval. Once 100% confluency was reached, cells were washed once with DPBS and incubated with 0.1 mL/cm^2 Accutase (Sigma Aldrich) for 5 mins at 37 °C. After detachment, cells were resuspended in FTDA medium containing 10 µM Y-27632 and centrifuged for 5 mins at 800 rpm. After removal of the supernatant, the cell pellet was resuspended in FTDA medium supplemented with 10 µM Y-27632. Subsequently, trypan blue stained cells were manually counted with a Neubauer cell counting chamber. A 3-day interval between splitting required a seeding density of 8.6x10^4 cells/cm^2, whereas a 4-day interval was achieved with a seeding number of 4x10^4 cells/cm^2. On the day of passaging, cells were plated in FTDA medium containing Y-27632. Medium changes were performed daily and the additional supplementation with Y-27632 was required only on the days of splitting. Stem cell culture quality was assessed on a regular basis by regular mycoplasma testing (5.2.2), karyotyping (5.8) as well as FACS analysis of the pluripotency marker, i.e., stage-specific embryonic antigen 3 (SSEA-3) (5.2.3).

5.2.2 Mycoplasma test

The sterility of stem cell cultures was ensured by frequent screening for the presence of mycoplasma in the cell culture media. In brief, hiPSCs were cultured for 72 hours without medium change. The sample preparation included incubation at 100 °C for 10 mins and centrifugation at 200×g for 5 mins. In the next step, 2 µL of the processed culture medium was used for the analysis by PCR, where additionally water served as a negative control and a contaminated culture medium was employed as a positive control. The products of the PCR reaction were detected by agarose gel electrophoresis on a 1% (w/v) gel. The mycoplasma testing of cell culture media was performed by June Uebeler and Anna Steenpaß (IEPT, UKE, Hamburg).

Table 5 Mycoplasma test reaction mix

Component	Volume per reaction
Nuclease-free water	25.75 µL
Q-solution	10 µL
10× buffer	5 µL
$MgCl_2$ (25 mM)	4 µL
Primer pool Myco-dw (10 pM)	1 µL
Primer pool Myco-up (10 pM)	1 µL
dNTPs	1 µL
Template	2 µL
Taq DNA polymerase	0.25 µL
Total	**50 µL**

Table 6 Thermocycler program for Mycoplasma test

Step	Temperature	Time
Initial denaturation	95 °C	15 minutes
40 cycles	94 °C	30 seconds
	56 °C	30 seconds
	72 °C	1 minute
Final extension	72 °C	10 minutes
Hold	4 °C	∞

5.2.3 Flow cytometry analysis of the pluripotency marker SSEA-3

A flow cytometry analysis was carried out to examine the expression of SSEA-3 in the WCB and hiPSCs during the expansion process. Around 1 million cells were collected and – to minimize unspecific binding – blocked in 1 mL of FCS for 15 minutes on ice. Afterwards, cells were washed with 1 mL FACS buffer consisting of DPBS + 5% FCS and centrifuged at 200×g for 2 minutes. Each sample was equally divided into two FACS tubes, one serving as a negative control and the other one as a test sample. An antibody solution was prepared by diluting the isotype control and PE-labelled anti-SSEA-3 antibodies (BD Biosciences) 1:50 in FACS buffer. 100 µL of the antibody solution was added to a corresponding tube and incubated at 4 °C for 45 mins; control tubes were incubated with 100 µL of the isotype control solution in parallel under the same conditions. Afterwards, cells were washed twice and resuspended in 250 µL of DPBS. The measurements were taken with FACSCanto II Flow Cytometer (BD Biosciences) at the FACS Core Facility (UKE, Hamburg, Germany). The analysis of the generated data was performed with FlowJo software, version 10.

5.3 Human induced pluripotent stem cell-derived cardiomyocytes

5.3.1 Differentiation protocol

To generate hiPSC-CMs, an embryoid body (EB)-based protocol was employed. In brief, hiPSCs were expanded in Geltrex^{TM}-coated T75 flasks and cultured until 100% confluency. On the starting day of differentiation (day 0), cells were pre-treated with 10 µM Y-27632 for 2 hours. Thereafter, hiPSCs were washed once with DPBS and detached with Accutase. Then, the Accutase-containing cell suspension was centrifuged at 800 rpm for 5 minutes and resuspended in EB-formation medium. The generation of the EBs was initiated by transferring 30 – 35x10^{4} hiPSCs/mL into a spinner flask and cultivating the cells overnight with a constant stirring at 40 rpm glass ball impeller rotation speed. On day 1 of differentiation, the volume of formed EBs was estimated using 15 mL centrifuge tubes (Sarstedt) and 180 – 250 µL of EBs were distributed into Pluronic-F127-coated T175 flasks and cultured in mesoderm induction medium. This step was performed under hypoxic conditions with a daily 50% medium change. After 3 days of culture in mesoderm induction medium, the EBs were washed and transferred into cardiac differentiation medium 1 with unchanged volume of 180 – 250 µL of EBs per Pluronic-F127-coated T175 flask. The EBs were cultured under normoxic conditions (21% O_2, 5% CO_2) for 3 days with a daily half medium change. In the next step, medium was completely removed and the EBs were transferred into cardiac differentiation medium 2 and cultured in it for 4 days. As in the previous steps, 50% medium exchange was performed daily. Finally, in the last stage of differentiation EBs were transferred into cardiac medium 3 for 7 days with daily 50% media exchange. The occurrence of rhythmic contractions in the EBs, typically observed during the second week of the culturing process, served as an indicative sign of successful cardiac differentiation. After a week-long culture in cardiomyocyte differentiation medium 3, EBs were dissociated into single-cell suspension. Firstly, EBs were collected via sedimentation at the bottom of the culture flask. Then, the medium was carefully removed and the EBs were washed twice with 25 mL of pre-warmed HBSS. Afterwards, HBSS was replaced with 20 mL of a collagenase II solution (200 units/mL in HEPES) supplemented with 30 µM N-benzyl-p-toluene sulfonamide (BTS) and 10 µM Y-27632. The dissociation was performed at 37 °C. The process was monitored every 30 minutes and was stopped by adding 20 mL of blocking solution once disaggregation of the EBs was observed. By pipetting the EB solution repeatedly but also carefully up and down, EBs were further dispersed into single cells. Next, the single cells were pelleted at 800 rpm for 8 minutes. The cell pellet was resuspended in RPMI medium and the cells were manually counted in the Neubauer counting chamber. Depending on the EHT type (e.g., hybrid, CM-only, multi-cell-type), a specific number of cells was either directly used for EHT casting or cryopreserved for later use. For freezing purposes, CMs were resuspended in 90% FCS + 10% DMSO and placed in isopropanol freezing container (Mr. Frosty) in -80 °C. After 24 hours, CMs were transferred to -150 °C for long-term storage.

5.3.2 Flow cytometry – cardiac troponin T

In order to evaluate the hiPSC-CM differentiation efficiency, the cells were stained for the CM-specific marker – cardiac troponin T (cTnT) – and analyzed via flow cytometry. For the analysis, cells were fixed with ROTI®Histofix for 20 minutes and permeabilized overnight at 4 °C. Each sample was equally divided and transferred into two separate FACS tubes. The cells in one FACS tube were stained with an isotype control antibody serving as a negative control. The cells in the other FACS tube were stained with a FITC- or PE-labelled anti-cTnT antibody (Miltenyi Biotec). Antibodies were diluted in permeabilization buffer and the staining was performed overnight at 4 °C. Next day, cells were washed three times and were resuspended in 500 µL of PBS. The samples were analyzed with FACSCanto II Flow Cytometer (BD Biosciences) at the FACS Core Facility (UKE, Hamburg, Germany). The generated data were evaluated with FlowJo software, version 10.

5.3.3 Immunofluorescence

For the immunofluorescence (IF) analysis, 10,000 CMs were seeded onto Geltrex™-coated µ-Slides 8-well (Ibidi). Cells were washed once with DPBS and fixed with ROTI®Histofix for 20 minutes at 4 °C. After fixation, cells were washed twice with DPBS and stained with primary antibodies diluted in permeabilization buffer. The list of the antibodies and the used dilutions can be found in section 9.4. For each well a staining volume of 100 µL was used and the incubation with primary antibody was performed overnight at 4 °C. The next day, cells were washed twice with DPBS and incubated with secondary antibody solution for 2 hours at RT. Additionally, a nuclear staining with DAPI was implemented in this step. After the incubation, cells were washed twice with DPBS and stored at 4 °C until imaged.

5.3.4 Cardiomyocyte purification – MACS

In circumstances when cardiac differentiations efficiency was <70% $cTnT^+$, a sorting approach with magnetic beads was employed to enhance the purity of differentiations, aiming for cTnT levels above 90%. For this purpose, cells were centrifuged at 200×g for 5 minutes, and the resulting pellet was resuspended in MACS buffer. In the next step, a Non-Cardiomyocyte Depletion Cocktail (Miltenyi Biotec) was added and mixed well with the cell suspension. After 5 minutes incubation at 4 °C, cells were washed with MACS buffer and centrifuged again. The resulting pellet was resuspended in MACS buffer and Anti-Biotin MicroBeads (Miltenyi Biotec) were added. The cells-beads mixture was incubated at 4 °C for additional 10 minutes. Afterwards, the LS columns were placed in the magnetic separator and a maximum of 40 million cells were applied onto a single column. The flow-through containing purified CMs was collected into conical tubes with NKM medium. After conducting three washes of the column with the NKM medium, the quantification of purified CMs was performed through manual counting in a Neubauer chamber, employing trypan blue staining.

Table 7 Regents used for purification of hiPSC-CMs

Component	Volume (for 5 million cells)
MACS buffer DPBS 0.5% FCS, inactivated 2 mM EDTA	80 µL
Non-Cardiomyocyte Depletion Cocktail	20 µL
Anti-Biotin MicroBeads	20 µL

5.4 Human induced pluripotent stem cell-derived endothelial cells

5.4.1 Three-dimensional differentiation protocol

The 3D differentiation of hiPSCs into ECs followed the protocol outlined in Tessa Werner's PhD thesis (2018). In brief, EBs were generated according to the procedure described in section 5.3.1. A volume of 180 – 250 µL EBs was transferred into Pluronic-F127-coated T175 flasks and cultured in Stage 1 medium under hypoxic conditions for 3 days. Half of the medium volume was exchanged every day. Following a 3-day incubation period, all EBs were pooled, and their collective volume was assessed in a 15 mL conical tube. Similarly, to the previous steps, 180 – 250 µL EBs were distributed into T175 flasks with 46 mL of Stage 2 medium. Again, half of the medium was changed every other day, except of the first day after the initiation of Stage 2. EBs were cultured in Stage 2 medium for 10 days in total. Afterwards, EBs were dissociated by incubation in a collagenase II (200 units/mL in HEPES) solution. Resulting single cells were sorted to isolate cells expressing the EC marker CD31. MACS was performed according to manufacturer's instructions and the required volumes of reagents can be found in the Table below.

Table 8 Regents used for purification of hiPSC-ECs

Component	Volume (for 10 million cells)
FcR Blocking Reagent	20 µL
CD31 MicroBeads	20 µL

After the enrichment, purified ECs were expanded in 1% gelatin-coated T75 flasks in EGM-2 medium (Lonza).

5.4.2 Two-dimensional differentiation protocol

To generate hiPSC-ECs in a 2D format, 500,000 hiPSCs were seeded into Geltrex^{TM}-coated 6-well plates in 2 mL FTDA medium supplemented with 10 µM Y-27632 and 1 µM CHIR-99021 (Cayman). After culturing the cells overnight, medium was exchanged to RPMI containing 100 ng/mL activin A, 2% B27 without insulin and Matrigel® (1:60). The cells were incubated for 17 hours at 37 °C in normoxic conditions. In the next step, medium was replaced with RPMI supplemented with 5 ng/mL BMP4, 1 µM CHIR-99021 and 2% B27. The medium was left unchanged for 24 hours. Next day, BMP4-containing medium was removed and the cells were cultured for 72 hours in StemPro-34 medium supplemented with 0.4 mM MTG, 2 mM L-glutamine, 50 µg/mL ascorbic acid, 10 ng/mL BMP4, 5 ng/mL FGF-2 and 300 ng/mL VEGF. After 3 days of culture, the cells were washed two times with DPBS and detached with Accutase. Around 675,000 cells were seeded in 0.1% gelatin-coated T75 flasks in EGM medium (Lonza) supplemented with 20 ng/mL VEGF, 20 ng/mL FGF-2 and 1 µM CHIR-99021. The cells were cultured in the above-mentioned medium for 9 days. Medium was exchanged every other day and cells were split with TrypLE Select Enzyme (Thermo Fisher Scientific) when a confluency of about 80% was reached.

5.4.3 Immunofluorescence

For the IF analysis, hiPSC-ECs were seeded into 0.1% gelatin coated 8-well µ-Slides (IBIDI). After removing the culture medium and washing two times with DPBS, cells were fixed with 250 µL ROTI®Histofix for 15 minutes at RT. Afterwards, cells were permeabilized with 0.5% Triton X-100 for 5 minutes and blocked with 2% BSA in PBS for 20 minutes at RT. Primary antibodies were diluted in 1% BSA + 0.3% Triton X-100 solution and the staining was performed overnight at 4 °C. Following that step, any unbound primary antibodies were thoroughly washed away with DPBS, and the cells were stained with secondary antibodies for 1.5 hours at RT. Additionally, nuclear staining with DAPI was included. After the incubation with secondary antibodies, cells were washed and stored in DPBS until imaged.

5.4.4 Flow cytometry

The preparation of the cells for the flow cytometry analysis was performed according to the procedure described in section 5.2.3.

5.4.5 Matrigel assay

To evaluate the angiogenic potential of the hiPSC-ECs a tube formation assay was performed. Around 200 µL of a Growth Factor Reduced (GFR) Matrigel® was added to each experimental well on a 24-well plate. Plates were incubated at 37 °C until Matrigel® polymerized and subsequently 100,000 cells were seeded on top of the scaffold. Cells were cultured in normoxic conditions for the next 2.5 hours and imaged at different time points.

5.5 Human induced pluripotent stem cell-derived macrophages

5.5.1 Differentiation protocol

For the Mφ differentiation, EBs were generated according to the procedure described in section 5.3.1. Following the estimation of EB volume, 90 – 100 µL of EBs were carefully transferred to a Pluronic-F127-coated T75 flask, where they were cultivated for 6 days in Stemdiff™ APEL™2 (Stemcells Technologies) medium supplemented with 20 ng/mL BMP4, 20 ng/mL VEGF, 20 ng/mL SCF (R&D) and 10 µM Y-27632. Every other day, half of the medium was replaced with a fresh one. Afterwards, the EBs were washed in X-VIVO 15 medium (Lonza) before being evenly distributed among the 0.1% gelatin-coated wells of 6-well plates, with a target of 25 – 35 EBs per well. From then on, EBs were cultured in X-VIVO 15 medium supplemented with 0.05 mM 2-Mercaptoethanol, 25 ng/mL IL-3 (R&D) and 50 ng/mL M-CSF (R&D). Medium exchange was performed weekly. Following a 2-week cultivation period, EBs initiated the generation of macrophage progenitors, harvestable into a conical tube, while simultaneously refreshing the medium for the EBs. The collected progenitors were centrifuged for 7 minutes at 800 rpm, resuspended in 1 – 5 mL medium, counted and 300,000 cells/well were seeded into uncoated 6-well plates in terminal differentiation medium. After additional 7 days of culture, Mφs were collected with 0.5 mM EDTA solution.

5.5.2 Flow cytometry

The expression of Mφ surface and intracellular markers was analyzed by flow cytometry. The preparation of the cells for the intracellular staining was performed according to the description in section 5.3.2. The anti-CD68 and macrophage maturation marker antibodies were diluted 1:100 in permeabilization buffer and 100 µL of the staining solution was added to the cells. The negative control sample was incubated overnight in permeabilization buffer without a primary antibody. Afterwards, cells were washed twice and stained with the secondary antibody goat anti-mouse Alexa Fluor 488 for 30 minutes at 4 °C. After incubation, samples were washed three times and were finally resuspended in 250 µL of DPBS. The stainings for the surface markers were performed according to section 5.2.3. Measurements were taken with FACSCanto II Flow Cytometer (BD Biosciences) at the FACS Core Facility (UKE, Hamburg, Germany). The obtained data were evaluated with FlowJo software, version 10.

5.5.3 Phagocytosis assay

For the phagocytosis assay, 100,000 cells/well were seeded in 100 µL terminal differentiation medium into 96-well plates with clear bottom (Grainer). Cells were incubated overnight to attach to the surface on the culture vessel. Next day, pHrodo™ Green Zymosan BioParticles™ (“beads”; Thermo Fisher Scientific) were resuspended in DPBS and sonicated in a glass tube for 5 minutes. After BioParticle preparation, culture medium was replaced with 100 µL of the bead’s suspension. After 2 – 3 hours of incubation at 37 °C the fluorescence was measured with FluoroCount Microplate Reader (Packard).

Additionally, the phagocytic activity of the Mφs was visualized by confocal microscopy. Therefore, prior to introduction of the pHrodo™ Green Zymosan BioParticles™, cell nuclei were stained with Hoechst 33342 for 20 mins at 37 °C and for additional 30 minutes with CellMask™ Plasma Membrane Stain (Thermo Fisher Scientific). After incubation with the beads, cells were fixed with ROTI®Histofix at RT for 15 – 20 minutes and stored in DPBS at 4 °C until imaged.

5.5.4 Polarization

To evaluate the phenotypical plasticity of hiPSC-Mφs, the cells were polarized into either the M1 or the M2 state. Thus, hiPSC-Mφs were stimulated for 24 – 48 hours with 100 ng/mL LPS (Thermo Fisher Scientific) and 20 ng/mL IFNγ (PeproTech) to induce the M1 phenotype (pro-inflammatory) or with 20 ng/mL IL-4 (PeproTech) to induce the M2 phenotype (anti-inflammatory).

5.5.5 Degradation assay

For the degradation assay, 180 mg NaCl and 100 mg gelatin were combined and dissolved in 50 mL di-sodium tetraborate decahydrate solution for 30 mins at 37 °C. Afterwards, 1.8 mg NHS-Rhodamine (Thermo Scientific) was incorporated into the mixture and the solution was further stirred for 2 hours. The Rhodamine-labelled gelatin was dialyzed overnight at 4 °C with the dialysis-membrane (Thermo Scientific). On the next day, sucrose solution (1 g/mL) was pre-heated to 37 °C and combined with previously dialyzed gelatin-rhodamine (1:50). In the next step, the solution was used to coat coverslips (50 µL/12 mm ∅ coverslip) for 15 minutes at RT. Coverslips were further washed two times with PBS and transferred into a 12-well plate with the coated side facing upwards. After two washes with PBS and one wash with RPMI, the coverslips were incubated in RPMI at 37 °C overnight. On the following day, approximately 65,000 hiPSC-Mφs were seeded in 65 µL of medium onto a single coverslip. After 5 hours, cells were fixed with pre-warmed 4% paraformaldehyde (PFA) (Thermo Scientific) for 15 minutes at 37 °C. Next, hiPSC-Mφs were washed two times with PBS and stained with anti-vinculin (Sigma-Aldrich) antibodies diluted in 0.1% Triton X-100, 10% NGS in PBS. After one hour incubation, cells were washed two times with PBS and stained with secondary antibodies and phalloidin (Molecular Probes) for 30 minutes at RT. The unbound secondary antibodies were removed by washing two times with PBS. In the next step, the coverslips were mounted to the microscopic slides with Mowiol (Roth) (6 µL/coverslip) and sealed with nail polish. The slides were left to dry overnight and imaged on the following days. The above-described experimental procedure as well as imaging and data analysis were performed by Dr. Artur Ratt (Department of Medical Microbiology, Virology and Hygiene, UKE, Hamburg, Germany)

5.5.6 Viability assay

The examination of Mφ viability in different medium compositions was performed with CellTiter-Blue® Cell Viability Assay (Promega). This assay is based on the ability of viable cells to reduce dark-blue resazurin to pink fluorescent resorufin. Therefore, approximately 10,000 hiPSC-Mφs/well were seeded onto 96-well plates with clear bottom (Grainer). The cells were cultured for 2, 4 – 5 or 7 days in the complete EHT medium without any additional supplementation or in the same medium with addition of 50 ng/mL M-CSF. On the day of analysis, cells were incubated with 20 µL CellTiter-Blue® Reagent for 4 hours at 37 °C. Afterwards, the fluorescence at 530/580 was measured with Safire 2 multi-detection plate reader (Tecan). The obtained data was analyzed by subtracting the background fluorescence (cell-free wells) from the experimental wells and calculating the difference in emitted fluorescence between the wells containing cells cultured with and without M-CSF.

5.6 Human induced pluripotent stem cell-derived smooth muscle cells

5.6.1 Differentiation protocol

The differentiation of hiPSCs into SMCs was based on the protocol from the doctoral thesis of T. Werner (2018). In brief, EB formation and mesoderm induction was performed according to the procedure described in section 5.3.1. Following mesoderm induction, the EB volume was estimated and 50 – 70 µL of EBs were seeded on Geltrex^{TM}-coated T75 flasks. The EBs were cultured in Epi medium containing 10 ng/ml BMP4, 5 ng/ml VEGF, 4 µM CHIR-99021 and 5.4 µM SB-431542 for 2 days under normoxic conditions. The differentiation continued in Epi medium supplemented with 5 ng/ml VEGF with medium change performed every other day. After 8 days of culture, EBs were dissociated into single cells with collagenase II (200 units/mL in HEPES solution) and 2 – 2.5 million cells were seeded onto Geltrex^{TM}-coated T75 flasks in Epi medium supplemented with 10 µM Y-27632. On the following day, the medium was replaced with Epi medium containing 5 ng/mL TGFβ1, and the cells were cultured for additional 4 days. Finally, in the last stage of differentiation, cells were cultured in Epi medium with 10 ng/mL FGF-2 for another 4 days. SMCs were harvested by dissociation with Accutase (37 °C, 5 mins) and were eventually used for further characterization or resuspended in cryopreservation medium (90% FCS + 10% DMSO).

5.6.2 Immunofluorescence

For confocal microscopy imaging, cells were cultured in clear bottom 96-well plates (Greiner). In the first step, cells were fixed with an ice-cold acetone/methanol solution (1:1 mixing ratio) for 20 minutes at -20 °C. After three times washing with DPBS, cells were permeabilized with 0.2% Triton X-100 in PBS for 5 minutes at RT. Then, the non-specific binding sites were blocked by incubation with 5% non-specific goat serum in IF buffer for 20 minutes at RT. The staining with primary antibodies was performed overnight at 4 °C. After an overnight primary antibody incubation, cells were washed three times with DPBS and stained with secondary antibodies for 2 – 3 hours at RT. After the cells were washed three times with DPBS, 250 µL of DPBS was added to each well and plates were stored at 4 °C until imaged.

5.6.3 Flow cytometry

On the last day of the differentiation process, a sample of approximately 1 million cells was collected for analyzing an intracellular SMC marker protein, namely α-SMA. This staining was performed according to the protocol described in the section 5.3.2.

5.7 Human induced pluripotent stem cell-derived cardiac fibroblasts

5.7.1 Three-dimensional differentiation protocol

The generation of hiPSC-CFs with the EB-based protocol was performed according to previously described procedure (Werner, 2018). Following identical steps to those described in section 5.6.1 for SMCs, this differentiation protocol differed only in the absence of TGFβ1 supplementation during CF differentiation. Instead, 10 ng/mL FGF-2 was continuously added from the splitting step until the completion of differentiation.

5.7.2 Two-dimensional differentiation protocol

In order to differentiate hiPSCs into CFs, 1.5 million cells were seeded onto GFR Matrigel®-coated 6-well plates in mTeSER1 medium (Stemcell Technologies) supplemented with 10 µM Y-27632. Cells were fed every day and cultured until 100% confluency was reached. In the next step (day 0), medium was exchanged to RPMI supplemented with B27 without insulin (1:50) and 12 µM CHIR-99021. After 24 hours of incubation, the medium was replaced with RPMI + B27 without insulin for the next 24 hours. After day 2 but before day 3, medium was exchanged to CFBM medium supplemented with 75 ng/ml FGF-2. This medium was used to feed the cells every other day over a time span of 17 days. On day 20, CFs were detached with 0.25% Trypsin-EDTA (Thermo Fisher Scientific) at 37 °C and seeded onto T75 flasks in FibroGRO (Millipore) medium with 2% FCS. Cells were fed every other day and passaged when 100% confluency was reached.

5.7.3 Fibroblast activation assay

The functional properties of hiPSC-CFs were examined by evaluating their potential to transition into the myofibroblast state. Therefore, cells were seeded onto laminin-coated 24-well plates in FibroGRO medium with 2% FCS. After an overnight culture, medium was exchanged to DMEM/F12 containing 0.4% FCS. Next day, wells were assigned to three experimental groups: I) control – unstimulated cells, II) TGFβ – cells stimulated with 20 ng/mL TGFβ1, III) SB group – cells stimulated with 10 µM SB-431542. The treatment was carried out for 5 days with a medium change performed every other day.

5.7.4 Flow cytometry

For the analysis of CF marker expression 0.5 – 1 million CFs were collected. To label the intracellular proteins, cells were fixed with 1% PFA and permeabilized with ice-cold methanol for 30 mins. Subsequently, cells were washed with 3 mL FACS buffer containing 0.5% BSA in DPBS and stained with primary antibodies overnight at 4 °C. Antibodies were diluted in 0.1% Triton X-100 in FACS buffer and the staining volume was adjusted to 100 µL/sample. After the overnight incubation, cells were washed once and stained with secondary antibodies for 30 minutes at RT. Secondary antibodies were diluted 1:1000 in FACS buffer with 0.1% Triton X-100. Finally, samples were washed two times and resuspended in 500 µL DPBS for analysis. The staining of surface markers was performed by incubation of cells with primary antibodies resuspended in FACS buffer (without Triton X-100) for 30 minutes at RT. Finally, cells were washed two times and resuspended in 500 µL DPBS. Measurements were taken with FACSCanto II Flow Cytometer (BD Biosciences) at the FACS Core Facility (UKE, Hamburg, Germany). The generated data were analyzed with FlowJo software, version 10.

5.7.5 Immunofluorescence

For the IF analysis, hiPSC-CFs were washed two times with DPBS and fixed with ROTI®Histofix for 15 minutes at RT. The permeabilization and further staining procedure were performed according to section 5.6.2.

5.8 Karyotyping

To exclude any chromosomal abnormalities of the WCB as well as the hiPSC-derivatives a karyotype analysis with the nCounter Human Karyotype Panel (Nanostring Technologies) was employed. Genomic DNA was isolated from all the samples with DNasy Blood & Tissue Kit (Qiagen). Subsequently, further processing of the samples was executed in accordance with the manufacturer's guidelines. In short, 250 ng of genomic DNA was enzymatically digested at 37 °C for 1 – 2 hours. The digestion efficiency was evaluated via agarose gel electrophoresis. In the next step, DNA was denatured into the single-stranded form at 95 °C for 5 mins and hybridized with probes at 65 °C for 16 hours. The analysis was performed with the nCounter system. DNA-probe complexes were applied into the nCounter Cartridge (Nanostring Technologies) and transferred to the nCounter Digital Analyzer (Nanostring Technologies). The nCounter CNV Collector Tool software (Nanostring) was used for the analysis of the generated chromosome-specific fluorescence intensity. Processing of the samples for the karyotype analysis was kindly performed by Elisabeth Krämer (Nanostring Core Facility, UKE, Hamburg, Germany) and the evaluation of the data was conducted by Dr. Giulia Mearini and Niels Pietsch (IEPT, UKE, Hamburg, Germany).

5.9 Engineered Heart Tissues

5.9.1 Generation of rat and human EHTs

EHTs were generated according to a protocol published by Mannhardt et al. (2017). In short, to create casting molds, 24-well plates were filled up with 60 °C warm 2% (w/v) agarose/DPBS solution. Before the agarose solidification polytetrafluorethylene (PTFE) spacers (EHT Technologies) were inserted into the wells. In the meantime, an EHT casting mix was prepared. Throughout the project, various casting mixes were employed, and their composition varied depending on the type of EHTs being generated. The number of cells, the used components as well as their volumes are depicted in the Tables below.

Table 9 EHT casting mix

Component	Quantity for 1 EHT
2x DMEM	5.6 µL
Y-27632 (10 µM)	0.1 µL
Fibrinogen (200 mg/mL)	2.5 µL
NKM medium	88.8 µL

Table 10 Cellular compositions of the EHTs

EHT type	Cellular composition (per 1 EHT)
Hybrid EHTs	200,000 – 400,000 rat non-CMs 600,000 – 800,000 hiPSC-CMs
hiPSC-CM EHTs (in hybrid EHTs experiments)	800,000 hiPSC-CMs
Rat EHTs	500,000 rat cardiac cells
CM-only EHTs	600,000 hiPSC-CMs
Multi-cell-type EHTs (600,000 CMs/EHT)	600,000 hiPSC-CMs 200,000 hiPSC-ECs 100,000 hiPSC-Mφs 50,000 hiPSC-CFs 50,000 hiPSC-SMCs
Multi-cell-type EHTs (1,000,000 CMs/EHT)	1,000,000 hiPSC-CMs 333,333 hiPSC-ECs 166,667 hiPSC-Mφs 83,333 hiPSC-CFs 83,333 hiPSC-SMCs

Following agarose solidification, spacers were carefully removed and the flexible polydimethylsiloxane (PDMS) racks (EHT Technologies) were transferred into the casting molds. To cast the tissues, 100 µL of the EHT master mix was swiftly combined with 3 µL of thrombin (100 U/mL) and pipetted into the agarose molds. Afterwards, the plates were incubated at 37 °C for 2 hours to allow the fibrin to polymerize. Once polymerized, 500 µL of EHT medium was pipetted in a drop-wise manner on top of each tissue and the plates were placed back in the incubator for additional 20 minutes. Finally, racks with the attached tissues were removed from the agarose molds and transferred to a fresh medium-containing 24-well plate. EHTs were cultured under hyperoxic conditions (37 °C, 7% CO_2, 40% O_2) with medium changes performed three times a week.

5.9.2 Video-optical contractility analysis

The functional performance of the EHTs was evaluated with a video-optical system as previously described in Hansen et al. (2010). This set-up consists of a glass-roofed humidified unit with controlled conditions (37 °C, 7% CO_2, 53% N_2, and 40% O_2) and a video camera placed above the incubation chamber. For the measurements, the 24-well plates with the EHTs were transferred to the incubation unit and the XYZ coordinates for each EHT were determined via user interface software. The camera was recording videos of each EHT. The acquired video files were further analyzed by the CTMV software (Consulting Team Machine Vision). Analysis was based on the semi-automated recognition of the ends of the tissues and evaluation of their movement resulting from the EHT contractions. The calculations of the functional parameters were derived from the magnitude of tissue shortening during contractions and the mechanical properties of the PDMS posts to which the EHTs were attached.

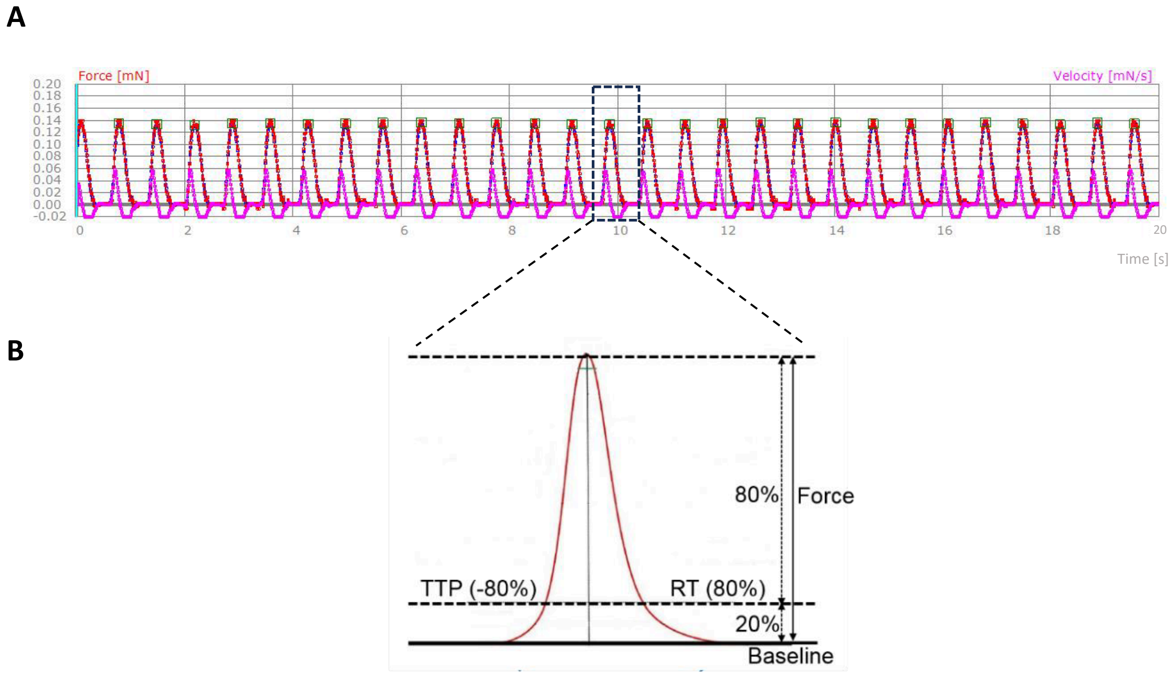

Figure 5 (A) An original recording of the EHT contractile activity over 20 seconds. Red traces represent force, pink traces depict the velocity of contractions. **(B)** Pictogram representing the contractility parameters derived from force recordings. Contraction time, i.e., TTP (-80%) or $TTP_{80\%}$: time to peak at 80% peak height, Relaxation time, i.e., RT (80%) or $RT_{80\%}$: relaxation time at 80% peak height. Adapted from Bangfen (2022).

5.9.3 Remodeling analysis

The assessment of tissue remodeling was carried out based on images obtained during functional measurements of the EHTs. Utilizing the Fiji software for image evaluation, the analysis involved setting a pixel-to-millimeter ratio derived from the scale bar present on the EHT images.

5.9.4 Stiffness measurements

For the stiffness measurements, the EHTs underwent a single wash in DPBS and were subsequently fixed overnight with ROTI®Histofix at 4 °C. In the next step, the fixed tissues were immersed in pre-warmed liquid agarose (4%) and placed at 4 °C until the agarose solidified. Small cubes of agarose containing embedded EHTs were then excised and stored in DPBS at 4 °C until further processing. On the day of the measurements, the samples were affixed to a stage, and a scalpel was used to remove the top layer of agarose. The stiffness of the EHTs was assessed with the nanoindentation technique, wherein a specific load was applied to an indenter in contact with the sample. This process measured the depth of penetration, which was subsequently recalculated to determine the Young's modulus of the analyzed material. The data was generated with CHIARO nanoindenter system (Optics11) and both the measurements and data analysis were conducted by Dr. Sandra Hemkemeyer (Institute of Clinical Chemistry and Laboratory Medicine, UKE, Hamburg, Germany).

5.9.5 Transmission electron microscopy

To prepare the EHTs for TEM, tissues were transferred into Tyrode's Solution containing 1.8 mM Ca^{2+} and 30 mM butanedione monoxime (BDM). EHTs were incubated at 37 °C until no further contractions were observed. In the next step, tissues were fixed with a solution containing 1% glutaraldehyde (GA) (Science Services) and 4% PFA (Thermo Fisher Scientific) in 0.1 M phosphate buffer. After the overnight fixation at 4 °C, EHTs were transported to the UKE Electron Microscopy Core Facility where the further sample processing and imaging was performed by Dr. Michaela Schweizer (Electron Microscopy Unit, Center for Molecular Neurobiology, UKE, Hamburg, Germany).

5.9.6 MACSima Imaging Cyclic Staining

One-week- and three-week-old EHTs were washed in DPBS and fixed with ROTI®Histofix overnight. Fixed tissues were embedded in paraffin with the kind support of Dr. Kristin Hartmann. Paraffin-embedded EHTs were cut into 6 – 8 µm sections on a microtome and transferred onto superfrost microscopic slides. Cut sections were placed on a 40 °C heating plate for 60 minutes and subsequently moved to a 40 °C incubator overnight. The deparaffinization of the sections consisted of a 20-minute incubation in xylene and a 1-minute incubation in each of the following ethanol concentrations: 100%, 95%, 80%, 70% and 50%. After the ethanol rehydration steps, slides were washed in VE-water. For the antigen retrieval the heat-induced epitope retrieval method (HIER) was used. The slides were placed into 85 °C TEC buffer and incubated for 20 minutes at 95 °C. Afterwards, the slides were removed from the slightly cooled buffer and mounted into MACSwell™ Four Imaging Frames (Miltenyi Biotec) according to manufacturer's instructions. Sections were pre-stained with DAPI Staining Solution from the MACSima™ Stain Support Kit (Miltenyi Biotec) for 10 minutes at RT and washed three times with MACSima Running Buffer (Miltenyi Biotec). Slides were stored in MACSima Running buffer at 4 °C until further processing. On the day of imaging, selected antibodies were pippeted into MACSwell™ Deepwell plates (Miltenyi Biotec). To the wells containing hybridoma antibodies an FcR Blocking Reagent was added. The slides were then placed in the MACSima imaging system (Miltenyi Biotec) together with the prepared MACSwell™ Deepwell plates. The DAPI signal of the tissues was visualized under a 20x objective, which allowed the selection of regions of interest (ROI) in the EHTs. The obtained images were processed and analyzed with MACS® iQ View analysis software (version 1.0.0, Miltenyi Biotec). After performing cell segmentation, an annotation-based strategy was used to quantify different cell populations. The resulting numeric data was visualized in GraphPad Prism.

5.9.7 Immunofluorescence

For histology, EHTs were washed in DPBS and fixed overnight with ROTI®Histofix at 4 °C. Afterwards, tissues were immersed in liquid 4% agarose and left until its solidification. Cubes of agarose with embedded EHTs were excised and glued onto a metal sample holder. EHTs were cut into 100 µm sections with a VT100S vibrating blade microtome (Leica). Sections were stored in DPBS in 24-well plate until stained. The staining procedure was initiated by blocking the samples in 250 µL blocking solution for 90 minutes at RT. Next, the blocking solution was replaced by an antibody solution containing primary antibodies in respective dilutions. Sections were incubated overnight at 4 °C. Next day, the antibody solution was removed and the samples were washed three times with DPBS for 5 minutes on a shaker. Afterwards, secondary antibody solutions were pipetted onto the sections and incubated for 90 minutes at RT. Stained samples were placed on microscopic slides and mounted with Fluoromount-G (Thermo Fisher Scientific). Slides were left overnight at RT to dry and were afterwards stored at 4 °C until imaged.

5.9.8 Action potential measurements

The recordings of the APs were performed in intact tissues cultured for 4 – 8 weeks. The APs were measured with standard sharp microelectrodes following a previously described protocol (Lemoine et al. 2017). In short, EHTs were placed in a recording chamber containing Tyrode's solution equilibrated with O_2-CO_2 [95:5] at 36.5 °C ± 0.5 °C, pH 7.4. Tissues were superfused with Tyrode's solution for at least 1 hour before the data acquisition was initiated. The measurements were performed by Anna Steenpaß and the analysis of the raw data was performed by Dr. Torsten Christ and Anna Steenpaß (IEPT, UKE, Hamburg).

5.9.9 Induction of a hypertrophic phenotype

5.9.9.1 Pharmacological treatment

After 4 – 5 weeks of culture, the EHT medium was changed from a standard culture medium containing 10% horse serum to medium with reduced serum (4%) for 1 day. Afterwards, the serum was completely withdrawn and medium was supplemented with 50 ng/mL hydrocortisone and 0.5 ng/mL triiodothyronine (T_3). On the first day of culture in medium without serum, the force of the EHTs was measured and tissues were divided into two groups with comparable mean force. To evoke a hypertrophic response, EHTs were stimulated with 20 µM PE and 50 nM ET-1 for 9 – 12 days in serum-free conditions. Medium was exchanged daily and the measurements were performed not earlier than 2 hours after medium change.

5.9.9.2 Afterload enhancement

In addition to pharmacological treatment, AE was employed to induce a hypertrophic phenotype. Tissues were transferred from serum-containing medium to serum-free conditions and divided into groups with comparable mean force as described in the section 5.9.9.1. One of the groups served as a control group whereas the EHTs from the second group were undergoing hypertrophic intervention by insertion of metal braces into the hollow posts to which the EHTs were attached. The mechanical intervention was carried out for 7 – 9 days with daily medium changes. On the final day of the intervention, braces were taken out from the posts, and subsequent contraction measurements were performed not earlier than 30 minutes after brace removal.

5.9.10 Analysis of a hypertrophic phenotype

5.9.10.1 Cell size measurements – Image Stream

In order to analyze the size of CMs that were cultured in the EHT format, the tissues were dissociated into a single-cell suspension. Therefore, a papain-based digestion was employed. First, the EHTs were washed three times in HBSS and subsequently transferred into the papain solution (5 U/mL) and incubated at 37 °C. The EHTs were dissociated in the wells of a 24-well plate in a total volume of 1.5 mL solution per well. Once the EHTs showed signs of disintegration, the cell suspension was transferred from the wells into 15 mL conical tubes and mixed with the equal volume of a blocking buffer containing 5% FCS in HBSS. The collected cell suspension was centrifuged for 8 minutes at 800 rpm. In the next step, cells were fixed, permeabilized and stained with the anti-cTnT antibody according to the protocol described in section 5.3.2. For the cell size analysis, stained samples were transferred to 1.5 mL reaction tubes and resuspended in 50 µL of Image Stream buffer containing 2% FCS and 2 mM EDTA in DPBS. Samples were measured with an Amnis Image Stream device in the FACS Core Facility (UKE, Hamburg, Germany). The acquired data were analyzed with the IDEAS software.

5.9.10.2 Cell size measurements – forward scatter

The forward scatter (FSC) analysis was used as a surrogate for estimation of CM size. For this analysis, cells were isolated from the EHTs through papain dissociation and stained with anti-cTnT antibody according to the procedure described in the 5.9.10.1. The single-cell suspension was analyzed with FACSCanto II Flow Cytometer (BD Biosciences) at the FACS Core Facility (UKE, Hamburg, Germany). The acquired data were evaluated by sequential gating allowing for the analysis of single cells expressing cTnT. The gating as well as the analyses of forward scatter area (FSC-A) of the cTnT$^+$ cell population were performed in the FlowJo software version 10 and Flowing Software 2.5.1.

5.9.10.3 Electrical pacing

Electrical pacing during the final tissue measurement was used to eliminate the effect of beating frequency on the force developed by the EHTs. The electrical stimulation was performed according to the procedures previously described (Hirt et al. 2014). The EHTs were transferred to fresh medium at least 2 hours before starting the experiment. The silicone racks containing the EHTs were then mounted on graphite pacing units (EHT Technologies) and stimulated with a Grass S88X Dual Output Square stimulator (Natus Neurology Incorporated). The EHTs in all experiments were paced at 2 Hz with an output voltage of 2 – 3 V and a biphasic pulse duration of 4 ms. Tissues that did not respond to the electrical stimulation were excluded from the analysis.

5.9.10.4 Glucose and lactate measurements

On the last day of the experiments, 1-day-old (25 hours) cell culture medium was collected. To remove cellular debris, the medium was centrifuged for 5 minutes at 1,000xg, 4 °C. The supernatant was transferred to new reaction tubes and stored at -20 °C. On the day of the measurement, samples were thawed at RT and analyzed with a blood gas analyzer ABL90 FLEX Analyzer (Radiometer). Approximately 0.5 mL of each sample was injected into the analyzer. Glucose consumption was calculated by subtracting the glucose concentration in the measured medium from the known glucose concentration in a fresh complete EHT medium (5 mM).

5.9.10.5 NT-proBNP measurements

The culture medium for NT-proBNP measurements was collected as described in the section 5.9.10.4. Frozen samples were transported to the UKE Biomarker Laboratory and analyzed with the Architect BNP assay. Data were collected with the Abbott Architect i2000 Immunoassay Analyzer. The measurements were kindly performed by the working group of Prof. Tanja Zeller (Molecular Cardiology, University Heart and Vascular Center Hamburg, Hamburg, Germany).

5.9.10.6 Bulk RNA-sequencing

Total RNA was isolated as described in 5.10.1. The quality and quantity of RNA was assessed with a Nanodrop ND-1000 spectrophotometer. Frozen RNA was shipped to the Core Facility Genomics of the University of Münster, Germany, where library preparation, sequencing and data analysis were performed.

5.9.10.7 Single nucleus RNA-sequencing

Single nucleus suspension preparation for snRNA-seq was performed by combining nucleus isolation with Nuclei Extraction Buffer (Miltenyi Biotec) in the gentleMACS OctoDissociator (Miltenyi Biotec) and magnetic bead-based purification with Anti-Nucleus MicroBeads (Miltenyi Biotec). First, frozen tissue was transferred to gentleMACS C tubes containing Nuclei Extraction Buffer with RNase inhibitor. The tubes were placed in the gentleMACS dissociator and a nuclei isolation program (4C_nuclei_1) was run. After completion of the program, the nuclear suspension was applied to a 70 µm MACS SmartStrainer and washed with 2 mL ice-cold Nuclei Extraction Buffer. Afterwards, nuclei suspension was centrifuged at 300xg at 4 °C for 5 minutes and applied on a 30 µm MACS SmartStrainer. The flow-through containing isolated nuclei was used for further purification with the Anti-Nucleus MicroBeads. Before starting the purification protocol, the number of nuclei was determined by DAPI staining and quantification of the DAPI-positive events by flow cytometry. Afterwards, nuclei were resuspended in nuclei separation buffer and Anti-Nucleus MicroBeads were added (Table 11). After 15 minutes incubation, 2 mL of separation buffer was added and the nuclei suspension was applied onto a LS column placed in the MACS separator. The column was washed two times with 1 mL of nuclei separation buffer. Then, the column was removed from the magnetic separator and the purified nuclei were flushed out by pushing a plunger into the column. The above-described procedure was established in collaboration with the Department of Cardiology at the University of Maastricht in the Netherlands and Miltenyi Biotec. The final sample processing for snRNA-seq, that is, nuclei isolation and purification as well as further library preparation, sequencing and data analysis was performed by Deepak Balamurali at the Department of Cardiology at the University of Maastricht in the Netherlands.

Table 11 Regents used for purification of isolated nuclei

Component	Volume (for 1 million nuclei)
Nuclei separation buffer	450 µL
Anti-Nucleus MicroBeads	50 µL

5.10 Molecular analysis

5.10.1 RNA isolation

The SPLIT RNA Extraction Kit (Lexogen) was used to isolate total RNA from the EHTs. The isolation procedure includes a phenol/chloroform extraction and a column-based purification. Tissues were homogenized in 400 µL isolation buffer and the homogenate was transferred to phase lock gel tubes. To each tube, 400 µL of TRIzol reagent (Thermo Fisher Scientific) was added and mixed by inverting 5 times. In the next step, samples were mixed with 150 µL acidic buffer and 200 µL of chloroform. After 2 minutes incubation at RT, samples were centrifuged for 2 minutes at 12,000xg, 18 °C. As a result of centrifugation, a clear separation of the organic phase (lower) and aqueous phase (upper) was visible. The upper phase containing the RNA was transferred into a new 2 mL reaction tube. To calculate the volume of isopropanol required in the next step, the volume of the upper phase was measured with a pipette and was multiplied by a factor of 1.75. After the addition of isopropanol, the samples were vortexed for 10 seconds and a maximum of 800 µL was loaded onto purification column placed in collection tube and centrifuged for 20 seconds. This step was repeated until the samples have been fully loaded. In the next step, columns were washed three times by applying 500 µL Washing Buffer and centrifuging for 20 seconds. Finally, purification columns were placed in 1.5 mL reaction tubes and 20 – 50 µL of Elution

Buffer was applied onto a column. After 1 minute incubation at RT, samples were centrifuged for 1 minute. The quantity and quality of RNA in the eluant was evaluated with Nanodrop ND-1000 Spectrophotometer.

RNA isolation from cells was performed with a phenol/chloroform extraction protocol. Cells were centrifuged and the pellet was lyzed in TRIzol Reagent. For each 1 mL of TRIzol used 0.2 mL of chloroform was added. Samples were mixed by shaking and incubated for 3 minutes at RT. Afterwards, the samples were centrifuged for 15 minutes at 12,000xg at 4 °C. The resulting phase separation allowed to collect the aqueous phase (upper) containing RNA by pipetting it out to a new reaction tube. To precipitate RNA 0.5 mL of isopropanol was added for each 1 mL of TRIzol used in the lysis step. Next, samples were incubated for 10 minutes on ice and centrifuged for 10 minutes at 12,000xg at 4 °C. The supernatant was removed by pipetting it out and the pellet was resuspended in 1 mL of 75% ethanol per 1 mL of TRIzol used for lysis. Samples were vortexed and centrifuged for 5 minutes at 7,500xg, 4 °C. The supernatant was removed and the RNA pellet was air-dried for 15 minutes. Afterwards the isolated RNA was resuspended in 20 – 50 µL RNase-free water.

5.10.2 Reverse transcription and quantitative real-time PCR

The synthesis of cDNA was performed with High-Capacity cDNA Reverse Transcription Kit (Thermo Fisher Scientific). For each reverse transcription reaction 400 ng of total RNA was used. The components included in the kit and their quantities needed for a single reaction are depicted in the Table below.

Table 12 Reverse transcription reaction mix

Component	Volume per reaction
10x RT buffer	2.5 µL
10x Random primer	2.5 µL
25x dNTPs (100 mM)	1 µL
MultiScribe reverse transcriptase (50 U/µL)	1 µL
RNA	400 ng
Nuclease-free water	Add to 25 µL

Table 13 Thermocycler program for reverse transcription reaction

Temperature	Time
25 °C	10 minutes
37 °C	120 minutes
85 °C	5 minutes
4 °C	∞

For the quantitative real-time PCR (qPCR) reactions, cDNA was diluted 1:10, and each gene was analyzed in three technical replicates. The composition of qPCR master mix for a single reaction is presented in Table 14 and the primer sequences can be found in the appendix (section 9.5). The reactions were performed with AbiPrism 7900HT Fast Real-Time PCR System (Applied Biosystems) and QuantStudio 5 Real-Time PCR System (Applied Biosystems). Gene expression was calculated based on the ΔΔCt method and depending on the experiment either *GAPDH* or *GUSB* was used as a housekeeping gene.

Table 14 qPCR reaction mix

Component	Volume per reaction
EvaGreen master mix	2 µL
Forward/Reverse primer mix (10 µM)	0.5 µL
cDNA	2 µL
Nuclease-free water	5.5 µL
Total	**10 µL**

Table 15 Thermocycler program for qPCR reaction

Cycles	Temperature	Time
1	50 °C	2 minutes
	95 °C	10 minutes
40	95 °C	15 seconds
	60 °C	1 minute
1	95 °C	15 seconds
	60 °C	15 seconds
	95 °C	15 seconds

5.11 Statistical analysis

The statistical analysis was performed with GraphPad Prism 10.0.2. Data are presented in a form of line graphs, dot plots or bar charts with mean and SEM displayed. The evaluation of statistically significant differences was conducted on datasets with $n \geq 3$. If applicable, datasets were examined for normal distribution and equal variances. Depending on the experimental configuration, the differences between the groups were analyzed with most suitable statistical test. The overview of statistical analyses used for comparison of datasets with 1 variable is presented in Table 16, whereas the datasets with 2 variables were analyzed with Two-Way ANOVA. The applied statistical tests were followed by appropriate post-hoc test for the correction of multiple comparisons. Differences with p-value below 0.05 were considered statistically significant.

Table 16 An overview of statistical tests used for the analysis of the datasets with one variable

Experimental design	Test type	Normal distribution	Assumption of equal SDs
Comparison of 2 groups	t-test	Yes	Yes
	Welch's test	Yes	No
	Mann-Whitney test	No	-
Comparison of > 2 groups with 1 variable	One-Way ANOVA	Yes	Yes
	Welch ANOVA	Yes	No
	Kruskal-Wallis test	No	-

6 Results

6.1 Human induced pluripotent stem cells

The starting point for all differentiations was the hiPSC line ERC001. Additionally, for EC differentiation, a genetically modified ERC001 line expressing GFP was used. Before cells were utilized for the differentiation experiments, quality control analyses of the WCB were carried out to test for pluripotency, genomic stability and microbiological sterility. In the first case, the expression of a stem cell surface marker SSEA-3 was examined. The cells were collected and stained with either isotype control antibody or human recombinant anti-SSEA-3 antibody. Flow cytometry analysis demonstrated high SSEA-3 expression in ERC001 cells, with over 90% of cells belonging to the SSEA-3 positive population, confirming the undifferentiated state of the cells (Figure 6A). Following the pluripotency examination, the WCB was analyzed for genomic stability. Therefore, karyotype analyses were performed by the Nanostring Core Facility of the UKE. The results showed no abnormalities in copy number in any of the analyzed loci, indicating the chromosomal integrity of the ERC001 line (Figure 6B). Moreover, the absence of copies recorded for Y chromosome, confirmed the female sex of the cell donor. Lastly, ERC001 was tested for its microbiological sterility. A PCR reaction utilizing a mycoplasma-specific primer set was used to identify possible mycoplasma contamination. The results of the PCR reaction showed no mycoplasma presence in the culture medium collected from ERC001 cells (Figure 6C, lanes 2 and 3). In conclusion, all quality control analyses characterized ERC001 as a mycoplasma-free and highly pluripotent cell line with no genomic abnormalities. Therefore, ERC001 met the quality requirements to be further utilized for differentiation purposes.

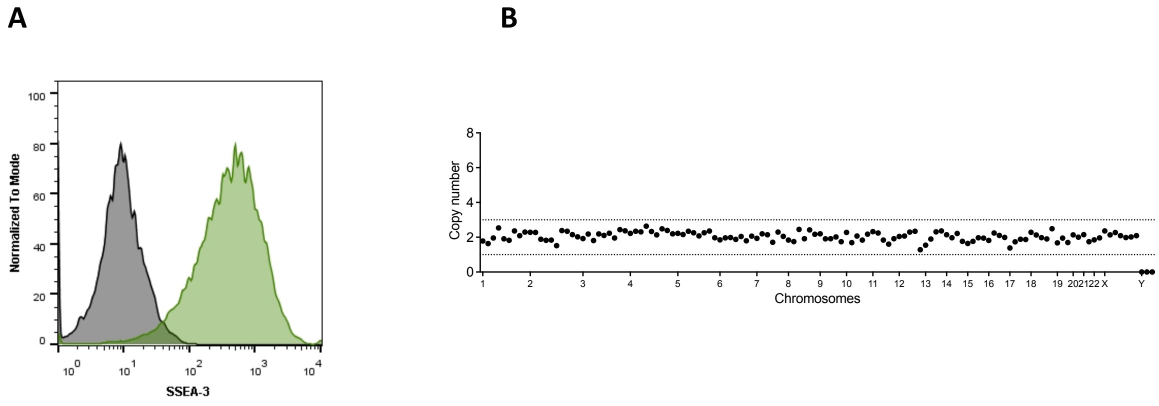

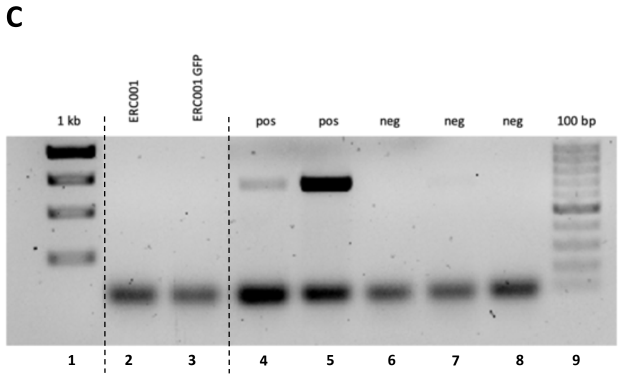

Figure 6 Quality control of the ERC001 cell line. **(A)** Flow cytometry analysis of the pluripotency marker SSEA-3. Isotype control is displayed in gray and ERC001 cells stained with the anti-SSEA-3 antibody are shown in green. **(B)** Nanostring nCounter karyotype analysis. The analysis demonstrated no abnormalities in copy number across different chromosomal regions. **(C)** Mycoplasma detection test. Lack of a PCR product in ERC001 and ERC001 GFP confirmed the absence of mycoplasma contamination. Lane 1: 1 kb ladder, lane 2: ERC001, lane 3: ERC001 GFP, lanes 4 to 5: positive controls, lanes 6 to 8: negative controls, lane 9: 100 bp ladder. At the position of dashed lines, additional unrelated samples were digitally removed.

6.2 Differentiation and characterization of hiPSC-derived cardiomyocytes

The differentiation of hiPSC-CMs was performed in a 3D format. After mesoderm induction and CM specification, EBs were dissociated into single cells and hiPSC-CMs were cryopreserved or directly used for EHT casting. To determine differentiation efficiency, the expression of cardiac markers in the generated cells was evaluated by two methods: flow cytometry and immunofluorescence. For the flow cytometry analysis, cells were stained with anti-cTnT antibody. The differentiation efficiency was ranging between 60 – 95% cTnT$^+$ cells. A representative histogram demonstrating successful differentiation with over 90% of cTnT$^+$ events is presented in Figure 7A. Moreover, immunofluorescent staining was used to visualize the cardiac proteins in the cells. The hiPSC-CMs were found to express multiple CM markers such as cardiac troponin I (cTnI), alpha actinin and cTnT (Figure 7C). Furthermore, karyotype analyses demonstrated no genomic abnormalities in the differentiated hiPSC-derivatives (Figure 7B). In addition to the analyses of cardiac-specific protein expression, the hiPSC-CMs were evaluated functionally in a 3D tissue format. Therefore, the differentiated cells were cast into fibrin-based EHTs. The contractile performance of these EHTs was followed over a period of 3 – 7 weeks. A detailed characterization of each EHT batch can be found in the chapters with the description of a respective experiment.

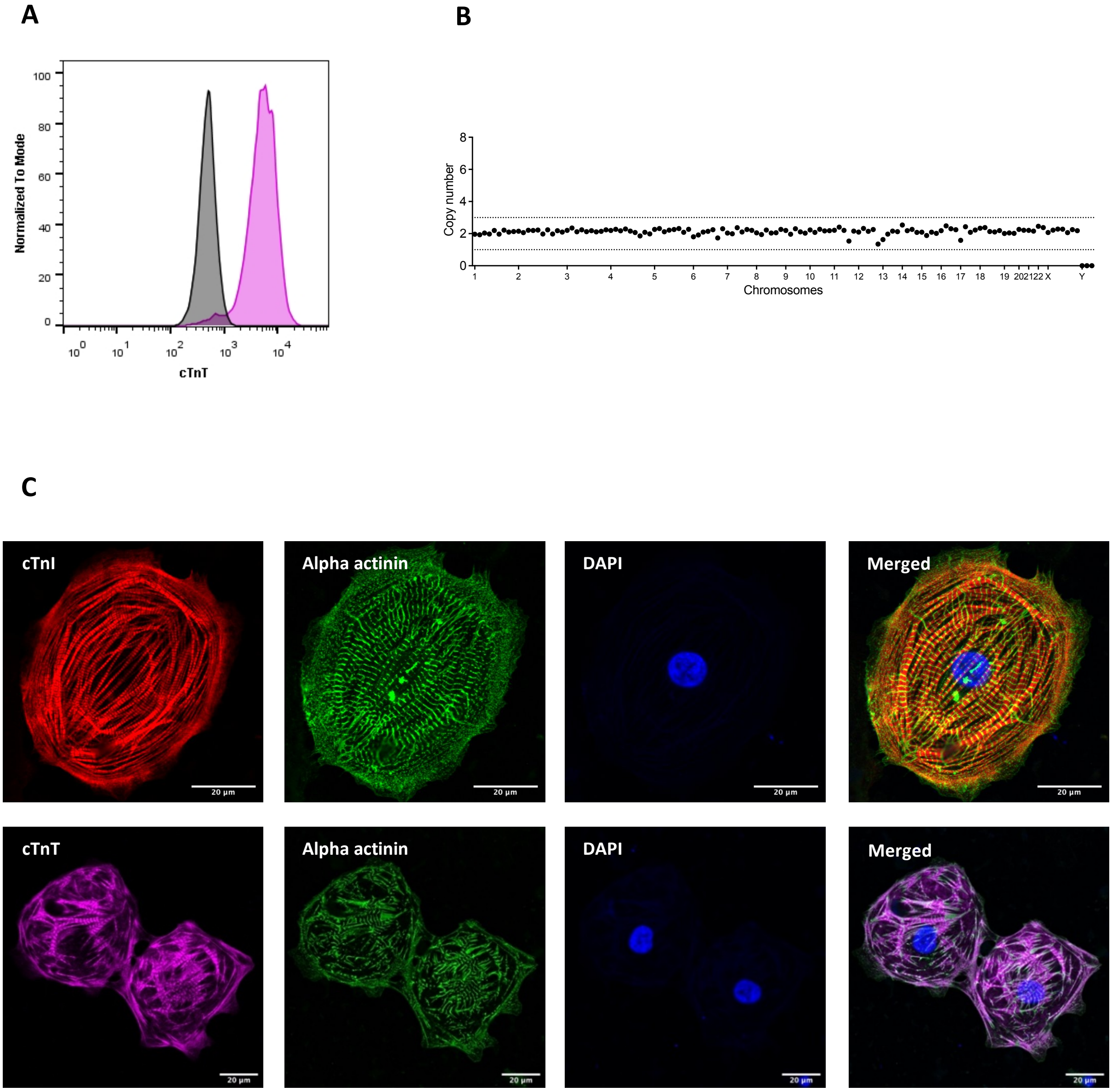

Figure 7 Characterization of hiPSC-CMs. **(A)** Exemplary histogram from the flow cytometry analysis of cTnT. Isotype control is shown in gray and the stained cells are displayed in magenta. **(B)** Nanostring nCounter karyotype analysis. No genomic abnormalities were detected. **(C)** The hiPSC-CMs were stained with antibodies against cardiac proteins. Red: cTnI, green: alpha actinin, magenta: cTnT, blue: DAPI. Scale bar: 20 µm.

6.3 Hybrid EHTs

6.3.1 Isolation of neonatal rat non-CMs

The first approach to establish functional EHTs consisting of multiple cell types was a combination of hiPSC-CMs and neonatal rat non-CMs. This system is referred to as “hybrid EHTs” and was compared to tissues solely composed of hiPSC-CMs. In order to separate the CMs from the non-CMs, in a first step, a trypsin/DNase digestion was carried out to isolate neonatal rat cardiac cells. In the next step, two methods were examined for the separation of the different cell fractions. The first method employed was a widely used pre-plating method. Here, different adhesion properties of CMs and non-CMs are exploited to separate the two cell fractions. For instance, CFs and ECs are known to attach faster to uncoated cell culture dishes in comparison to CMs. Three rounds of pre-plating were performed in order to separate non-CMs from CMs. RT-qPCR analyses were employed to examine the expression of cell-type-specific markers in the isolated cell fractions. The results demonstrated increased expression of fibroblast (*POSTN*, *VIM*), endothelial cell (*PECAM-1*, *ICAM-2*) and immune cell (*PTPRC*, *CD68*) markers in the non-CM fraction. The cardiomyocyte markers (*ACTA1*, *TNNT2*) were more abundant in the CM fraction, showing a successful enrichment of CMs with the pre-plating method. However, pre-plating was found to have low efficiency in separating SMCs from CMs, represented by the comparable expression of *ACTA2* in both fractions as well as lower expression of *MYH11* in the non-CM component (Figure 8).

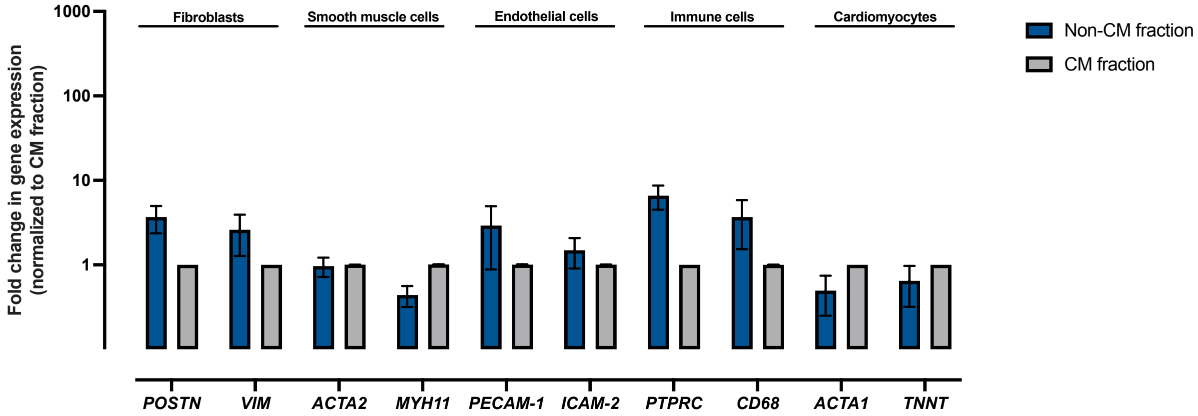

Figure 8 Efficiency of non-CM and CM separation by pre-plating. For the analysis, Ct values of target genes were normalized to *GAPDH*. The $2^{-\Delta\Delta Ct}$ values are shown on the graph. Data are presented as mean ± SEM; n = 3 biological replicates.

To improve the separation of the two distinct cellular fractions, an antibody-based method (MACS) was used. The description of this separation approach can be found in the section 5.1.3. The two isolated fractions were analyzed by RT-qPCR for the expression of non-CM and CM markers. As a result, MACS allowed for a more precise separation of the two cell fractions as evidenced by the higher differences in expression of markers characterizing respective cell population. In particular, the isolation of ECs, immune cells and SMCs was more efficient with MACS than with the pre-plating method. Moreover, a higher purity of the CM fraction was achieved represented by low expression of CM markers in the non-CM compartment (Figure 9). These results demonstrate a higher efficiency of MACS in separating non-CMs and CMs. Consequently, the MACS method was selected as the optimal approach for the isolation of neonatal rat non-CMs for the hybrid EHTs.

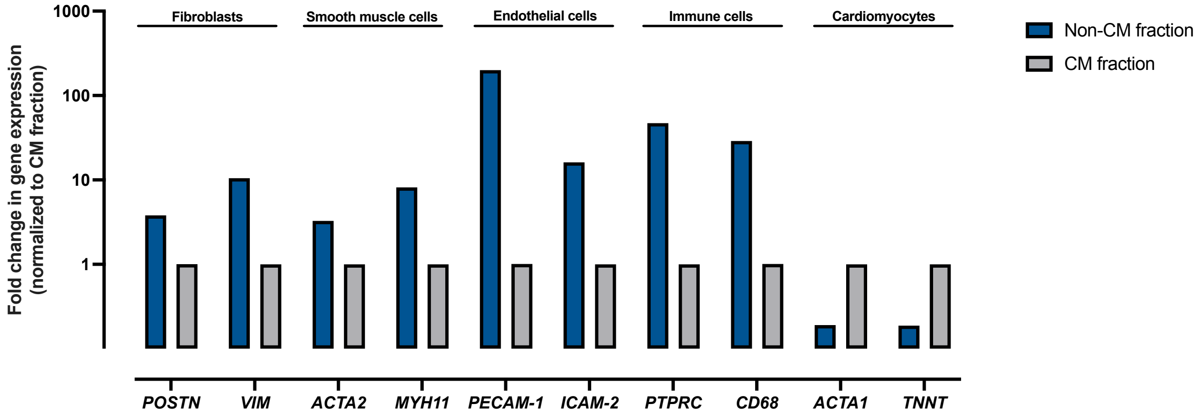

Figure 9 Efficiency of non-CM and CM separation by MACS. For the analysis Ct values of target genes were normalized to *GAPDH*. The $2^{-\Delta\Delta Ct}$ values are shown on the graph. Data are presented as mean; n = 1 biological replicate.

6.3.2 Characterization of hybrid EHTs

6.3.2.1 Isolation of rat non-CMs with MACS

After establishing conditions that separate CMs from non-CMs with high efficiency and specificity, the next step was to examine the impact of the bead-based separation procedure on the non-CM survival. Therefore, isolated non-CMs were plated in NKM medium and cultured for 6 days. The majority of adherent cells exhibited a healthy morphology, with no signs of cellular flattering or enlarged vacuoles typically associated with senescence (Figure 10A). Additionally, no beating cells were observed in the flasks, thereby confirming the successful separation of the non-CMs and CMs. The next step was to generate hybrid EHTs consisting of hiPSC-CMs and neonatal rat non-CMs. Here, 200,000 neonatal rat non-CMs and 800,000 hiPSC-CMs were combined into a single EHT (in one experiment 400,000 rat non-CMs and 600,000 hiPSC-CMs). Due to the use of magnetic beads in MACS method, the antibody-bead complexes attached to the isolated non-CMs were still visible in the EHT matrix as red dots (Figure 10B).

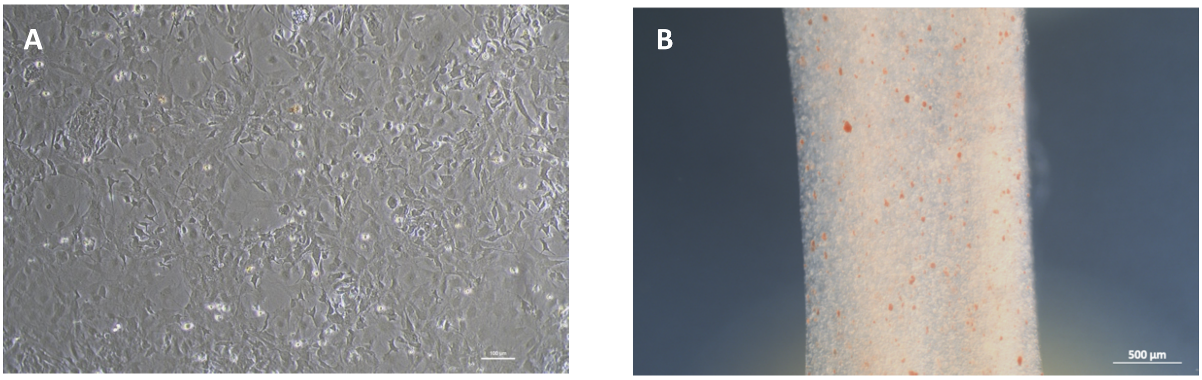

Figure 10 (A) 2D culture of isolated non-CMs. Scale bar: 100 µm. **(B)** Brightfield image of a hybrid EHT on the 1st day of culture. Scale bar: 500 µm.

6.3.2.2 Hybrid EHTs – remodeling analysis

The remodeling of the EHTs was evaluated based on the images taken while contractile properties of the tissues were measured. The results demonstrated that the hybrid EHTs, which contained neonatal rat non-CMs and hiPSC-CMs, underwent accelerated remodeling compared to those consisting exclusively of hiPSC-CMs. The hybrid EHTs exhibited a significantly smaller diameter (hiPSC-CM EHTs: 2.31 mm ± 0.07 mm; hybrid EHTs:

0.97 mm ± 0.02 mm; Figure 11A) and slightly smaller resting length (hiPSC-CM EHTs: 4.6 mm ± 0.09 mm; hybrid EHTs: 4.26 mm ± 0.09 mm; Figure 11B) compared to hiPSC-CM EHTs, indicating more extensive remodeling of these tissues (Figure 11C).

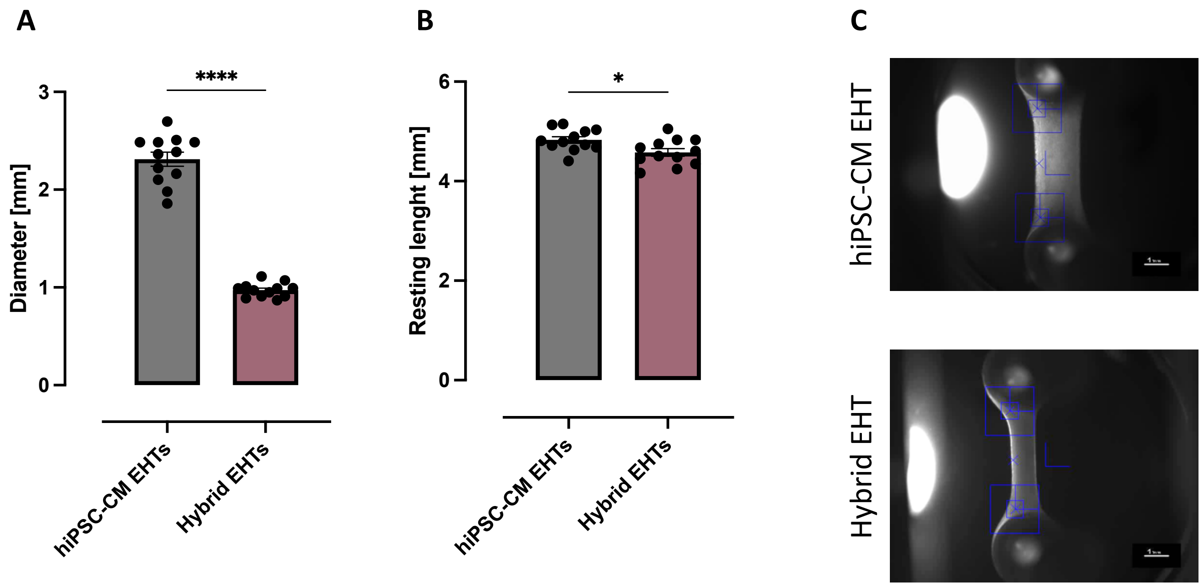

Figure 11 Remodeling analysis of the EHTs on the 8th day of culture. **(A-B)** Measurements of EHT diameter and resting length. Data are presented as mean ± SEM; n = 12 EHTs/group. Statistical analysis: (A) Welch's t test, (B) unpaired t test; $^*p < 0.05$, $^{****}p \leq 0.0001$. **(C)** Exemplary images of hiPSC-CM and hybrid EHTs. Scale bar: 1 mm.

6.3.2.3 Hybrid EHTs – functional analysis

In terms of functional performance, EHTs containing neonatal rat non-CMs developed faster compared to hiPSC-CM EHTs. In all three batches, hybrid EHTs exhibited an earlier onset of beating. The faster development of hybrid EHTs resulted in higher contractile forces and beating frequencies of these tissues in the first 10 days after casting. The force development of hybrid EHTs reached a plateau in the second week of culture, whereas the hiPSC-CM EHTs showed a continued rise in force, finally exceeding the values of hybrid EHTs (Figure 12A). Moreover, the spontaneous beating frequencies of hybrid EHTs were greater than those of hiPSC-CM tissues in the first week following casting. The subsequent culture period was defined by a reduction in the beating rates of hybrid EHTs, resulting in significantly lower frequencies of the hybrid EHTs compared to hiPSC-CM EHTs in the third week of culture (Figure 12B). No differences in contraction and relaxation time of the tissues were observed after 14 days of culture (Figure 12C, Figure 12D).

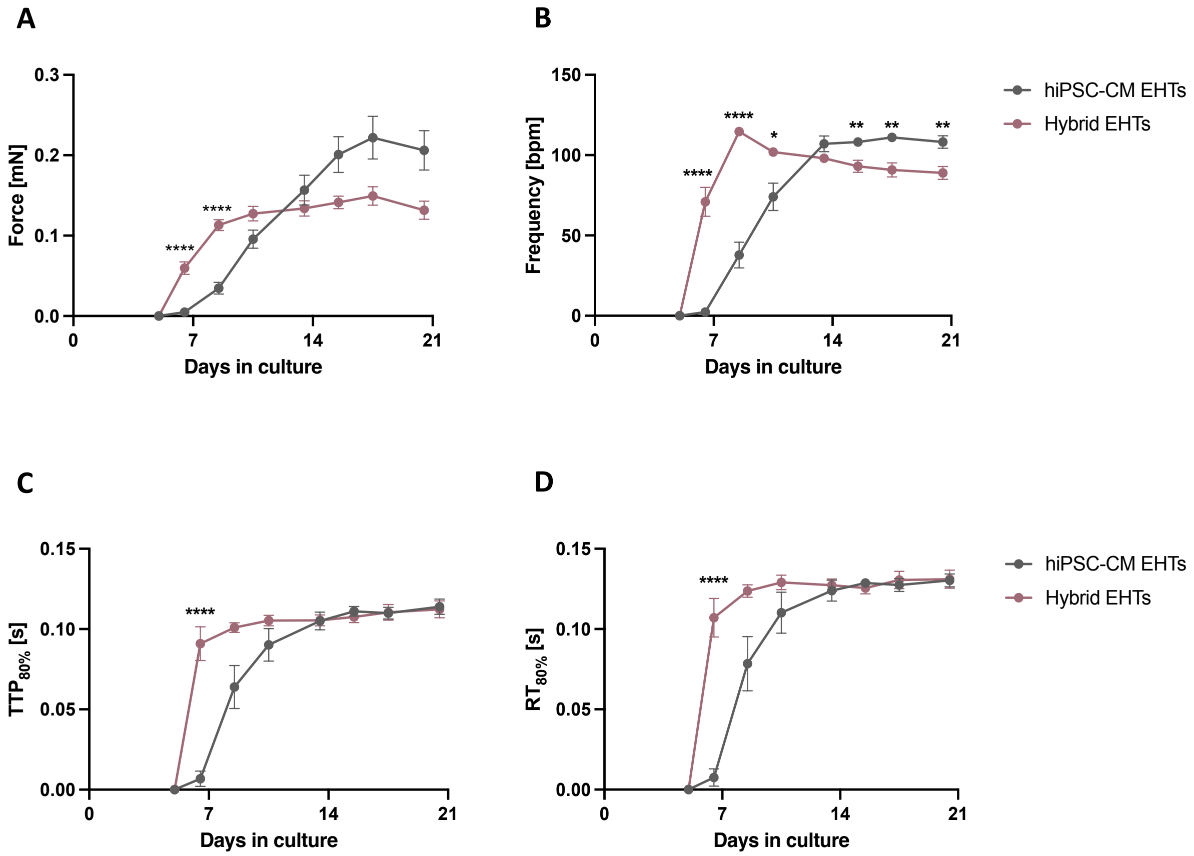

Figure 12 Functional analysis of hybrid and hiPSC-CM EHTs. **(A-D)** The impact of non-CMs on the EHT contractile parameters: **(A)** force, **(B)** frequency, **(C)** contraction time and **(D)** relaxation time. Data are presented as mean ± SEM; n = 27 – 34 EHTs/group from 3 independent batches. Statistical analysis: Repeated measures ANOVA with Bonferroni's post-hoc test for multiple comparisons; *$p < 0.05$, **$p \leq 0.01$, ****$p \leq 0.0001$.

Hybrid EHTs were compared not only to hiPSC-CM EHTs but also to neonatal rat EHTs (rEHTs) generated from unpurified ventricular cells. In this analysis, hybrid EHTs exhibited the highest degree of remodeling when compared to rEHTs or hiPSC-CM EHTs (hybrid EHTs vs rEHTs: -23%; hybrid EHTs vs hiPSC-CM EHTs: -48%; Figure 13A). The hiPSC-CM EHTs were the least remodeled tissues in this comparison. Furthermore, the rEHTs demonstrated the lowest contractile force from all three EHT groups (mean force: hiPSC-CM EHTs: 0.47 mN, hybrid EHTs: 0.29 mN, rEHTs: 0.21 mN; Figure 13B). In line with previous results, hybrid EHTs displayed comparable $RT_{80\%}$ values but lower beating frequencies compared to hiPSC-CM tissues. The values of these two parameters were found to have a statistically significant difference between the hybrid EHTs and rEHTs, i.e., higher beating frequency and lower $RT_{80\%}$ values of the rat tissues (Figure 13C, D). Moreover, hybrid EHTs generated rhythmic contractions, following the characteristics of hiPSC-CM EHTs, rather than bursts of contractions observed in rEHTs (Figure 13E-G). Overall, the inclusion of neonatal rat non-CMs into EHTs with hiPSC-CMs resulted in an intermediate phenotype of the hybrid EHTs. Despite the fact that statistically significant differences between rat and hybrid EHTs were detected, features of hybrid EHTs, namely, degree of remodeling or magnitude of generated force, resembled rather the characteristics of rEHTs than hiPSC-CM tissues. On the other hand, beating frequency, beating pattern or $RT_{80\%}$ of the hybrid tissues followed the patterns observed in hiPSC-CM EHTs.

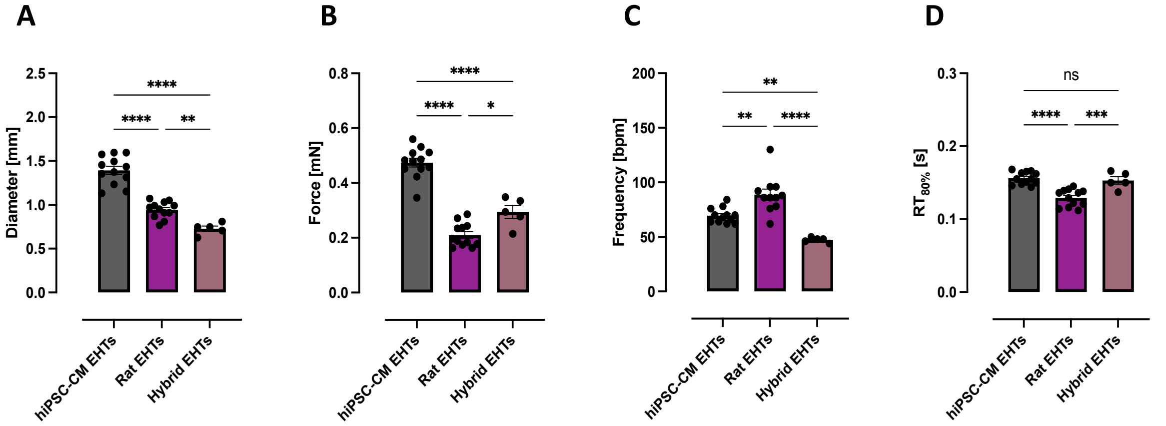

E

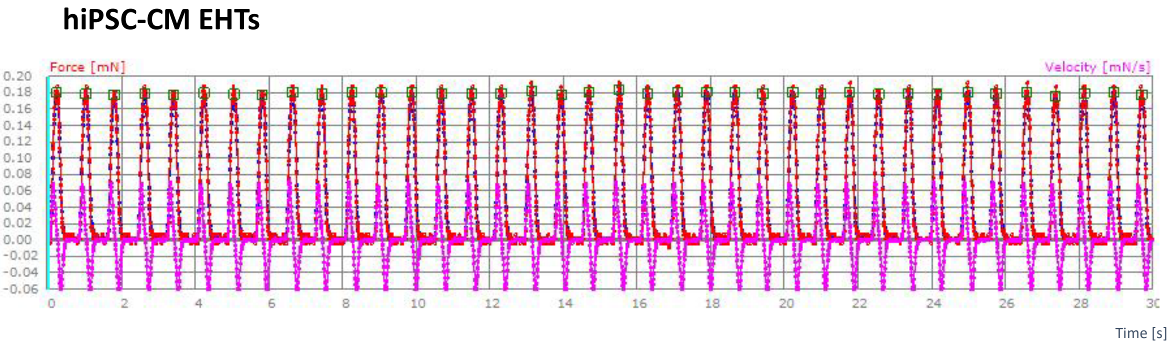

F

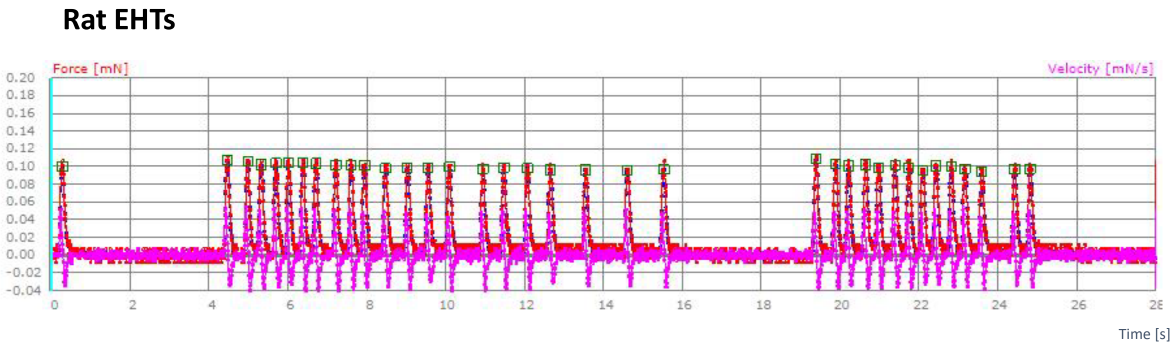

G

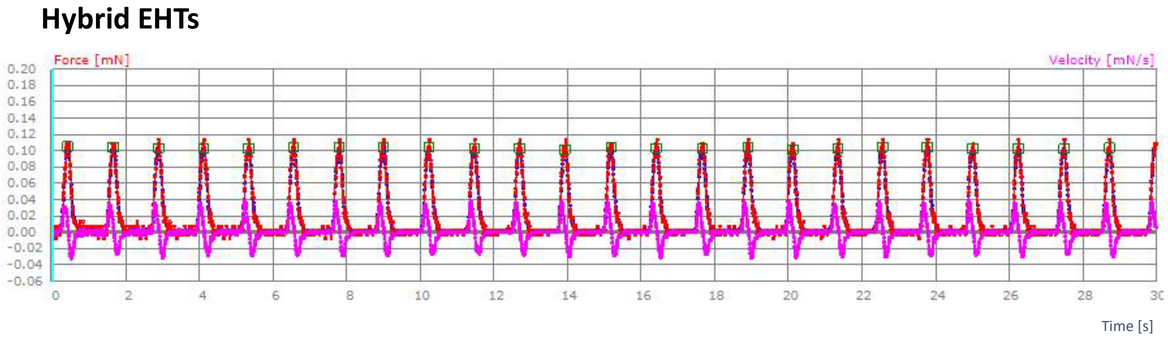

Figure 13 Comparison of hiPSC-CM, rat and hybrid EHTs. **(A-D)** Remodeling and functional analysis. The parameters from day 22 of culture were used for the analysis. Data are presented as mean ± SEM; n = 5 – 12 EHTs/group. Statistical analysis: (A) Welch ANOVA with Dunnett's T3 post-hoc test for multiple comparisons, (B-D) One-Way ANOVA with Tukey's post-hoc test for multiple comparisons, ns $p \geq 0.05$, *$p < 0.05$, **$p \leq 0.01$, ***$p \leq 0.001$, ****$p \leq 0.0001$. **(E-G)** Recordings of EHTs contractions over 30 seconds. Image depiction: x-axis – time, y-axis – force magnitude; red – force recordings, pink – contraction velocity (dF/dt).

6.3.3 Hybrid EHTs – hypertrophy

In this section the contribution of non-CMs to the establishment of pathological hypertrophy in the EHTs is described as this aspect constituted a significant part of the presented project hypothesis. In order to evaluate whether the neonatal rat non-CMs exert an effect on the induction of the pathological phenotype, EHTs were subjected to a mechanical challenge by increasing the afterload (also called afterload enhancement; AE). These experiments were conducted by inserting metal braces into the hollow posts to which the EHTs were anchored. Following 7 days of culture, the braces were removed, and the contractile parameters of the AE-EHTs were compared to their respective controls. The previously described accellerated remodeling of hybrid EHTs (=shortening) caused extensive stretching of the tissues by insertion of the braces that were adapted to a standard EHT. This led to the loss of numerous hybrid EHTs throughout the mechanical challenge. For the analysis, only the tissues that remained attached to the posts were considered, as these EHTs remained fully intact. The functional properties of the tissues were measured at least 30 minutes after the removal of the braces. As pathological hypertrophy is characterized by a decline in force and an increase in relaxation time, the analysis of these parameters was the primary focus in the characterization of the AE effect on the EHTs. The results obtained from the contractility measurements demontrated no enhancing or reducing effect of the AE neither on the force (hiPSC-CM EHTs: -22.6%; hybrid EHTs: + 8.9%, Figure 14A) nor on the relaxation time (hiPSC-CM EHTs: + 2.8%; hybrid EHTs: + 3.2% Figure 14B) of hiPSC-CM and hybrid EHTs.

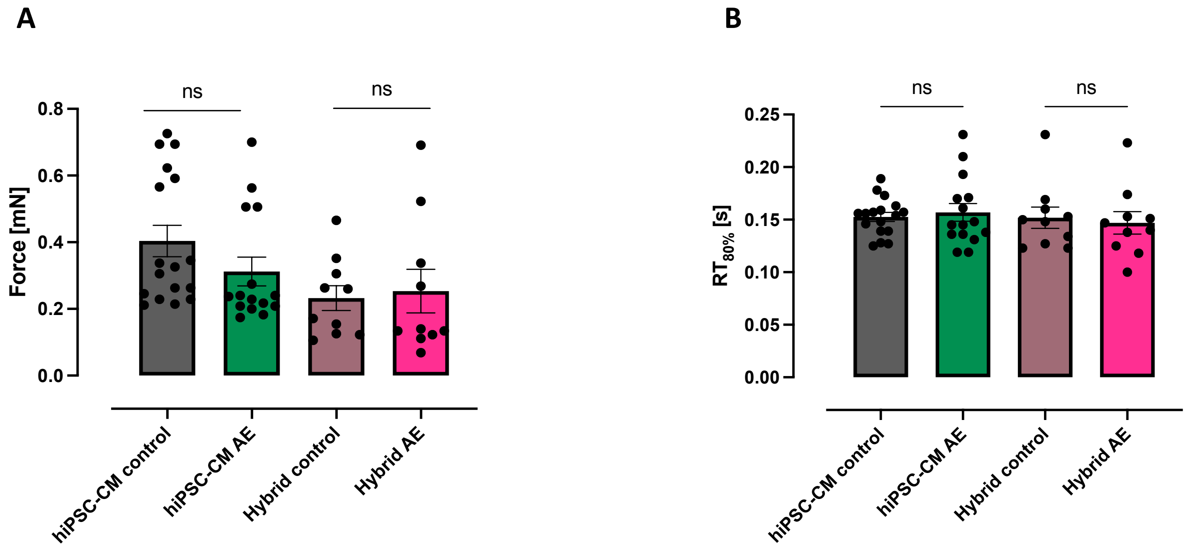

Figure 14 Afterload enhancement in the EHTs – functional analysis. The effect of AE in the hiPSC-CM and hybrid EHTs on the **(A)** force and **(B)** relaxation time. Data are presented as mean ± SEM; n = 10 – 17 EHTs/group from 3 independent batches. Statistical analysis: Two-Way ANOVA with Bonferroni's post-hoc test for multiple comparisons; ns $p \geq 0.05$.

Another hallmark of pathological hypertrophy is the activation of the fetal gene program. It is characterized by upregulation of genes encoding two natriuretic peptides, namely ANP (*NPPA*) and BNP (*NPPB*), as well as downregulation of a gene encoding the sarcoplasmic/endoplasmic reticulum calcium ATPase 2, abbreviated as SERCA2a (*ATP2A2*). Expression analysis of these genes was performed by RT-qPCR. The analysis indicated a tendency towards elevated expression of *NPPA* and *NPPB* in both types of EHTs. On the other hand, the downregulation of *ATP2A2* following AE was more pronounced in the hiPSC-CM EHTs. Nevertheless, none of the observed changes reached statistical significance (Figure 15).

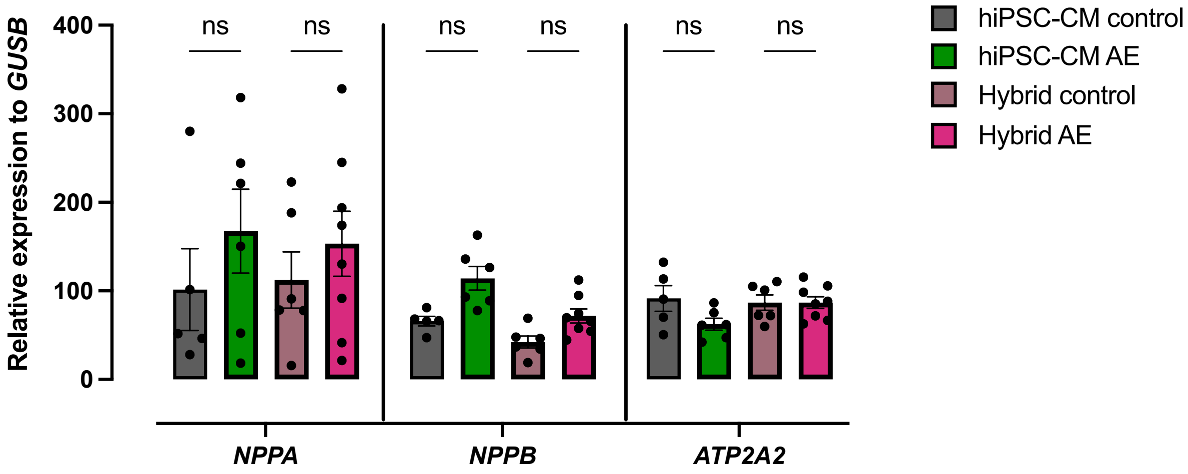

Figure 15 Afterload enhancement in the EHTs – hypertrophic gene program. For the analysis Ct values of target genes were normalized to *GUSB*. The $2^{-\Delta Ct}$ values are shown on the graph. Data are presented as mean ± SEM; n = 5 – 8 EHTs/group from 3 independent batches. Statistical analysis: Two-Way ANOVA with Bonferroni's post-hoc test for multiple comparisons; ns $p \geq 0.05$.

Overall, the experiments demonstrated no significant effect of AE on the induction of hypertrophic phenotype in the multiple cell type (hybrid) system. It could not be excluded that the distinct species origin of the non-CMs was a contributing factor in the lack of a pathological response of AE in the hybrid system. As a consequence, the next steps of the project were to generate multi-cell-type EHTs consisting of hiPSC-CMs and human non-CM populations differentiated from the same hiPSC line.

6.4 Differentiation and characterization of hiPSC-derived cell populations

The generation of EHTs containing hiPSC-derived CMs, ECs, CFs and SMCs was previously described in the doctoral thesis of T. Werner (Werner, 2018). For the current study, the differentiation protocols of the four human iPSC-derivatives were initially based on the established protocols. However, for generating ECs and CFs, modifications of the standard protocols were necessary due to a low differentiation efficiency. A key part of the project was the generation and integration of hiPSC-Mφs into the EHT system. As there were no standard protocols for Mφ differentiation from ERC001 line, a novel protocol needed to be developed to generate this cell type. Therefore, this thesis includes a more detailed description of Mφ differentiation protocol and the characterization of hiPSC-Mφs.

6.4.1 Differentiation and characterization of hiPSC-derived macrophages

The protocol to generate hiPSC-Mφs was established by combining the hematopoietic specification described for the NK cells by Zhu & Kaufman (2019) and macrophage-lineage differentiation published by Ackermann et al. (2018). The final setup of the protocol included the expansion of stem cells and generation of EBs. The EBs were then transferred into medium containing cytokines driving the differentiation into the hematopoietic specification. A crucial step in the development of the protocol was the optimization of the volume of EBs seeded per flask. Typically, volumes exceeding 100 µL of EBs/T75 flask resulted in EB aggregation and subsequently led to low differentiation efficiency. On the seventh day of differentiation, EBs were seeded onto gelatin coated 6-well plates in X-VIVO 15 medium supplemented with IL-3 and M-CSF. The coating supported EB attachment, and promoted the formation of a surrounding cell layer. After attachment to the well surface, a change in the morphology of the EBs could be observed: the initial compact morphology changed to a structure characterized by seemingly hollow protrusions with an overall “bubblier” morphology. After 2 weeks of culture, the EBs started to produce macrophage progenitors, which were released into the medium and further matured for 7 days in terminal differentiation medium. Normally, EBs could constantly produce macrophage progenitors for up to 12 – 15 weeks. In the last differentiation stage, the progenitor cells were cultured in presence of M-CSF for additional 7 days. Cells that completed a week-long maturation step were used for the downstream analysis. Exemplary cell culture depictions of the distinct differentiation stages are shown in Figure 16.

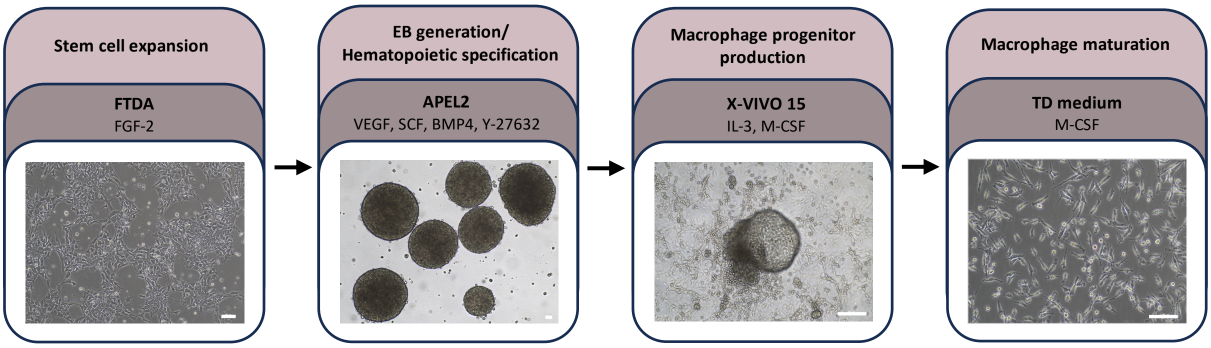

Figure 16 Schematic representation of the macrophage differentiation protocol. In brief, after stem cell expansion, cells were transferred into spinner flasks for EB formation. Around 90 µL of EBs/T75 was cultured for 6 days in STEMdiff™ APEL™ 2 medium containing VEGF, SCF, BMP4 and Y-27632. Afterwards, EBs were seeded onto gelatin-coated 6-well plates in X-VIVO 15 medium supplemented with M-CSF and IL-3. After 2 weeks of culture, EBs started to produce macrophage progenitors which were further matured in terminal differentiation (TD) medium for 7 days. Scale bar: 100 µm.

To monitor the differentiation progress, the expression patterns of stem cell and lineage-specific markers were assessed in samples collected from different stages of the differentiation process. The expression of *SOX2* and *NANOG* (stem cells markers) was decreasing over time of the differentiation and showed highest values in ERC001 sample. The genes specific for the mesodermal/hemogenic endothelium (HE) stage were exclusively upregulated during the EB stage. Expression of *PTPRC* (encoding CD45) and *CD14* (macrophage-lineage genes) was mainly detected in macrophage progenitors and peaked with the highest values in fully matured cells (Figure 17).

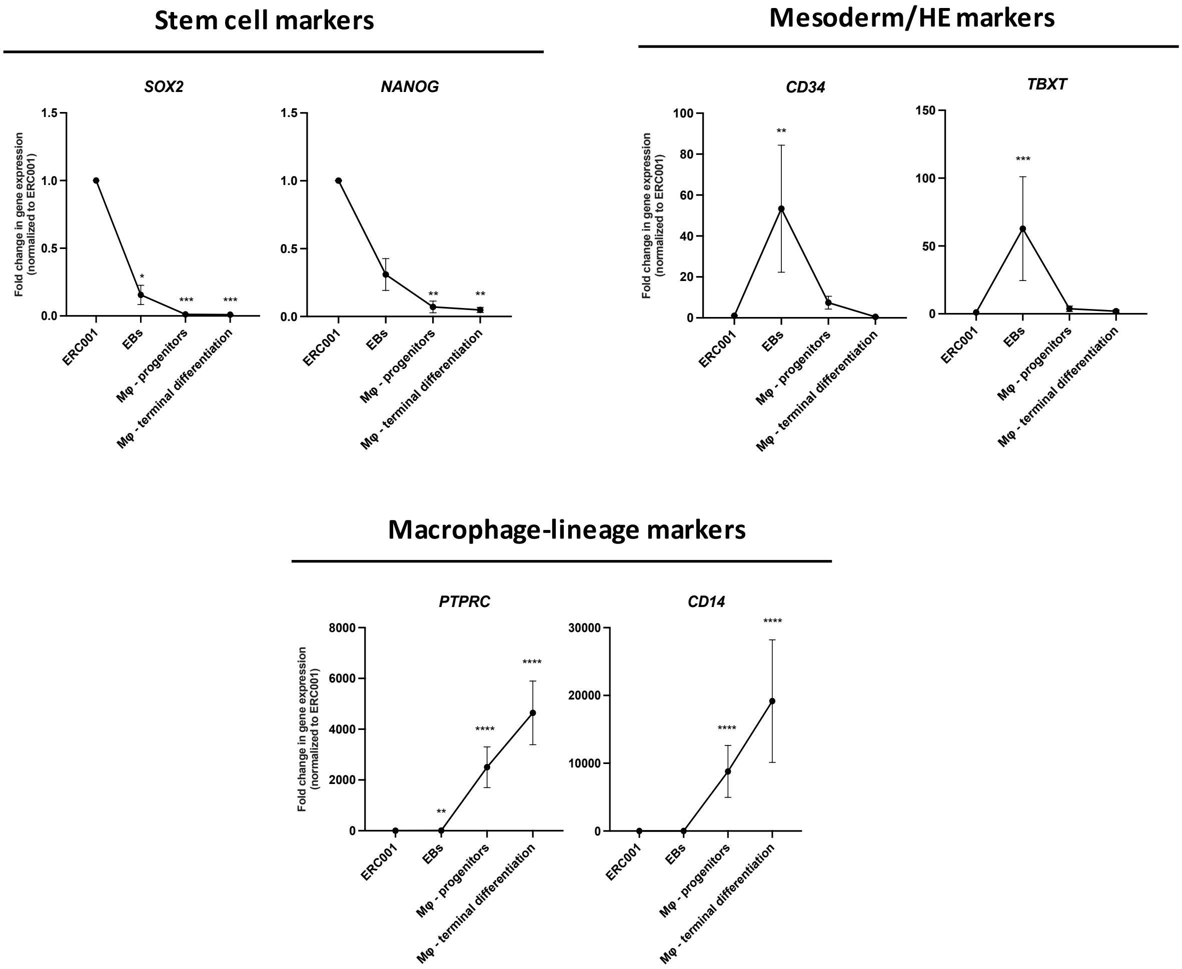

Figure 17 Gene expression analysis of stage-specific markers by RT-qPCR. For the analysis Ct values of target genes were normalized to *GAPDH*. The $2^{-\Delta\Delta Ct}$ values are shown on the graph. Data are displayed as mean ± SEM; n = 3 biological replicates. Statistical analysis was based on the comparison of different stages of differentiation to the undifferentiated state (ERC001 samples). Statistical analysis: One-Way ANOVA with Dunnett's post-hoc test for multiple comparisons; $^{*}p < 0.05$, $^{**}p \leq 0.01$, $^{***}p \leq 0.001$, $^{****}p \leq 0.0001$.

Moreover, to control for the occurrence of genetic changes during the differentiation process, a karyotyping of hiPSC-Mφs was performed. The analysis showed no evidence of genetic changes in the hiPSC-derived cells and confirmed the maintenance of genomic stability throughout the differentiation process (Figure 18).

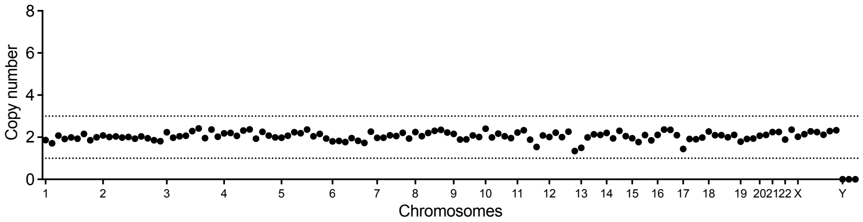

Figure 18 Nanostring nCounter karyotype analysis of hiPSC-Mφs.

The expression of the macrophage markers on the protein level was evaluated by flow cytometry. Cells on the last day of differentiation were collected and stained with antibodies against lineage-specific and myeloid proteins. The hiPSC-Mφs expressed CD45 (leukocyte marker), as well as CD14 and CD68 (myeloid-specific proteins). Additionally, hiPSC-Mφs displayed high expression of a mature macrophage marker which is found on the cell surface and intracellular vesicles of mature Mφs but is absent in immature Mφs or other hematopoietic cells. Furthermore, the terminal differentiation and maturity of the cells was confirmed by the lack of the expression of SSEA-3 (Figure 19).

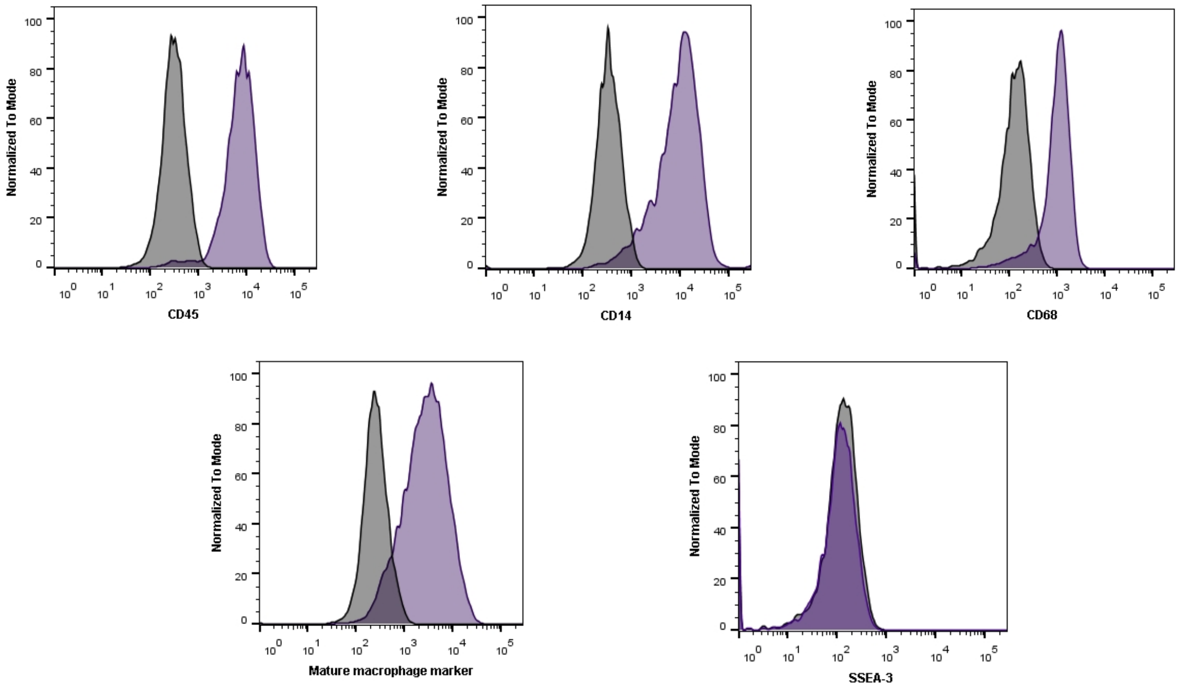

Figure 19 Flow cytometry analysis of hiPSC-Mφs. On the last day of differentiation, cells were harvested and analyzed for the expression of the lineage and myeloid marker proteins. The flow cytometry measurements of different markers were performed with corresponding isotype controls. The isotype controls are displayed in gray; the stained for the marker of interest samples are shown in purple.

The functional assessment of the hiPSC-Mφs was based on the phagocytotic activity of the cells, the ability to change their polarization status in response to various stimuli and their degradation properties. To analyze the phagocytotic activity, Mφs were exposed to pH-sensitive bioparticles. Only upon exposure to low pH values (as in phagosomes of Mφs) these bioparticles start to fluoresce (Figure 20A). In the performed experiments, hiPSC-Mφs exhibited higher particle uptake than ERC001 (10-fold) or hiPSC-CMs (11.2-fold), which was represented by an elevated fluorescent signal in this group (Figure 20B). Additionally, beads ingested by hiPSC-Mφs could be visualized by confocal microscopy (Figure 20C).

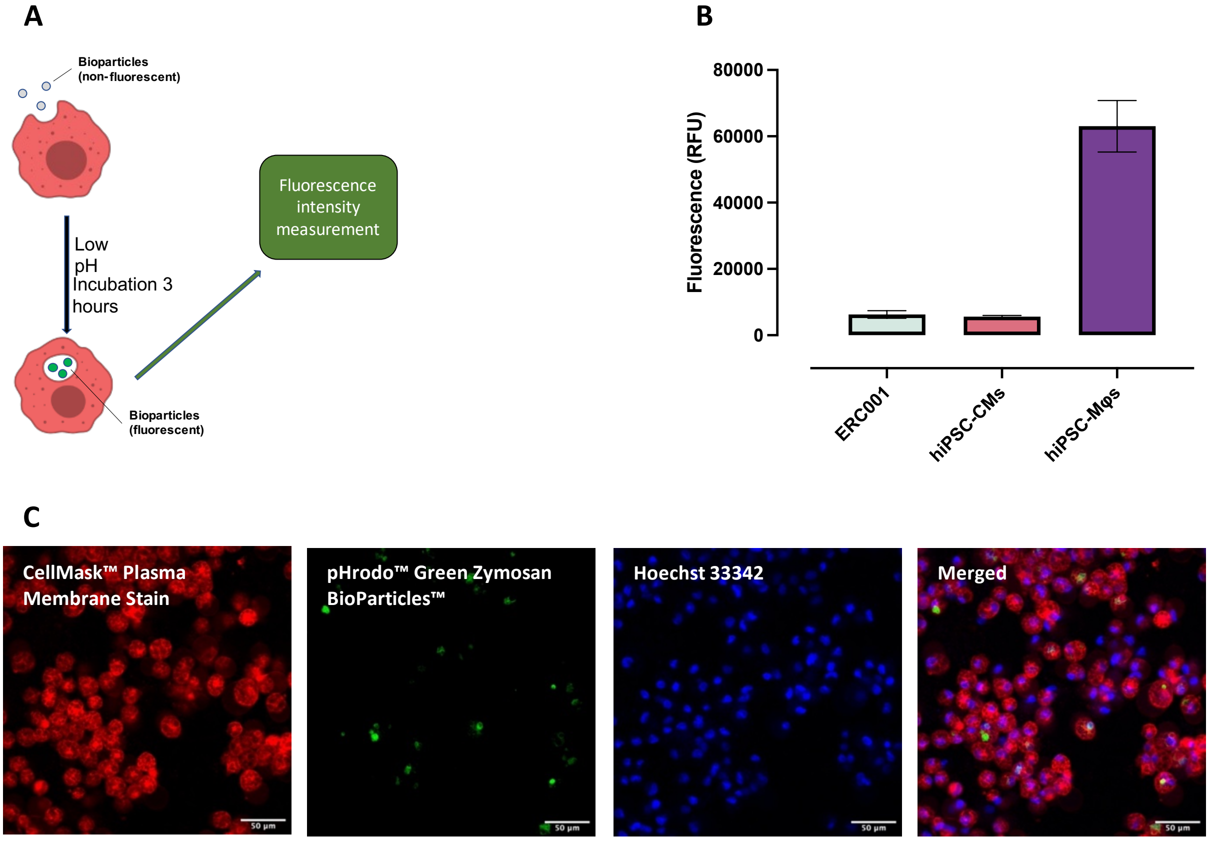

Figure 20 Phagocytosis assay. Phagocytic activity of hiPSC-Mφs was evaluated by incubating the cells with pHrodo™ Green Zymosan BioParticles™. **(A)** Schematic representation of the assay. Created with BioRender.com. **(B)** Fluorescence intensity measurements after 3 hours of incubation with the Zymosan particles. Data are presented as mean ± SEM; n = 6 ERC001, n = 3 hiPSC-CMs, n = 6 hiPSC-Mφs technical replicates, from 1 – 2 independent experiments. **(C)** Immunofluorescent images of the hiPSC-Mφs at the end of the assay. Red: CellMask™ Plasma Membrane Stain, green: pHrodo™ Green Zymosan BioParticles™, blue: Hoechst 33342. Scale bar: 50 µm.

Another characteristic of Mφs is their ability to adopt different phenotypes in response to distinct stimuli or microenvironment. In order to examine whether hiPSC-Mφs demonstrate similar attributes as their native counterparts, cells were stimulated with LPS and IFNγ to evoke the pro-inflammatory phenotype (M1) or with IL-4 for the anti-inflammatory phenotype (M2). The success of the treatment was evaluated by the analysis of marker expression associated with these two distinct activation states via RT-qPCR. The results from these analyses demonstrated that hiPSC-Mφs responded to LPS and IFNγ treatment by increasing the expression of genes encoding for cytokines indicative for the inflammatory states, i.e., *TNFA* (10-fold increase) and *IL-6* (277-fold increase). Additionally, the expression of *CD86*, a routinely used M1 macrophage marker, was upregulated (10.8-fold increase) under LPS and IFNγ treatment compared to untreated cells. However, only the differences in *IL6* and *CD86* expression displayed statistical significance. On the contrary, the stimulation with IL-4 resulted in the elevated expression of the anti-inflammatory cytokine *IL-10* (2-fold), chemokine *CCL24* (56.3-fold) and upregulation of *MRC1* (2.3-fold), which encodes CD206 and has been described as a suitable marker for the alternatively activated (M2) Mφs. However, only the difference in *CCL24* expression was found to be statistically significant (Figure 21).

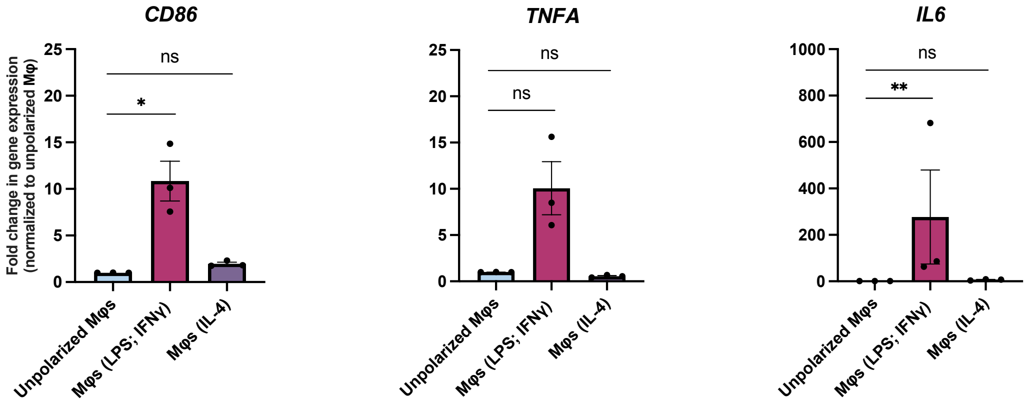

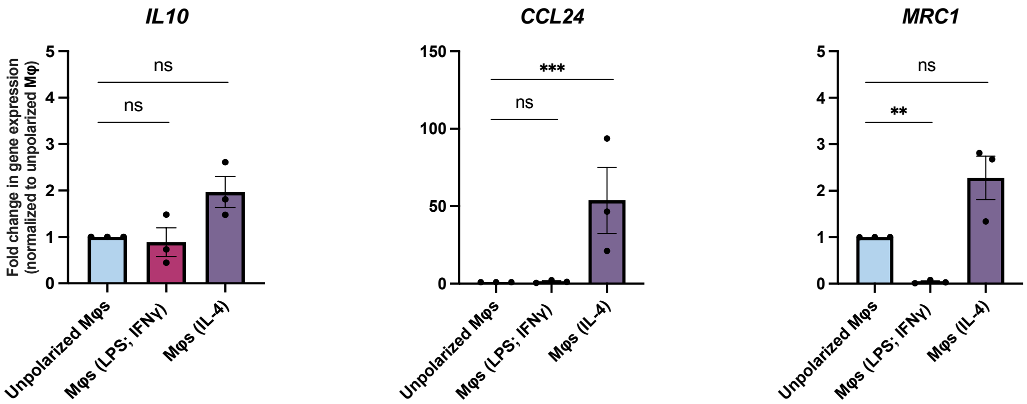

Figure 21 Macrophage polarization – gene expression analysis. The hiPSC-Mφs were stimulated with 20 ng/mL IFNγ + 100 ng/mL LPS (M1 phenotype) or 20 ng/mL IL-4 (M2 phenotype) for 24 – 48 hours. For the analysis, Ct values of target genes were normalized to *GAPDH*. The $2^{-\Delta\Delta Ct}$ values are shown on the graph. Data are displayed as mean ± SEM; n = 3 biological replicates. Statistical analysis: One-Way ANOVA with Dunnett's post-hoc test for multiple comparisons; ns $p \geq 0.05$; *$p < 0.05$; **$p \leq 0.01$; ***$p \leq 0.001$.

In addition to the gene expression analyses, the efficiency of macrophage polarization was evaluated on the protein level. Thus, cells were stained with antibodies recognizing marker proteins specific for the two activation states, namely, CD86 for the pro-inflammatory Mφs and CD206 for the anti-inflammatory ones. In the analysis of CD86 expression, 14.1% of the untreated hiPSC-Mφs were found to be CD86^{+}. A moderate increase of cells expressing CD86 was detected when Mφs were stimulated with IL-4 (22.7% CD86^{+} cells). However, a more pronounced elevation in the number of CD86 expressing cells was observed after LPS and IFNγ treatment, where 93.0% of cells belonged to the CD86^{+} population (Figure 22A). The expression of the M2 marker CD206 increased from 3.92% positive cells in the unpolarized state to 86.3% in the IL-4 treated group. More importantly, only 0.38% of LPS and IFNγ treated Mφs expressed CD206, indicating an IL-4 specific effect (Figure 22B).

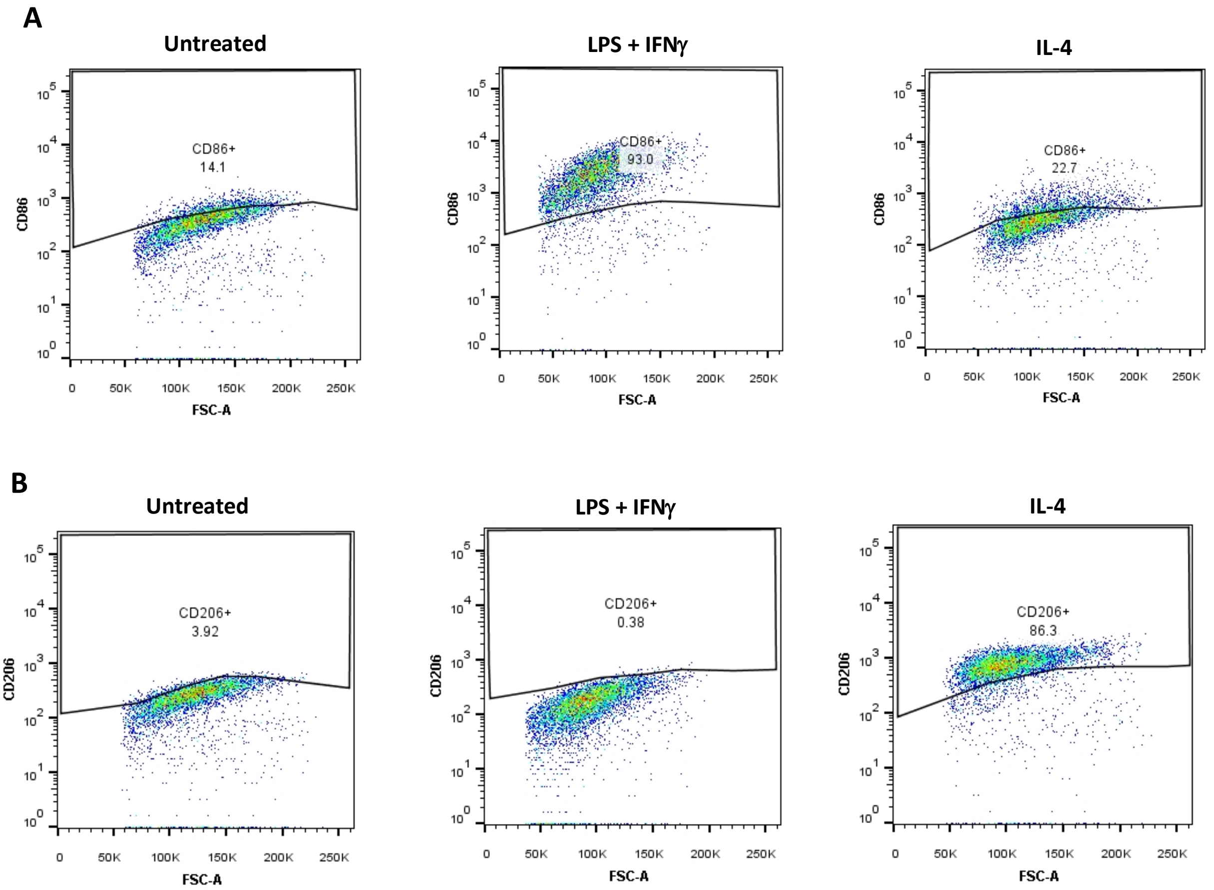

Figure 22 Macrophage polarization analyzed by flow cytometry. **(A)** Analysis of the CD86 expression in untreated (left), stimulated with LPS + IFNγ (middle) and treated with IL-4 cells (right). **(B)** Analysis of the CD206 expression in untreated (left), stimulated with LPS + IFNγ (middle) and treated with IL-4 cells (right). Each sample has been stained with the corresponding isotype control and fluorescently labelled antibody against CD86/CD206. Gating was adjusted to the isotype controls. Only anti-CD86/206 stained samples are displayed.

A functional hallmark of primary Mφs is the expression of MMPs and the ability to degrade ECM components (e.g., collagen or elastin). To evaluate whether hiPSC-Mφs share similar properties, cells were seeded onto a rhodamine-labelled gelatin (partially hydrolyzed form of collagen) and their degradative activity was evaluated (see section 5.5.5). Phalloidin and vinculin were visualized in the cells, indicating the presence of the podosomes (MMPs producing sites). The functional degradation by the hiPSC-Mφs was confirmed though identification of non-fluorescent areas in the rhodamine-labelled gelatin at the macrophage position indicating gelatin degradation (Figure 23).

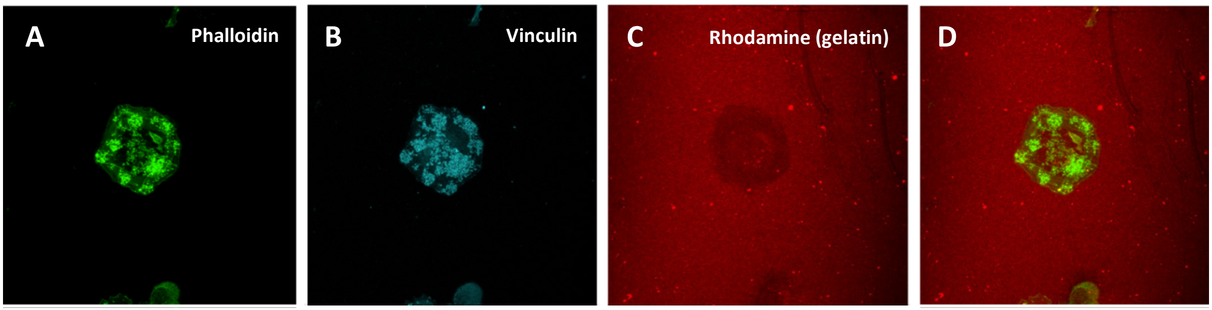

Figure 23 Macrophage degradation assay. The hiPSC-Mφs were seeded onto rhodamine-labelled gelatin and incubated for 5 hours. Podosomes were visualized by staining phalloidin and vinculin in the cells. Green: phalloidin, teal: vinculin, red: gelatin.

In summary, multiple experiments confirmed the efficient and effective hiPSC-Mφ generation with the newly established differentiation protocol. The hiPSC-Mφs demonstrated high expression of myeloid markers evaluated on gene and protein level. Additionally, the functionality of the differentiated cells was confirmed in degradation, phagocytosis and polarization assays. The successful establishment of the differentiation protocol proven by the production of functional hiPSC-Mφs was a first step in the generation of human iPSC-derived non-CM populations consisting of several major cardiac cell types. Hence, the next steps of the project involved the generation of ECs, CFs and SMCs from the same hiPSC line.

6.4.2 Differentiation and characterization of hiPSC-derived endothelial cells

The generation of hiPSC-ECs was initially based on the protocol described in Werner (2018). The mesoderm and endothelial specification were induced in a 3D format (EBs). The EBs were later dissociated and the cells expressing the EC marker CD31 were isolated through MACS and further expanded. This protocol required large quantities of hiPSCs in order to generate EBs, i.e., 30,000,000 cells/100 mL of EB generation medium. After the EB dissociation only 13% of all cells were CD31$^+$ (Figure 24). Moreover, the CD31 expression was decreasing during the cell expansion. The entire differentiation process covered a time frame of approximately 3 – 4 weeks, depending on the number of passages in the expansion step.

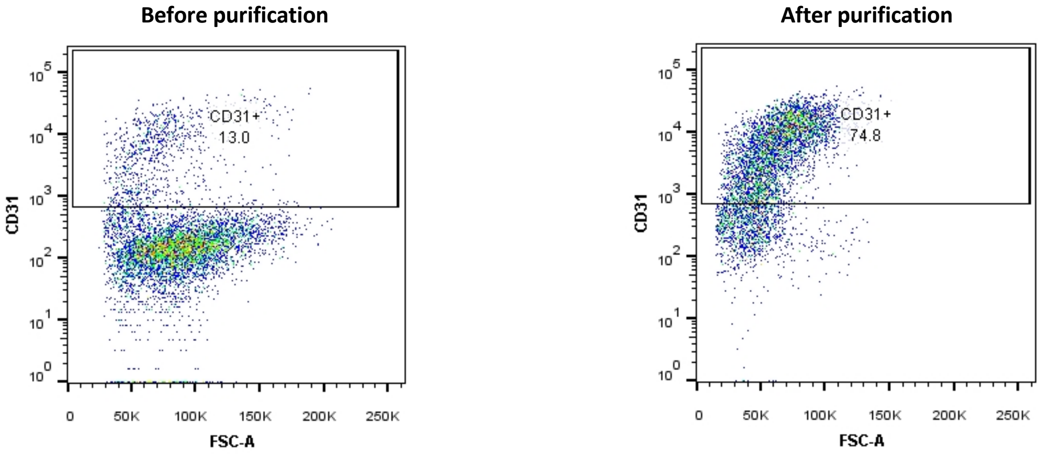

Figure 24 Efficiency of EC differentiation with the EB-based protocol. Cells were stained with the anti-CD31 antibody. Gating was adjusted to the compatible isotype controls. Only anti-CD31 stained samples are displayed on the graphs.

Due to suboptimal outcomes of the differentiation in terms of quality and quantity of the cells, the protocol for hiPSC-ECs was modified. For differentiating hiPSCs into ECs, a new protocol that allowed for the generation of ECs in a 2D format was adapted (see section 5.4.2). In contrast to the 3D protocol, the 2D protocol required lower initial input of hiPSCs and generated high-purity ECs without the necessity for an additional purification step. Additionally, the duration of the differentiation process was reduced from 21 – 28 to 14 days. The differentiation was performed with the standard ERC001 line and genetically modified ERC001 expressing GFP. The hiPSC-ECs generated with this protocol expressed high levels of EC markers such as CD31, CD144, CD34 and CD309. The expression of CD31 and CD144 was additionally visualized in the cells by confocal microscopy (Figure 25A-D). Moreover, a karyotype analysis did not reveal any genomic abnormalities that might have been induced throughout the differentiation process (Figure 25E).

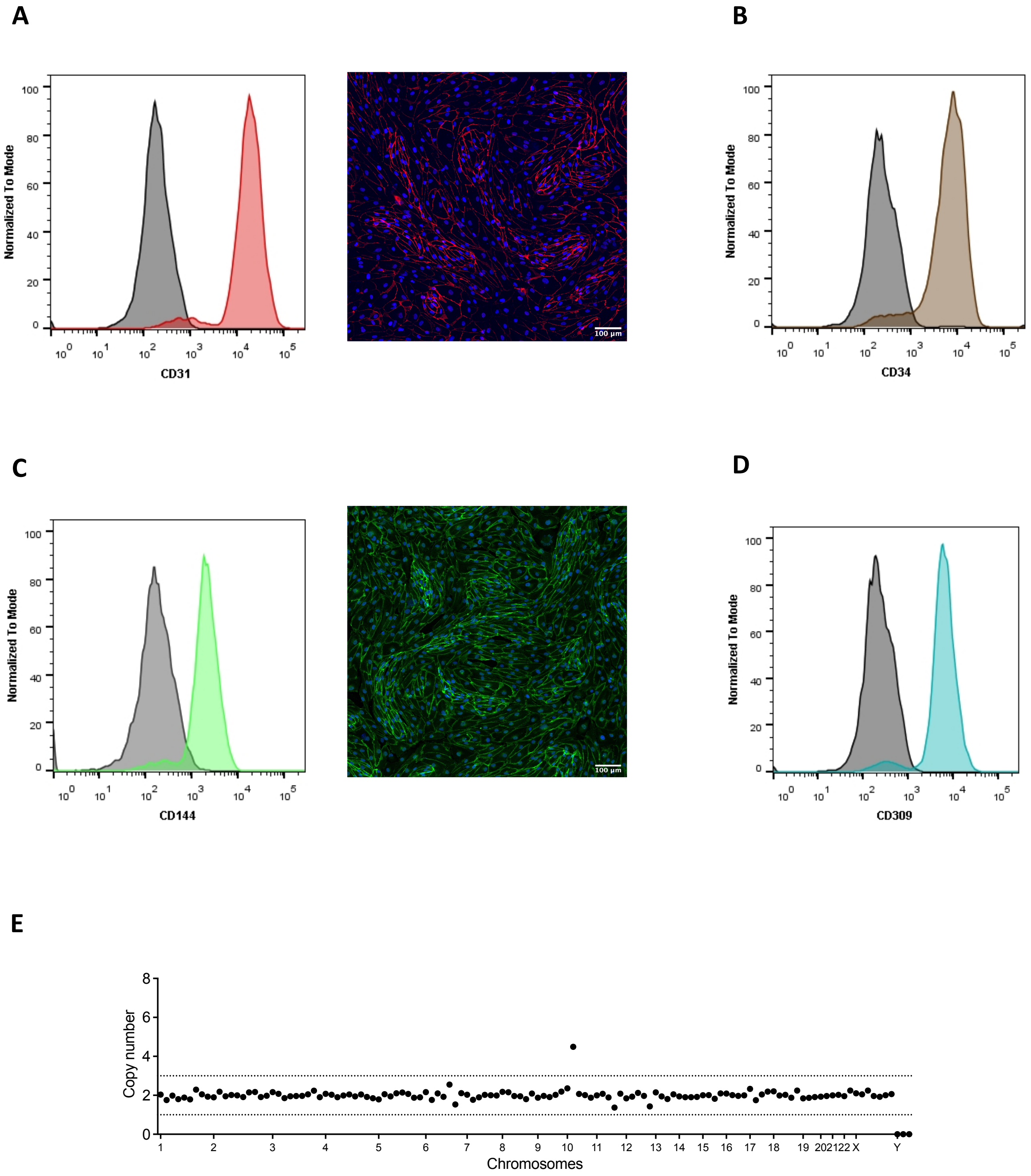

Figure 25 Characterization of hiPSC-ECs. **(A)** Expression of CD31. Left: Flow cytometry analysis. Isotype control is displayed in gray, cells stained with anti-CD31 antibody are displayed in red. Right: immunofluorescent image of CD31 expression. Red: CD31, blue: DAPI. Scale bar: 100 µm. **(B)** Flow cytometry analysis of CD34. Gray: isotype control, brown: anti-CD34 stained cells **(C)** Expression of CD144. Left: Flow cytometry analysis. Isotype control is displayed in gray, cells stained with anti-CD144 antibody are displayed in green. Right: immunofluorescent image of CD144 expression. Green: CD144, blue: DAPI. Scale bar: 100 µm. **(D)** Flow cytometry analysis of CD309. Gray: isotype control, teal: anti-CD309 stained cells. **(E)** Nanostring nCounter karyotype analysis.

In order to evaluate the functionality of the hiPSC-ECs, a tube formation assay was employed. It allows to examine the capabilities of ECs to form capillary-like structures. In short, hiPSC-ECs were seeded onto a Matrigel® scaffold and cultured in EGM medium. As a result, already 1 hour after seeding hiPSC-ECs started to rearrange and generate tubular-like structures which became more prominent after 2.5 hours of incubation (Figure 26).

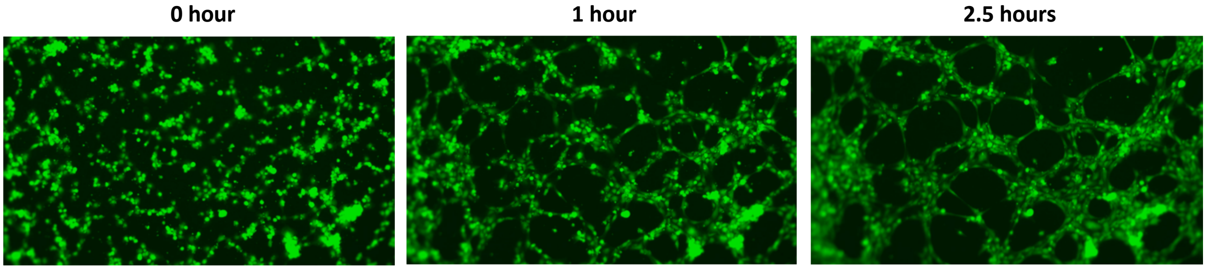

Figure 26 Tube formation assay. On the last day of differentiation cells were collected, seeded onto a Matrigel® scaffold and incubated at 37 °C. Over time, cells started to rearrange and after 2.5 hours of incubation capillary-like structures were observed. Data was collected with a Nikon Live Cell Imaging System.

6.4.3 Differentiation and characterization of hiPSC-derived smooth muscle cells

The hiPSC-SMCs were generated with a 3D-based protocol. In a first step, an epicardial induction was initiated in the EB format. Then, for the subsequent epithelial-mesenchymal transition, EBs were dissociated into single cells and further expanded in a 2D format. Smooth muscle cell specification was achieved by treatment with TGFβ1 followed by stimulation with FGF-2. In a previously described protocol (Werner 2018), the EB dissociation was carried out with a combination of collagenase II and 0.05% Trypsin-EDTA, and the isolated single cells were expanded in Geltrex™-coated flasks. Nevertheless, despite repeated attempts, this process consistently resulted in impaired cell attachment and a further decline in the number of differentiated cells. Thus, this step of differentiation necessitated further modifications. The alternations involved dissociation with collagenase II alone and the implementation of 0.1% gelatin as a coating agent. This resulted in enhanced cellular attachment and a higher number of differentiated cells. Therefore, this process was implemented into the differentiation protocol. The efficiency of differentiation was assessed based on flow cytometry analysis of the SMC marker α-SMA (Figure 27A). The average efficiency of SMC differentiation with the newly modified protocol reached 88.6% of α-SMA$^+$ cells from three differentiation rounds (Figure 27B). Moreover, the expression of additional SMC markers such as MYH11 and TAGLN was evaluated by immunofluorescent staining. The hiPSC-SMCs were found to uniformly express α-SMA, MYH11 and TAGLN confirming the high efficiency of differentiation (Figure 27D). Finally, hiPSC-SMCs did not display any genomic abnormalities (Figure 27C).

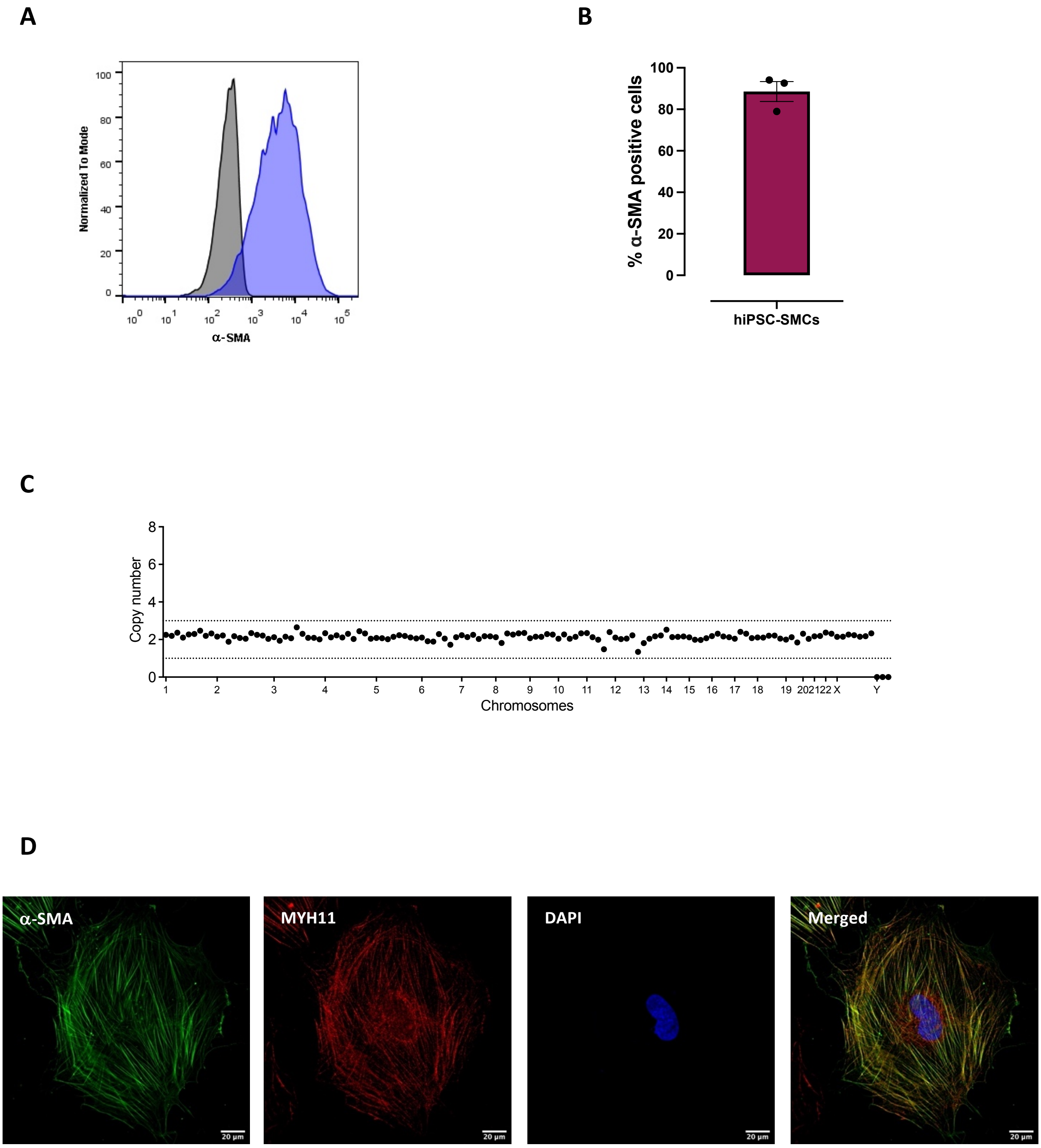

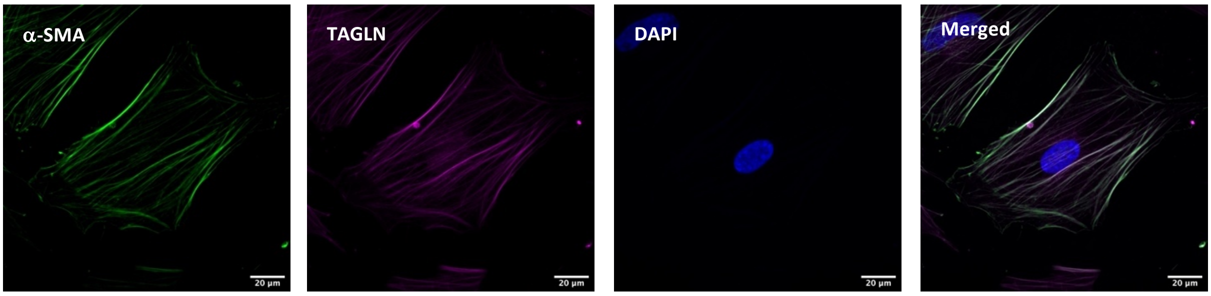

Figure 27 Characterization of hiPSC-SMCs. **(A)** Exemplary histogram demonstrating α-SMA expression in hiPSC-SMCs analyzed by flow cytometry. Cells stained with anti-α-SMA antibody are shown in purple, isotype control is displayed in gray. **(B)** Flow cytometry analysis of the α-SMA expression. Data from three independent differentiation experiments. Data are presented as mean ± SEM; n = 3 biological replicates. **(C)** Nanostring nCounter karyotype analysis. **(D)** Immunofluorescent staining of SMC markers. Green: α-SMA, red: MYH11, magenta: TAGLN, blue: DAPI. Scale bar: 20 µm.

6.4.4 Differentiation and characterization of hiPSC-derived cardiac fibroblasts

In the initial stages of the project, hiPSC-CFs were differentiated in a 3D format according to a previously described protocol (Werner 2018). In this protocol, the first step involved epicardial induction with a subsequent CF specification step with FGF-2 stimulation. Despite the frequent use of the differentiation procedure, the protocol consistently demonstrated limited effectiveness with insufficient numbers of differentiated cells. The average cell numbers harvested at the end of differentiation were ranging between 125,000 – 335,000 cells/T75 flasks (data from three independent runs of differentiation). Due to low efficiency of the hiPSC-CF generation, a new 2D protocol was implemented. In that protocol, the hiPSC-CF differentiation was based on mesoderm induction following a fibroblast specification by treatment with FGF-2 in high concentration. After 3 weeks of differentiation, cells were split and could be further propagated in a medium supplemented with low serum. The adapted protocol modifications yielded a significantly higher output of differentiated cells, with an average of 23,500,000 cells per 6-well plate on day 20 of culture. Moreover, the comparison of CFs derived from both differentiation protocols showed higher expression of fibrotic markers (*ACTA2*, *POSTN*) in the cells generated from the EB-based protocol and pointed to a higher activation state of these cells (Figure 28). Taking into account the low efficiency of differentiation and the high activation state of the hiPSC-CFs, the subsequent generation of CFs was conducted with the recently introduced 2D-based differentiation protocol.

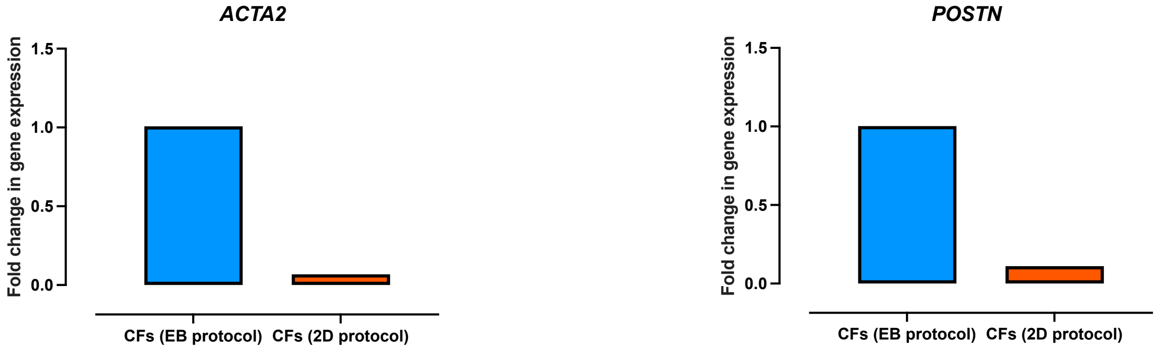

Figure 28 Expression of fibrotic markers in hiPSC-CFs differentiated from 3D and 2D protocol. For the analysis Ct values of target genes were normalized to *GAPDH*. The $2^{-\Delta\Delta Ct}$ values are shown on the graph. Data are presented as mean of 3 technical replicates.

The characterization of CFs was based on the flow cytometry and immunofluorescence analysis of fibroblast proteins such as TE-7, vimentin, Thy-1 (CD90) and collagen I. A high differentiation efficiency was achieved, with 98% of cells expressing vimentin and 91.7% of cells belonging to the CD90$^+$ population (Figure 29A). Moreover, the expression of CF marker proteins could be visualized by immunofluoresce. The hiPSC-CFs were uniformly expressing fibroblast specific protein TE-7. Interestingly, only a small amount of the cells expressed collagen I, confirming the quiescent phenotype of these cells (Figure 29C). In addition, karyotype analysis of the hiPSC-derivatives showed no genomic abnormalities (Figure 29B).

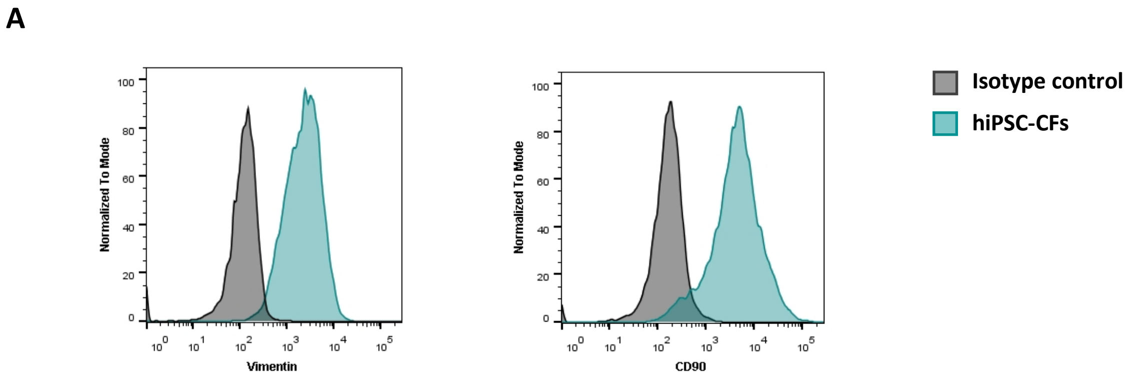

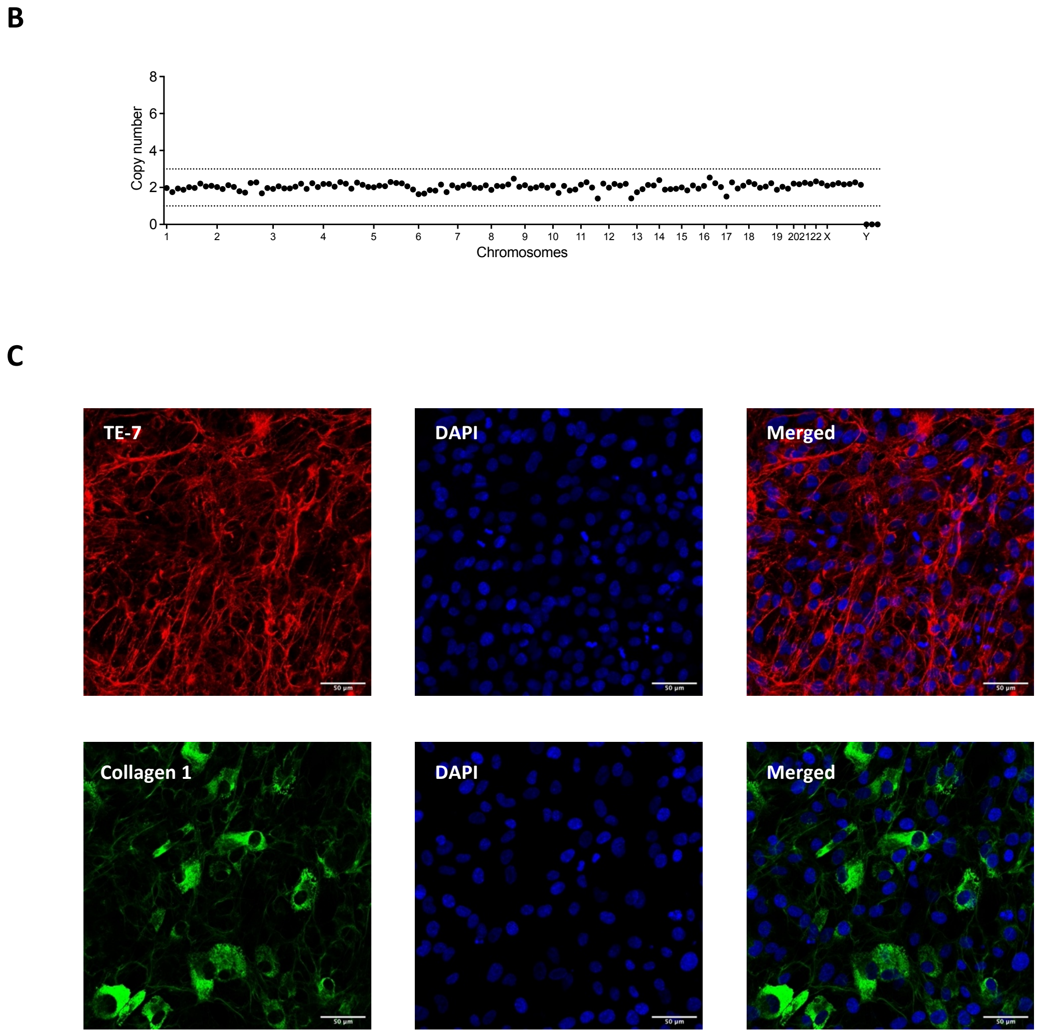

Figure 29 Characterization of hiPSC-CFs. **(A)** Flow cytometry analysis of an intracellular protein vimentin and a surface marker CD90. Isotype control: gray, stained samples are displayed in teal. **(B)** Nanostring nCounter karyotype analysis. **(C)** Immunofluorescent staining of fibroblast markers. Performed stainings: red: TE-7, green: collagen I, blue: DAPI. Scale bar: 50 μm.

The functionality of the hiPSC-CFs was evaluated based on their collagen production properties. Thus, cells were stimulated for 5 days with 20 ng/mL TGFβ1 to induce collagen expression and the transition of the cells to an activated state. Another experimental group was treated with the TGFβ1 antagonist SB-431542 in order to induce the quiescent phenotype of the cells. Additionally, to maintain the low activity state of the cells, hiPSC-CFs were seeded onto laminin-coated plates and the stimulation was performed in a medium with low serum content (0.4%). The hiPSC-CFs reacted to TGFβ1 stimulation by increasing the expression of fibrotic markers, the most prominent one being *POSTN* (over 9-fold higher). Moreover, the expression of genes encoding for collagen 1 (*COL1A1*) and connective tissue growth factor (*CCN2*) was increased under TGFβ1 treatment (*COL1A1*: 2.83-fold higher; *CCN2*: 5.74-fold higher). Nevertheless, the expression of *COL1A1*, *POSTN* and *ACTA2* was also observed to be higher in the unstimulated group than in the SB-431542 treated group, indicating that the environment in which the experiment was performed (presence of the serum in the medium, high stiffness of the plastic cell culture plates) led to the activation of hiPSC-CFs (Figure 30). However, TGFβ1 treatment further augmented the activation, signifying the cells' functional capacity.

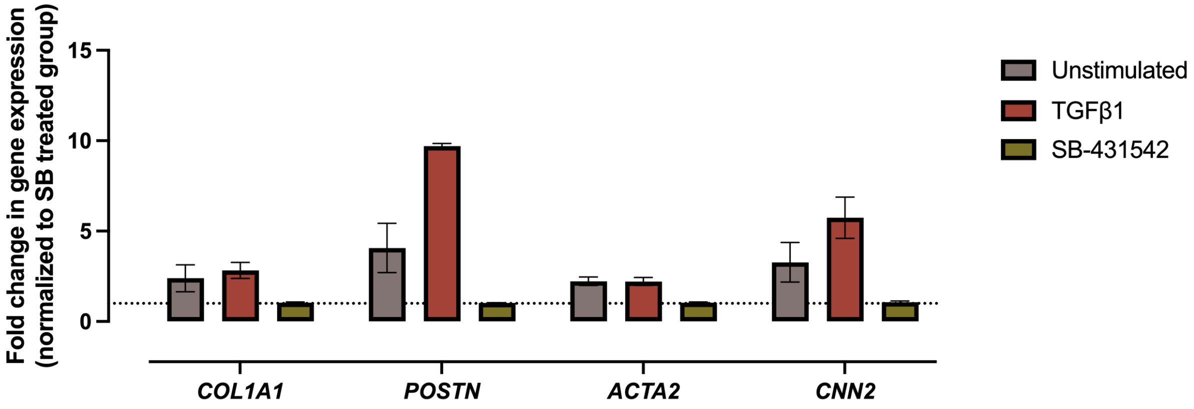

Figure 30 Transition of hiPSC-CFs into myofibroblast state. The hiPSC-CFs were treated for 5 days with 20 ng/mL TGFβ1 or 10 μM SB-431542. For the analysis Ct values of target genes were normalized to *GAPDH*. The $2^{-\Delta\Delta Ct}$ values are shown on the graph. Data are presented as mean ± SEM; n = 2 biological replicates.

6.4.5 Incorporation of hiPSC-derived non-CMs into EHTs

The successful execution of differentiation protocols allowed for generation of fully functional five cardiac cell populations. The subsequent phase of the project focused on the implementation of the hiPSC-derivatives into multi-cell-type EHTs and their comparison to the tissues containing CMs exclusively. In the prior experiments with multi-cell-type EHTs, an experimental arrangement employing a cellular composition of 30% CMs and 70% non-CMs was examined. However, most probably due to the low content of CMs, these EHTs failed to demonstrate contractile activity. Therefore, for the present study, the cellular composition was modified and the content of contractile cells per EHT was increased to 60%. The remaining 40% was assigned to the non-CMs in the following percentages: 20% ECs, 10% Mφs, 5% CFs and 5% SMCs. In order to compare the functional properties of multi-cell-type EHTs to CM-only tissues, the absolute numbers of CMs in both types of EHTs were equalized. The chosen approach included stepwise characterization of the effects of non-CMs on CMs by generation of two-cell-type EHTs containing CMs with each non-CM population separately and further combining all cell types together into multi-cell-type tissues.

6.4.6 Two-cell-type EHTs: effect of non-CM populations on the tissue remodeling and CM function in the EHTs

To characterize the impact of non-CM populations independently from each other, CMs were combined with each cell type separately. In the routinely used protocol for EHT generation, the total cell number per tissue is set to 1 million. Taken into account the anticipated final cellular composition of the single multi-cell-type EHT, i.e., 0.6 million CMs, 0.2 million ECs, 0.1 million Mφs, 0.05 million CFs and 0.05 million SMCs, the two-cell-type EHTs were generated with equal numbers of each cell type as in multi-cell-EHTs. The established cellular composition of the two-cell-type EHTs is presented in the Table below.

Table 17 Cellular composition of two-cell-type EHTs

EHT type	Cellular composition/EHT
CMs + ECs	0.6 million CMs + 0.2 million ECs
CMs + Mφs	0.6 million CMs + 0.1 million Mφs
CMs + CFs	0.6 million CMs + 0.05 million CFs
CMs + SMCs	0.6 million CMs + 0.05 million SMCs

The chosen cell culture medium was based on the standard EHT medium supplemented with 30 ng/mL VEGF to ensure the survival of ECs and 0.2 mM tranexamic acid to prevent excessive remodeling of the tissues.

To analyze the impact of non-CMs on the morphology of the tissues the diameter of the EHTs on the 7th day of culture was determined. In order to exclude the possibility of increased remodeling due to higher cell density in the tissues, the two-cell-type EHTs were compared to CM-only EHTs containing equal CM number per EHT. The result of the analysis showed an increased remodeling of two-cell-type EHTs compared to CM-only EHTs. The highest degree of remodeling was recorded in the EHTs containing CMs and CFs where the diameter of the tissues was 59% smaller than their CM-only counterparts. The EHTs containing SMCs or ECs demonstrated smaller thickness compared to CM-only EHTs by 42% and 52%, respectively. Interestingly, the lowest degree of remodeling amongst the non-CM populations was observed in the two-cell-type EHTs containing Mφs, which exhibited average diameters reduced by 35% in comparison to CM-only constructs (Figure 31).

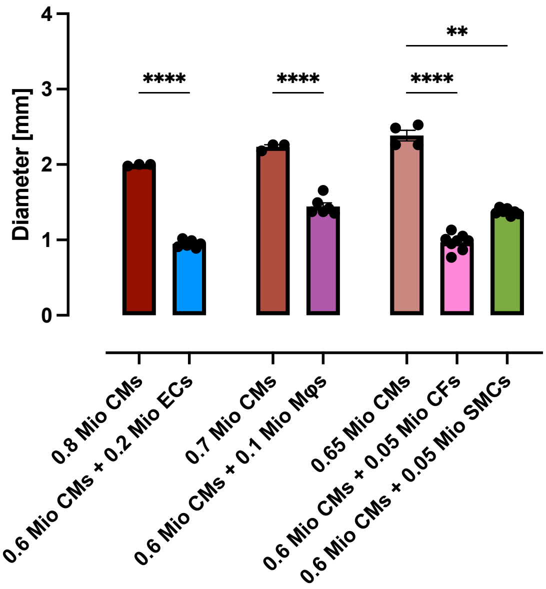

Figure 31 The effect of non-CMs on the EHT remodeling. On day 7 of culture the diameter of the constructs was measured with the Fiji software for image analysis. Data are presented as mean ± SEM; n = 3 – 8 EHTs/group. Statistical analysis: Welch ANOVA with Dunnett's T3 post-hoc test for multiple comparisons; $^{**}p \leq 0.01$; $^{****}p \leq 0.0001$.

The incorporation of non-CMs into the tissues also had an effect on the functional performance of the EHTs. All groups of the two-cell-type EHTs exhibited earlier onset of beating and higher contractile forces than CM-only tissues in the first 3 weeks after casting (Figure 32A-D).

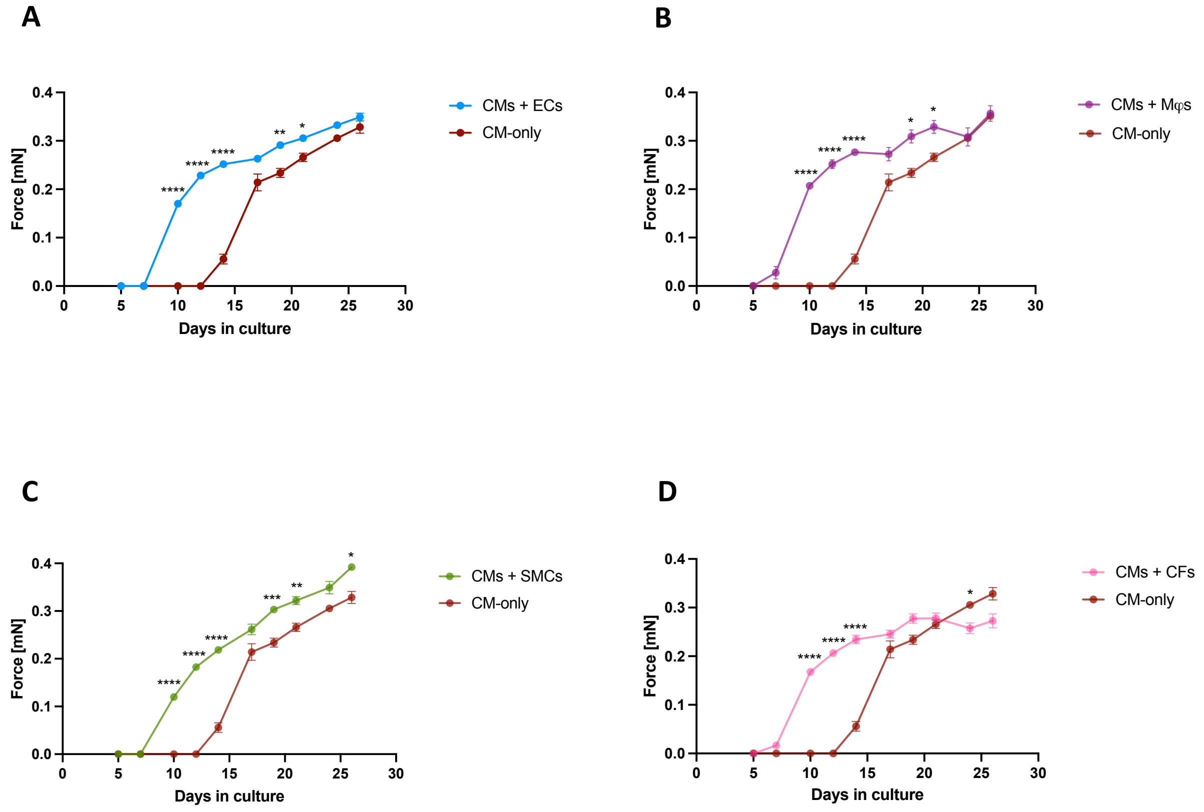

Figure 32 Force development of two-cell-type and CM-only EHTs. **(A-D)** The functional performance of two-cell-type EHTs was followed over 26 days of culture. Two-cell-type EHTs exhibited accelerated development marked by earlier onset of beating and developed higher contractile forces compared to CM-only tissues in the first 3 weeks of culture. Data are presented as mean ± SEM; n = 6 – 8 EHTs/group. Statistical analysis: Repeated measures ANOVA with Bonferroni's post-hoc test for multiple comparisons; *p < 0.05, **p ≤ 0.01, ***p ≤ 0.001, ****p ≤ 0.0001.

However, on the last day of culture (day 26), no significant differences in force between the groups were recorded, except of the tissues containing SMCs, which showed higher contractile forces than the CM-only EHTs (Figure 32C). Analysis of additional parameters, i.e., frequency and relaxation time showed no significant differences between CM-only tissues and either of the two-cell-type EHTs groups (Figure 33A-B).

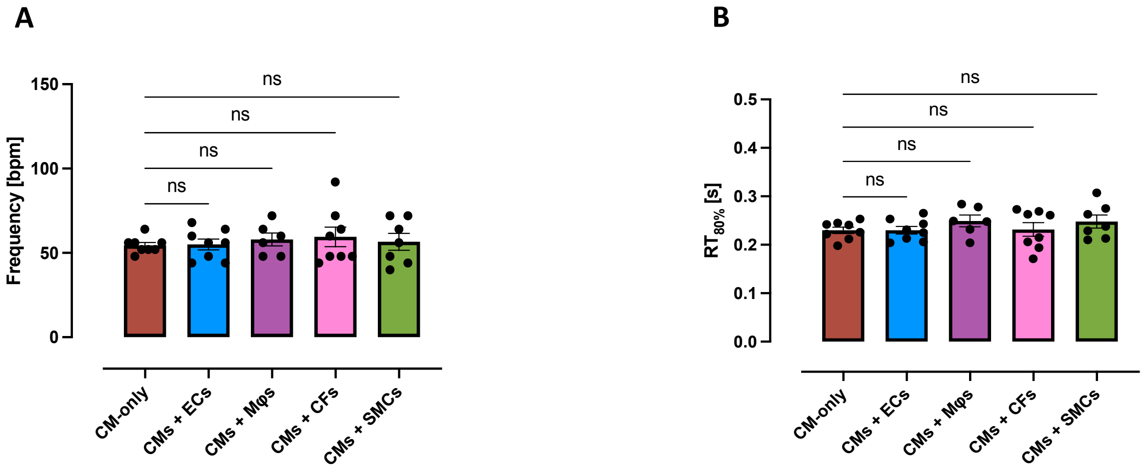

Figure 33 Functional analysis of two-cell-type EHTs and CM-only EHTs on the last day of culture. **(A-B)** The effect of non-CM populations on the EHT functional parameters. On the 26th day of culture the **(A)** frequency and **(B)** relaxation time of two-cell-type EHTs was compared to CM-only tissues. Data are presented as mean ± SEM; n= 6 – 8 EHTs/group. Statistical analysis: One-Way ANOVA with Dunnett's post-hoc test for multiple comparisons; ns p ≥ 0.05.

6.4.7 Hypertrophy in the EHTs containing macrophages

As the project was initially focused on the hiPSC-Mφs and their impact on the EHTs and AE-induced hypertrophic response, the following experiments were performed in the tissues consisting of 90% CMs and 10% Mφs. In the first step, the CMs + Mφs EHTs contained one of three distinct Mφs populations: unpolarized, LPS+IFNγ or IL-4 stimulated Mφs. In the second step, the treatment to induce different Mφ phenotypes was performed either before casting the tissues or while the Mφs were already incorporated in the EHTs after 3 – 4 weeks of culture as described in section 5.5.4. The results of the mechanical challenge revealed no clear impact of Mφs on the improvement in the induction of hypertrophy in EHT system. The results of the AE experiments in the CMs + Mφs EHTs can be found in the supplementary data (Supplementary Figure 1, Supplementary Figure 2, Supplementary Figure 3). Given that the Mφs have been shown to interact with different cell types other than CMs, all five hiPSC-derivatives were combined in order to generate multi-cell-type EHTs and evaluate a combined effect of multiple cardiac non-CM populations of the hypertrophy establishment in the EHT model.

6.5 Multi-cell-type EHTs

6.5.1 Characterization of multi-cell-type EHTs cultured with VEGF only

In this part of the project, five distinct hiPSC-derivatives were cast together into multi-cell-type EHTs and compared to the CM-only tissues. The total cell number in the multi-cell-type tissues was set to 1 million (0.6 million CMs, 0.2 million ECs, 0.1 million Mφs, 0.05 million CFs and 0.05 million SMCs), whereas the CM-only EHT contained 0.6 million CMs. No modifications of the cell culture conditions were performed, i.e., EHTs were cultured in standard EHT medium supplemented with 30 ng/mL VEGF and 0.2 mM tranexamic acid.

6.5.1.1 Remodeling and functional analysis

The analysis of EHT morphological features revealed increased remodeling of the multi-cell-type EHTs, indicated by 30% smaller diameter on the 1st day after casting compared to CM-only EHTs. This difference became more prominent after 6 days of culture when the difference in width between the groups increased to 58%. An extensive thinning of the multi-cell-type tissues was observed throughout the first 7 days after casting, whereas the CM-only EHTs remodeled continuously over time of culture (Figure 34).

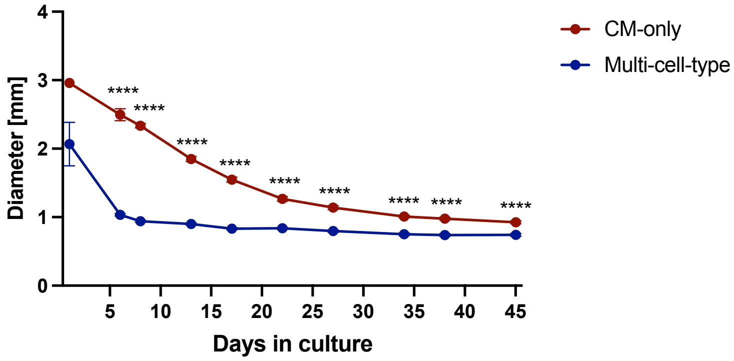

Figure 34 Remodeling analysis of the EHTs. The diameter of multi-cell-type and CM-only EHTs was measured throughout 45 days of culture with the Fiji software for image analysis. Data are presented as mean ± SEM; n = 28 – 31 EHTs/group. Statistical analysis: Repeated measures ANOVA with Bonferroni's post-hoc test for multiple comparisons; ****$p \leq 0.0001$.

On the functional level, multi-cell-type EHTs displayed higher contractile forces in the first 3 weeks of culture compared to CM-only tissues. Nevertheless, in the later period of culture, this difference diminished and the forces generated by CM-only tissues were equivalent to the multi-cell-type counterparts (Figure 35A). The analysis of further parameters on day 24 of culture showed significantly higher beating frequencies of multi-cell-type EHTs compared to CM-only EHTs. Moreover, the implementation of non-CMs into the tissues slightly prolonged the relaxation time of the EHTs, but had no effect on the contraction time (Figure 35B).

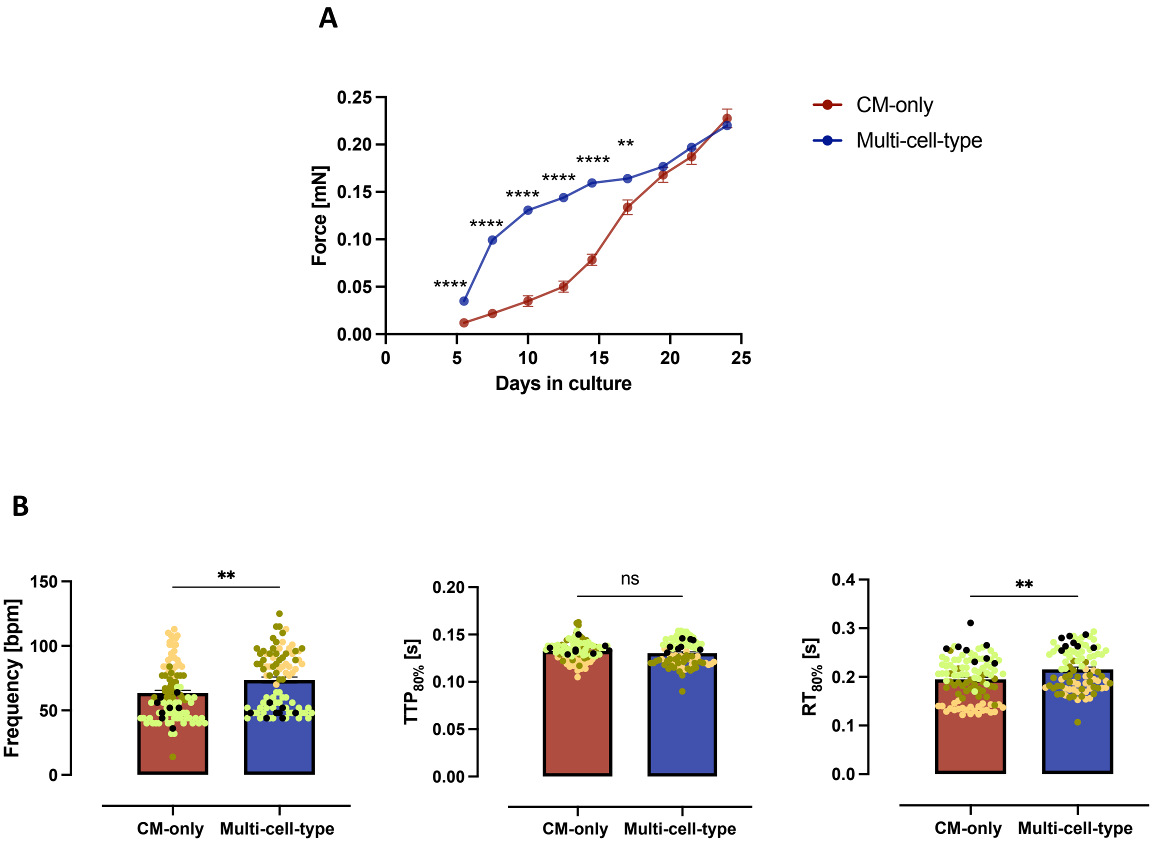

Figure 35 Functional analysis of the multi-cell-type EHTs. **(A)** Force development of the EHTs over the course of culture. **(B)** Evaluation of further contractile parameters: frequency (left), contraction time (middle), relaxation time (right) on the 24th day of culture. Data are presented as mean ± SEM; n = 91 – 102 EHTs/group from 4 independent batches. Data points belonging to the same batch are displayed in matching color. Statistical analysis: (A) Repeated measures ANOVA with Bonferroni's post-hoc test for multiple comparisons, (B) Mann-Whitney test; ns $p \geq 0.05$, $^{**}p \leq 0.01$, $^{****}p \leq 0.0001$.

6.5.1.2 Transcriptomic analysis

The implementation of non-CMs into the EHT system had a clear effect on the functional performance of the tissues. To further investigate the impact of non-CMs on the EHTs, the multi-cell-type and CM-only tissues were compared on the transcriptome level by performing directional mRNA sequencing. The principal component analysis (PCA) revealed high degree of transcriptomic differences between the multi-cell-type and CM-only tissues as presented on the PCA plot (PC1: 72.38%). Moreover, the CM-only tissues were found to group more closely together compared to the multi-cell-type tissues, which exhibited a higher variance across the PC2 (Figure 36A). The higher numbers of normalized counts recorded for different cell-type-related markers indicated the presence of non-CMs in the multi-cell-type tissues corroborating the large difference between the groups displayed in PC1 (Figure 36B-F). Further analysis of differentially expressed genes (DEGs) was performed with the R package DESeq2. The genes with absolute $\log_2$foldchange ($\log_2$FC) > 0.5 and an adjusted p-value <0.05 were identified as significant and relevant for the next steps in the analyses. As a result of the previous filtering process, 1083 genes were found to be upregulated and 128 genes were downregulated in the multi-cell-type tissues compared to CM-only EHTs (Figure 36G). Among the upregulated genes, macrophage-related genes were the most prominent, such as *CD68*, *HLA-DRA*, *SIGLEC1*. This observation was confirmed by the results of gene ontology analysis identifying the enrichment of biological processes related to macrophage activation, phagocytosis or inflammatory response. Additionally, an enrichment of extracellular structure organization and extracellular matrix organization was identified, indicating fibroblast activity in the multi-cell-type tissues (Figure 36H).

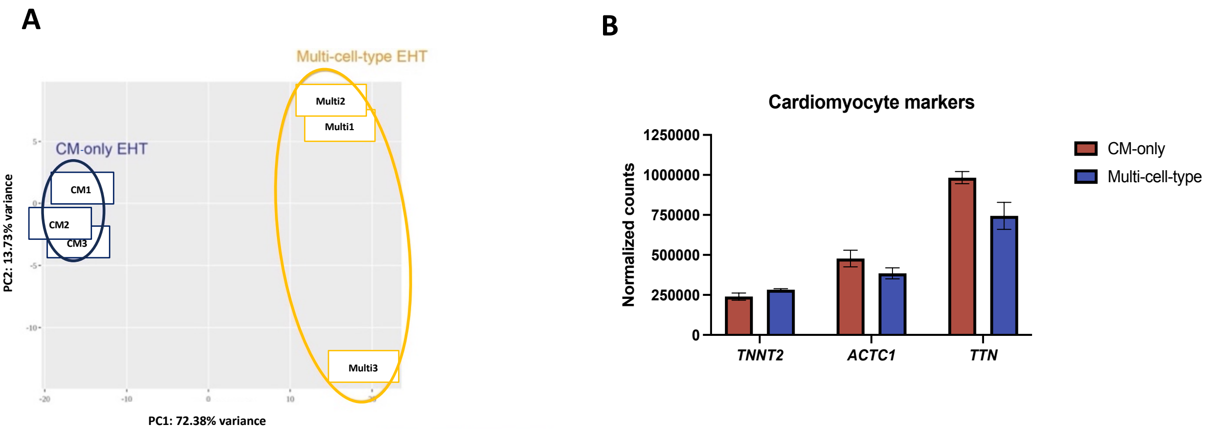

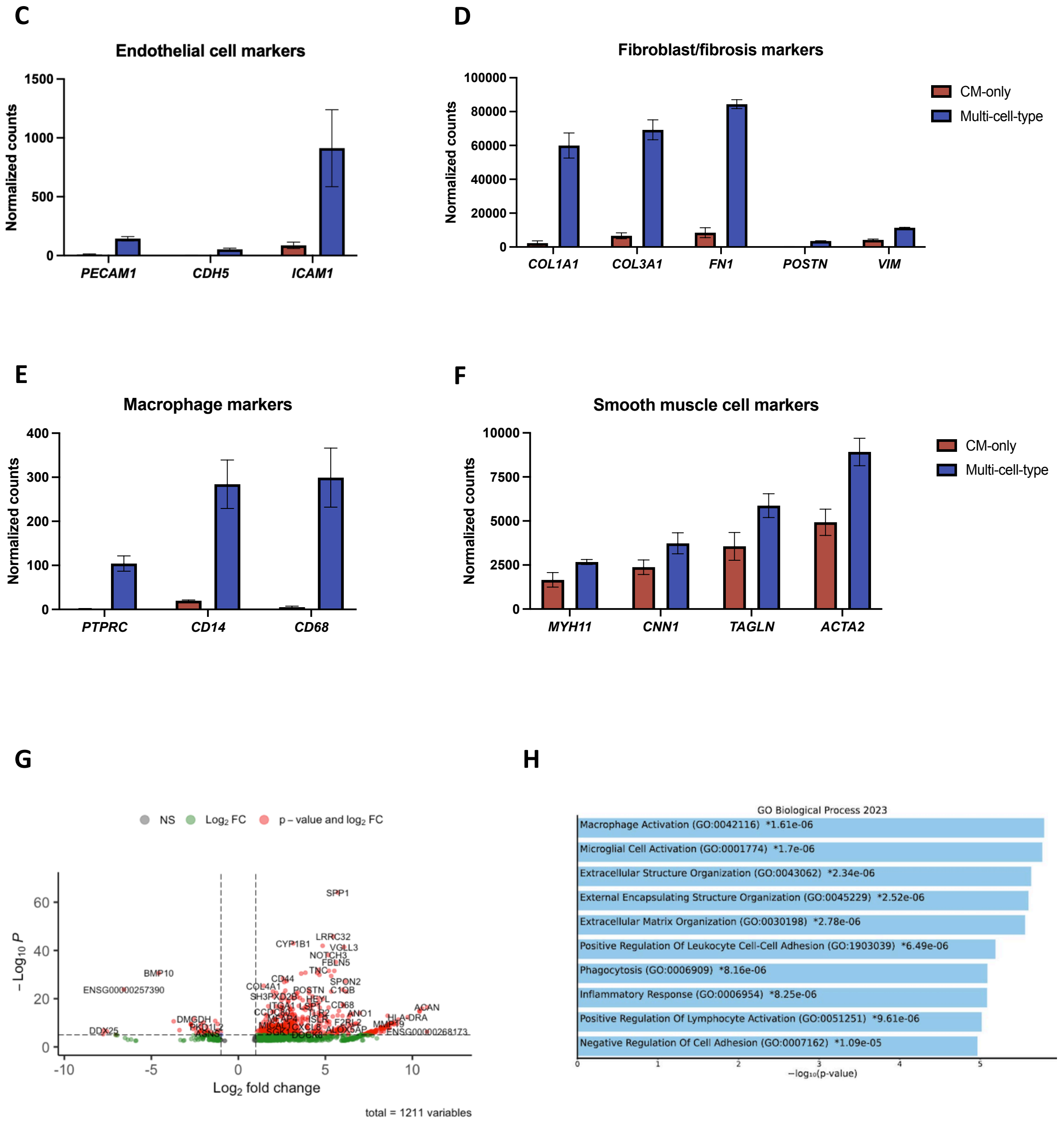

Figure 36 Transcriptomic analysis of multi-cell-type and CM-only EHTs. **(A)** PCA plot presenting large transcriptomic differences between multi-cell-type and CM-only EHTs as well as clustering of same group samples. **(B-F)** Comparison of multi-cell-type and CM-only EHTs in expression of cell-type-related markers based on the normalized count numbers. Data are presented as mean ± SEM; n = 3 EHTs/group. **(G)** Volcano plot demonstrating distribution of differentially expressed genes (absolute $\log_2$FC > 0.5 and adjusted p-value < 0.05) identified by comparison of multi-cell-type and CM-only EHTs. **(H)** Gene ontology analysis of significantly upregulated genes – biological processes.

6.5.1.3 Transmission electron microscopy

In the subsequent part of the project, TEM was employed in order to further characterize the tissues on the structural level. For this analysis, 3-week-old EHTs were harvested and incubated in a solution containing 30 mM BDM to inhibit tissue contractions and accomplish sarcomere relaxation. The suppression of spontaneous beating occurred instantly after placing the EHTs in BDM solution. Subsequently, tissues were transferred into a fixation solution (4% PFA + 1% GA) and stored until further processing as described in section 5.9.5. The staining with methylene blue revealed a more compact structure of the multi-cell-type EHTs and a better incorporation of the cells in the matrix (Supplementary Figure 5). The CMs in the multi-cell-type EHTs appeared to be more viable and displayed a higher maturation state (dense sarcomere structures, well developed intercalated discs; Figure 37E-H). Z-disks appeared sharper and M-bands were apparent (Figure 37E) that were lacking in CM-only EHTs. Mitochondria were larger and exhibited better organization of cristae (Figure 37H). Furthermore, more instances of cell-to-cell contacts were evident in the multi-cell-type tissues. A number of non-CMs were identified in the multi-cell-type tissues (Figure 37F). However, a precise identification of the cell populations required further staining of cell-type-specific markers. Interestingly, the evaluation of sarcomeres in the tissues revealed greater sarcomere length in the multi-cell-type EHTs compared to the CM-only constructs (CM-only 1.78 μm ± 0.02 μm; multi-cell-type 2.04 μm ± 0.04 μm; Figure 37I). These findings suggest a promotion of CM maturation through co-culture with non-CMs within the EHT format.

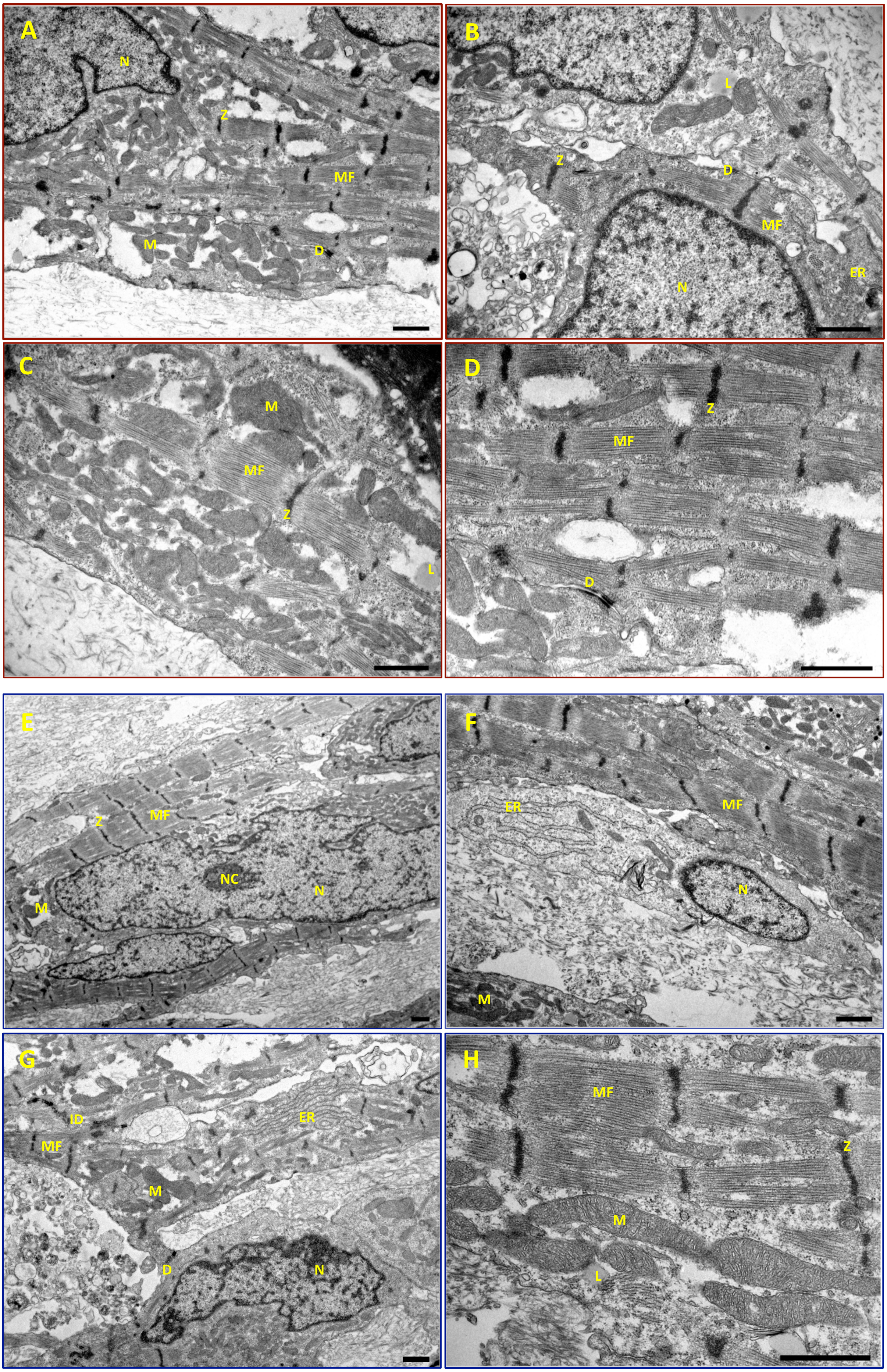
A
N
Z
MF
M
D
B
L
Z
D
MF
ER
N
C
M
MF
Z
L
D
Z
MF
D
E
Z
MF
NC
N
M
F
ER
MF
N
M
G
ID
MF
ER
M
D
N
H
MF
Z
M
L

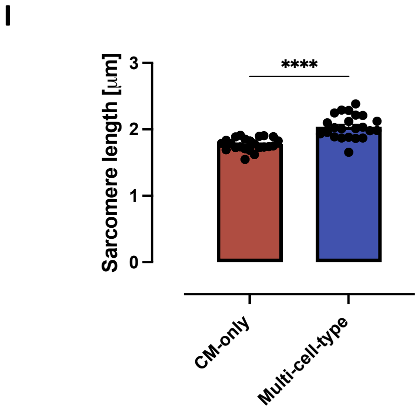

Figure 37 Ultrastructural analysis of CM-only and multi-cell-type EHTs. TEM images of **(A-D)** CM-only EHTs and **(E-H)** multi-cell-type tissues. Image legend: M: mitochondria, MF: myofilaments, Z: z line, D: desmosomes, N: nucleus, NC: nucleolus, ER: endoplasmic reticulum, ID: intercalated disc. Scale bar: 1 µm. **(I)** Comparison of sarcomere length in the CM-only and multi-cell-type EHTs. Data are presented as mean ± SEM; n = 23 sarcomeres/group. Statistical analysis: Welch's t test; ****$p < 0.0001$.

6.5.1.4 Evaluation of EHT cellular composition – MACSima Imaging Cycling Staining

During the casting process of multi-cell-type EHTs, different cell populations were combined, ensuring the maintenance of pre-defined cell proportions, i.e., 60% CMs, 20% ECs, 10% Mφs, 5% SMCs and 5% CFs, whereas the CM-only tissues were generated exclusively from the purified CMs. However, throughout the culture period, a number of factors, including the composition of the base medium, the type of the supplements, the presence of growth factors and the extent of oxygen penetration into the tissue, could potentially influence the behavior and survival of the cells, leading to changes in the abundance of cell populations within the EHTs. To assess the impact of culture on cell composition, multi-cell-type tissues were harvested at designated time points and analyzed for cell survival and population quantification with MACSima^{TM} Imaging Cyclic Staining (MICS) technology. MICS is based on immunofluorescent staining of histological samples performed in automated repetitive cycles. A single cycle of MICS can be divided into three phases:

1) Immunostaining: staining of cell-type characteristic proteins with highly specific antibodies conjugated to fluorochromes exhibiting no or minimal overlap in their fluorescence spectra
2) Image acquisition
3) Signal erasure by photobleaching

The workflow of sample preparation and analysis by MICS is presented in Figure 38.

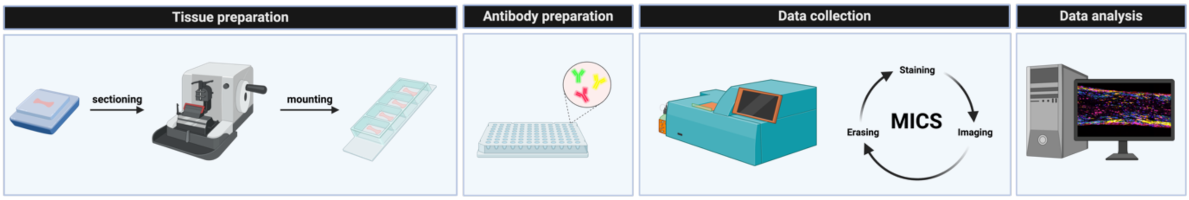

Figure 38 Sequential steps in sample preparation and analysis by MICS. Created with BioRender.com.

Application of the MICS technology allows for analysis of numerous proteins on a single tissue section, additionally providing spatial information. The versatility of this technique promoted an in-depth analysis of cell distribution within EHTs, enabling the precise determination of their cellular composition.

The acquired imaging data was analyzed with MACS iQ View software. Segmentation settings were adjusted to identify nuclei of a size ranging between 20 pixels (px) and 150 px with a high detection sensitivity, whereas the detection of cytoplasmic staining was set in a distance of 15 px from the nuclei. To ensure comparable results, the segmentation settings were consistent between all analyzed samples. The application of these segmentation parameters led to the identification of a 40% decrease in nuclei number between 1-week-old and 3-week-old multi-cell-type EHTs, suggesting decreased cell survival over time of culture (1-week-old: 4293 ± 94 nuclei; 3-week-old: 2585 ± 304 nuclei; Figure 39B).

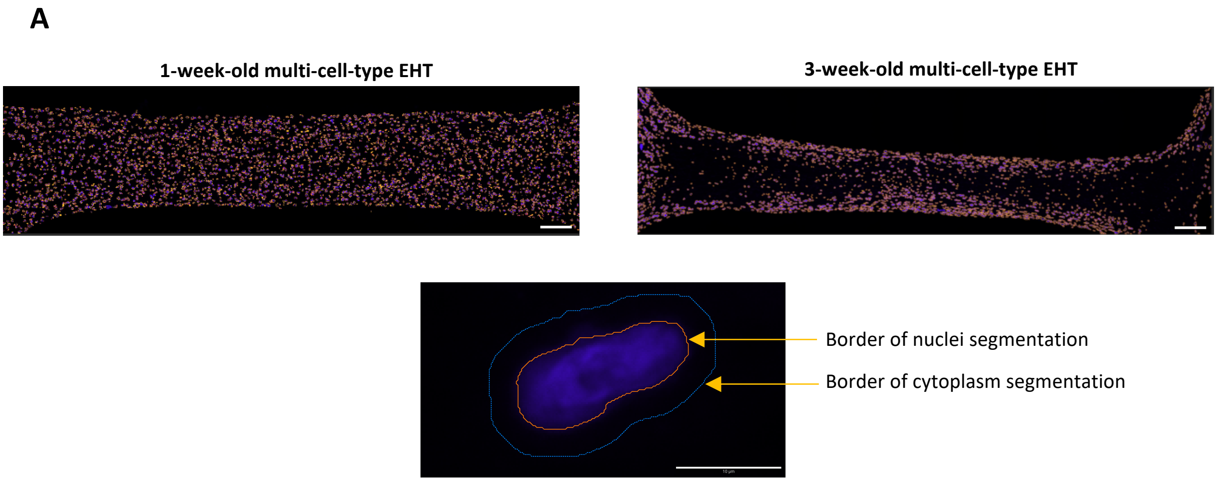

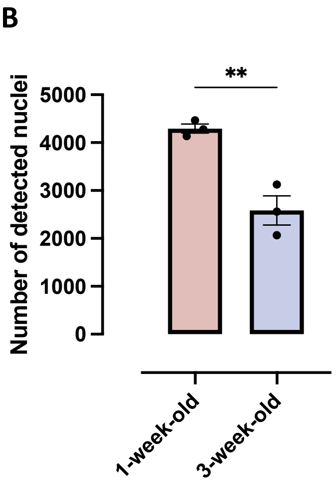

Figure 39 (A) Nuclei and cytoplasmic segmentation of 1-week-old (upper left) and 3-week-old (upper right) multi-cell-type EHTs. Scale bar: 200 μm. Recognized nuclei are encircled in orange and the borders of the cytoplasmic segmentation are displayed in blue (lower panel). Scale bar: 10 μm. **(B)** Quantification of detected nuclei in 1-week-old and 3-week-old multi-cell-type tissues. Data are presented as mean ± SEM; n = 3 EHTs/group. Statistical analysis: Unpaired t test; **p < 0.01.

The determination of different cell populations was based on the detection of cell-type-related protein expression. The list of the markers used for identification of different cell types is displayed in Table 18.

Table 18 List of markers used to determine cell populations in MICS analysis

Cell type	Analyzed marker	Color code
Cardiomyocytes (ventricular phenotype)	MLC2v	🟦
Cardiomyocytes (atrial/immature phenotype)	MLC2a	🟧
Endothelial cells	CD31	🟪
Macrophages	CD14	🟩
Smooth muscle cells	MYH11	🟨
Cardiac fibroblasts	VIM	🟥

The immunofluorescent staining of the above-mentioned proteins confirmed the presence of all five cell types in the multi-cell-type EHTs on both analyzed time points of culture. In 1-week-old tissues, the MLC2v$^+$, MLC2a$^+$, CD31$^+$, MYH11$^+$ and VIM$^+$ cells were uniformly distributed throughout different regions of the EHTs, whereas CD14$^+$ were predominantly localized on the outermost parts of the EHTs (Figure 40A). Interestingly, the spatial distribution of cell population showed a distinct pattern in the tissues cultured for 3 weeks. These EHTs were more compact with the majority of cells aligned along the edges of the constructs (mainly MLC2v$^+$, MLC2a$^+$, MYH11$^+$ and VIM$^+$). The center of the tissues was primarily occupied by CD31$^+$ cells. However, a small proportion of MLC2v$^+$, MLC2a$^+$, CD14$^+$ and VIM$^+$ cells was identified in this region of the tissues as well (Figure 40B).

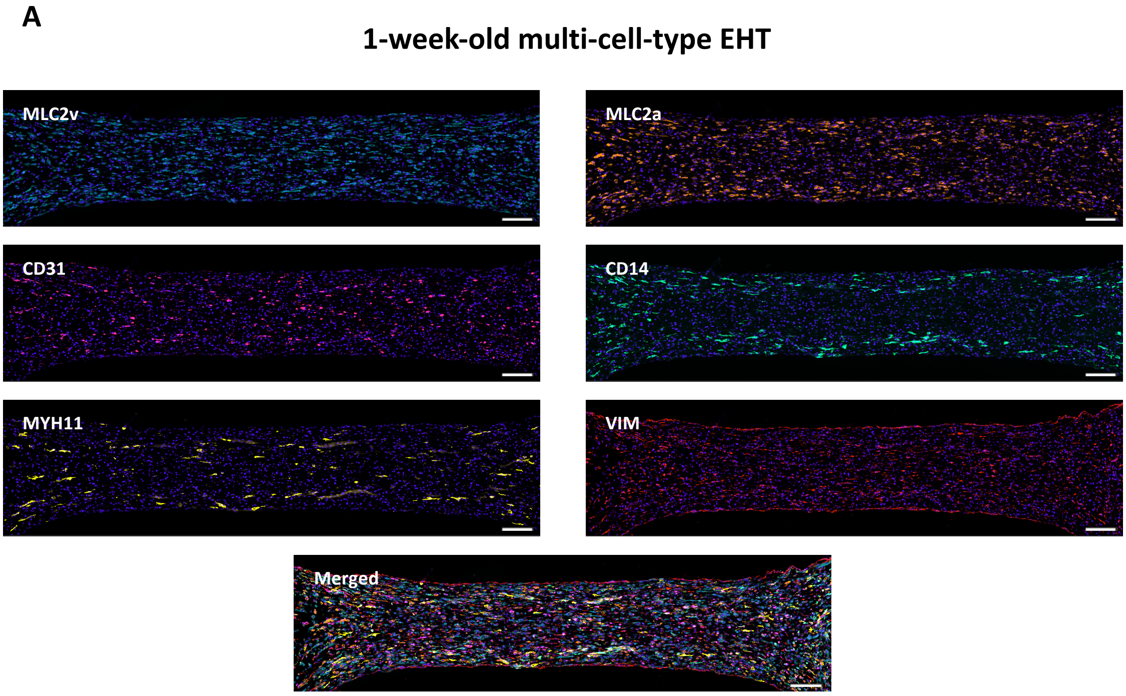

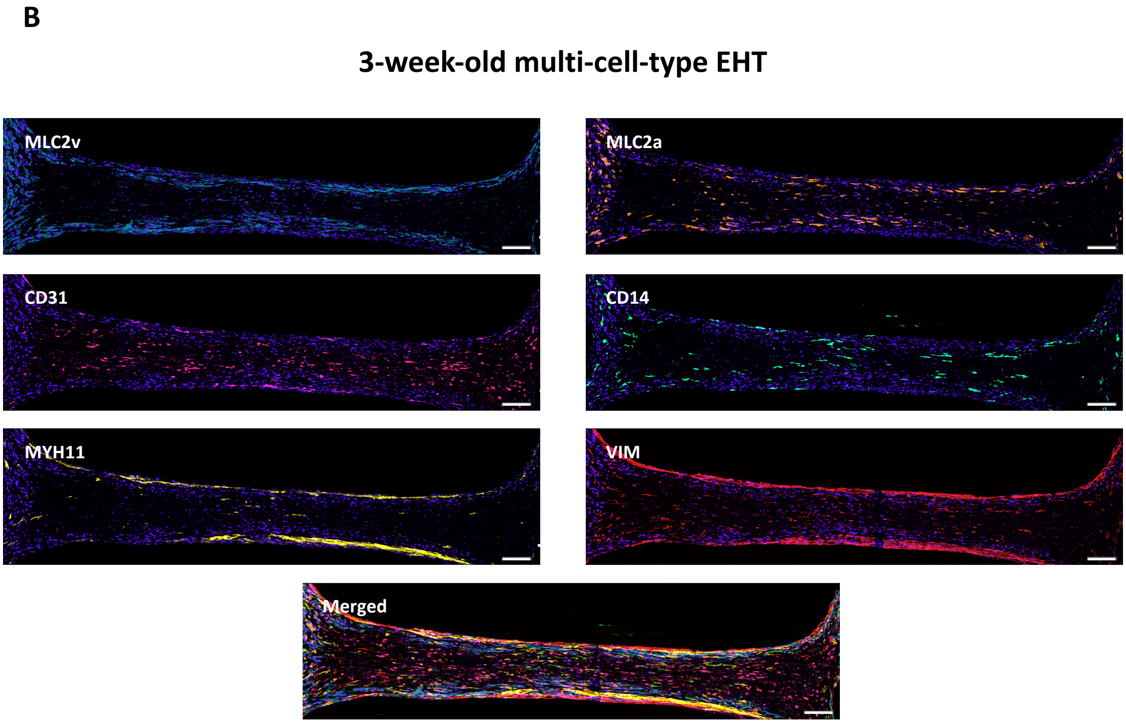

Figure 40 Immunofluorescent staining of **(A)** 1-week-old and **(B)** 3-week-old multi-cell-type EHT. Top left: teal: MLC2v, blue: DAPI; top right: orange: MLC2a, blue: DAPI; middle left: pink: CD31, blue: DAPI; middle right: green: CD14, blue: DAPI; bottom left: yellow: MYH11, blue: DAPI; bottom right: red: vimentin, blue: DAPI. The last picture displays the overlay of all channels together. Scale bar: 200 μm.

As the immunofluorescent staining could only confirm the presence of different cell types in the tissues, the analysis of cellular composition of the EHTs required application of various gating strategies allowing for quantification of the contribution of single cell populations in relation to whole tissue. The assessment of positive and negative cell fractions was performed based on the intensity of biomarker expression within the distance of 15 px (cytoplasmic segmentation) from the recognized nuclei. The MACS iQ View software allows for precise adjustment of the gates by linking every recognized nucleus presented as a single dot on a plot to its position on an image, providing the possibility to manually asses the expression of the marker of interest. An example plot is presented in Figure 41A. The first segmentation strategy applied in order to quantify the ratios of different cell types in the multi-cell-type EHTs was based on the assessment of the expression of cell-type-related proteins in the overall population of recognized nuclei. The analysis of 1-week-old multi-cell-type tissues demonstrated high prevalence of CMs in the EHTs with 25.5% of all the cells being recognized as MLC2v$^+$ cells, 19.0% cells expressing MLC2a and 13.3% co-expressing these two markers. Nearly 6% of all recognized cells showed the expression of CD31, whereas 6.6% were identified as CD14$^+$ cells. Interestingly, only 2.5% of cells expressed MYH11, constituting the smallest cell population detected in 1-week-old multi-cell-type tissues. On a contrary, VIM was found to be the most dominantly expressed protein in the tissues with 27.2% cells exhibiting the expression of this marker (Figure 41B). The analysis of 3-week-old tissues, demonstrated changes in the CM population in the multi-cell-type EHTs. The number of cells expressing MLC2v increased by 6.3 percentage point (pp), whereas the MLC2a$^+$ and MLC2v$^+$MLC2a$^+$ populations decreased by 8.9 pp and 4.8 pp, respectively. The shift in the expression of different isoforms of MLC2 can be associated with the progress in CM maturation within the EHTs. No significant differences in the number of cells expressing CD31 and CD14 were found between the 1-week- and 3-week-old multi-cell-type tissues. On the other hand, an increase of 7.1 pp and 2.1 pp was noted in the populations expressing MYH11 and VIM, respectively (Figure 41C).

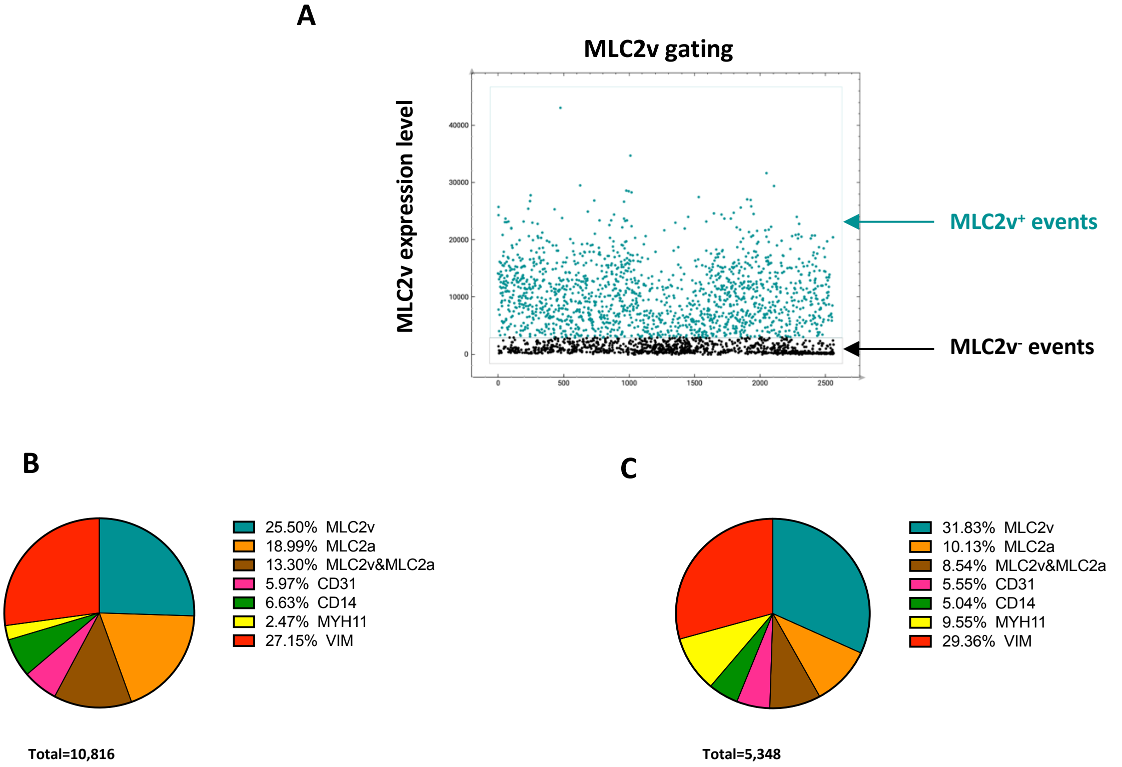

Figure 41 (A) An exemplary plot presenting the gating of MLC2v$^+$ cells in MACS iQ View software. **(B)** Cellular composition of 1-week-old multi-cell-type EHTs. **(C)** Cellular composition of 3-week-old multi-cell-type EHTs. The percentages of different cell populations in the tissues were calculated in relation to the overall sum of all cells identified with the segmentation strategy. Data are presented as mean of 3 EHTs/time-point.

Application of this segmentation strategy allowed for the determination of different cell populations within the EHTs. However, as each gate was established on the same population of cells, a high percentage of nuclei was assigned to more than one cell population due to close proximity of different cytoplasmic markers to one nucleus. An exemplary situation is presented in Figure 42A. The Mφ marker CD14 (green) overlaps with CM marker MLC2a (orange), resulting in two distinct cytoplasmic signals being associated with a single nucleus. By utilizing the above-described segmentation strategy these unambiguous events could not be distinguished. Therefore, another gating strategy, allowing for identification of cells expressing exclusively one of the analyzed markers was introduced. Notably, VIM is known to be expressed by various mesenchymal cells with no restriction to CFs. Therefore, in this analysis CFs were identified as only those vimentin positive cells that were previously not assigned to SMC, EC, CM or Mφ populations.

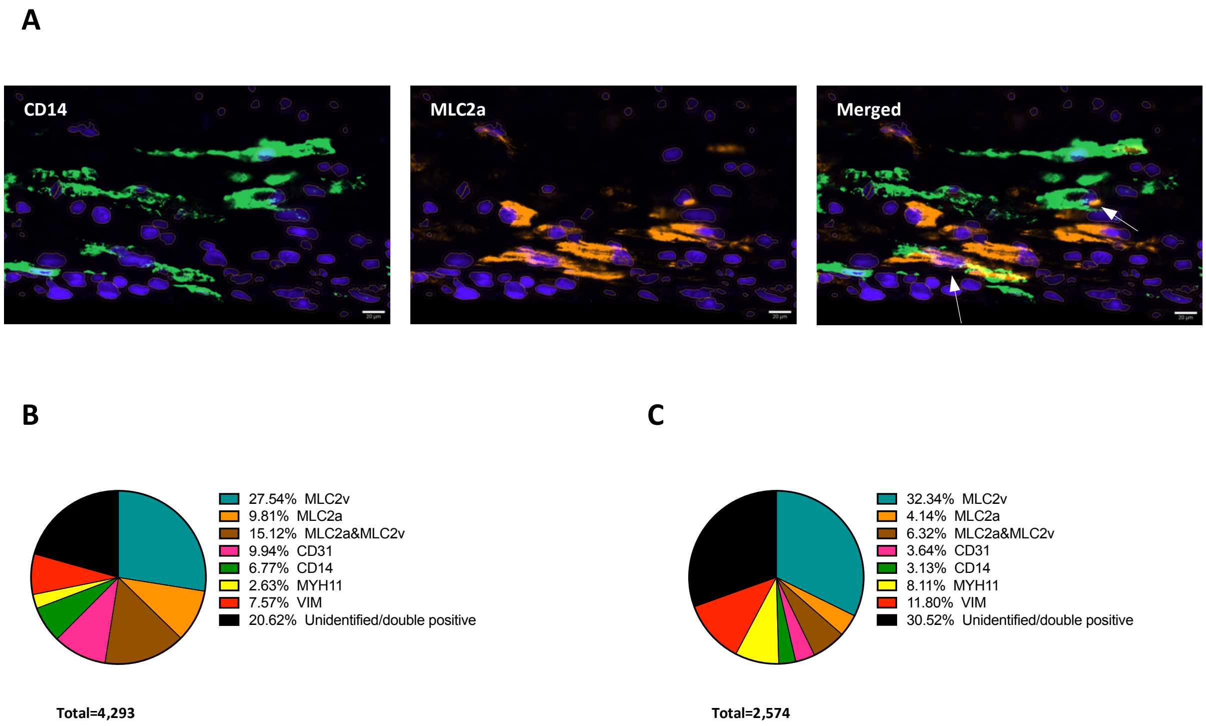

Figure 42 (A) Image illustrating overlapping staining of CD14 (green) and MLC2a (orange). The left image demonstrates CD14, DAPI (blue); middle: MLC2a, DAPI (blue); right: merged. The coinciding staining is indicated by the white arrows. Scale bar: 20 µm. **(B)** Cellular composition of 1-week-old multi-cell-type EHTs. **(C)** Cellular composition of 3-week-old multi-cell-type EHTs. Data are presented as mean of 3 EHTs/time-point.

Similar to the results obtained with the less stringent segmentation strategy, the predominant form of MLC2 identified in the multi-cell-type EHTs was MLC2v (27.5% in 1-week-old EHTs, 32.3% in 3-week-old EHTs). The percentage of MLC2a$^+$ and MLC2v$^+$MLC2a$^+$ was decreasing with culture time indicating the enhanced maturation of CMs in the tissues (MLC2a$^+$: 9.8% in 1-week-old EHTs vs. 4.1% in 3-week-old EHTs, MLC2v$^+$MLC2a$^+$: 15.1% in 1-week-old EHTs vs. 6.3% in 3-week-old EHTs). The implementation of additional gating steps and removal of double positive cells allowed to identify a reduction of CD31 and CD14 positive cells throughout the culture period (CD31: -6.4 pp, CD14: -3.6 pp), suggesting decreased survival of ECs and Mφs in the EHTs. In contrast, the numbers of MYH11$^+$ and VIM$^+$ cells increased with prolonged culture time displaying 5.5 pp elevation in MYH11$^+$ population and 4.2 pp in VIM$^+$ population, indicating the proliferation of CFs and SMCs in the tissues (Figure 42B-C).

A remarkable example of proliferative activity of the cells in the EHTs was observed in one of the analyzed 3-week-old multi-cell-type EHTs. The VIM$^+$ cells formed protrusions in the tissues with high expression of the proliferation marker Ki67 (Figure 43A-B). The highly proliferative cells were identified as CFs due to lack of overlapping staining with MYH11 or MLC2v in the Ki67$^+$ regions of the tissue (Figure 43C-D).

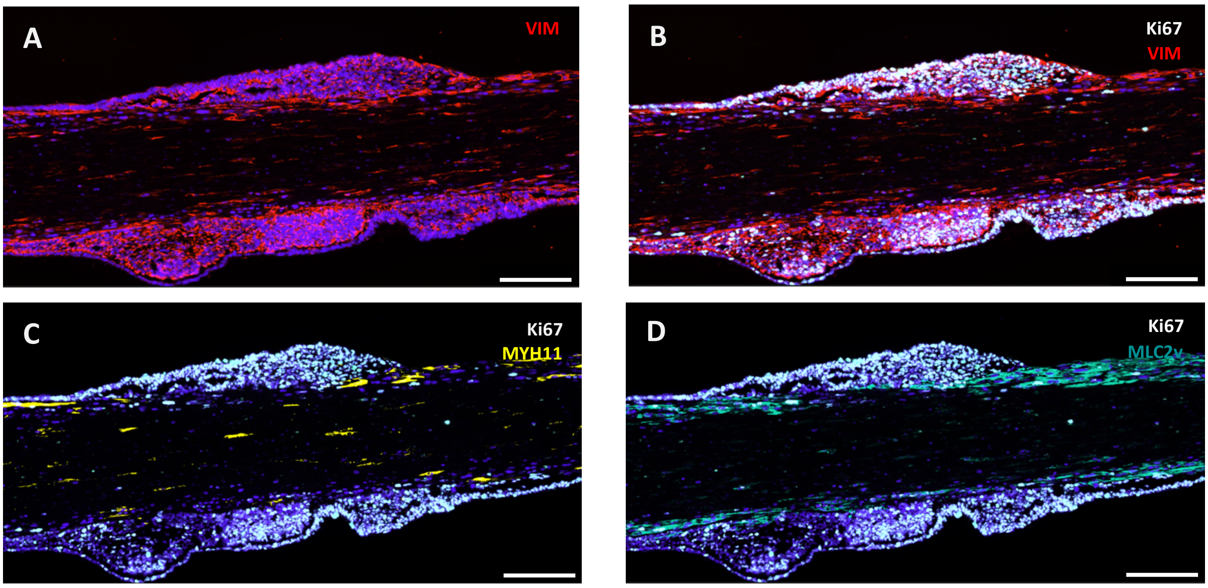

Figure 43 Immunofluorescent staining of 3-week-old multi-cell-type EHT demonstrating a population of proliferative CFs. **(A)** Red: vimentin, blue: DAPI. **(B)** Red: vimentin, white: Ki67, blue: DAPI. **(C)** Yellow: MYH11, white: Ki67, blue: DAPI. **(D)** Teal: MLC2v, white: Ki67, blue: DAPI. Scale bar: 200 μm.

In both cases, CMs were the major cell population identified in the tissues with the dominant form of MLC2v, most pronounced in 3-week-old tissues. The reduction in MLC2a$^+$ and MLC2v$^+$MLC2a$^+$ was observed in datasets obtained with different segmentation approaches. Similarly, the increase of cells expressing MYH11 and VIM was detected with both methods. The major difference was found in the determination of CD14$^+$ and CD31$^+$ cells. The segmentation strategy based on the assignment of one nucleus to a single population with the exclusion of double positive cells resulted in identifying a reduction of Mφ and EC populations between 1-week-old and 3-week-old multi-cell-type EHTs, whereas this difference was not recognized with the less stringent segmentation strategy. Figure 44 demonstrates the graphical representation of the location of the identified cell populations by both segmentation approaches.

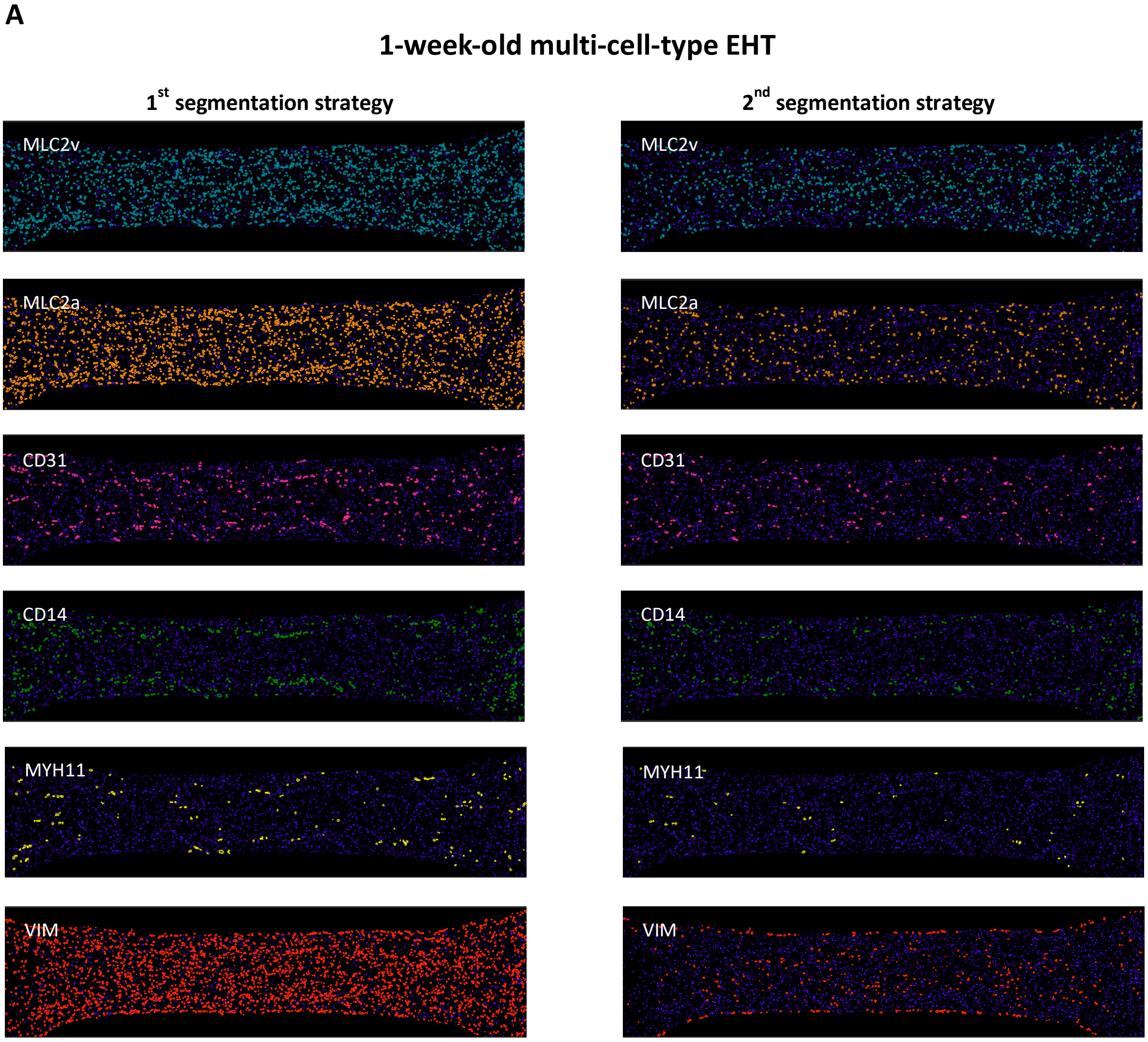

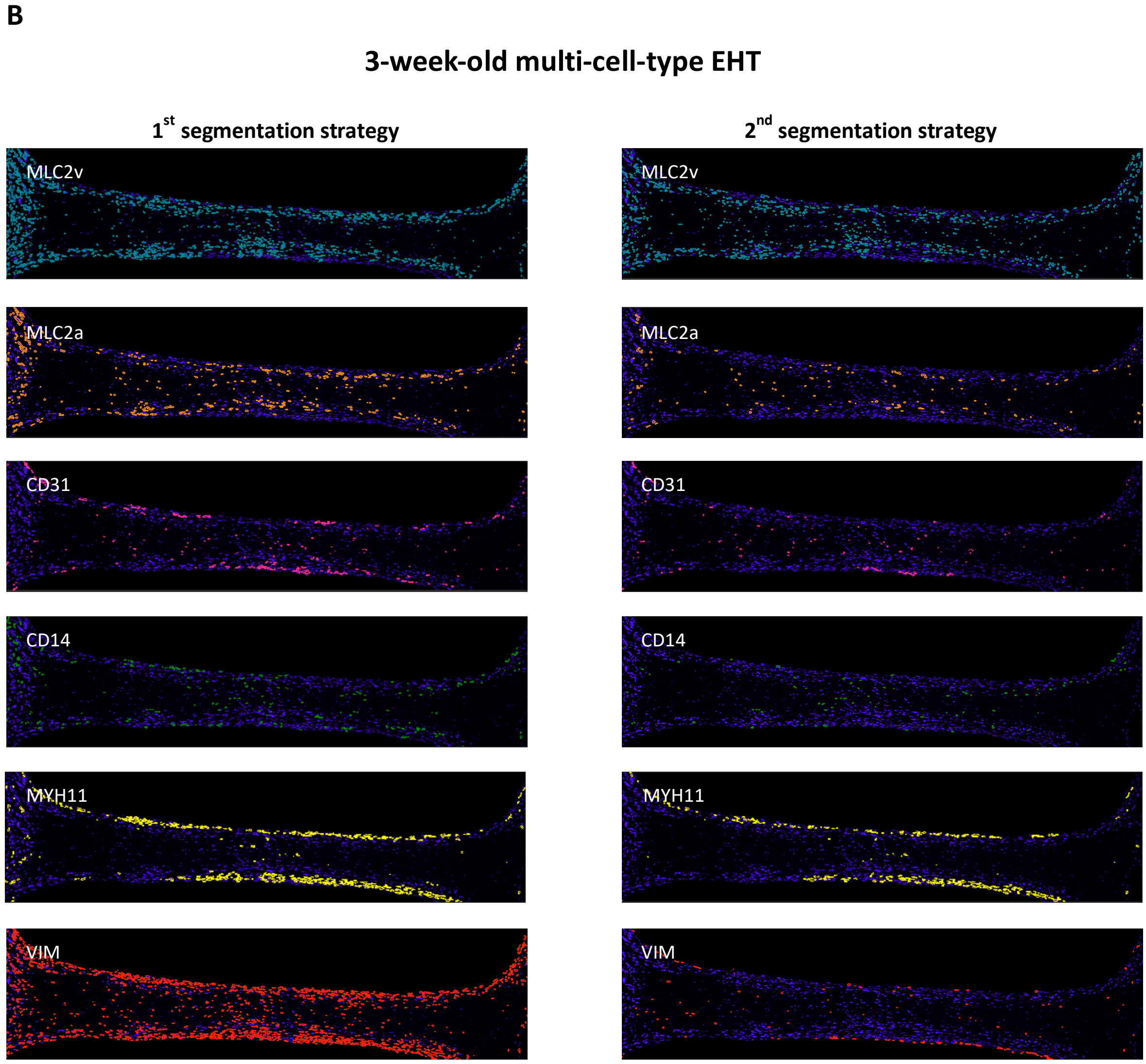

Figure 44 Localization of different cell populations based on the results from both segmentation strategies. **(A)** 1-week-old multi-cell-type EHT. **(B)** 3-week-old multi-cell-type EHT. Left panels represent data obtained by with the 1st segmentation strategy, whereas right panels are generated by 2nd segmentation approach.

The application of MICS technology and analysis of cell-type specific markers allowed for confirmation of non-CM presence in the multi-cell-type tissues at different time points of culture. Moreover, as presented in Figure 43, CFs were found to be biologically active in the EHTs and demonstrate proliferative activity. This corroborated the results of gene ontology analysis depicted in Figure 36. Aside increased proliferation, activated CFs are expected to produce collagen, which could impact the mechanical properties of the tissues. To examine the collagen deposition in multi-cell-type EHTs, tissues were co-stained with an antibody recognizing collagen I, the most common type of collagen found in cardiac tissues. In both analyzed time points, collagen I was detected in the multi-cell-type tissues, confirming the activated state of CFs (Figure 45A-B). Interestingly, a high content of collagen I could be observed in EHTs cultured for one week (Figure 45A), suggesting activation of CFs at early stages of culture.

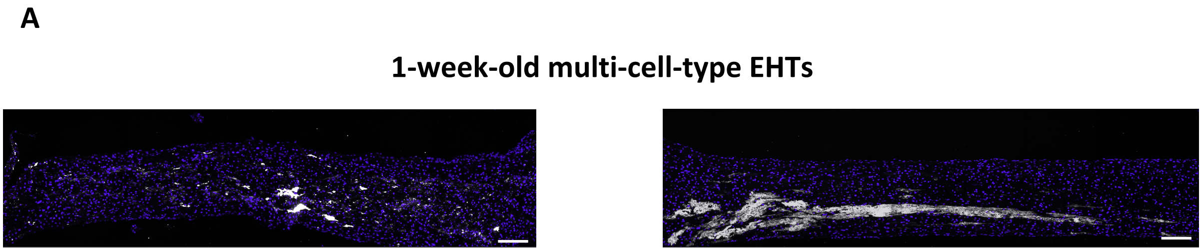

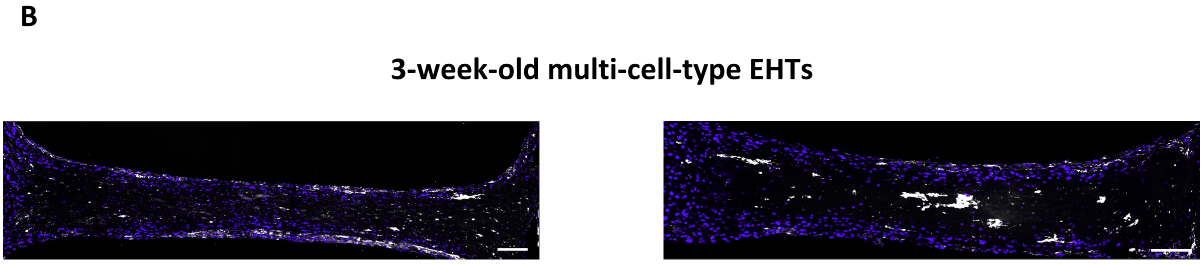

Figure 45 Immunofluorescent staining of collagen I in **(A)** 1-week-old and **(B)** 3-week-old multi-cell-type EHTs. White: collagen I, blue: DAPI. Scale bar: 200 μm.

6.5.1.5 Stiffness measurements

To evaluate whether the deposited collagen affects the mechanical properties of the EHTs, the stiffness of age-matched tissues was examined by nanoindentation. The measurements in living tissues were challenging due to the contractile activity of the EHTs. Thus, for the final measurements, tissues were fixed and embedded in agarose. Different thicknesses of vibratome sections (200, 300 and 400 μm) were tested. The most consistent data with the lowest variability was obtained from the thickest sections. Therefore, all subsequent measurements were conducted on fixed, intact tissues embedded in agarose, with only the upper layer removed to ensure sufficient tissue material for the measurement with the nanoindentation instrument (Figure 46A). As a control for the analysis, a cell-free EHT was used. The application of this method showed a 3-fold higher stiffness of tissues containing CMs in comparison to the cell-free fibrin matrix. Moreover, the multi-cell-type EHTs were found to exhibit the highest stiffness with 10.3-fold greater values than cell-free samples and 3.4-fold higher stiffness than the CM-only EHTs (Figure 46B).

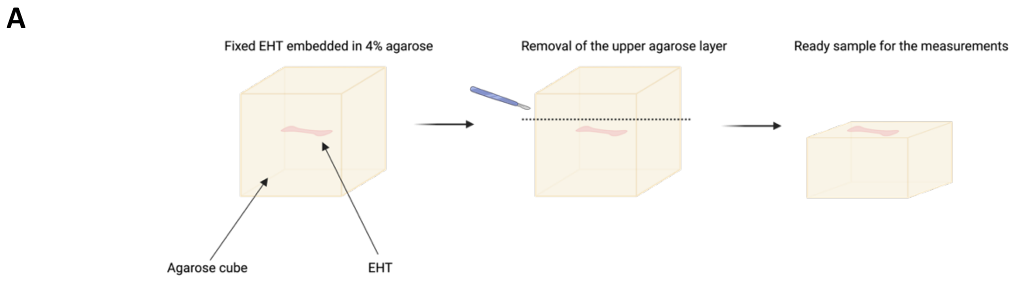

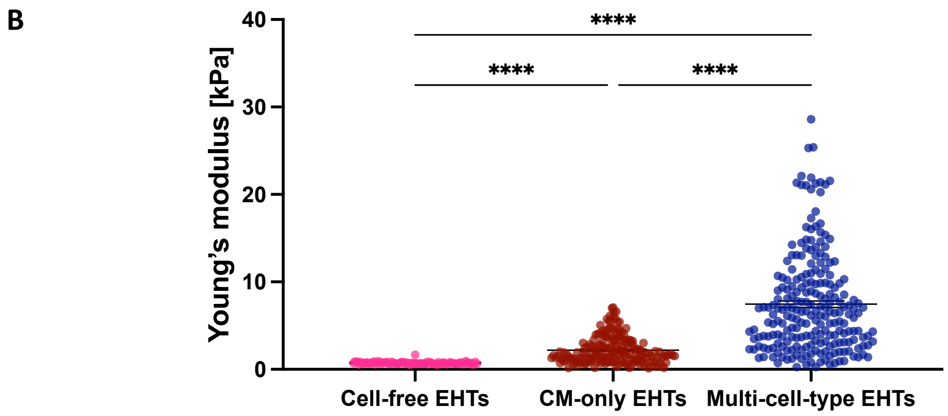

Figure 46 Stiffness measurements of 2 – 3-week-old CM-only and multi-cell-type EHTs. **(A)** A pictogram depicting the sample preparation process. **(B)** The stiffness of the tissues was evaluated by nanoindentation. Each data point represents a value of a single measurement area. Data are presented as mean ± SEM; n = 3 – 4 EHTs/group. Statistical analysis: Kruskall-Wallis test with Dunn's post-hoc test for multiple comparisons; ***p ≤ 0.001.

6.5.2 Culture medium composition

The MICS analysis revealed a decrease in the numbers of viable Mφs and ECs in the multi-cell-type tissues over time of culture. In order to improve the survival of these two cell populations, EHT medium containing 10% horse serum was supplemented with growth factors/cytokines identified as the most essential for Mφ and EC viability.

6.5.2.1 Macrophage survival

The macrophage colony stimulating factor (M-CSF) is described as a primary cytokine improving the survival, viability and proliferation of Mφs. Thus, preliminary experiments were performed in 2D format, where Mφs were cultured in EHT medium with or without supplementation of 50 ng/mL M-CSF. The viability of the cells under different culture conditions was evaluated with the CellTiter® Blue Cell Viability Assay (section 5.5.6). The cell survival was examined after 2, 4 – 5 and 7 days of culture. The measurements performed at different time points of culture demonstrated increased metabolic activity and indicated better survival of Mφs when cultured with the supplementation of M-CSF (day 2: +297%; day 4 – 5: +470%; day 7: +1,285.8%; Figure 47).

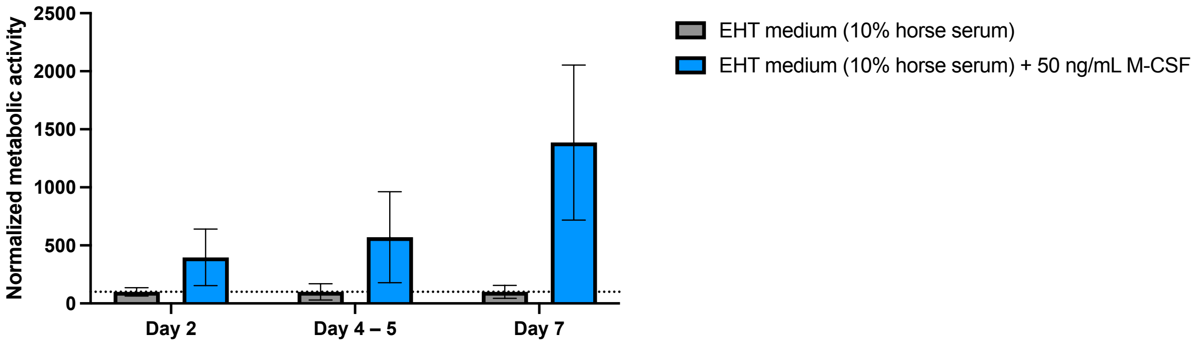

Figure 47 The viability assay was conducted on hiPSC-Mφs. Cells were cultured for 7 days in EHT medium with or without the supplementation of 50 ng/mL M-CSF. The data was collected on days 2, 4 – 5 and 7 by measurement of fluorescent signal emitted by reduced version of resazurin. Data are presented as mean ± SEM, n = 2 biological replicates with 3 technical replicates each.

Taking the results from the 2D experiments into account, two-cell-type EHTs containing 10% Mφs and 90% CMs were generated and cultured in EHT medium without or with 50 ng/mL M-CSF to evaluate the survival of Mφs in the adjusted culture conditions in the EHT format. In EHTs cultured without the supplementation of M-CSF, only a moderate number of cells was observed outside of the EHTs (Figure 48B). These cells were attached to the bottom of the wells and were not found in the EHTs containing only CMs (Figure 48A). Surprisingly, the addition of M-CSF into the culture medium markedly increased the number of cells found attached to the bottom of the wells (Figure 48D), indicating that these mobile cells were Mφs.

These results suggest that the marked loss of Mφs within the EHTs could be related to their motile properties rather than unsuitable survival conditions within the EHTs.

CM-only EHTs (w/o M-CSF) CMs + Mφs (w/o M-CSF)

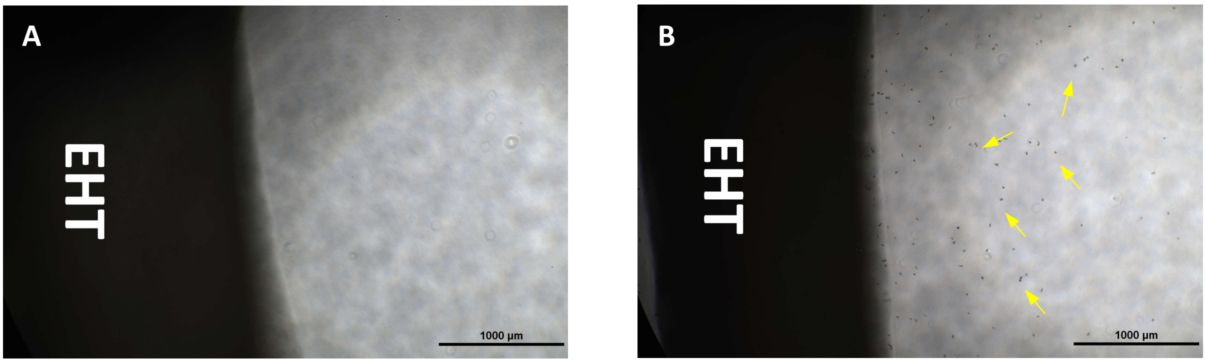

CM-only EHTs (w/ M-CSF) CMs + Mφs (w/ M-CSF)

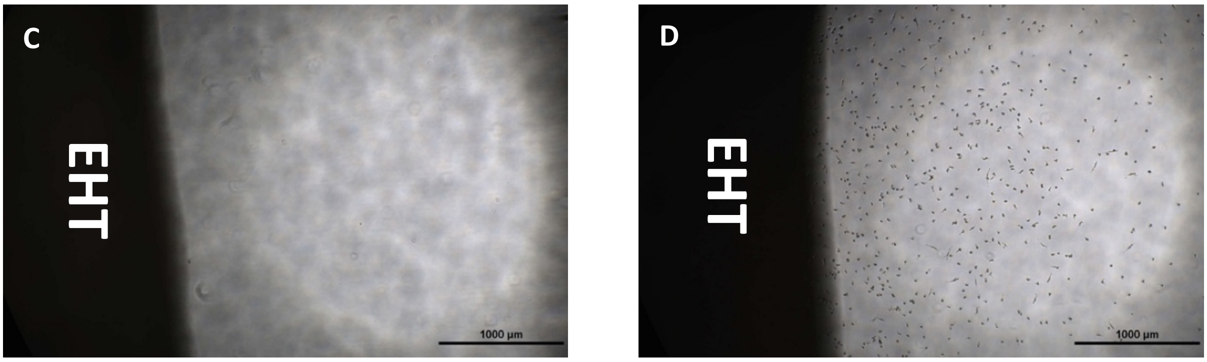

Figure 48 Brightfield images of CM-only and CMs + Mφs EHTs cultured for 4 days **(A-B)** without and **(C-D)** with the supplementation of 50 ng/mL M-CSF. Note that the image was focused on the cell culture bottom. The addition of M-CSF into the culture medium resulted in the presence of considerably higher numbers of cells on the bottom of the cell culture vessel, indicating higher Mφ mobility. Scale bar: 1000 µm.

The increasing loss of Mφs from the EHTs under M-CSF supplementation could be observed throughout the whole duration of culture time. Interestingly, as depicted in Figure 49 withdrawal of the M-CSF from the medium on day 4 of culture did not prevent the further movement of cells towards the medium.

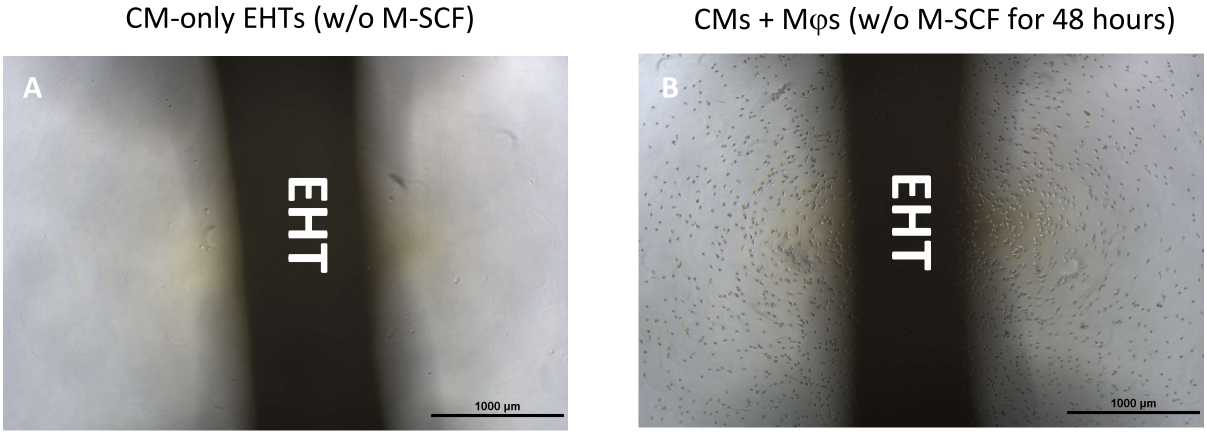

CM-only EHTs (w/o M-SCF)

CMs + Mφs (w/o M-SCF for 48 hours)

Figure 49 Brightfield images of 6-day-old CM-only EHT cultured **(A)** without M-CSF and **(B)** two-cell-type tissue after 48 hours of M-CSF withdrawal. Scale bar: 1000 μm.

In summary, Mφs were observed to move from the tissue towards the medium and exit the tissues in both analyzed conditions. The number of activated cells was significantly higher when EHT medium was supplemented with M-CSF. Considering these observations, M-CSF supplementation of the culture medium was abolished for subsequent experiments. The decrease in Mφ number within the EHTs, as illustrated in Figure 48 and Figure 49, can therefore be attributed, at least in part, to the inherent migratory nature of these cells.

6.5.2.2 Endothelial cell survival

In order to increase the viability of ECs in the multi-cell-type tissues, two strategies have been employed. The first one was based on the increase of VEGF concentration in the EHT medium. The tested concentrations were accordingly: 30 ng/mL, 60 ng/mL and 90 ng/mL. The 30 ng/mL was a concentration initially used in the previously described experiments (section 6.5.1). The second strategy was based on the combination of different VEGF concentrations with FGF-2, another growth factor known to promote EC viability. In order to ensure accurate monitoring of cell survival in the tissues, ECs expressing Venus or GFP were used in the experiments. It was observed that none of the tested concentrations of VEGF supported the survival of the ECs in the tissues. In contrast, the addition of FGF-2 to the medium increased the EC viability and persistence in the EHTs, independent of the VEGF concentration (Figure 50A-F).

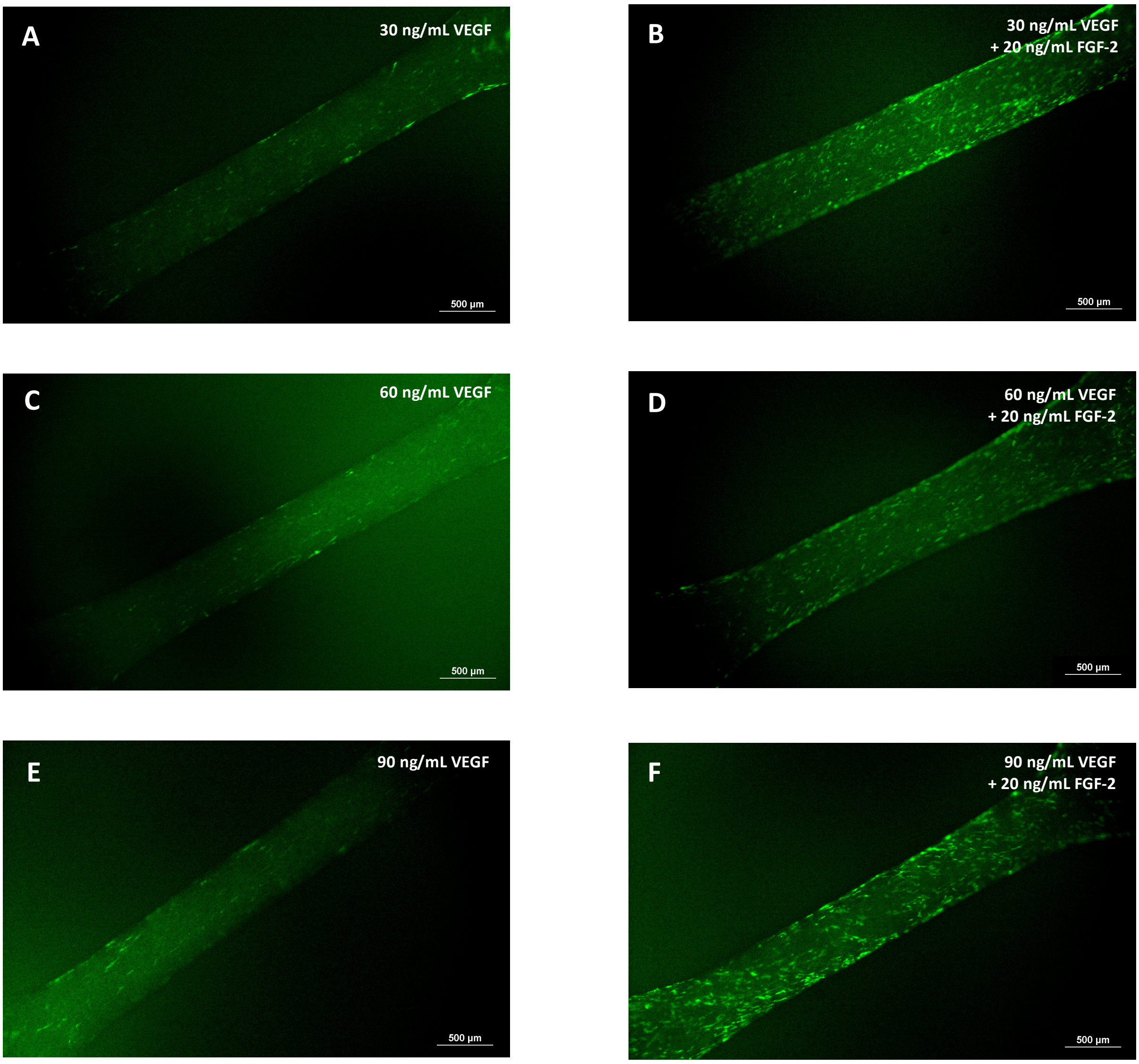

Figure 50 Endothelial cell survival in the multi-cell-type EHTs (3-weeks-old). Tissues containing Venus-ECs (provided by T. Werner) were cast to visualize the ECs within the EHTs. Different concentrations of VEGF alone or in combination with FGF-2 were tested. **(A-B)** Images of the tissues cultured in EHT medium supplemented with (A) 30 ng/mL VEGF and (B) 30 ng/mL VEGF + 20 ng/mL FGF-2. **(C-D)** Images of the EHTs cultured in EHT medium supplemented with (C) 60 ng/mL VEGF and (D) 60 ng/mL VEGF + 20 ng/mL FGF-2. **(E-F)** Images of the tissues cultured in EHT medium supplemented with (E) 90 ng/mL VEGF and (F) 90 ng/mL VEGF + 20 ng/mL FGF-2. Scale bar: 500 µm.

Interestingly, the EC survival in two-cell-type EHTs, i.e., containing CMs and ECs was greater than in multi-cell-type tissues, despite the lack of FGF-2 supplementation. After 3 days of culture in both types of EHTs, ECs were detectable in the post area of the tissues. However, the ECs in two-cell-type EHTs appeared as a more compact cellular network compared to the ECs found in the multi-cell-type EHTs (Figure 51). The discrepancy in ECs survival was enhanced throughout the culture, demonstrating further loss of ECs in multi-cell-type tissues and improved viability in two-cell-type EHTs. These results suggest the presence of possible interactions between ECs and other non-CMs in multi-cell-type tissues, which have a negative impact on EC survival in the tissues. Of note, the total number of cells per tissue differed between two-cell-type EHTs (800,000 total cells = 200,000 ECs, 600,000 CMs) and multi-cell-type tissues (1,000,000 total cells = 200,000 ECs, 600,000 CMs, 100,000 Mφs, 50,000 SMCs, 50,000 CFs). Therefore, the reduced compactness of the tissue could additionally improve the survival of the ECs in the constructs consisting only of two cell types indicated by the more developed EC network as depicted in Figure 51B, D.

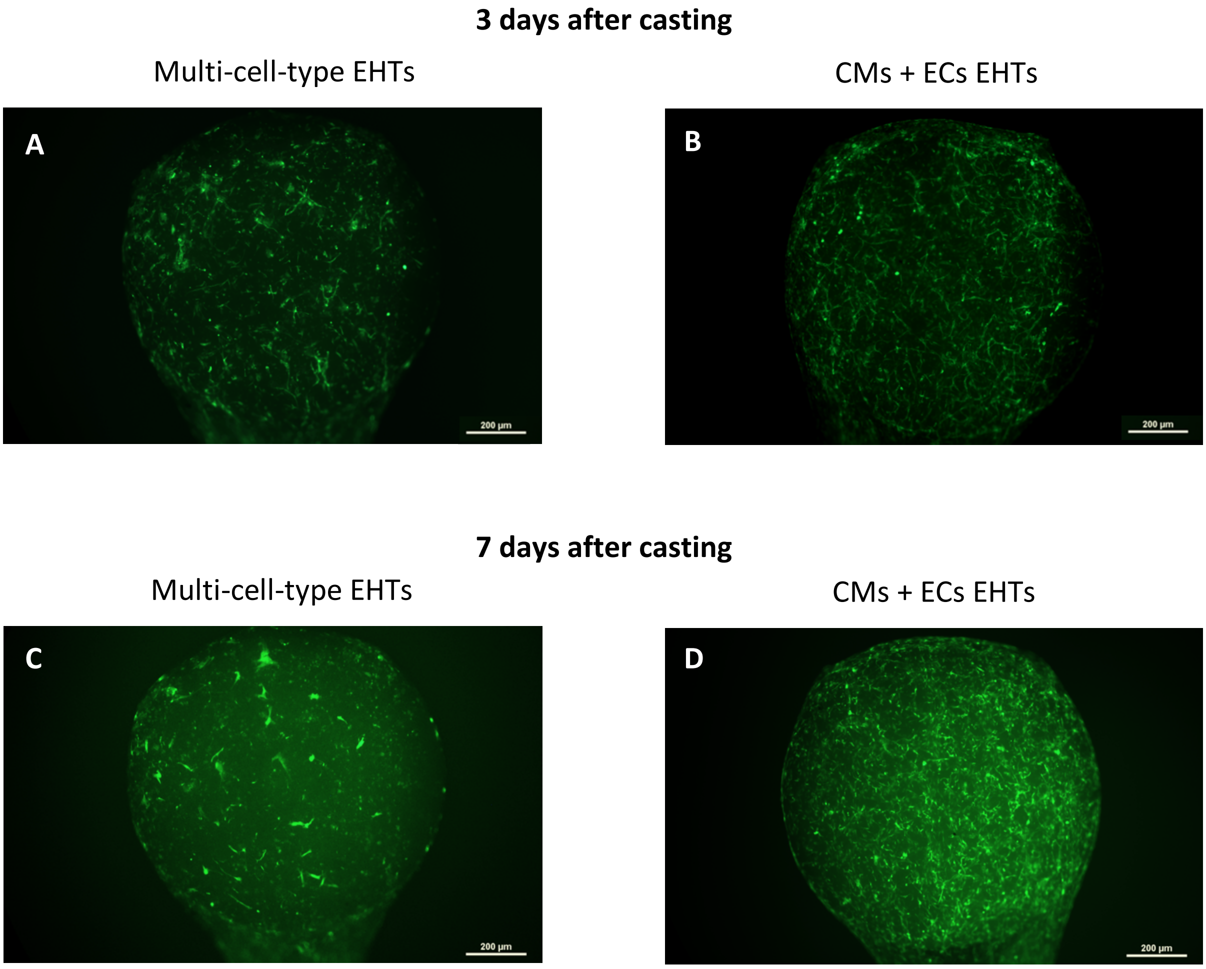

3 days after casting

Multi-cell-type EHTs

CMs + ECs EHTs

7 days after casting

Multi-cell-type EHTs

CMs + ECs EHTs

Figure 51 Comparison of EC survival in two-cell-type and multi-cell-type EHTs cultured in EHT medium supplemented with 30 ng/mL VEGF **(A-B)** for 3 days or **(C-D)** for 7 days. The images were taken of the EHT post area. ECs express GFP for simplified visualization within the tissues. Scale bar: 200 µm.

In conclusion, the ECs demonstrated higher viability in two-cell-type EHTs than in multi-cell-type EHTs. This phenomenon could result from (negative) interactions of ECs and the other non-CM populations in the tissues or lower total number of cells in the construct. Nevertheless, as further experiments were planned to be performed in multi-cell-type EHTs, based on the experiment demonstrated in Figure 50, the EHT culture medium was supplemented with 30 ng/mL VEGF and 20 ng/mL FGF-2.

6.5.3 Characterization of multi-cell-type EHTs cultured with VEGF and FGF-2

Following the discoveries from the EC survival experiments, for the further EHT experiments, medium was supplemented with 30 ng/mL VEGF and 20 ng/mL FGF-2. The addition of FGF-2 improved the survival of the ECs. However, it was also found to have an effect on the contractile performance of the EHTs. In this set-up, the force development of the multi-cell-type EHTs was distorted reaching its plateau already after 12 days after casting with low mean values. In effect, after 2 weeks of culture the CM-only EHTs exhibited higher contractile forces than the multi-cell-type tissues (Figure 52A). In line with the results from the batches cultured without FGF-2, multi-cell-type EHTs exhibited higher beating frequencies compared to CM-only tissues. However, in this set-up, the contraction and relaxation time of the CM-only tissues were significantly longer than their multi-cell-type counterparts (Figure 52B).

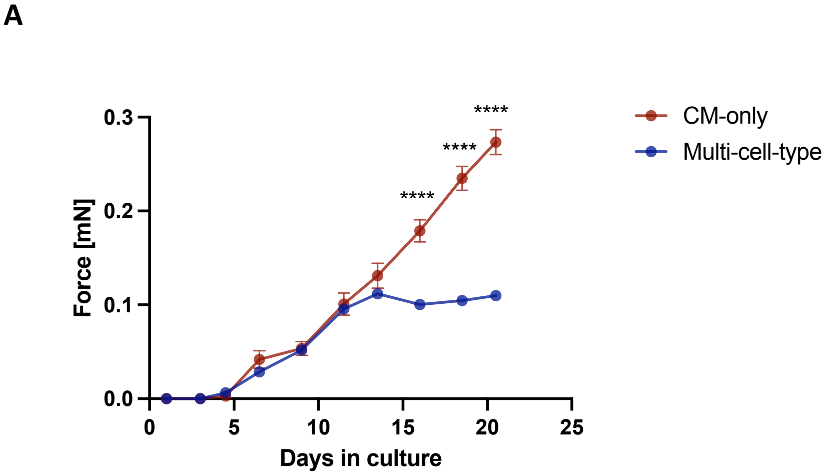

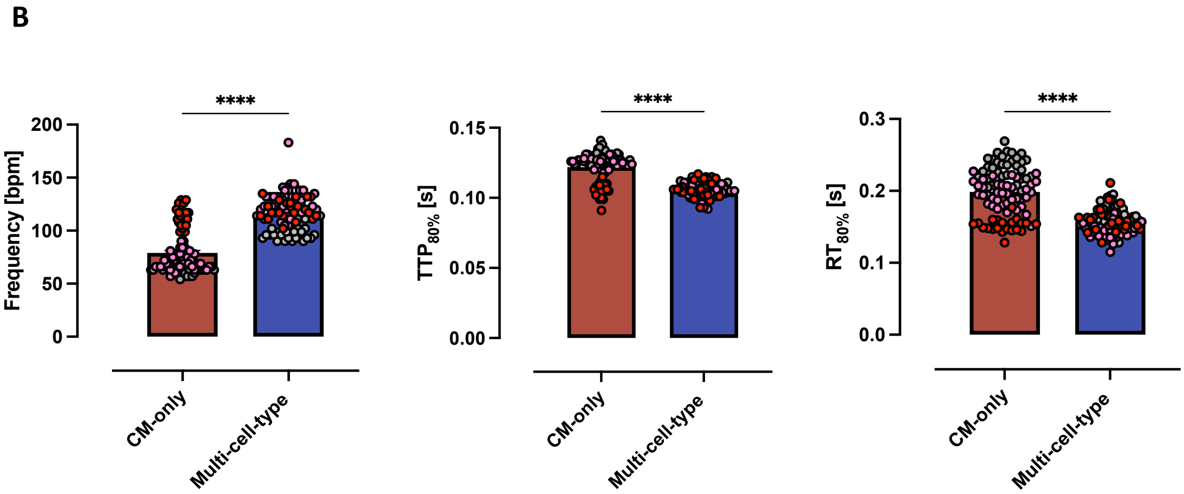

Figure 52 Functional analysis of CM-only and multi-cell-type EHTs cultured with the supplementation of FGF-2. **(A)** Force development throughout 3 weeks of culture. **(B)** Further analysis of functional parameters on day 20 – 21 of culture: frequency (left), contraction time (middle), relaxation time (right). Data are presented as mean ± SEM (in Fig. 52A SEM below display resolution); n = 90 – 92 EHTs/group from 3 independent batches. Data points belonging to the same batch are displayed in matching color. Statistical analysis: (A) Repeated measures ANOVA with Bonferroni's post-hoc test for multiple comparisons, (B) Mann-Whitney test; ****$p \leq 0.0001$.

Analogous to previous experiments, the mechanical properties of the EHTs cultured with FGF-2 were evaluated by nanoindentation. The results of this analysis showed an 11-fold higher stiffness of the tissues containing five cell types compared to the CM-only EHTs (Figure 53). Furthermore, the values recorded for the multi-cell-type tissues cultured with FGF-2 were 2-fold greater than the ones cultured without it (Figure 46, Figure 53). Overall, this result confirmed the observations from the prior experiments, showing a direct effect of non-CMs on the tissues' mechanical attributes. Moreover, culture with FGF-2 demonstrated an impact on the multi-cell-type tissues, increasing their stiffness by the factor of two when compared to tissues cultured without FGF-2. The effect of FGF-2 on CM-only EHTs was further evaluated and is presented in section 6.5.6 of this thesis.

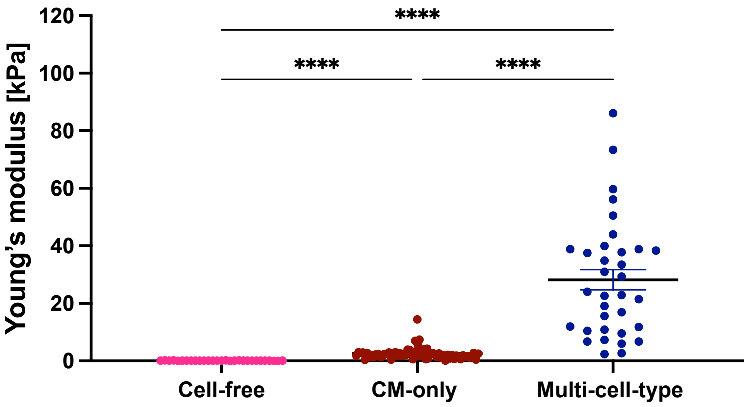

Figure 53 Three-week-old EHTs were fixed and embedded in 4% agarose. The stiffness of the tissues was evaluated by nanoindentation. Each data point represents a value for a single measurement area. Data are presented as mean ± SEM; n = 3 EHTs/group. Statistical analysis: Kruskall-Wallis test with Dunn's post-hoc test for multiple comparisons; ***$p \leq 0.001$.

6.5.3.1 Modifications of the EHT system – increase in cell number and fibrin content

The routinely used EHT generation protocol utilizes a defined seeding density of 1 million CMs per EHT. The above-characterized multi-cell-type EHTs contained 600,000 CMs and 400,000 non-CMs/construct, whereas the CM-only EHTs consisted solely of 600,000 CMs. To examine whether an increase of CMs/tissue to 1 million would improve their contractile performance, "high cell number" EHTs were established. This term refers to multi-cell-type tissues consisting of 1 million CMs and non-CM populations in previously defined proportions. Therefore, the overall cell number/construct in the "high cell number" multi-cell-type EHTs was 1.67 million cells/tissue. On the other hand, the CM-only EHTs consisted of 1 million CMs, following the established EHT generation procedure.

On the functional level, the increase of cell number in the tissues did not lead to improved contractile performance of the EHTs. In this set-up, multi-cell-type EHTs exhibited significantly lower maximal forces compared to CM-only tissues. Moreover, multi-cell-type EHTs did not display a common pattern of force development (i.e., plateau phase being reached after 3 – 4 weeks of culture), indicating a negative effect of high cellular density on the EHT performance (Figure 54).

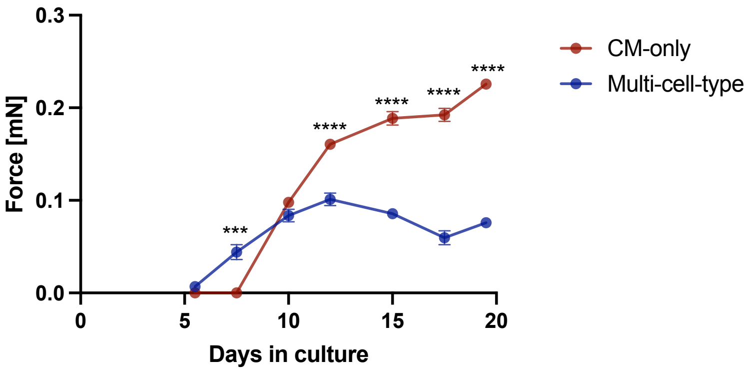

Figure 54 Force development of the EHTs with high cell density. Data are presented as mean ± SEM; n = 12 – 16 EHTs/group from 2 independent EHT batches. Statistical analysis: Repeated measures ANOVA with Bonferroni's post-hoc test for multiple comparisons; ***p ≤ 0.001, ****p ≤ 0.0001.

The increase in cell number per tissue resulted in a more rapid EHT remodeling. This effect was prominent already 1 day after casting where "high cell number" multi-cell-type EHTs exhibited a 42% smaller diameter compared to the multi-cell-type tissues with lower cell density. The effect of increased remodeling in "high cell number" EHTs was also found in the CM-only groups, however the difference was at a level of 10% (Figure 55A). The high degree of remodeling in the multi-cell-type system was often leading to a premature ripping/breaking of the EHTs.

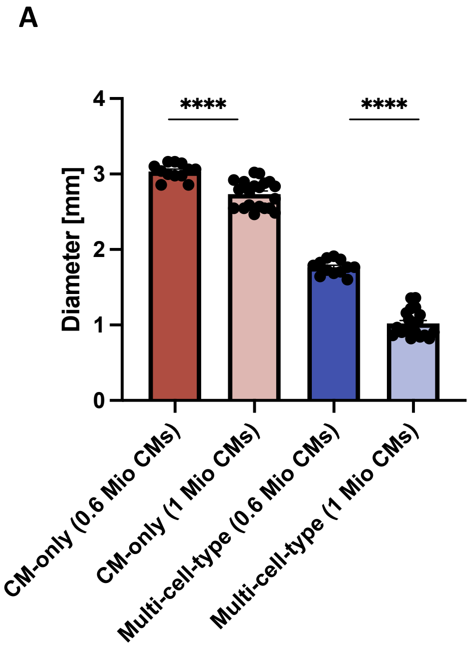

B

“Low cell number” multi-cell-type EHTs

C

“High cell number” multi-cell-type EHTs

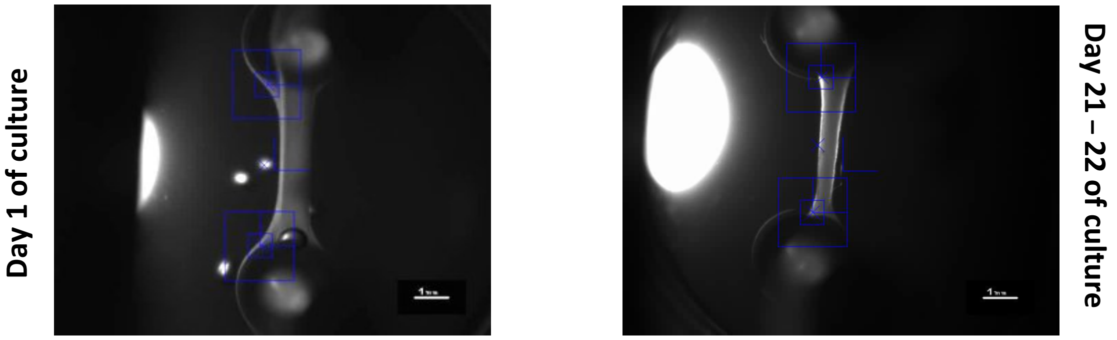

Figure 55 Remodeling analysis of high cell number EHTs on the first day of culture. **(A)** Diameter analysis of the EHTs 1 day after casting. **(B**-**C)** Representative images of multi-cell-type EHTs with **(B)** 0.6 million CMs/tissue and **(C)** 1 million CMs/EHT**.** Scale bar: 1 mm. Data are presented as mean ± SEM; n = 12 – 20 EHTs/group. Statistical analysis: Two-Way ANOVA with Bonferroni’s post-hoc test for multiple comparisons; ****p ≤ 0.0001.

To prevent over-remodeling of the EHTs, an approach of increasing the fibrin content in the tissues was investigated. Therefore, multi-cell-type EHTs as well as CM-only EHTs in two different cell densities (0.6 million CMs/tissue and 1 million CMs/tissue) were cast with doubled fibrin concentration. In terms of remodeling, the increase in fibrin content resulted in greater width of the tissues on the first day after casting. That was observed in both tested set-ups, with EHTs consisting of 0.6 million CMs and 1 million CMs (Figure 56A). A similar pattern was observed after 3 weeks of culture, where the EHTs with increased fibrin concentration exhibited significantly greater diameters compared to their counterparts generated with the standard fibrin concentration (Figure 56B).

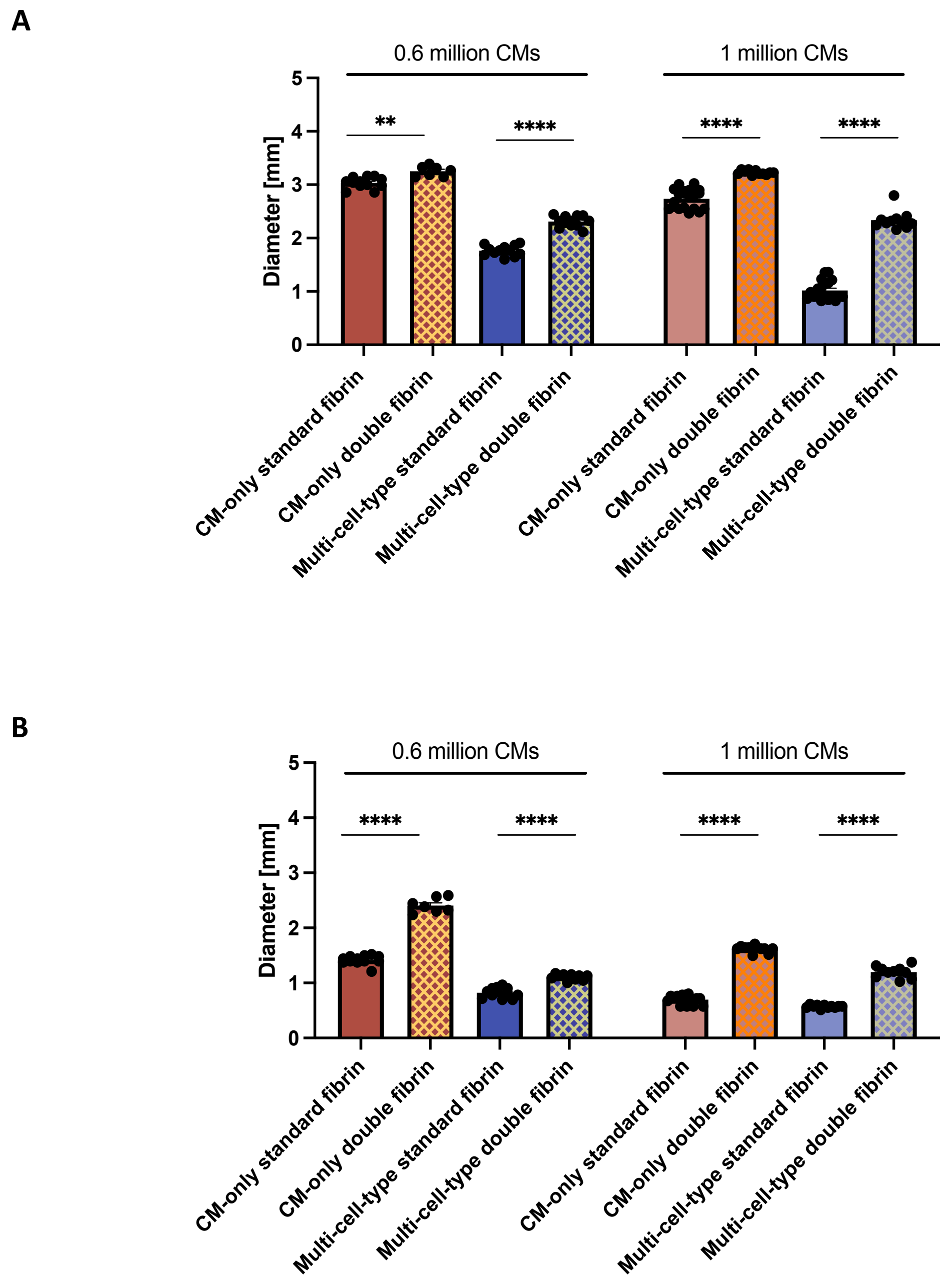

Figure 56 Comparison of the EHTs with standard and doubled fibrin content – remodeling. **(A)** Remodeling analysis after 1 day of culture. **(B)** Remodeling analysis after 3 weeks of culture. Data are presented as mean ± SEM; n = 7 – 20 EHTs/group. Statistical analysis: Two-Way ANOVA with Bonferroni's post-hoc test for multiple comparisons; $^{**}p \leq 0.01$, $^{****}p \leq 0.0001$.

However, in both cases, the increase of fibrin concentration and hence an elevated construct stiffness, resulted in delayed development of contractile properties of the tissues. This could be observed by a delay in the onset of beating, i.e., day 15 for “high cell number” multi-cell-type and CM-only EHTs (Figure 57B) and day 14 for “low cell number” multi-cell-type tissues (Figure 57A). Interestingly, CM-only EHTs with 0.6 million CMs started to beat on day 24 of culture and continued to develop over time of culture (Figure 57A). In both set-ups, the maximal contractile forces generated by the multi-cell-type tissues were lower compared to CM-only EHTs.

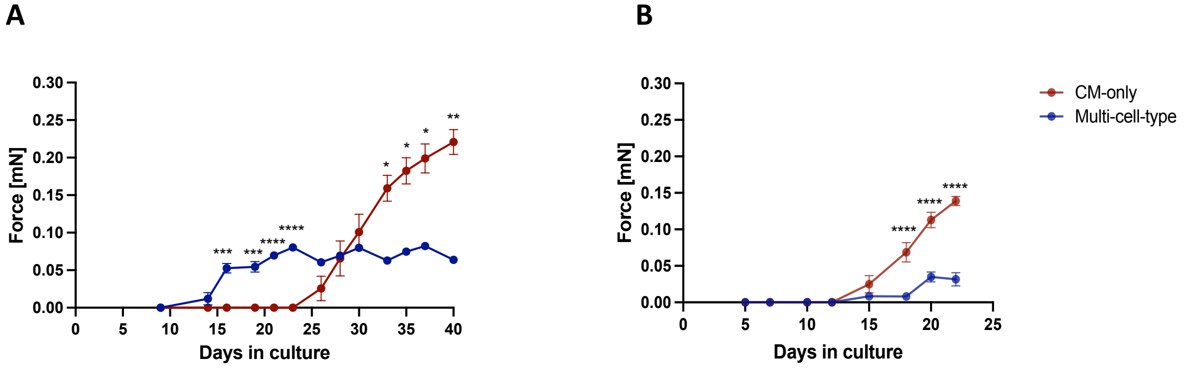

Figure 57 Force development of the EHTs generated with increased fibrin content. **(A)** EHTs containing 0.6 million CMs/EHT. **(B)** EHTs containing 1 million CMs/EHT. Data are presented as mean ± SEM; n = 7 – 11 EHTs/group. Statistical analysis: Repeated measures ANOVA with Bonferroni’s post-hoc test for multiple comparisons; $*p < 0.05$, $**p \leq 0.01$, $***p \leq 0.001$, $****p \leq 0.0001$.

Based on the experiments conducted in order to establish a functional multi-cell-type system, further studies have been performed:

1) with supplementation of FGF-2 in order to increase EC survival
2) with 0.6 million CMs/tissue in order to prevent over-remodeling of the constructs
3) with standard fibrin concentration in order not to disturb the development of contractile properties of the tissues

6.5.4 Hypertrophy induction

One of the main aims of the project was to establish an *in vitro* model for pathological cardiac hypertrophy based on the EHTs. As the previous attempts conducted in hybrid EHTs and hiPSC-CM EHTs were suboptimal (section 6.3.3), an approach utilizing human multi-cell-type EHTs was evaluated. Therefore, multi-cell-type EHTs and CM-only EHTs were either pharmacologically stimulated with pro-hypertrophic compounds (20 μM PE + 50 nM ET-1) or mechanically challenged (AE) in order to induce a pathological hypertrophic phenotype.

6.5.5 Hypertrophy in the EHTs cultured in the medium supplemented with VEGF and FGF-2

6.5.5.1 Pharmacological treatment

The pharmacological stimulation was initiated after EHT forces had reached a plateau in serum-free medium. The duration of the treatment was set to 9 – 12 days. The stimulation of multi-cell-type and CM-only EHTs with a combination of PE+ET-1 resulted in a decrease of contractile force by 60% in the multi-cell-type group and 16% in the CM-only EHTs. However, a statistically significant difference was identified exclusively in the multi-cell-type tissues (Figure 58A-B). Interestingly, in contrast to CM-only EHTs, the drop in contractile force under PE+ET-1 treatment in the multi-cell-type tissues was prominent already after 1 day of stimulation (Figure 58A). Treatment with PE is known to increase the spontaneous beating frequencies of the EHTs, however no elevation in this parameter under PE+ET-1 stimulation was observed in both EHT types (Figure 58C). Moreover, the hypertrophic treatment showed no effect on the relaxation time of the tissues (Figure 58D).

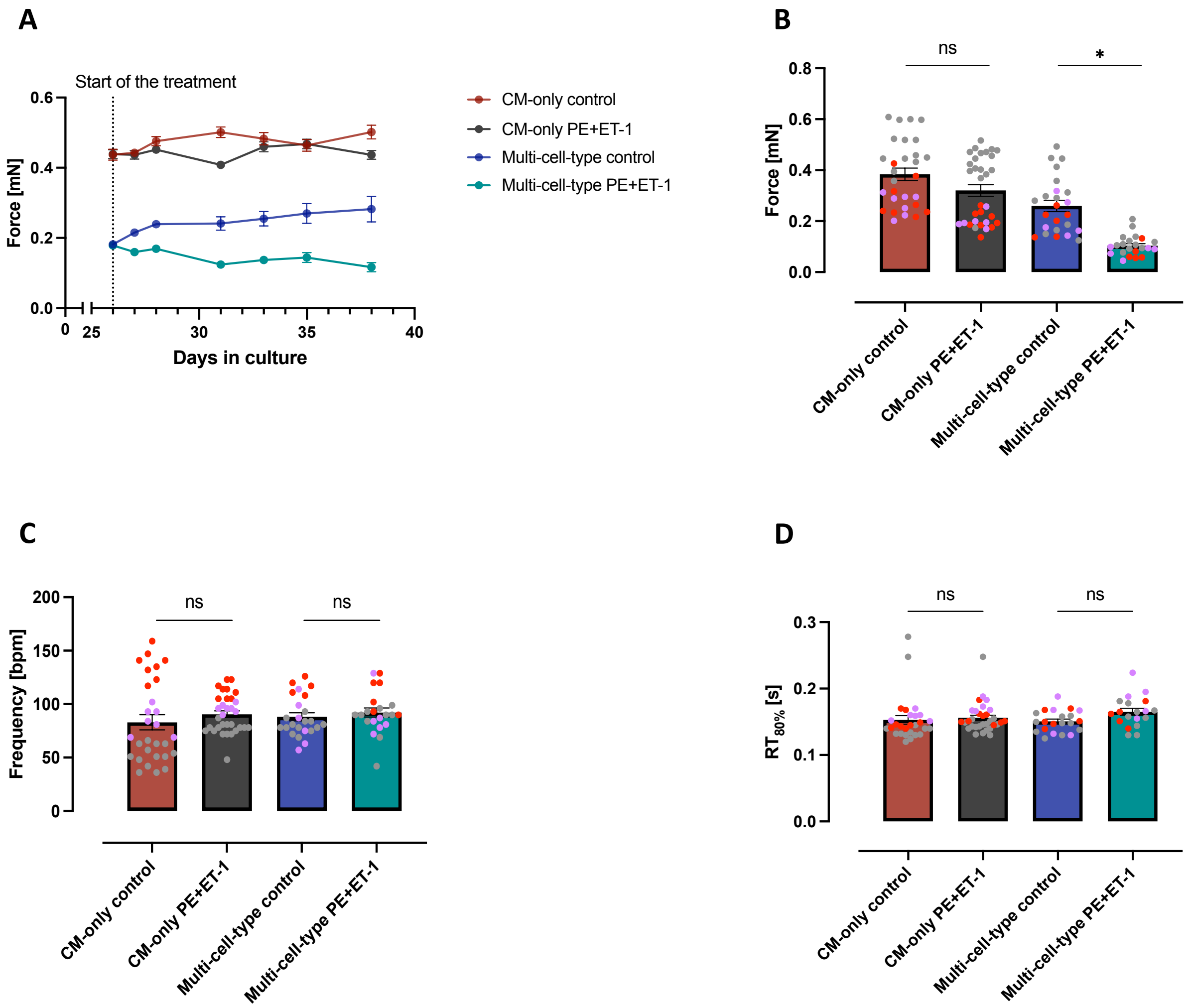

Figure 58 Hypertrophic treatment with PE+ET-1 – functional analysis. **(A)** Representation of PE+ET-1 effect over the 12-day-long treatment period on contractile force in a single batch of EHTs. **(B-D)** Functional parameters measured on the last day of stimulation. **(B)** Force analysis – EHTs paced at 2 Hz. **(C)** Analysis of the spontaneous beating frequency. **(D)** Relaxation time analysis – EHTs paced at 2 Hz. Data are presented as mean ± SEM; (A) n = 13 – 16 EHTs/group, (B-D) n = 22 – 32 EHTs/group from 3 independent batches. Data points belonging to the same batch are displayed in matching color. Statistical analysis: Two-Way ANOVA with Bonferroni's post-hoc test for multiple comparisons; ns $p \geq 0.05$, *$p < 0.05$.

In addition to the functional analyses, the effect of PE+ET-1 was evaluated on the transcriptome level (Figure 59, Supplementary Figure 15). Unexpectedly, the expression of two widely-used hypertrophic markers, i.e., *NPPA* and *NPPB,* remained unchanged under the PE+ET-1 treatment. Another gene commonly associated with pathological hypertrophy is *ATP2A2*. Both types of EHTs displayed a 48% reduced expression of this gene in response to PE+ET-1 treatment (Figure 59).

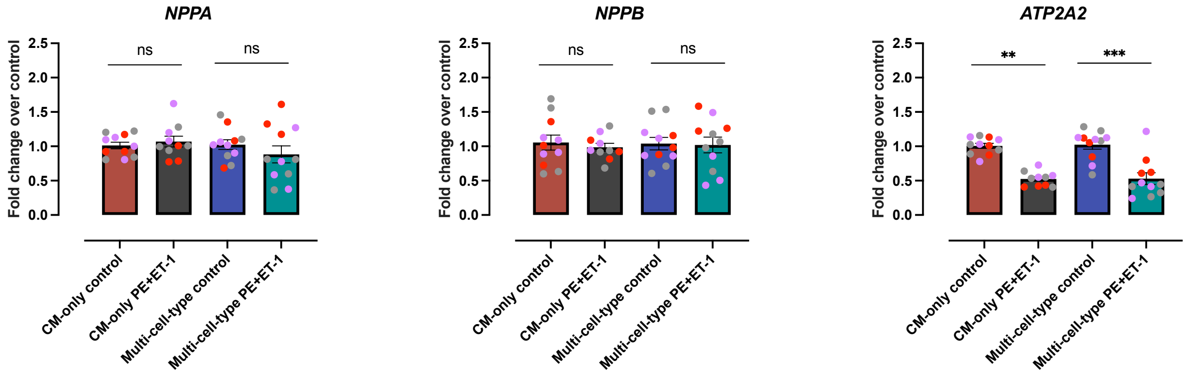

Figure 59 Hypertrophic treatment with PE+ET-1 – gene expression analysis. For the analysis, Ct values of target genes were normalized to *GUSB*. The $2^{-\Delta\Delta Ct}$ values are shown on the graph. Data are presented as mean ± SEM; n = 10 – 11 EHTs/group. Data points belonging to the same batch are displayed in matching color. Statistical analysis: Two-Way ANOVA with Bonferroni's post-hoc test for multiple comparisons; ns $p \geq 0.05$.

Additionally, the concentration of a hypertrophic marker used in the clinical evaluation of HF, i.e., NT-proBNP was evaluated in the culture medium of the EHTs on the last day of treatment. The concentrations of NT-proBNP recorded in the samples were normalized to the time between last medium change and collection of the medium, that is, the time the EHTs were in culture. The results of this analysis demonstrated significantly higher production of NT-proBNP/hour in the CM-only EHTs stimulated with PE+ET-1 (+78%) compared to the untreated controls. However, no statistically significant difference in the amount of secreted NT-proBNP/hour by the control and PE+ET-1 treated EHTs was recorded in the multi-cell-type group (Figure 60).

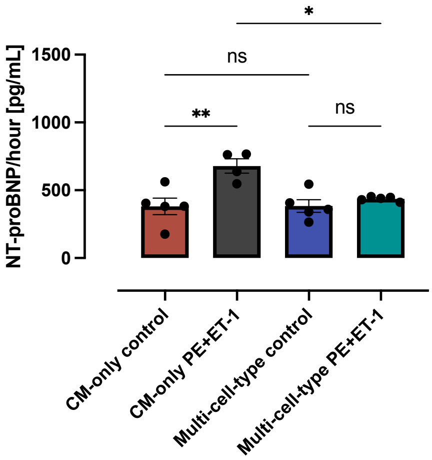

Figure 60 Hypertrophic treatment with PE+ET-1 – NT-proBNP production. Cell culture medium from the last day of stimulation was examined. The raw values were normalized to the EHT incubation time in the medium. Data are presented as mean ± SEM; n = 4 – 5 EHTs/group. Statistical analysis: Two-Way ANOVA with Tukey's post-hoc test for multiple comparisons; ns $p \geq 0.05$, $^*p < 0.05$.

6.5.5.2 Afterload enhancement

Another method to induce pathological hypertrophy is a mechanical intervention (also referred to as afterload enhancement [AE]) involving the insertion of metal braces into the hollow posts to which the EHTs are attached. It causes the afterload in the system to increase and mimics the pathological environment that could lead to induction of hypertrophy. To evaluate if this approach would result in the hypertrophic phenotype in the EHTs, multi-cell-type and CM-only EHTs underwent mechanical intervention for 9 days. On the last day, braces were removed and the properties of EHTs belonging to AE group were compared to the control tissues. Unexpectedly, no statistically significant differences in force between the control and AE treated group were observed in either type of EHTs (Figure 61A-C) (CM-only: -19%; multi-cell-type: +4.8%). Furthermore, no significant differences in relaxation time between the groups were recorded (Figure 61D).

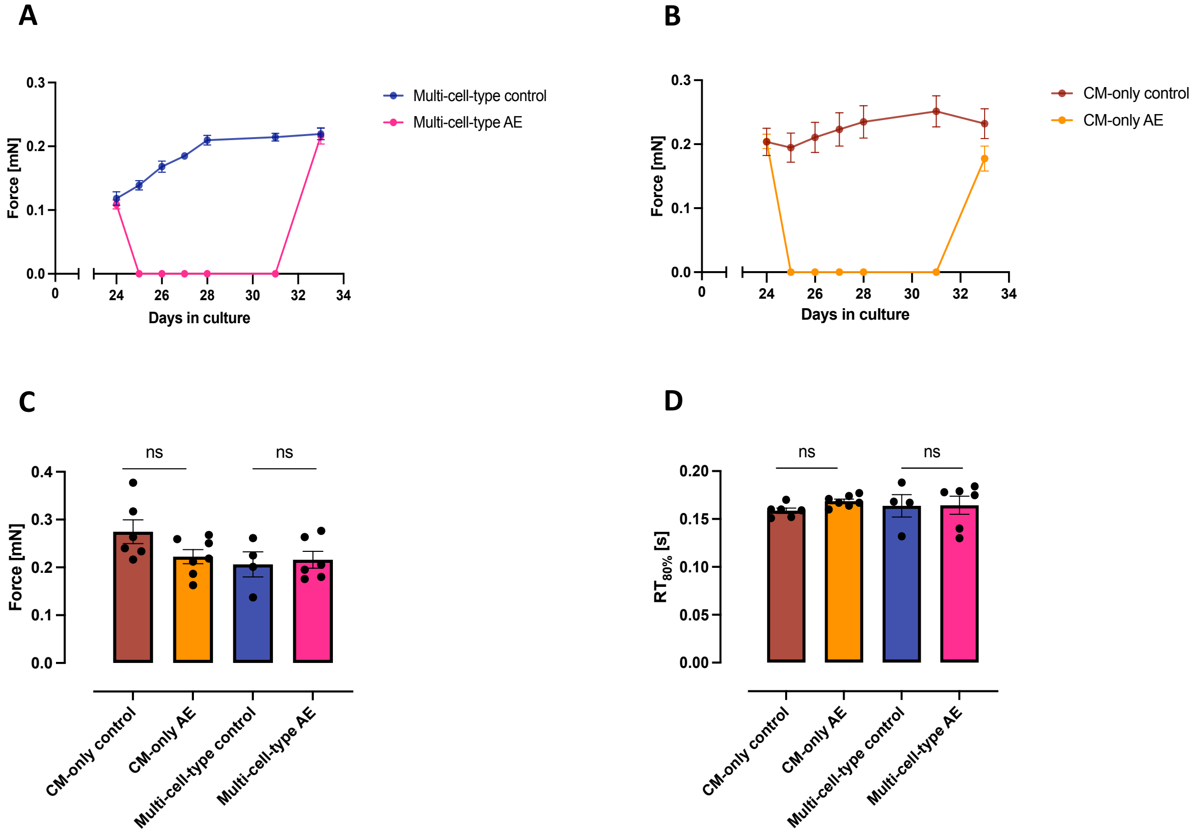

Figure 61 AE in the EHTs – functional analysis. **(A-B)** The time course of afterload enhancement in the **(A)** multi-cell-type and **(B)** CM-only EHTs under spontaneous beating conditions. **(C)** Force analysis in the paced EHTs (2 Hz) after brace removal. **(D)** Analysis of relaxation time in the paced EHTs (2 Hz) after completing the mechanical challenge. Data are presented as mean ± SEM; n = 4 – 7 EHTs/group. Statistical analysis: Two-Way ANOVA with Bonferroni's post-test for multiple comparisons; ns $p \geq 0.05$, $^*p < 0.05$.

Moreover, the analysis of the hypertrophy-related gene expression showed no change in the levels of hypertrophic markers such as *NPPA*, *NPPB*, *ATP2A2* in both types of EHTs (Figure 62).

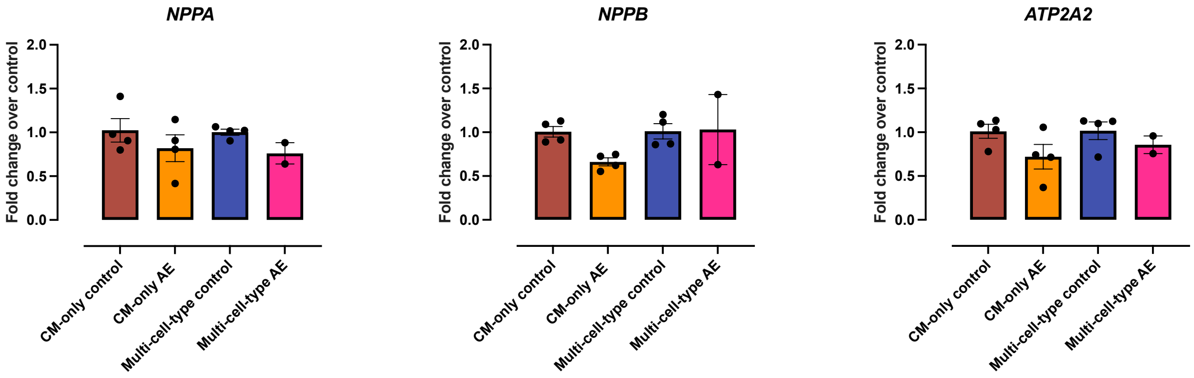

Figure 62 AE in the EHTs – gene expression analysis. For the analysis Ct values of target genes were normalized to *GUSB*. The $2^{-\Delta\Delta Ct}$ values are shown on the graph. Data are presented as mean ± SEM; n = 2 – 4 EHTs/group.

In summary, two approaches of hypertrophy induction were tested in the multi-cell-type and CM-only EHTs, namely, pharmacological stimulation with PE+ET-1 and AE. The treatment with PE+ET-1 did not result in an induction of a canonical hypertrophic phenotype in both tested EHT models. In the CM-only EHTs, the functional parameters were unaffected by PE+ET-1 treatment. Multi-cell-type EHTs and CM-only EHTs exhibited the same expression pattern of hypertrophic genes. However, in CM-only system a significant increase of NT-proBNP under PE+ET-1 treatment was recorded. In the multi-cell-type tissues, the sole impact of the intervention on the contractile performance of the tissues was demonstrated in the decreased contractile force of the EHTs (by 60%). However, genes associated with hypertrophy such as *NPPA*, *NPPB* showed no change in the expression profile under PE+ET-1 treatment. Moreover, no increase of NT-proBNP secretion was observed in this system.

In the second approach the EHTs underwent the mechanical intervention via AE for 9 days. The results showed no effect of the increased afterload on the force nor the relaxation time of the EHTs from both types. The analysis of hypertrophic marker expression demonstrated no significant change of *NPPA*, *NPPB* and *ATP2A2* in both systems. Taken together, both approaches did not result in a full, cohesive pathological hypertrophic phenotype in either of the models used in the study.

Table 19 Summary of PE+ET-1 effects in multi-cell-type and CM-only EHTs (culture medium w/ FGF-2)

Pharmacological treatment with PE+ET-1 (w/ FGF-2)		
Group / Parameter	**CM-only EHTs**	**Multi-cell-type EHTs**
Increase in beating frequency	X	X
Decrease in force	X*	✓
Increase in relaxation time	X	X
Upregulation of *NPPA*	X	X
Upregulation of *NPPB*	X	X
Downregulation of *ATP2A2*	✓	✓
Increase in NT-proBNP secretion	✓	X*

*The effect was in a magnitude of ≥10%. However the difference was statistically not significant or it differed between analyzed batches of EHTs.

Table 20 Summary of AE effects in the multi-cell-type and CM-only EHTs (culture medium w/ FGF-2)

Afterload enhancement (w/ FGF-2)		
Group / Parameter	**CM-only EHTs**	**Multi-cell-type EHTs**
Decrease in force	X*	X
Increase in relaxation time	X	X
Upregulation of *NPPA*	X	X
Upregulation of *NPPB*	X	X
Downregulation of *ATP2A2*	X*	X*

*The effect was in a magnitude of ≥10%. However the difference was statistically not significant or it differed between analyzed batches of EHTs.

6.5.6 Hypertrophic effect of FGF-2 in CM-only EHTs

During the optimization phase of the EHT culture, FGF-2 has been implemented as a component of culture medium crucial for EC survival. Interestingly, the effect of FGF-2 in the EHT system was not limited only to the improvement of EC viability in the tissues. FGF-2 also demonstrated an effect on the functional performance of the EHTs and their mechanical properties, i.e., markedly enhanced stiffness (compare Figure 53 with Figure 46). Moreover, FGF-2 has been widely described in the literature as a pro-hypertrophic factor. We hypothesized that the pleiotropism of FGF-2 actions, and in particular its pro-hypertrophic effect, could be an underlying reason of the incomplete recapitulation of the hypertrophic phenotype described in the sections 6.5.5.1 and 6.5.5.2. Therefore, to investigate the hypertrophic effect of FGF-2 in the EHT system, CM-only EHTs underwent a long-term (30 days) and a short-term (9 days) treatment with FGF-2. The long-term exposure is a stimulation performed from the initiation to the termination of culture, whereas short-term treatment designates the treatment started after 3 weeks of culture. First, CM-only EHTs were divided into 2 groups: cultured with or without FGF-2 from the beginning of culture. On day 21, half of the EHTs cultured in absence of FGF-2 were exposed to FGF-2 containing medium (FGF-2 d21). In the first 3 weeks of culture, EHTs cultured with FGF-2 exhibited higher maximal contractile force. A positive inotropic effect was also observed when FGF-2 was added to the medium of EHTs cultured for 3 weeks without this growth factor. The exposure of the EHTs to FGF-2 resulted in a nearly 48% increase in force between day 21 and 23. Upon completion of treatment, the contractile force generated by EHTs cultured with or without FGF-2 since the beginning of culture displayed comparable magnitudes. The contractile force of the EHTs from the FGF-2 d21 group was significantly increased in comparison to the other experimental groups (Figure 63A). Additionally, the relaxation time in the EHTs treated with FGF-2 was significantly prolonged compared to non-treated EHTs (Figure 63C).

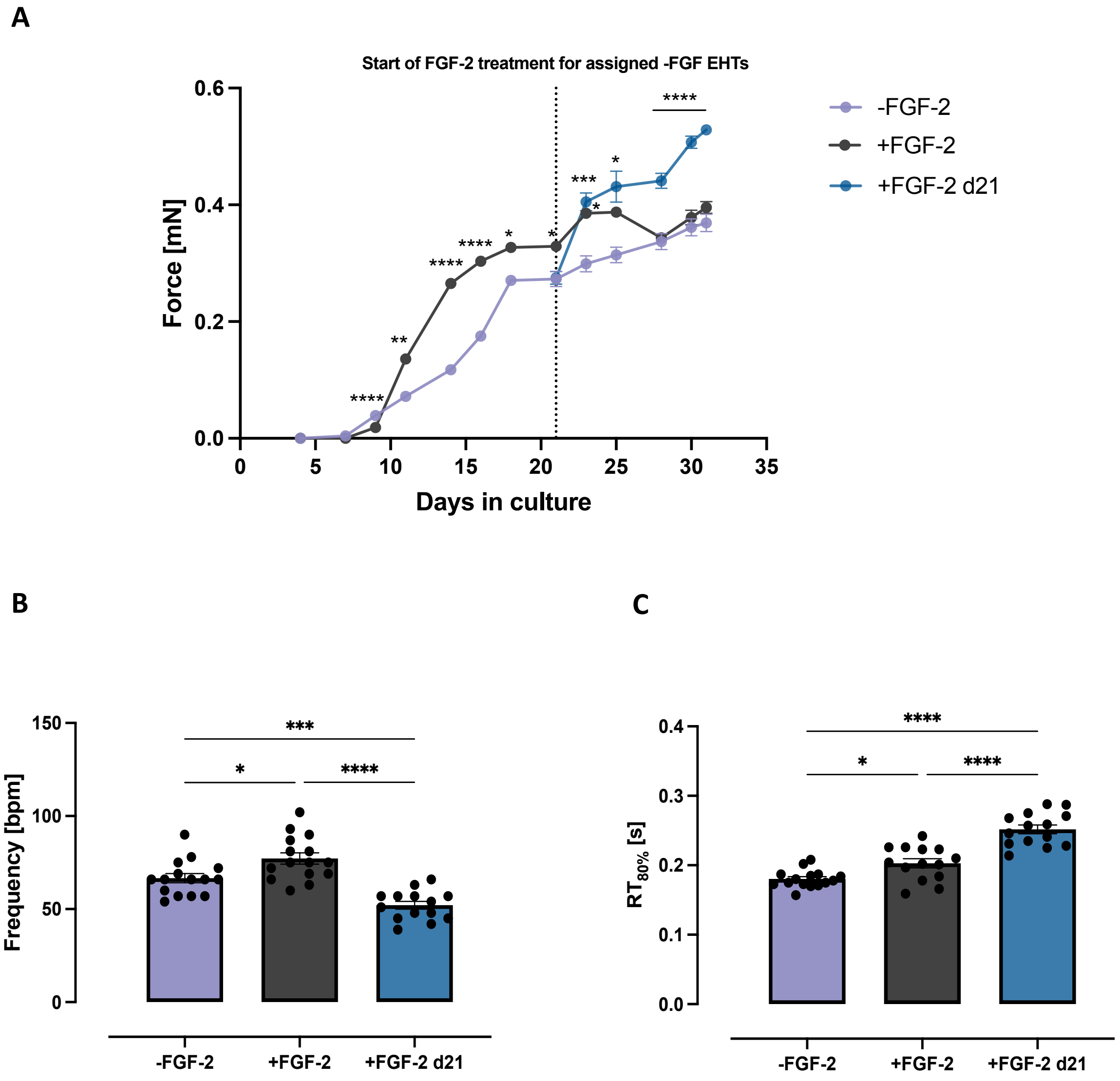

Figure 63 The long- and short-term treatment with FGF-2. **(A)** Force development over time of culture. **(B-C)** Comparison of contractile parameters on the last day of treatment under spontaneous beating conditions: **(B)** frequency, **(C)** relaxation time. Data are presented as mean ± SEM; n = 24 EHTs cultured without FGF-2 (-FGF-2) until day 21, after day 21: n = 15 EHTs -FGF-2; n = 14 EHTs treated with FGF-2 from day 21 (FGF-2 d21); n = 15 EHTs cultured with FGF-2 (+FGF-2). Statistical analysis: (A) Repeated measures ANOVA with Bonferroni's post-hoc test for multiple comparisons; significance calculated in comparison to -FGF-2 group, (B) One-Way ANOVA with Tukey's multiple comparisons test, (C) Welch ANOVA with Dunnett's T3 multiple comparisons test; ns $p \geq 0.05$, *$p < 0.05$, **$p \leq 0.01$, ***$p \leq 0.001$, ****$p \leq 0.0001$.

The analysis of potential hypertrophic effects of FGF-2 in short-term and long-term treatment included gene expression analysis, CMs size assessment, production of NT-proBNP and evaluation of metabolic activity of the tissues. Long-term culture with FGF-2 led to an upregulation of the hypertrophic markers *NPPA* (2.6-fold) and *NPPB* (3.8-fold), indicating the induction of a hypertrophic phenotype. The short-term treatment demonstrated a comparable effect on the expression of both of these hypertrophic genes (*NPPA*: 2.4-fold increase; *NPPB*: 4.3-fold increase). The decreased expression of *ATP2A2* was observed in both FGF-2 stimulated groups, nevertheless only the difference in the long-term treatment group was statistically significant (Figure 64).

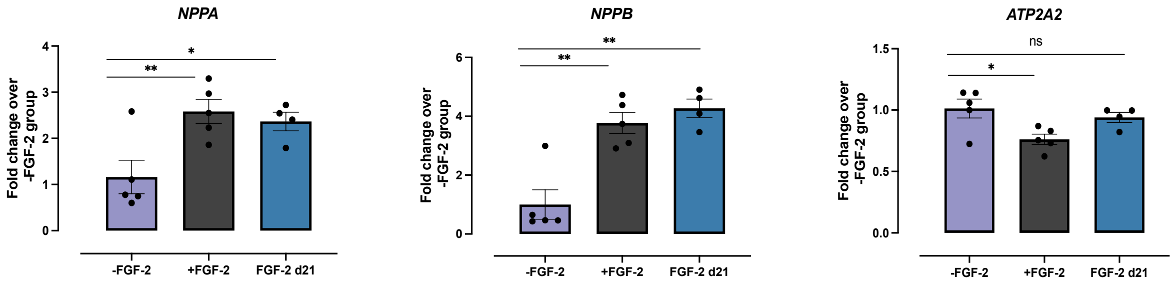

Figure 64 The effect of a long- and short-term treatment with FGF-2. For the analysis Ct values of target genes were normalized to *GUSB*. The $2^{-\Delta\Delta Ct}$ values are shown on the graph. Data are presented as mean ± SEM; n = 4 – 5 EHTs/group. Statistical analysis: One-Way ANOVA with Dunnett’s post-hoc test for multiple comparisons; ns $p \geq 0.05$, *$p < 0.05$, **$p \leq 0.01$.

On the last day of culture, EHTs were dissociated and the isolated CMs were stained with fluorescently labelled anti-cTnT antibody for flow cytometry analysis. The results demonstrated a significant decrease in the cTnT positive population in long-term treatment with FGF-2 (from 95% to 72.4% cTnT^{+} population), which was less pronounced in the short-term treatment group (95% to 79.4% cTnT^{+} population) (Figure 65A). This observation could indicate the promotion of non-CM proliferation by long exposures to FGF-2, which was further confirmed by immunofluorescent staining of non-CMs in the tissues (Supplementary Figure 12). Interestingly, the elevation in CM size was observed solely under long-term treatment with FGF-2, suggesting a time-dependent effect of this growth factor on the CM enlargement (Figure 65B).

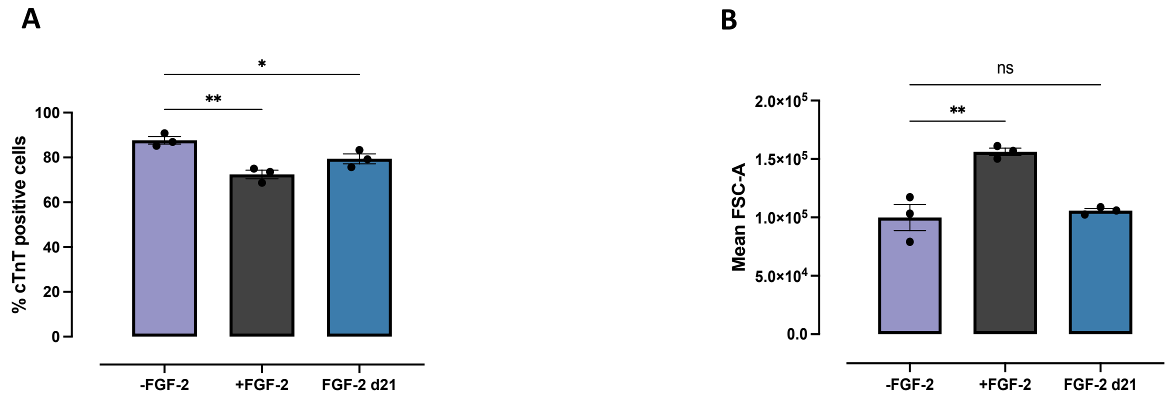

Figure 65 Flow cytometry analysis of CMs isolated from the EHTs cultured without FGF-2 and treated with FGF-2 for 30 days (+FGF-2) or 9 days (FGF-2 d21). **(A)** Flow cytometry analysis – cTnT expression. **(B)** FSC-A analysis of cTnT$^+$ cells. Data are presented as mean ± SEM; n = 3 EHTs/group. Statistical analysis: One-Way ANOVA with Dunnett's multiple comparisons test; ns $p \geq 0.05$, *$p < 0.05$, **$p \leq 0.01$.

Furthermore, the culture medium was collected to assess the NT-proBNP quantity. Original values are displayed in Table 21. The control group showed an average NT-proBNP concentration of 5.034 pg/mL. Conversely, the FGF-2-cultured groups displayed strongly elevated levels exceeding the detection limits of the employed assay (> 35,000 pg/mL).

Table 21 Concentrations of NT-proBNP in culture medium

NT-proBNP concentration [pg/mL]			
No.	**CM-only -FGF-2**	**CM-only +FGF-2**	**CM-only +FGF-2 d21**
1	3,708	>35,000	>35,000
2	1,248	>35,000	>35,000
3	3,922	>35,000	>35,000
4	5,627	>35,000	>35,000
5	4,993	>35,000	>35,000
6	9,990	>35,000	>35,000
7	3,944	>35,000	>35,000
8	6,838	>35,000	>35,000

Another signature of pathological hypertrophy is a switch to anaerobic glucose energy metabolism. To analyze the metabolic activity of the EHTs under long- and short-term FGF-2 treatment, the content of glucose and lactate in the medium was determined with blood gas analyzer. The results demonstrated an increased glucose consumption in both FGF-2 treated groups (+FGF-2: +34.3%, +FGF-2 d21: +52.4%, Figure 66A). Moreover, the analysis demonstrated significantly elevated levels of lactate in both FGF-2 stimulated groups indicating a shift towards anaerobic glycolysis in the EHT metabolism (Figure 66B).

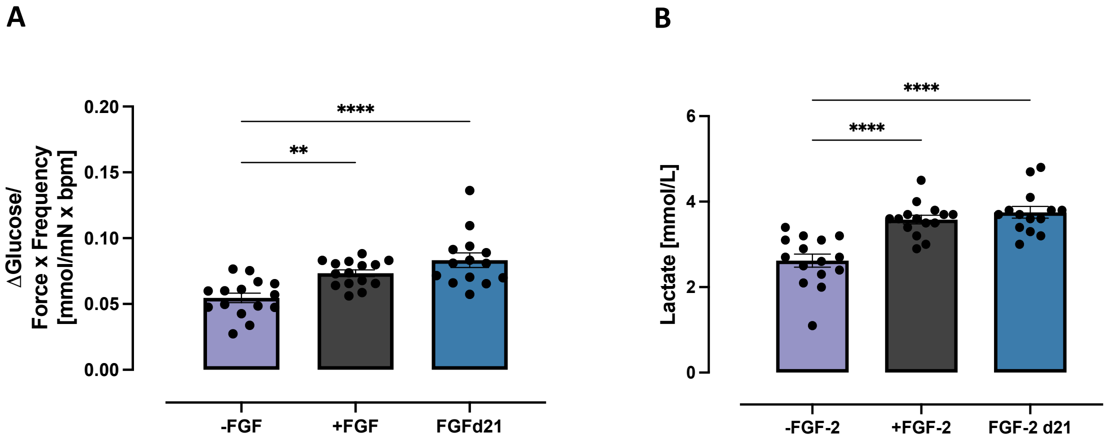

Figure 66 The FGF-2 effect on EHT metabolic activity. Evaluation of **(A)** glucose consumption and **(B)** lactate production under long-term and short-term FGF-2 treatment. Data are presented as mean ± SEM; n = 14 – 15 EHTs/group. Statistical analysis: One-Way ANOVA with Dunnett's multiple comparisons test; ns $p \geq 0.05$, $^{**}p \leq 0.01$, $^{****}p \leq 0.0001$.

To conclude, throughout the course of the experiments, FGF-2 was identified as a growth factor improving the survival of ECs in the multi-cell-type EHTs. However, a broad range of contractile parameters, also in CM-only tissues, was affected by exposure to FGF-2. Therefore, the effect of long-term and short-term treatment of CM-only EHTs with FGF-2 was further evaluated. Both forms of FGF-2 treatment resulted in a positive inotropic and chronotropic effect as well as negative lusitropic effect on the CM-only EHTs. Furthermore, in both cases, FGF-2 led to a decline in the cTnT^{+} cell population, suggesting a promotion of non-CM proliferation under FGF-2 stimulation. The pro-hypertrophic effect of FGF-2 was evaluated by the analysis of CM size, the expression of hypertrophic genes, NT-proBNP secretion and well as metabolic activity. In both tested treatment durations, FGF-2 led to upregulation of *NPPA* and *NPPB*, increase in glucose consumption and elevation in NT-proBNP and lactate production. Additionally, long-term FGF-2 treatment resulted in a significantly downregulated *ATP2A2* and led to an increase in CM size (based on the FSC-A measurements), resembling changes observed in the pathological type of hypertrophy.

Table 22 The effects of FGF-2 treatment detected in CM-only EHTs

Treatment with FGF-2		
Group / Parameter	**Long-term**	**Short-term**
Increase in beating frequency	✓	✓
Decrease in force	X	X
Increase in relaxation time	✓	✓
Upregulation of *NPPA*	✓	✓
Upregulation of *NPPB*	✓	✓
Downregulation of *ATP2A2*	✓	X
Increase in NT-proBNP secretion	✓	✓
Increase in CM size	✓	X
Increase in glycolytic activity	✓	✓

6.5.7 Hypertrophy in the EHTs cultured in the medium supplemented with VEGF only

6.5.7.1 Pharmacological treatment

The experiments described in the section 6.5.6 demonstrated a direct pro-hypertrophic effect of FGF-2 in the EHT system. Based on these results, the FGF-2 supplementation in the medium was suspended in order to reduce the baseline level of hypertrophy in the tissues and enhance the effect of the applied hypertrophic interventions. Hence, multi-cell-type and CM-only EHTs were stimulated with a combination of PE and ET-1 for 9 – 12 days performed in serum-free medium supplemented with VEGF only. The efficiency of the treatment was reflected in the increase of spontaneous beating frequencies in the treated EHT groups (CM-only EHTs: +40.3%; multi-cell-type: +107%, Figure 67A). Moreover, the PE+ET-1 stimulation reduced the contractile force of the CM-only tissues by 37.1% and multi-cell-type

EHTs by 31.4% (Figure 67B). The effect of the hypertrophic treatment on the relaxation time was exclusively observed in the CM-only tissues, where the $RT_{80\%}$ in the treated group was 13% longer than in the control EHTs (Figure 67C).

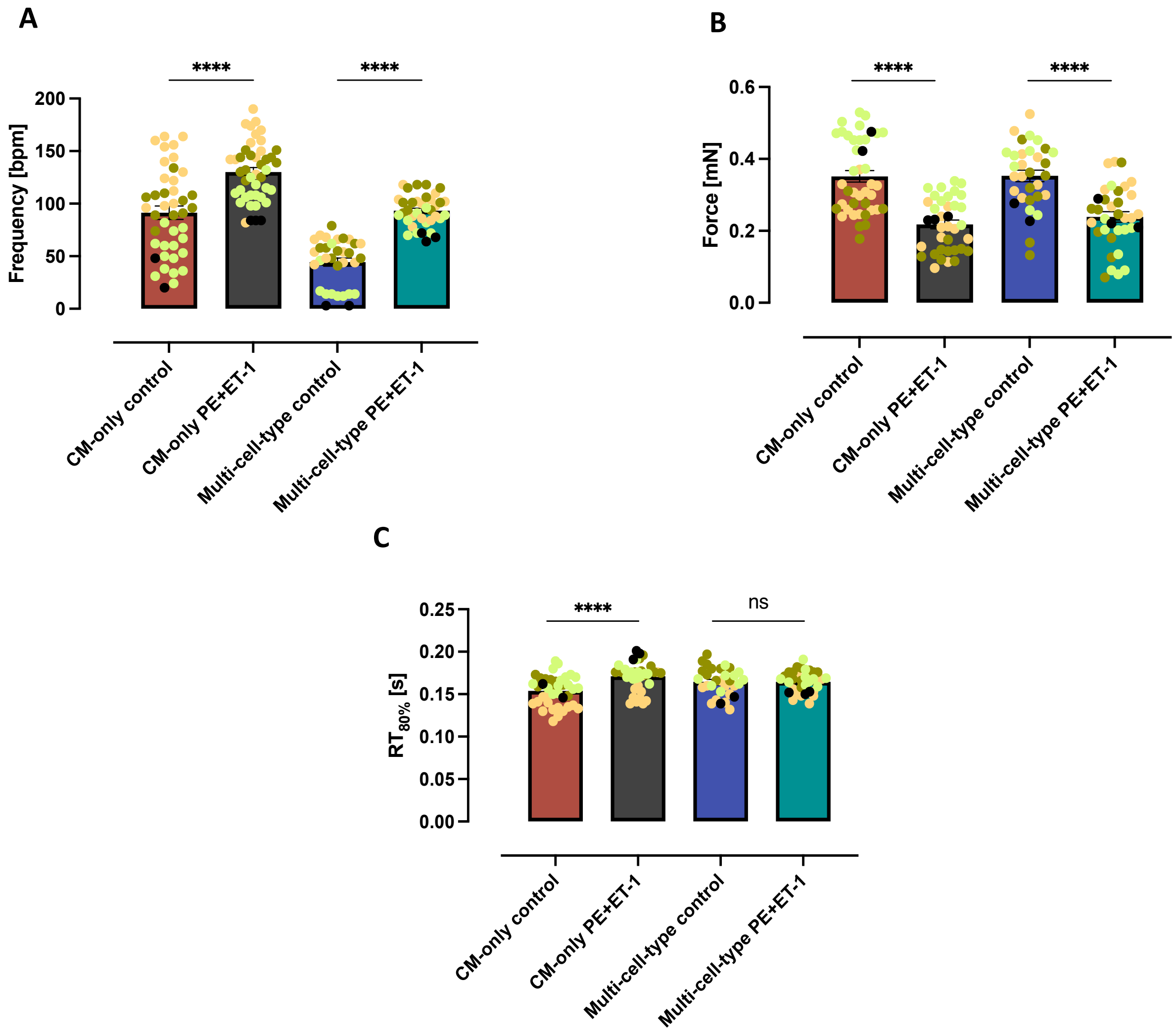

Figure 67 Hypertrophic treatment with PE+ET-1 (culture medium w/o FGF-2) – functional analysis. **(A)** Spontaneous beating frequencies on the last day of treatment. **(B)** Contractile force analysis – EHTs paced at 2 Hz. **(C)** Analysis of relaxation time – EHTs paced at 2 Hz. Data are presented as mean ± SEM, n = 31 – 40 EHTs/group from 4 independent batches. Data points belonging to the same batch are displayed in matching color. Statistical analysis: Two-Way ANOVA with Bonferroni's post-hoc test for multiple comparisons; ***$p \leq 0.001$, ****$p \leq 0.0001$.

The analysis of transcriptomic changes under hypertrophic stimulation was evaluated based on directional mRNA sequencing. The PCA analysis evidenced distinct clustering of control and PE+ET-1 treated samples (CM-only: 55%, multi-cell-type: 61%). In both EHT types, control samples showed higher level of variance compared to PE+ET-1 treated tissues, demonstrated on PC2 (Figure 68A-B). The evaluation of DEGs was performed with the R package DESeq2. In the analysis, only the genes with absolute log2foldchange ($\log_2$FC) > 0.5 and adjusted p-value <0.05 were considered significant and relevant for further analyses. In the CM-only EHTs, PE+ET-1 treatment led to the upregulation of 56 genes and downregulation of 75 genes. On the other hand, multi-cell-type EHTs showed a more pronounced reaction to the stimulation indicated by dysregulation of 679 genes in total from which 339 were identified to be upregulated and 340 downregulated (Figure 68C-D). The gene ontology analysis of the DEGs in CM-only samples demonstrated enrichment in the terms "actin filament-based movement", "heart contraction", "muscle system process", whereas in the multi-cell-type tissues most prominent biological processes were "collagen fibril organization", "extracellular matrix organization" or "chromatid segregation" (Figure 68E-F). Most importantly, the PE+ET-1 treatment resulted in a significant upregulation of fibrosis-related genes exclusively in the multi-cell-type tissues (*COL1A1*: 2.8-fold increase, *FN1*: 3.8-fold increase, *POSTN*: 6.3-fold increase, *FAP*: 3.9-fold increase, Figure 68G).

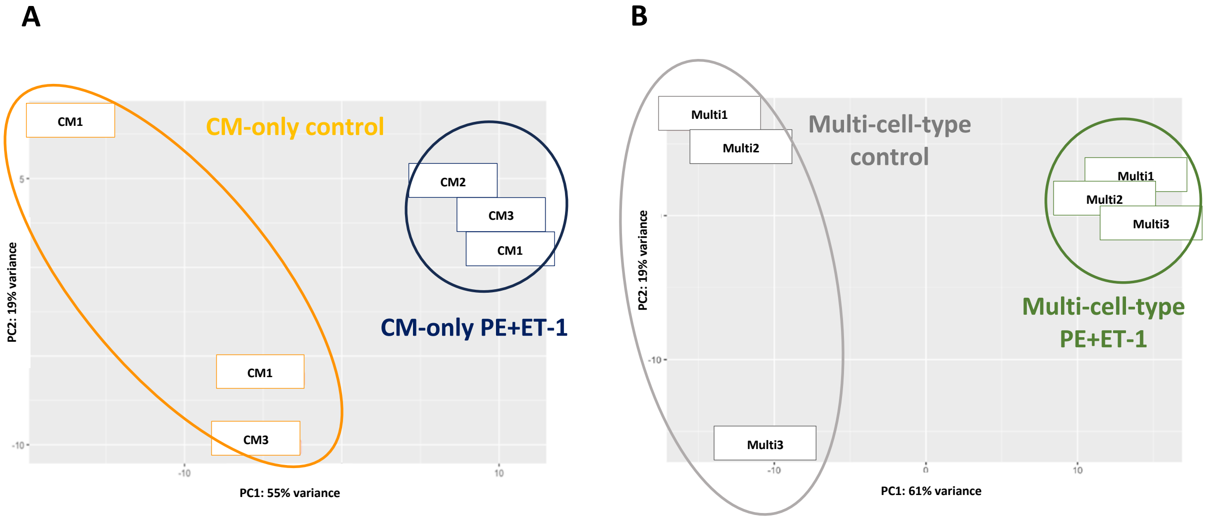

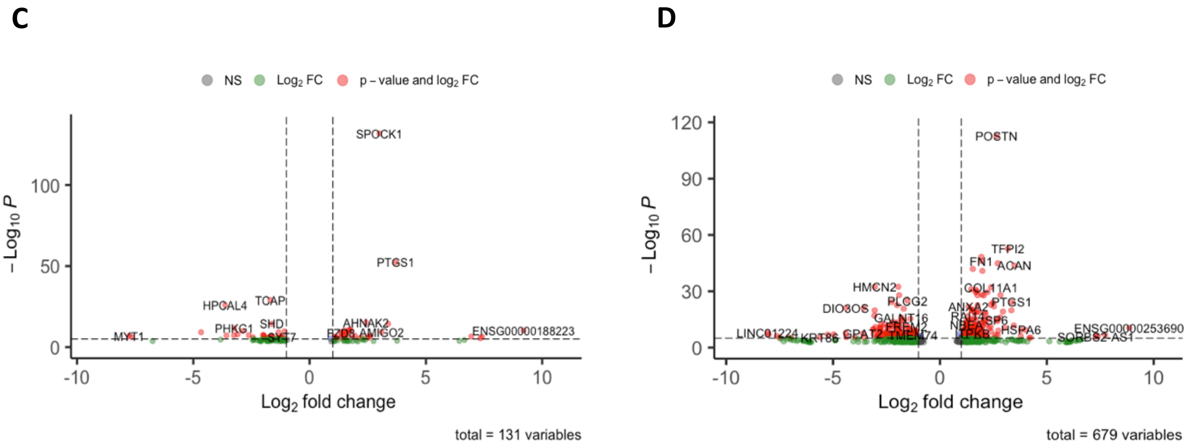
C
NS
Log2 FC
p – value and log2 FC
– Log10 P
100
50
0
-10
-5
0
5
10
Log2 fold change
total = 131 variables
SPOCK1
PTGS1
HPCAL4
TCAP
PHKG1
SHD
MYT1
AHNAK2
AMIGO2
ENSG00000188223
D
NS
Log2 FC
p – value and log2 FC
– Log10 P
120
90
60
30
0
-10
-5
0
5
10
Log2 fold change
total = 679 variables
POSTN
TFPI2
FN1
ACAN
COL11A1
HMCN2
PLCG2
DIO3OS
GALNT16
ANXA2
PTGS1
HSPA6
LINC01224
KRT86
GPAT2
TMEM74
ENSG00000253690
SOBE82-AS1

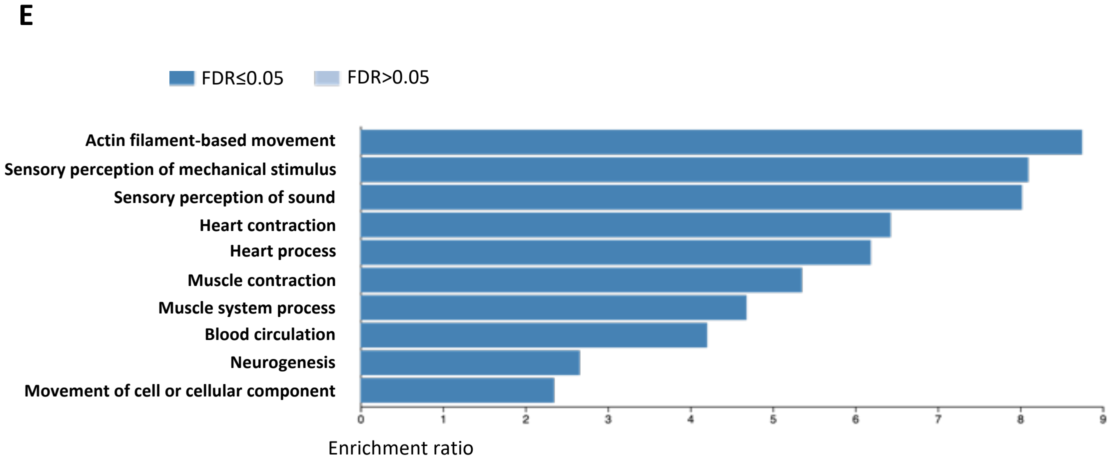
E
FDR≤0.05
FDR>0.05
Actin filament-based movement
Sensory perception of mechanical stimulus
Sensory perception of sound
Heart contraction
Heart process
Muscle contraction
Muscle system process
Blood circulation
Neurogenesis
Movement of cell or cellular component
0
1
2
3
4
5
6
7
8
9
Enrichment ratio

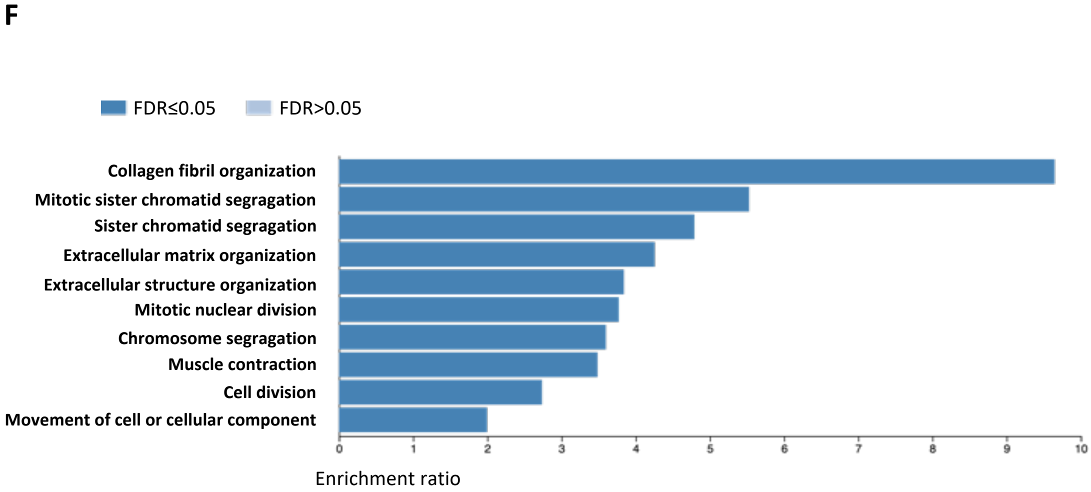
F
FDR≤0.05
FDR>0.05
Collagen fibril organization
Mitotic sister chromatid segragation
Sister chromatid segragation
Extracellular matrix organization
Extracellular structure organization
Mitotic nuclear division
Chromosome segragation
Muscle contraction
Cell division
Movement of cell or cellular component
0
1
2
3
4
5
6
7
8
9
10
Enrichment ratio

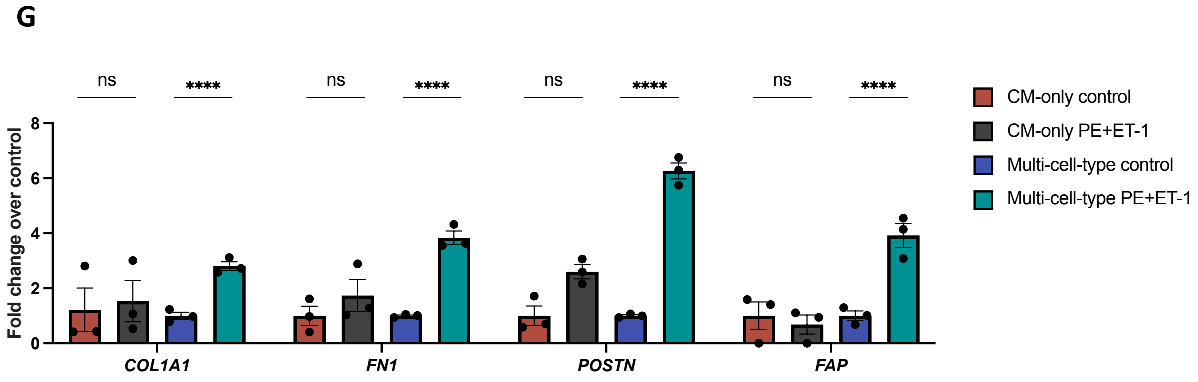

Figure 68 Hypertrophic treatment with PE+ET-1 (culture medium w/o FGF-2) – gene expression analysis by bulk RNA-seq. **(A-B)** PCA plots demonstrating clustering of **(A)** CM-only samples and **(B)** multi-cell-type samples. **(C-D)** Volcano plots visualizing distribution of differentially expressed genes (absolute $\log_2$FC > 0.5 and adjusted p-value < 0.05) identified in the **(C)** CM-only tissues and **(D)** multi-cell-type EHTs with DESeq2. **(E-F)** Gene ontology analysis of DEGs in the **(E)** CM-only and **(F)** multi-cell-type tissues – biological processes; FDR: false discovery rate. **(G)** Expression of fibrotic markers in CM-only and multi-cell-type tissues. Fold change for each sample was calculated as a relation of normalized counts of the sample to an average of the normalized counts of control samples. Data are presented as mean ± SEM; n = 3 EHTs/group. The significance of changes is displayed as adjusted p-value and was determined with the R package DESeq2; ns $p \geq 0.05$, ****$p \leq 0.0001$.

The differentially expressed genes and gene ontology analysis did not reveal a clear hypertrophic gene expression pattern under PE+ET-1 stimulation in both types of EHTs. Nevertheless, evaluation of single hypertrophy-related genes showed *NPPA, NPPB* upregulation and *ATP2A2* downregulation exclusively in the multi-cell-type tissues. The CM-only tissues did not show statistically significant changes in the expression of three hypertrophic genes, corroborating the previous results of more pronounced pathological phenotype in the tissues containing non-CMs (Figure 69).

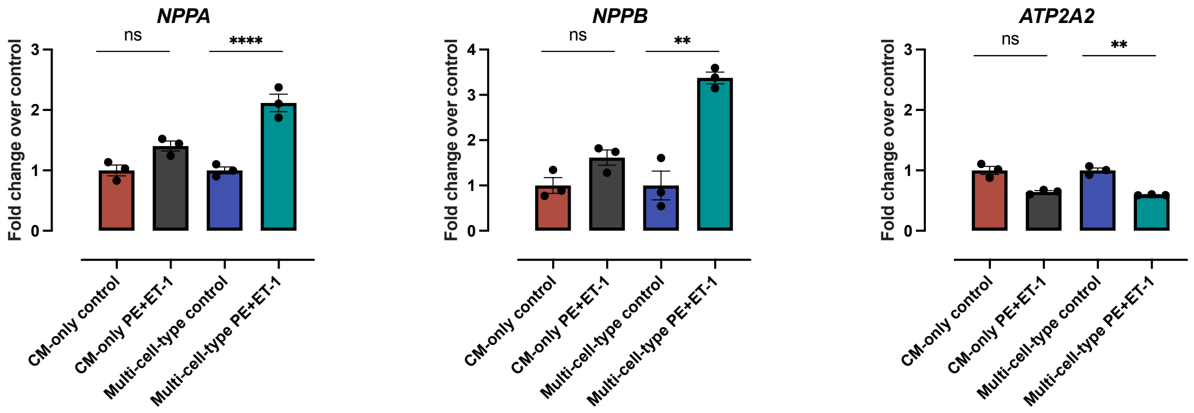

Figure 69 Hypertrophic treatment with PE+ET-1 (culture medium w/o FGF-2) – gene expression analysis by bulk RNA-seq. Fold change for each sample was calculated as a relation of normalized counts of the sample to an average of normalized counts of control samples. Data are presented as mean ± SEM; n = 3 EHTs/group. The significance of changes is displayed as unadjusted p-value and was determined with the R package DESeq2; ns $p \geq 0.05$, **$p < 0.01$, ****$p \leq 0.0001$.

In order to extend the RNA-seq findings, the analysis of *NPPA*, *NPPB* and *ATP2A2* expression was perfomed by RT-qPCR including samples from two additional EHT batches. The results indicated a tendency of *NPPA* and *NPPB* upregulation in both types of EHTs. Consistent with the results obtained by mRNA sequencing, the differences were more pronounced in the multi-cell-type tissues, and only in these samples the differences reached statistical significance. The inclusion of greater number of samples allowed for identification of significant reduction of *ATP2A2* expression in the CM-only EHTs. In the multi-cell-type tissues, the differences detected in *ATP2A2* expression by the RT-qPCR (30.5% reduction) were identified as statistically not significant (Figure 70).

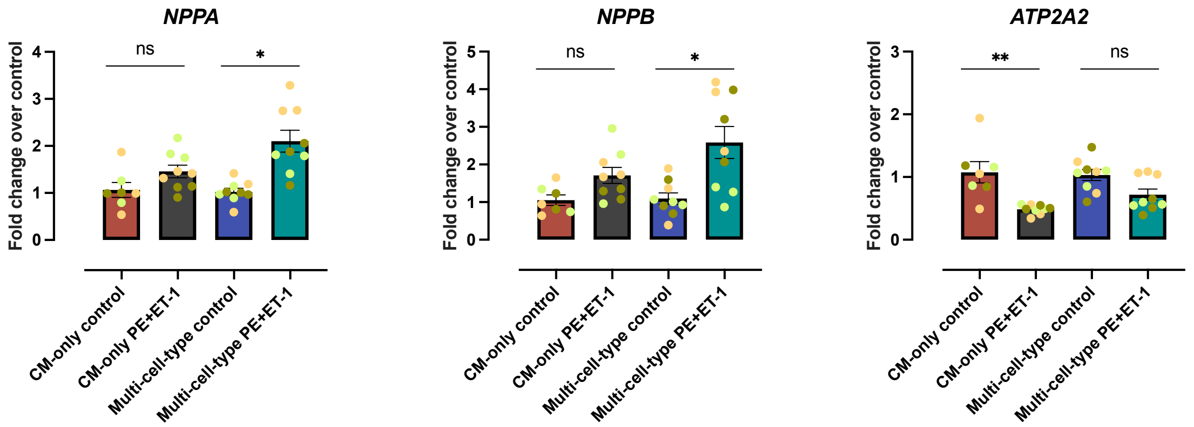

Figure 70 Hypertrophic treatment with PE+ET-1 (culture medium w/o FGF-2) – gene expression analysis by RT-qPCR. For the analysis Ct values of target genes were normalized to *GUSB*. The $2^{-\Delta\Delta Ct}$ values are shown on the graph. Data are presented as mean ± SEM; n = 7 – 9 EHTs/group. Data points belonging to the same batch are displayed in matching color. Statistical analysis: Two-Way ANOVA with Bonferroni's post-hoc test for multiple comparisons; ns p ≥ 0.05, *p < 0.05, **p ≤ 0.01.

Similarly to previous experiments, the concentration of NT-proBNP secreted into the culture medium was evaluated based on the chemiluminescence immunoassay. The results of this analysis showed a significant increase of NT-proBNP secretion under PE+ET-1 treatment (CM-only: +117.1%; multi-cell-type: +148.9%). Importantly, the values recorded for multi-cell-type tissues were significantly higher than their CM-only counterparts (Figure 71).

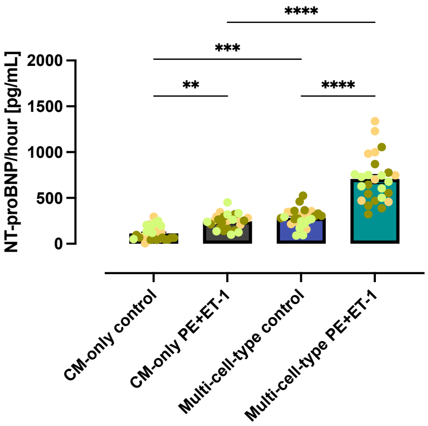

Figure 71 Hypertrophic treatment with PE+ET-1 – NT-proBNP production (culture medium w/o FGF-2). Data are presented as mean ± SEM, n = 26 – 28 EHTs/group from 3 independent batches. Data points belonging to the same batch are displayed in matching color. Statistical analysis: Two-Way ANOVA with Tukey's post-hoc test for multiple comparisons; **p ≤ 0.01, ***p ≤ 0.001, ****p ≤ 0.0001.

The hallmark of hypertrophy is an increase of CM size. To evaluate the size of CMs isolated from the multi-cell-type and CM-only EHTs, tissues were dissociated and analyzed with the Image Stream device. As Image Stream combines the properties of a flow cytometer and a fluorescent microscope, CMs were stained with a fluorescently labelled antibody against the cardiac marker (cTnT) and the size of the events falling into cTnT$^+$ population was determined. The analysis of CM size showed moderate effect of the PE+ET-1 treatment on the size of the CMs isolated from CM-only tissues (+5.1% in cell area; +9.9% in diameter; +1.6% in length). More pronounced differences were detected in the CMs originating from the multi-cell-type EHTs (+34.6% in cell area; +23.7% in diameter; +28.6% in length). Interestingly, the CMs isolated from the multi-cell-type EHTs exhibited greater cell area compared to the CMs from the CM-only tissues (multi-cell-type control vs. CM-only control: +54.1%; multi-cell-type PE+ET-1 vs. CM-only PE+ET-1: +97.4%) (Figure 72).

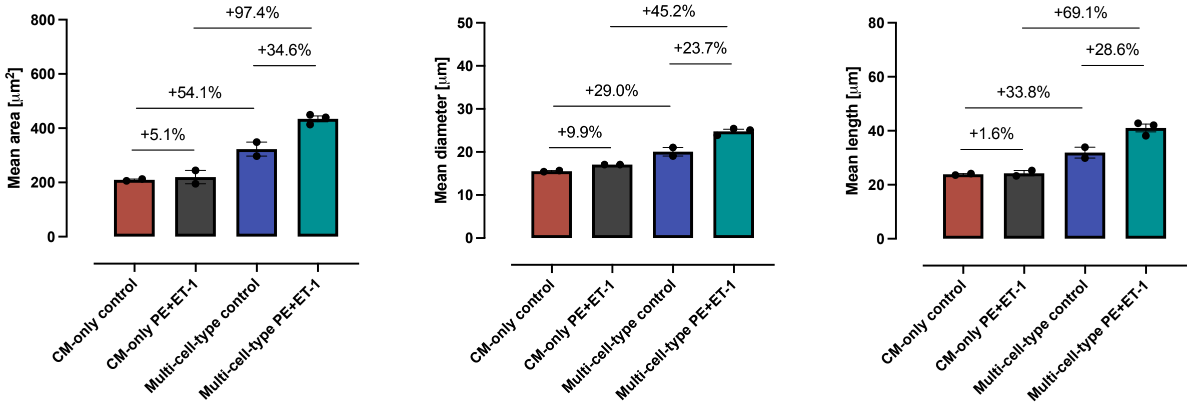

Figure 72 Hypertrophic treatment with PE+ET-1 – CM size (culture medium w/o FGF-2). On the last day of treatment, EHTs were dissociated and stained with a fluorescently labelled antibody against the cardiac marker (cTnT). CMs were analyzed with Image Stream device, where CMs could be gated based on their fluorescent signal. Subsequently, the mean area (left panel), diameter (middle panel) and length (right panel) of the gated cells could be determined with IMAGINE software. Each point represents a mean of the values calculated for 5,500 – 35,000 CMs/EHT. Data are presented as mean ± SEM, n = 2 – 3 EHTs/group.

6.5.7.2 Afterload enhancement

To evaluate whether the AE also induces a hypertrophic phenotype in the EHTs cultured without FGF-2, EHTs underwent the mechanical intervention for 9 continuous days according to the previously described procedure. As a result, the EHTs from the AE groups showed lower contractile forces compared to the control EHTs (CM-only EHTs: -17.4%; multi-cell-type: -11.4%), however the difference in the multi-cell-type group did not reach statistical significance (Figure 73A). Moreover, the relaxation time remained unaffected by the mechanical intervention in both EHT types (Figure 73B).

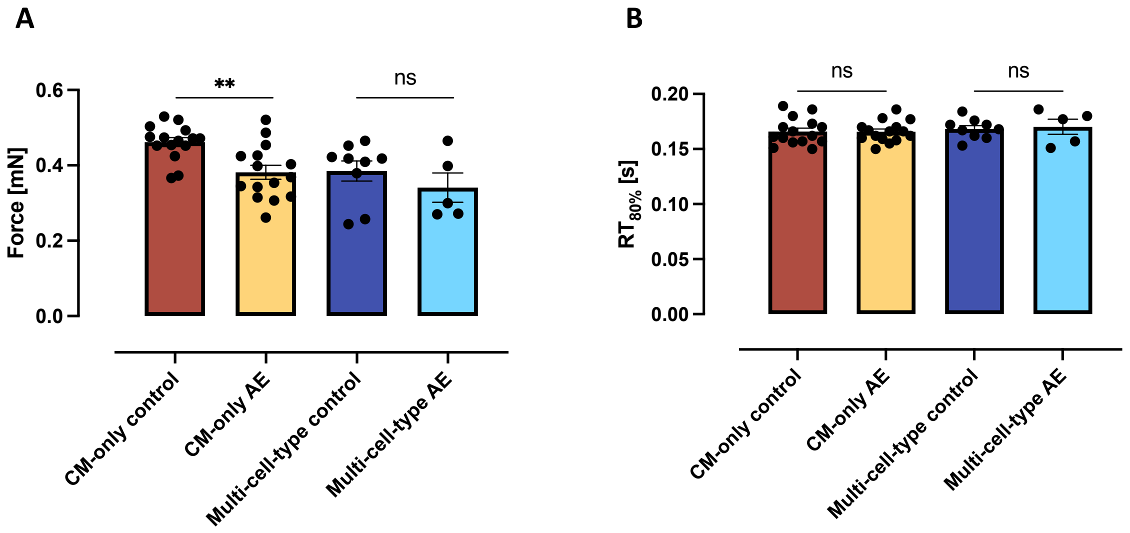

Figure 73 Afterload enhancement in the EHTs (culture medium w/o FGF-2) – functional analysis. Analysis of **(A)** contractile force and **(B)** relaxation time performed in the paced EHTs (2 Hz) after brace removal. Data are presented as mean ± SEM, n = 5 – 15 EHTs/group. Statistical analysis: Two-Way ANOVA with Bonferroni's post-hoc test for multiple comparisons; ns $p \geq 0.05$, $^{**}p < 0.01$.

Additionally, NT-proBNP in the culture medium was determined. The measurements demonstrated higher concentrations of NT-proBNP in the AE-treated EHTs. The NT-proBNP secretion was elevated by 80.8% in the CM-only and by 93.3% in the multi-cell-type tissues, however only the difference recorded in the multi-cell-type system was statistically significant (Figure 74).

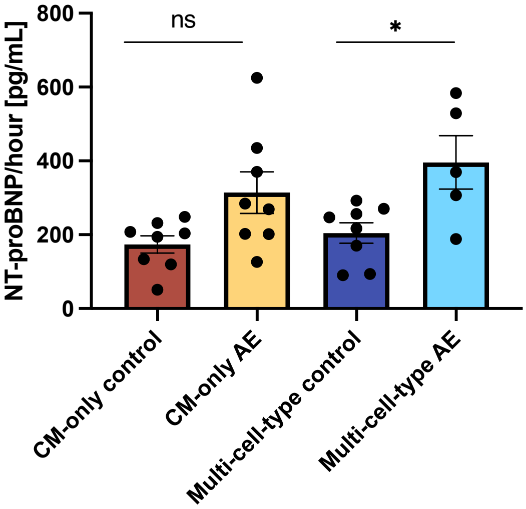

Figure 74 Afterload enhancement in the EHTs – NT-proBNP (culture medium w/o FGF-2). Data are presented as mean ± SEM, n = 5 – 8 EHTs/group. Statistical analysis: Two-Way ANOVA with Bonferroni's post-hoc test for multiple comparisons; ns $p \geq 0.05$, *$p < 0.05$.

As the mechanical intervention stretches out the EHTs and generates resistance against the spontaneous contractions of the tissues, the EHTs undergoing this intervention are prone to breakage or detachment from the posts. Due to high level of remodeling of the multi-cell-type tissues, the number of EHTs that completed the AE experiments was low, leading to restricted availability of the tissues for further analysis. Therefore, the profiling of the hypertrophic genes by RT-qPCR was performed exclusively in CM-only tissues and available multi-cell-type EHTs were further processed for a more comprehensive analysis by single nucleus RNA-sequencing.

The RT-qPCR analysis on the CM-only EHTs, revealed a tendency for *NPPA* and *NPPB* upregulation and *ATP2A2* downregulation under the mechanical challenge (Figure 75). However, due to limited availabilty of the tissues and therefore low n number, the statistical analysis of siginificant differences could not be performed.

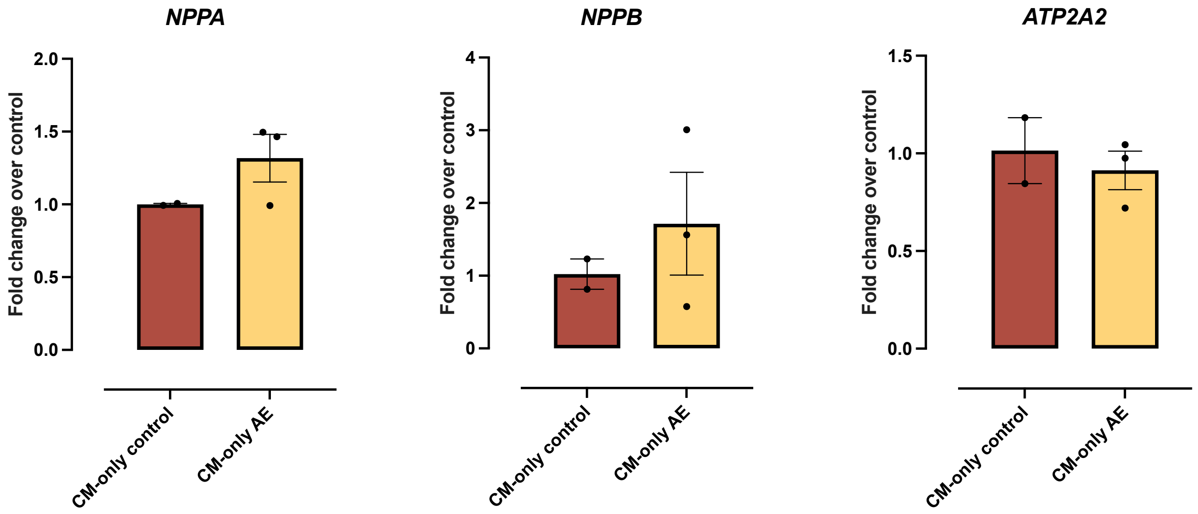

Figure 75 Afterload enhancement in the EHTs – gene expression analysis (culture medium w/o FGF-2). For the analysis Ct values of target genes were normalized to *GUSB*. The $2^{-\Delta\Delta Ct}$ values are shown on the graph. Data are presented as mean ± SEM, n = 2 – 3 EHTs/group.

In conclusion, the induction of a pathological hypertrophic phenotype by PE+ET-1 treatment or AE in the EHTs cultured with the supplementation of FGF-2 failed to recapitulate changes that are typical of pathological cardiac hypertrophy. As a consequence, FGF-2 was withdrawn from the culture medium, and the experiments involving pharmacological stimulation and AE were repeated. Stimulation with PE+ET-1 successfully induced a pathological phenotype in both CM-only and multi-cell type tissues, as evidenced by a decreased contractile force and elevated NT-proBNP secretion. Significant downregulation of *ATP2A2* was detected solely in CM-only EHTs, but showed a strong tendency also in multi-cell-type EHTs. On the other hand, upregulation of *NPPA*, *NPPB* and fibrosis-related genes were only observed in multi-cell type EHTs. Crucially, PE+ET-1 treatment induced CM enlargement exclusively in multi-cell-type tissues. While CM hypertrophy could also be induced in CM-only EHTs by long-term FGF-2 treatment (Figure 65B), the evocation of CM enlargement by PE+ET-1 in the absence of FGF-2 could be fully attributed to the presence of non-CMs in the multi-cell-type EHTs and their interactions with each other and CMs.

In comparison to pharmacological treatment, application of AE did not effectively recapitulate a hypertrophic phenotype in either EHT system. The mechanical intervention in CM-only tissues recapitulated only one hypertrophic feature, i.e., decreased contractile force. Further characteristics such as prolonged relaxation time or activation of the hypertrophic gene program remained unaffected by the AE. In the multi-cell-type system, elevated NT-proBNP secretion was the only characteristic of pathological hypertrophy that could be reproduced. The technical difficulties related to the mechanical intervention siginificantly reduced the number of multi-cell-type EHTs that remained attached to the posts throughout the experiment, ultimately limiting the availability of the tissues for the analysis. For this reason, the gene expression analysis and cell size measurements could not be performed.

Table 23 Summary of PE+ET-1 effects in multi-cell-type and CM-only EHTs (culture medium w/o FGF-2)

Pharmacological treatment with PE+ET-1 (w/o FGF-2)		
Group Parameter	**CM-only EHTs**	**Multi-cell-type EHTs**
Increase in beating frequency	✓	✓
Decrease in force	✓	✓
Increase in relaxation time	✓	X
Upregulation of *NPPA*	X*	✓
Upregulation of *NPPB*	X*	✓
Downregulation of *ATP2A2*	✓	X*
Upregulation of fibrotic genes	X*	✓
Increase in NT-proBNP secretion	✓	✓
Increase in CM size	X	✓

*The effect was in a magnitude of ≥10%. However the difference was statistically not significant or it differed between analyzed batches of EHTs.

Table 24 Summary of AE effects in the multi-cell-type and CM-only EHTs (culture medium w/o FGF-2)

Afterload enhancement (w/o FGF-2)		
Group / Parameter	**CM-only EHTs**	**Multi-cell-type EHTs**
Decrease in force	✓	X*
Increase in relaxation time	X	X
Upregulation of *NPPA*	X*	?
Upregulation of *NPPB*	X*	?
Downregulation of *ATP2A2*	X	?
Increase in NT-proBNP secretion	X*	✓
Increase in CM size	?	?

*The effect was in a magnitude of ≥10%. However the difference was statistically not significant or it differed between analyzed batches of EHTs.

? = analyses not performed due to low numbers of EHTs.

7 Discussion

The main goal of this thesis was to establish a functional, human multi-cell-type *in vitro* model of pathological cardiac hypertrophy based on the EHT system. In previous studies, the hypertrophic intervention (pharmacological and mechanical) in the EHTs containing hiPSC-CMs led only to a partial recapitulation of the typical hypertrophic phenotype. More specifically, the absence of characteristic hypertrophic features such as CM enlargement and fibrosis were hypothesized to be associated with the unicellularity of the EHTs and the lack of interactions with the non-CMs. Thus, the aim was to modify the human EHT system by implementing the non-CM fraction. Two new EHT models were generated: 1) hybrid EHTs containing neonatal rat non-CMs and hiPSC-CMs and 2) multi-cell-type EHTs consisting of five major cardiac cell populations (CMs, ECs, Mφs, CFs and SMCs) differentiated from one hiPSC line. Both novel EHT models were compared with the traditional CM-only EHT model, composed solely of hiPSC-CMs, regarding their functionality and hypertrophic response. The main results of the thesis, which are discussed in the following sections, include:

1) Establishment of a hybrid EHT system and evaluation of the AE effect
2) Successful differentiation of five cardiac cell types from one hiPSC line
3) Integration of the hiPSC-derived non-CMs into the EHT system: two-cell-type and multi-cell-type EHTs
4) Characterization of the pharmacological stimulation and AE effect on multi-cell-type and CM-only EHTs
5) Recapitulation of a pathological hypertrophic phenotype in the multi-cell-type system
6) Discovery of the FGF-2 effect on CM-only EHTs

7.1 Establishment of a hybrid EHT system

7.1.1 Isolation of neonatal rat non-CMs

The first approach to introduce non-CMs into a human EHT system was based on the isolation of neonatal rat non-CMs and combining them with hiPSC-CMs. Two methods of neonatal rat non-CM isolation were evaluated, i.e., pre-plating and MACS. The pre-plating takes advantage of differential adhesion properties of cardiac cell populations, whereas the MACS method is an antibody-based separation. The comparison of these two techniques showed a more efficient separation of CMs and non-CMs with MACS (Figure 8, Figure 9). The application of this antibody-based method improved the isolation of ECs, immune cells and SMCs from the CM pool. Yang and colleagues could also demonstrate successful isolation of neonatal rat CMs by pre-plating, Percoll gradient separation, MACS and separation with superparamagnetic iron oxide particles (SIOP). Here, based on flow cytometry analysis of cTnT expression, the pre-plating method showed the lowest efficiency in purification at 71.9% ± 2.9%, compared to the Percoll gradient protocol 95.6% ± 2.1%, SIOP 93.4% ± 2.6% and MACS separation 94.9% ± 2.3% (Yang et al. 2018). Thus, this study corroborates the results obtained in this thesis, demonstrating high accuracy of the MACS method in separating neonatal rat CMs from the non-CM fraction. The MACS beads are 20 – 100 nm superparamagnetic particles made up of iron oxide and polysaccharide, which imparts biodegradable properties to the beads and ensures their minimal cytotoxic effects (Laghmouchi et al. 2020). A number of studies demonstrated high viability and functionality of cells isolated with MACS beads (Pan & Wan 2020; Zelenka et al. 2022). Moreover, under culture conditions, MACS beads were shown to detach from the isolated cells in a time-dependent fashion (Müller et al. 2017). These observations are in line with the findings of non-cytotoxic effects of MACS beads and clearance of the beads over time in cultured cells observed in this work (Figure 10A). In conclusion, MACS was a method that allowed the separation of the neonatal rat CMs and non-CMs, ensuring high viability of the cells. The next step was to combine the non-CM fraction with hiPSC-CMs into hybrid EHTs.

7.1.2 Establishment of the hybrid EHT model and evaluation of hypertrophic intervention

The hybrid EHTs were composed of 600,000 – 800,000 hiPSC-CMs and 200,000 – 400,000 neonatal rat non-CMs. The addition of non-CMs increased the remodeling kinetics of the tissues, leading to a smaller diameter of the constructs with similar dimensions described for the rEHTs (Figure 11A) (Hansen et al. 2010). The changes in tissue diameter are likely due to the activity of non-CMs such as CFs or Mφs, which have the ability to break down fibrin matrices and lead to thinner, more compact tissues (Motley et al. 2016; Boucard et al. 2022). Another aspect to consider in this context is the overall number of cells in the EHTs. In the dataset presented in Figure 13A, hiPSC-CM EHTs were constituted of 800,000 hiPSC-CMs, rEHTs of 500,000 neonatal rat cardiac cells and hybrid EHTs of 800,000 hiPSC-CMs and 200,000 neonatal rat non-CMs. In line with previously published data, the highest level of remodeling was observed in tissues with the highest cell density/EHT, i.e., hybrid EHTs. Nevertheless, despite lower cell number in the tissues, the rEHTs were significantly more remodeled than hiPSC-CMs, leading to the conclusion that the elevated remodeling of hybrid EHTs and rEHTs could be attributed directly to the presence of non-CMs in the constructs, rather than the simple cell density in the EHTs.

On the functional level, non-CMs decreased the force of the EHTs, which could be associated specifically with the negative impact of CFs (Figure 12A). In a study performed by Pedrotty et al., paracrine factors produced by neonatal rat CFs led to an induction of a phenotype observed in cardiac pathologies. Namely, culturing CMs with CF-conditioned medium resulted in a decrease in cardiac conduction velocity, a prolongation of APD and an increase in resting membrane potential of neonatal CMs, demonstrating a negative impact of CFs on CMs (Pedrotty et al. 2009). Moreover, several studies showed impaired contractility and viability of rat CMs when directly co-cultured with CFs or cultured with CF-conditioned medium (Cartledge et al. 2015; Laframboise et al. 2007). Other possible explanations for the differences between hybrid EHTs and hiPSC-CM EHTs are loss of human CMs or loss of functionality of the human CMs in the hybrid EHT system due to interspecies differences. It cannot be excluded that rat immune cells (e.g., Mφs) were activated by the presence of human cells. This activation could result in the secretion of pro-apoptotic factors and/or induction of phagocytosis, which in turn could have negative effects on the viability of human CMs in the hybrid EHT tissues. However, this hypothesis would have to be confirmed by staining of immune cell markers to confirm the localization and activation status of the rat immune cells as well as analysis of apoptotic markers or determination of cTnI in the culture medium.

The main features shared by hybrid and rEHTs were strong remodeling and lower contractile forces. However, there were also distinct differences between these EHT systems, for instance in beating frequency pattern (Figure 13E-G). In this thesis, the rEHTs demonstrated high beating frequency and irregular, burst-like beating, aligning with previously published data (Hirt et al. 2014). In contrast, the hybrid EHTs showed rhythmic contractions, resembling the phenotype observed in hiPSC-CMs EHTs. Therefore, in the hybrid EHTs the beating pattern of CMs was not affected by the non-CMs in the tissues, suggesting species-dependent characteristics of this feature. Nevertheless, it cannot be excluded that the lack of the full recapitulation of rat phenotype in hybrid EHTs could be an effect of species mismatch and lack of functional interactions between hiPSC-CMs and rat non-CMs within the hybrid EHTs. Kadota and colleagues showed that hiPSC-CMs injected into uninjured neonatal rat hearts could survive in the rat myocardium for 14 – 84 days, but their phenotype was only partially mature. In these experiments, the hiPSC-CMs increased in size and expressed gap junction proteins. However, most of the cells expressed the fetal slow skeletal troponin I and showed no formation of T tubules. In contrast, the neonatal rat CMs demonstrated a fully mature phenotype. In summary, the results of Kadota and colleagues show limited integration and impact of neonatal rat cells and hiPSC-CMs on the functional and structural level, which could explain the results obtained in the presented study (Kadota et al. 2017). To better understand the interaction of rat non-CMs and hiPSC-CMs in the EHT format it would be important to verify if the non-CMs can, indeed, directly interact with hiPSC-CMs and whether the hiPSC-CMs are reactive to the factors that rat non-CMs secrete.

In terms of hypertrophy, a study of Hirt et al. showed that a 7-day-long mechanical intervention in rEHTs resulted in, among others, reactivation of the fetal gene program, decrease in force and increase of the relaxation time of the EHTs (Hirt et al. 2012). In the hybrid model these features could not be recapitulated (Figure 14, Figure 15). The absence of the effect of rat non-CMs on the induction of a hypertrophic phenotype might be attributed to the species differences and a possible lack of functional interactions of the non-CM population and hiPSC-CMs.

In summary, inclusion of rat non-CMs in hiPSC-CM EHTs recapitulated the rat EHT phenotype in terms of tissue remodeling and the magnitude of generated force. Other contractile features of hiPSC-CMs in the hybrid EHTs such as regularity of beating or $RT_{80\%}$ were unaffected by the rat non-CMs. The hypertrophic intervention did not result in the establishment of a pathological phenotype. The most likely explanation is the interspecies mismatch. As a consequence, the generation of a fully human model of multi-cell-type EHTs was the next step in the study of *in vitro* models of cardiac hypertrophy.

7.2 Generation of hiPSC-derived non-CMs and optimization of differentiation protocols

The next part of the study was focused on the generation of hiPSC-derived cardiac cell populations from the hiPSC line ERC001. All the protocols initially used in this project were based on the 3-dimensional EB system. The main advantages of EB-based protocols are scalability and often higher efficiency of differentiations (Guo et al. 2020). The ability to scale up the culture and generate large numbers of differentiated cells was particularly important for the generation of hiPSC-CMs, as this cell type was a major component of the EHTs. Cardiac differentiation was based on mesoderm induction and cardiac specification through modulation of WNT signaling (Breckwoldt et al. 2017; Mannhardt et al. 2016). The application of this protocol led to a high efficiency of differentiation with an average of 71.5% cTnT$^+$ cells/run (average of 12 differentiation runs) and did not require additional optimization.

7.2.1 Macrophage differentiation

The differentiation of Mφs from hiPSCs was achieved by combining two protocols: hematopoietic progenitor cell production based on the publication of Zhu and Kaufman (2019) and macrophage specification described in a study of Ackermann and colleagues (2018) (Ackermann et al. 2018; Zhu & Kaufman 2019). The first steps of differentiation were performed in EB format. The EBs were cultured in STEMdiff™ APEL™ 2 medium supplemented by SCF, VEGF, BMP4 and Y-27632 in order to induce the mesoderm and confer the HE specification. Subsequently, EBs were seeded onto 0.1% gelatin coated plates and cultured in serum-free hematopoietic cell medium (X-VIVO 15) containing IL-3 and M-CSF. The primary role of IL-3 is to support the formation and proliferation of hematopoietic progenitor cells and myeloid cells, whereas M-CSF drives the differentiation of myeloid cells into Mφs (Lopez-Yrigoyen et al. 2020). The final step involves terminal differentiation of macrophage progenitor cells in medium containing serum and M-CSF.

The application of this newly developed differentiation protocol allowed for the production of cells expressing high levels of macrophage proteins, e.g., CD45, CD14, CD68 and macrophage maturation marker (Figure 19). The functionality of Mφs was confirmed in phagocytosis and degradation assays (Figure 20, Figure 23). Moreover, when stimulated with LPS and IFNγ, Mφs demonstrated upregulation of inflammation-related genes, such as *CD80* and *IL6*. Conversely, the incubation with IL-4 resulted in the induction of an anti-inflammatory phenotype characterized by an elevated expression of *CCL24* and a tendency towards *IL10* and *MRC1* upregulation (Figure 21). The efficiency of the polarization was additionally confirmed on the protein level by the analysis of CD86 and CD206 expression in differentially stimulated Mφ groups (Figure 22). These results align with the data obtained by other research teams (Lopez-Yrigoyen et al. 2020; van Wilgenburg et al. 2013) and demonstrate the successful differentiation of functional human Mφs.

The utilization of this differentiation protocol allowed for continuous production of Mφs for up to 3 months with harvests of macrophage progenitors performed weekly or bi-weekly. The disadvantage of the experimental procedure was the limited ability to cryopreserve the macrophage progenitors, which resulted in low numbers of viable cells after thawing.

Over the last years numerous protocols to differentiate Mφs from hiPSCs were published. The main differences lie in the methods of mesoderm/HE induction and the formats, in which it is being carried out (3D vs. 2D). The first method is based on the EB system, where the mesoderm/HE specification can be performed with or without the addition of exogenous growth factors. The second method utilizes sequential exogenous growth factor stimulations in a 2D format. Importantly, the method of Mφ generation appears to affect the phenotype of the cells. For instance, the EB-dependent protocol with spontaneous mesoderm/HE induction yielded Mφs producing higher amounts of IL-6, CCL2 and CXCL1 in their resting state than Mφs generated with EB-independent protocol. On the other hand, Mφs generated without the EB formation step were enriched in genes involved in anti-inflammatory response (Klepikova et al. 2022).

Although protocols differ in the initial stages of the differentiation, the main scheme of Mφ generation is similar in all procedures. The application of distinct differentiation protocols generally results in production of cells with comparable characteristics regarding cell morphology, expression of macrophage markers, phagocytic activity and responsiveness to pro-inflammatory stimulation (Klepikova et al. 2022).

7.2.2 Endothelial cell differentiation

The EB-based protocol to differentiate ECs was initially described in the PhD thesis of K. Breckwoldt (2015) and was further adapted by T. Werner (2018). This protocol combines two differentiation procedures published previously (Orlova et al. 2014; White et al. 2013). The first two steps consisted of mesoderm induction and endothelial specification in a 3D format. EBs were then dissociated and single cells underwent MACS procedure to isolate the $CD31^+$ population, which was further expanded in a 2D format. In the present work, the endothelial induction exhibited low efficiency, with 13% of cells expressing $CD31^+$ (Figure 24). This result is consistent with the data published by K. Breckwoldt (2015) which also demonstrated only 13% of $CD31^+$ cells prior to MACS separation. In the initial protocol, the $CD31^+$ cells were further expanded in EC-SFM medium supplemented with 1% platelet poor plasma, 30 ng/ml VEGF and 20 ng/ml FGF-2. However, due to technical difficulties in acquiring platelet poor plasma, in this work, the application of another commercially available EGM-2 medium, known for its ability to support EC growth was assessed (Gu 2018; Hu et al. 2011). As described in the results section, the isolated $CD31^+$ cells remained viable when cultured in the EGM-2 medium. However, the cultured cells did not display the characteristic cobblestone morphology typical for ECs. Moreover, the expression of $CD31^+$ declined over the first two weeks of culture. As a consequence, an alternative, previously described protocol for the differentiation of ECs in a 2D-format (Palpant et al. 2017) was adapted. The 2D protocol allowed for the generation of hiPSC-ECs with higher yields and higher efficiency without the need of an additional purification step. The hiPSC-ECs displayed over 90% positivity of EC markers, such as CD31, CD144, CD34 and CD309 confirmed by immunofluorescence and flow cytometry (Figure 25A-D). Moreover, the 2D protocol was more time-efficient than the previously used protocol. The experimental hands-on time was effectively halved (2D: 2 weeks vs. 3D: 3 – 4 weeks). The expansion medium used in the 2D protocol (EGM) differed from that used in the 3D protocol (EGM-2). The EGM medium contained bovine brain extract (BBE) and lacked exogenous VEGF. It has been previously shown that the BBE contains growth factors that support EC growth, therefore the supplementation of the medium with BBE, promoted EC survival and proliferation (Leopold et al. 2019). The experiments performed in this thesis demonstrated that the inclusion of BBE and supplementation of the EGM medium with fresh 20 ng/mL VEGF and 20 ng/mL FGF-2 improved the proliferation of hiPSC-ECs, simultaneously promoting the EC differentiation evidenced by high expression of EC markers after completion of the differentiation process. To sum up, the modification of the differentiation protocol improved the generation of hiPSC-ECs by reducing the differentiation time and increasing the number of generated cells, which demonstrated proliferative activity and high purity without the necessity of performing additional purification steps.

7.2.3 Cardiac fibroblast and smooth muscle cell differentiation

The differentiation of CFs and SMCs used in the initial phases of this project was based on the mesoderm induction and subsequent epicardial differentiation through activation of WNT and BMP signaling (Witty et al. 2014). In the following differentiation steps, epicardial cells are undergoing epithelial-to-mesenchymal transition (EMT) and CFs are generated by continuous stimulation with FGF-2, whereas the differentiation of SMCs required treatment with TGFβ1, followed by FGF-2 (Witty et al. 2014). This protocol should very efficiently combine the generation of two different cell types and reduce the complexity of performing multiple differentiations in parallel. Nonetheless, despite several attempts, only low yields in generating CFs and SMCs were achieved with this protocol. Therefore, the SMC differentiation procedure was optimized, and a new protocol was adapted for CF generation.

7.2.3.1 Cardiac fibroblasts

In the initial stages of the project, CFs were differentiated with a 3D-based protocol designed to generate CFs of epicardial origin. In comparison to undifferentiated hiPSCs, the generated CFs demonstrated low expression of stem cell markers (*Nanog*, *OCT4*, *SOX2*) and high expression of commonly used CF markers, such as *POSTN*, *COL1A1* and *DDR2* (Supplementary Figure 4A). This confirmed the differentiated state of the cells and their fibroblast-like phenotype. The epicardial CFs displayed high expression of fibrosis-related genes and proteins, which indicated the activation of the cells and transition into the myofibroblast state (Supplementary Figure 4B-C). In essence, implementation of the 3D-based protocol facilitated the generation of cells closely resembling CFs. However, employing this protocol resulted in low yields of differentiated cells and presented technical challenges. Therefore, a new 2D-based protocol was adapted from Zhang et al. (2019). The differentiation procedure aimed to generate CFs from second heart field progenitors. The protocol followed mesoderm induction by CHIR-99021 treatment and subsequent fibroblast specification by FGF-2 stimulation. The CFs generated with this protocol demonstrated a high expression of fibroblast-associated proteins such as vimentin, TE-7, CD90 and collagen I (Figure 29 A, C). This is consistent with several studies describing the differentiation of CFs from hiPSCs (Kahn-Krell et al. 2022; Floy et al. 2021; Zhang et al. 2019). Moreover, when stimulated with TGFβ1, CFs were able to transition into an activated state, evidenced by upregulation of *POSTN*, *COL1A1* and *CNN2* (Figure 30). The application of the 2D protocol enabled the generation of high purity CFs displaying a more quiescent phenotype compared to 3D-derived CFs (Figure 28). In addition, the 2D protocol resulted in a higher number of differentiated cells and required less hands-on work compared to the 3D-based protocol.

As previously highlighted, CFs differentiated by 3D and 2D protocols have different developmental origins. The comparison of epicardial and second heart field derived CFs was described by Floy and colleagues (2021). The authors observed several differences at the transcriptional level related to the developmental origin of the cells, e.g., upregulation of *MYH10* in epicardial CFs, increased expression of *SALL1* in second heart field CFs. The distinct CFs populations showed differences in the secretion of ECM proteins. The epicardial CFs displayed higher production of collagen IV and laminins compared to second heart field CFs. The activation potential of epicardial CFs was also found to be more pronounced, based on the higher percentage of SMA$^+$ cells after TGFβ1 stimulation. Nonetheless, in this thesis, epicardial CFs displayed an activated state under baseline conditions in contrast to second heart field CFs, therefore suggesting a stronger activation potential of 2D-derived CFs. In the study of Floy et al. (2021), the second heart field and epicardial CFs unanimously supported the CM function. There were no differences in calcium handling in CM co-cultured with epicardial vs. second heart field CFs. Moreover, the two distinct CF types similarly facilitated the assembly of cardiac tissues (Floy et al. 2021). Within the framework of this project, the differences between EHTs generated with epicardial CFs and second heart field CFs were predominantly attributed to biological variations between the EHT batches, rather than to phenotypic differences among CFs. Therefore, combining data from both epicardial and second heart field CFs into a single dataset was deemed admissible.

7.2.3.2 Smooth muscle cells

The main issue encountered in the generation of SMCs was the step of dissociating EBs after epicardial lineage induction and plating single cells onto Geltrex^{TM}-coated flasks for further culture. The dissociation was performed in a step-wise manner by initial incubation with collagenase II followed by digestion with 0.05% Trypsin-EDTA. This combination of enzymes allowed for efficient dissociation of EBs, yielding on average 7.3 million cells/flask of EBs. Nevertheless, cell attachment was disrupted as evidenced by a large number of cells floating in the medium, leading to failure in adhering to the culture flasks. The low cell density in the cell culture dishes resulted in an overall insufficient output of the entire differentiation run, averaging 0.4 million SMCs/T75 flask (average from three independent runs). Changing the coating substrate to a higher gelatin concentration did not improve cell attachment. In contrast, removal of 0.05% trypsin-EDTA, and dissociation with collagenase II alone significantly enhanced cell attachment and increased differentiation efficiency, indicating that trypsin destroys surface receptors, such as integrins, that are critical for cell attachment. The optimized protocol allowed for the generation of higher number of hiPSC-SMCs with high purity (avg. 88% α-SMA$^+$ cells; Figure 27A-B). Moreover, hiPSC-SMCs displayed expression of SMC specific proteins such as MYH11 and TAGLN (Figure 27D), therefore sharing similar features to hiPSC-SMCs described by other groups (Dash et al. 2016; Gao et al. 2021).

The implementation and optimization of cell-type-specific differentiation protocols facilitated the generation of hiPSC-derivatives. These derivatives were intended for the utilization in the subsequent phase of the study, which focused on the establishment of two-cell-type and multi-cell-type EHTs.

7.3 Inclusion of non-CMs in the EHTs

7.3.1 Two-cell-type EHTs

Prior to the generation of multi-cell-type EHTs containing all five hiPSC-derived cardiac cell types, the impact of single cell populations on the performance of CMs in the tissues was evaluated. Therefore, two-cell-type EHTs were established by combining CMs and each non-CM population separately. The number of CMs in the tissues was the same in all conditions, which allowed for the comparison of the functional features of the different types of EHTs. In all combinations, the inclusion of non-CMs in the tissues led to accelerated and enhanced remodeling of the EHTs (Figure 31). Interestingly, the level of remodeling was not correlated with the number of non-CMs in the EHTs, as the tissues containing the highest number of non-CMs, i.e., CMs + ECs (200,000 ECs/EHT) were less remodeled than the EHTs consisting of CMs + CFs (50,000 CFs/EHT), indicating enhanced activity of CFs in the EHTs. This observation varies from the data obtained by Giacomelli and colleagues (2020), where the cardiac organoids containing 85% CMs and 15% ECs had a smaller diameter than organoids comprised of 85% CMs and 15% CFs. Of note, in that study, the organoids consisting of CMs and ECs were found to contain significantly fewer cells in the constructs, despite the same initial cell number used for the generation of the organoids. This could explain the smaller size of the organoids and might suggest loss of cells during the culture (e.g., induced by apoptosis). However, this point was not addressed by the authors. The remodeling potential of the non-CMs was also observed in other studies and was mainly interpreted as improved maturation of the tissues (Reed et al. 2022; Tiburcy et al. 2017).

On the functional level, the incorporation of non-CMs resulted in the acceleration of EHT development, characterized by earlier onset of beating. Moreover, in the first 3 weeks of culture, the contractile forces generated by two-cell-type EHTs were higher than the ones developed by CM-only EHTs (Figure 32A-D). This advantage diminished with time in culture, resulting in no significant difference in force between CMs + ECs, CMs + Mφs EHTs and CM-only tissues at the end of the culture period. In case of CMs + SMCs EHTs, the maximal contractile forces on the last day of culture were significantly higher in the tissues containing SMCs than CM-only EHTs (Figure 32C). Conversely, the CMs + CFs tissues reached their maximal force earlier (after 3 weeks of culture) than CM-only EHTs, but final force was lower

(Figure 32D). Further analysis of contractile parameters on the last day of culture demonstrated no effect of non-CMs on beating frequency or relaxation time (Figure 33A-B).

The effect of fibroblasts on the functional performance of EHT has been widely described in the literature, but often with conflicting results (Tiburcy et al. 2017; Bangfen 2022; Werner 2018). The study of Tiburcy and colleagues tested different percentages of human foreskin fibroblasts (HFF) in engineered human myocardium (EHM), demonstrating highest forces generated by tissues containing 70% CMs and 30% HFF as an initial input of cells. This set-up was found to be superior to 50% CMs + 50% HFF and 90% CMs + 10% HFF combinations. In fact, tissues with the lowest percentage of HFF generated lowest force (Tiburcy et al. 2017). Interestingly, the experiments performed by T. Werner and P. Bangfen in the EHT system containing 95% CMs and 5% epicardial CFs, showed batch-to-batch and cell line dependent effects on the generated force of the tissues. In the PhD thesis of T. Werner (2018) the inclusion of 5% CFs into the EHTs containing cells generated with the C25 cell line resulted in a significant increase of the force and prolonged the $RT_{80\%}$ of the tissues. However, the same set-up performed with the ERC018 cell line exhibited no impact of the implementation of the CFs into the EHT system (Werner 2018). Varying outcomes were also described in the PhD thesis of P. Bangfen (2022). Three independent batches generated with the same cell line (ERC001) showed three distinct effects of CFs on the EHT force. In the first batch, the addition of 5% CFs led to a significant increase of EHT force, whereas in the second batch the EHTs containing CFs developed significantly lower forces compared to CM-only EHTs. On the other hand, in the third batch, no impact of CFs on EHT force was observed (Bangfen 2022).

In conclusion, the incorporation of non-CMs into the EHTs increased the remodeling of the tissues and enhanced tissue development, evidenced by earlier onset of beating. The contractile parameters, i.e., beating frequency and relaxation time were unaffected by non-CMs, whereas the effect on force was dependent on the non-CM fraction included in the tissues. Importantly, the time course experiments show that a valid conclusion about an effect of non-CMs on EHT development needs to take into account long-term effects. If the experiments were finalized, e.g., after 2 weeks of culture, large beneficial effects would have been noted. In contrast, an integrated evaluation of a 4-week period shows that the main effect of mixing in non-CMs into EHT was an acceleration of tissue development and not a final improvement of function. Further conclusions cannot be drawn as molecular details have not been analyzed. In any case, the data encouraged the evaluation of the impact of a combined effect of all cells in multi-cell-type EHTs.

7.3.2 Establishment of the multi-cell-type system

One of the main aims of this project was the generation of fibrin-based multi-cell-type EHTs. The five hiPSC-derivatives were combined together in set proportions and compared to the tissues containing exclusively CMs. The comparison included remodeling, functionality and ultrastructural analysis.

7.3.2.1 Combined effect of hiPSC-derived non-CM populations in the EHTs cultured in the EHT medium supplemented with VEGF only

After evaluating the effects of individual non-CM populations, all five hiPSC derivatives were combined into the multi-cell-type EHT system. The choice of cellular composition of the multi-cell-type tissues was based on previous experiments performed by T. Werner (2018), where the EHTs were generated by combining 70% CMs, 20% ECs, 5% SMCs and 5% CFs. In the current study, this system was further modified by addition of hiPSC-Mφs, resulting in a final tissue composition of 60% CMs, 20% ECs, 10% Mφs, 5% SMCs and 5% CFs. The analysis of tissue dimensions demonstrated an increase of remodeling resulting from the presence of non-CMs in the tissues (Figure 34). This observation confirms the previous results in hybrid and two-cell-type EHTs and is consistent with the data published by other groups (Reed et al. 2022; Tiburcy et al. 2017; Werner 2018; Masumoto et al. 2016). Similar to the data obtained in the experiments with the two-cell-type EHTs, multi-cell-type EHTs displayed earlier onset of beating and higher contractile forces in the first 17 days of culture (Figure 35A). Nonetheless, the analysis of additional contractile parameters showed significant differences between multi-cell-type and CM-only EHTs that were not observed in two-cell-type tissues (Figure 35B). The implementation of four non-CM populations into the EHT system increased the beating frequency and relaxation time of the tissues. The elevated beating frequencies are in line with the data obtained by Ravenscroft et al. (2016), where the authors observed a positive chronotropic effect of ECs and CFs on the CMs in cardiac microtissues (Ravenscroft et al. 2016). As these effects were not observed in the two-cell-type EHTs, an interaction between the non-CMs and their cumulative effect on the CM functional performance is a likely explanation of these results. For instance, activation of Mφs resulting from interactions with other cell types could promote EGF production, which was shown to exert chronotropic effects on CMs (Rabkin et al. 1987). Moreover, the inclusion of the non-CMs in the EHT system increased the stiffness of the tissues and could be one of the factors contributing to increased $RT_{80\%}$ of the multi-cell-type EHTs (Figure 35B, Figure 46). However, as discussed below, longer APs of CMs in multi-cell-type EHTs rather argue for a higher maturity of CMs in these tissues.

The main drawback of hiPSC-CMs is their immature phenotype. Various methods have been examined in order to improve the maturity of hiPSC-CMs, such as metabolic modulation, electrical stimulation or co-culture with non-CMs (Tu et al. 2019). Numerous features were identified that suggested a more matured state of CMs in the multi-cell-type EHTs. In the ultrastructural analysis conducted by TEM, the multi-cell-type tissues exhibited a higher degree of sarcomere organization, density and alignment (Figure 37A-H, Supplementary Figure 5). Quantification of sarcomere length also indicated a more mature state of CMs in the multi-cell-type EHTs, as their sarcomeres were significantly longer compared to CMs found in CM-only EHTs (Figure 37I). Of note, the experiments were done in EHTs subjected to sarcomere arrest with BDM, ensuring complete relaxation and excluding artefacts due to fixation-induced contractures. The values obtained for CM-only EHTs (1.78 μm ± 0.02 μm) are comparable with the previously published data obtained from the EHT system (1.6 μm ± 0.1 μm) (Mannhardt et al. 2016). More importantly, the sarcomere length in multi-cell-type tissues (2.04 μm ± 0.04 μm) resemble more closely the values described for adult CMs (Wu et al. 2021). This corroborates the results from other models of cardiac tissue, where the sarcomere length was found to be significantly higher in organoids containing CMs, ECs and CFs in comparison to the ones composed of CMs and CFs or CMs and ECs (Giacomelli et al. 2017). Further ultrastructural evidence for the maturation of CMs by co-culture with non-CMs was provided by Masumoto et al. (2016). The authors demonstrated organized myofibrillar structures in engineered cardiac tissues (ECTs) containing CMs in combinations with ECs and mural cells (MCs). Interestingly, in tissues composed of CMs, ECs and MCs, CMs resembled a more mature phenotype, as mitochondria in these cells were localized in between myofibrils, a feature that was not consistently present in tissues containing CMs and

ECs, or CMs and MCs separately (Masumoto et al. 2016). Supporting results on enhanced CM maturation through culture with non-CMs were also shown by Kahn-Krell et al. (2022), where incorporation of non-CMs (ECs, SMCs or ECs, SMCs and CFs) resulted in increased sarcomere length and width compared to CM-only cardiac organoids (Kahn-Krell et al. 2022).

Another feature that differs between immature hiPSC-CMs and mature adult CMs is the cell size. The hiPSC-CMs are smaller than their native counterparts. Therefore, the cell size is often used as a maturity parameter of CMs. In this thesis, the evaluation of morphological features of the CMs isolated from multi-cell-type and CM-only EHTs demonstrated bigger cell area, diameter and length of CMs in the multi-cell-type tissues (Figure 72), suggesting a more mature phenotype of CMs when co-cultured with non-CMs. Assuming a cylindrical shape of the CMs, the cellular volumes can be calculated based on the diameter and length of cells following the equation $V_{cell} = \pi \times r^2 \times h$. Thus, the mean CM volumes obtained in the hypertrophic experiment (Figure 72) would amount to: 4,542.0 μm^3 CM-only control, 5,572.7 μm^3 CM-only PE+ET-1, 10,086.3 μm^3 multi-cell-type control, 19,947.8 μm^3 multi-cell-type PE+ET-1. Following the same assumption and equation, the volume of adult CMs (diameter: 20 μm; length: 100 μm; Karbassi et al. 2020) would equal 31,410 μm^3, therefore demonstrating 6.9-fold and 3-fold greater volume compared to the CMs isolated from CM-only and multi-cell-type tissues (controls), respectively. However, it is important to point out that the published values for cell area, diameter and width of CMs vary depending on the method used for size quantification (e.g., microscopy in 2D, histology, flow cytometry) and the cell culture conditions (e.g., composition of cell culture medium), duration of culture, substrate the cells are seeded on, which makes accurate comparisons difficult (Knight et al. 2021; Prondzynski et al. 2017). The method employed in this thesis has the advantage that it visualizes individual suspended cells and provides not only the size, but a photo of each single cell. The quantification is done on thousands of cells in an automated fashion and thereby eliminates potential observer bias.

The immaturity of hiPSC-CMs is also evident in their unusual electrophysiological properties. For example, hiPSC-CMs display a less negative resting membrane potential, lower upstroke velocity and shorter APD than adult CMs (Tan & Ye 2018; Karbassi et al. 2020). In this thesis, the electrophysiological characteristics of the CM-only and multi-cell-type EHTs were evaluated by AP measurements with the sharp microelectrode measurements in intact EHTs (Supplementary Figure 7). This classical technique provides the most reliable evaluation of the integrated electrophysiology of cardiac tissues (Ismaili et al. 2023; Heijman & Christ 2023), as it is free of the important confounders of cell isolation and small size of hiPSC-CMs. The results demonstrated longer APD_{90} in multi-cell-type EHTs compared to CM-only tissues (Supplementary Figure 7B). The values of ~325 ms (versus ~230 ms in CM-only EHTs) come close to those in tissue samples from native human LV (Lemoine et al. 2018). On the other hand, a lower AP amplitude of these tissues (102 mV vs. 124 mV; Supplementary Figure 7D) has often been described as a feature of an immature CM phenotype (Tan & Ye 2018). The explanation of this difference is not clear at present. However, possible discrepancies in the expression, distribution/density of Na^+ channels or active CM-non-CM coupling could contribute to the observed phenotype (Jacquemet & Henriquez 2008). In any case, the longer APD_{90} strongly supports a more mature state of the CMs in co-culture with non-CMs.

During CM development a number of contractile proteins adapt a more mature phenotype to ensure effective cellular contractions. The most commonly described transitions are: *MYH6* (α-MHC) to *MYH7* (β-MHC), *TNNI1* (troponin I1, slow skeletal type; ssTnI) to *TNNI3* (troponin I3, cardiac type) and *MYL7* (MLC2a) to *MYL2* (MLC2v) (Karbassi et al. 2020). The assessment of the proportions between the mature and immature forms of the above-mentioned proteins is used to assess the CM maturation status. In the presented study, these ratios were calculated based on the normalized counts reported for each gene in the RNA-seq analysis. The results revealed predominant expression of genes encoding the immature forms of all evaluated contractile proteins (ratios below 1) in both types of EHTs. However, direct comparison of the values recorded in the CM-only vs. multi-cell-type tissues showed higher *MYH7*/*MYH6* and *MYL2*/*MYL7* ratios in the multi-cell-type EHTs, whereas the *TNNI3*/*TNNI1* was elevated in the CM-only tissues (Supplementary Figure 6). Nevertheless, only the difference recorded in *MYH7*/*MYH6* expression between the groups was found to be statistically significant. Taken together, although the fetal forms of the contractile proteins were prevailing in both groups, the co-culture with non-CMs resulted in an increased expression of CM maturation gene marker (*MYH7*) and could therefore suggest greater CM maturity in the multi-cell-type tissues.

In summary, the structural analysis based on the TEM indicated higher maturation state of CMs in the tissues containing non-CMs (Table 25). However, further electrophysiological analysis did not fully support this conclusion, as the AP amplitude displayed more mature characteristics in the CM-only EHTs. Moreover, on the functional level multi-cell-type EHTs demonstrated higher beating frequencies which are generally associated with the immaturity of CMs. It is important to note that the electrophysiological and functional performance of CMs in the multi-cell-type EHTs can be directly affected by the coupling to non-CMs and the factors released by them. To analyze the functional performance of solely CMs in these tissues, the elimination of the real-time effect of non-CMs would be necessary, for example through tissue dissociation, CM isolation and functional analysis either in 2D or 3D format. To state a final conclusion, further evaluation of features associated with CM maturity (e.g., metabolism, cellular respiration) is necessary.

Of note, the above-mentioned results apply to EHTs cultured with VEGF only. As described in section 6.5.3, the supplementation of the culture medium with VEGF and FGF-2 altered the characteristics of the tissues (e.g., increased the force of CM-only EHTs and elevated the stiffness of the tissues). The effect of FGF-2 on the EHTs is further discussed in the section 7.5.

Table 25 Evaluation of features associated with CM maturity in CM-only and multi-cell-type EHTs

Type of analysis	Feature	CM-only EHTs	Multi-cell-type EHTs	Indications of higher maturity observed in	Figure
Structural analysis	Remodeling	Slow	Rapid	Multi-cell-type	Figure 34
	Cellular organization in the tissues	CMs dispersed in the tissues, often round-shaped	CMs aligned, elongated	Multi-cell-type	Supplementary Figure 5
	CM size [area; µm^2]	209.4 ± 3.28	322.8 ± 25.83	Multi-cell-type	Figure 72
	Cell-to-cell contacts	Present, scattered cell-to-cell contacts	Present, well-developed IDs	Multi-cell-type	Figure 37
	Sarcomere organization	Mostly aligned, Z-lines present, no M-bands	Aligned, dense, sharp Z-lines, M-bands present	Multi-cell-type	
	Sarcomere length [µm]	1.78 ± 0.02	2.04 ± 0.04	Multi-cell-type	
	Mitochondria	Round/elongated, sparsely developed cristae	Round/elongated, well-defined cristae	Multi-cell-type	
Functional analysis (4th week of culture)	Force [mN]	0.23 ± 0.01	0.22 ± 0.00	-	Figure 35
	Beating frequency [bpm]	63.48 ± 2.13	73.51 ± 2.33	CM-only	
	Relaxation time [s]	0.19 ± 0.00	0.22 ± 0.00	Multi-cell-type	
Electrophysiological analysis	APD$_{90}$ [ms]	229.4 ± 7.77	324.6 ± 21.89	Multi-cell-type	Supplementary Figure 7
	MDP [mV]	-76.48 ± 1.74	-77.24 ± 2.46	-	
	APA [mV]	123.8 ± 5.88	102.4 ± 5.84	CM-only	
Molecular analysis	*MYH7/MYH6*	0.15	0.33	Multi-cell-type	Supplementary Figure 6
	TNNI3/TNNI1	0.92	0.39	CM-only*	
	MYL2/MYL7	0.69	0.86	Multi-cell-type*	

*The effect was in a magnitude of ≥10%. However the difference was statistically not significant.

7.4 Evoking a hypertrophic phenotype in EHTs cultured in medium supplemented with VEGF only

After the establishment of a working protocol for the generation of multi-cell-type EHTs and their comprehensive characterization, CM-only and multi-cell-type tissues were assessed in their abilities to recapitulate a pathological hypertrophic phenotype. Two methods of evoking hypertrophy were evaluated, that is, pharmacological treatment (PE+ET-1) and AE. Both of these approaches were previously shown to be effective in the EHT model (Hirt et al. 2012; Madsen et al. 2021; Bangfen 2022). However, in this thesis, both hypertrophic induction methods were tested for the first time in an isogenic multi-cell-type EHT model. In detail, the hypertrophy experiments were performed after the contractile forces of EHTs reached a plateau and under serum-free conditions, to avoid hypertrophy-inducing effects of the undefined horse serum. It was previously shown that the withdrawal of serum lead to a force reduction in rEHTs and ultimately result in contractile inactivity of the tissues. The tissue contractility could be maintained by supplementing serum-free medium with T_3 and hydrocortisone. Therefore, T_3 and hydrocortisone were present in the medium during the hypertrophy experiments (Hirt et al. 2012).

To evoke hypertrophy in the EHTs through pharmacological stimulation, tissues were treated with a combination of pro-hypertrophic compounds, i.e., PE and ET-1. Both of these G protein coupled receptors (GPCRs) agonists have been used for decades to induce a hypertrophic phenotype in neonatal rat CMs (Simpson 1985; Bogoyevitch et al. 1993) and animals (Magga et al. 1994). Interaction of PE and ET-1 with GPCRs leads to activation of phospholipase C (PLC) and subsequent hydrolysis of phosphatidylinositol bisphosphate (PIP_2) into diacylglycerol (DAG) and inositol trisphosphate (IP_3). IP_3 binds to its receptor in the sarcoplasmic and endoplasmic reticulum which results in a release of Ca^{2+} into the cytosol (Jalili et al. 1999). Increased cytosolic Ca^{2+} activates multiple mediators in the cell which are related to hypertrophy. Ca^{2+} activates protein phosphatase 2B (PP2B), also known as calcineurin which dephosphorylates the nuclear factor of activated T cells (NFAT) and leads to its translocation into the nucleus where it is involved in induction of the expression of hypertrophic genes (Molkentin 2004). Furthermore, increased cytosolic concentrations of Ca^{2+} activate Ca^{2+}/calmodulin dependent kinase II (CaMKII) which phosphorylates class II histone deacetylase (HDAC) and dissociates it from myocyte-specific enhancer factor 2A

(MEF2A) enabling the transcription of hypertrophy-related genes (McKinsey et al. 2000). Additionally, the Ca^{2+}/calmodulin complex activates protein kinase Cα (PKCα), which further activates protein phosphatase 1 (PP1) and dephosphorylates phospholamban (PLN), subsequently inhibiting SERCA2a. The impairment of SERCA2a function drives the accumulation of Ca^{2+} in the cytosol and results in diastolic and systolic dysfunctions (Braz et al. 2004).

Previous experiments demonstrated induction of a hypertrophic phenotype in hiPSC-CMs cultured in 2D and stimulated with pro-hypertrophic factors, e.g., PE, ET-1 (Johansson et al. 2022; Tanaka et al. 2014; Aggarwal et al. 2014). The 2D studies primarily used gene expression analysis and cell size measurements as read-outs. In contrast to the 2D systems, EHTs enable functional assessments of pharmacologic intervention by PE+ET-1. The multi-cell-type and CM-only EHTs were stimulated for 9 – 12 days with PE+ET-1. The treatment resulted in a decrease of contractile force and elevation of beating frequencies of both EHT types (Figure 67A-B). This is in line with previously published data (Madsen et al. 2021; Bangfen 2022). It should be noted that an increase in beating frequency is not a characteristic attribute of pathological hypertrophy. The aforementioned observation could be associated with the properties of PE, which has been shown to exhibit positive chronotropic effects in isolated CMs (Srivastava et al. 1977; Simpson 1985) and atria through interactions with the β1-adrenergic receptors (Wagner & Reinhardt 1974). In pathological hypertrophy, reduction of force is correlated with a disability of calcium clearance from the cytosol, due to impaired function of SERCA2a, encoded by *ATP2A2* (Hasenfuss et al. 1994). As shown in Figure 69 and Figure 70, the expression of *ATP2A2* was decreased in both type of EHTs under PE+ET-1 stimulation, recapitulating the feature observed in native cardiac tissue. The downregulation of *ATP2A2,* possibly resulting in lower protein expression of SERCA2a, could contribute to the reduced contractile force of the EHTs. Another explanation for the force reduction is the decrease in CM content observed in the tissues treated with PE+ET-1 (Supplementary Figure 8). In both types of EHTs the percentages of CMs decreased, namely by 34 pp (multi-cell-type) and 38 pp (CM-only), which could affect the contractile performance of these tissues. Interestingly, Tiburcy and colleagues demonstrated a similar reduction in CM content in the EHM model containing CMs and HFF under ET-1 stimulation, which supports the results obtained in this study (Tiburcy et al. 2017). Possible explanations for this observation include apoptosis of CMs under ET-1/PE+ET-1 treatment and induction of non-CM proliferation leading to overgrowth of the tissues and a (relative) reduction in the content of CMs. Nevertheless, to provide a definitive statement, further analysis of apoptotic markers and a quantitative assessment of cellular composition of the EHTs after hypertrophic treatment is necessary.

Furthermore, the concentrations of a clinically used biomarker of pathological hypertrophy, NT-proBNP, were assessed in the EHT culture media (Mouly-Bertin et al. 2008). The analysis showed elevated secretion of NT-proBNP by tissues treated with PE+ET-1 in both types of EHTs (Figure 71). Although the CM-only and multi-cell-type EHTs reacted to the treatment in a similar manner regarding force, frequency and NT-proBNP production, other parameters such as relaxation time, collagen expression or reactivation of the fetal gene program were non-unanimous. The $RT_{80\%}$ was prolonged exclusively in CM-only tissues (Figure 67C). However, it is essential to highlight that the analysis of the contractile parameters on the last day of treatment was performed under constant stimulation with PE, which could affect the contraction kinetics and blunt the long-term prolonged relaxation in the EHTs under treatment. To determine the true effect of the treatment on the $RT_{80\%}$, it would be necessary to repeat these experiments with PE+ET-1 withdrawn on the last day. The most pronounced differences between CM-only and multi-cell-type tissues were demonstrated in the gene expression pattern and CM size analysis (Figure 68, Figure 69, Figure 70 and Figure 72). The multi-cell-type EHTs recapitulated the pathological hypertrophic phenotype more faithfully than the CM-only tissues. The PE+ET-1 stimulated multi-cell-type EHTs displayed upregulation of established hypertrophic markers *NPPA* and *NPPB*, whereas the CM-only tissues showed no statistically significant change in expression of these genes. The expression of *ATP2A2* was reduced in both EHT types under hypertrophic stimulation. However, the difference in multi-cell-type EHTs did not reach statistical significance (Figure 70). Nevertheless, in the bulk RNA-seq dataset this gene was found to be downregulated in the multi-cell-type tissues (Figure 69). Additionally, the RNA-seq analysis demonstrated higher expression of fibrosis-related genes under PE+ET-1 treatment in the multi-cell-type tissues compared to CM-only EHTs, resembling a fibrotic phenotype, which so far has not been established in the human EHT model (Figure 68G). Most importantly, one of the hallmarks of hypertrophy, the increase of CM size, was exclusively observed in multi-cell-type tissues (Figure 72). This indicates the necessity of the interactions between CMs and non-CMs in the tissues to evoke a full pathological hypertrophic phenotype.

The second method of hypertrophy induction – AE – is based on the increase of resistance against EHT contractions by elevation of the post stiffness. This approach was used in the study of Hirt at el. 2012 to successfully induce a hypertrophic response in rEHTs. Additionally, in the thesis of T. Werner (2018), AE was used to evoke a hypertrophic response in CM-only EHTs and two-cell-type EHTs containing CMs and CFs, derived from two cell lines (C25 and ERC018). In these experiments, the CM-only and two-cell-type EHTs, regardless of cell line origin, did not display any molecular or functional phenotype of hypertrophy after AE and/or ET-1 treatment (analyzed parameters: force, $RT_{80\%}$, CM size, *NPPA* expression; ET-1 only analyzed in C25 cell line) (Werner 2018).

In this thesis, AE was performed in multi-cell-type and CM-only tissues. The EHTs from both tissue types demonstrated an AE-induced decrease in contractile force (Figure 73A). However, these differences in the multi-cell-type tissues were not pronounced enough to reach statistical significance. The AE had no effect on the $RT_{80\%}$ in either EHT type (Figure 73B). Interestingly, the production of NT-proBNP was similarly elevated in CM-only and multi-cell-type tissues that underwent AE (Figure 74). However, only the difference in the multi-cell-type group was identified as statistically significant. Further analysis of the hypertrophic phenotype was hampered by technical constraints precluding the examination of hypertrophic gene expression in multi-cell-type EHTs. The gene expression analysis in CM-only EHTs demonstrated no changes in *NPPA*, *NPPB* or *ATP2A2* after the AE intervention (Figure 75), similar to the findings published by T. Werner (2018).

The process of AE requires a high level of technical proficiency and experience. It involves skillful placement of metal braces into the hollow post while the EHTs remain attached to these pillars. The handling steps increase the probability of contamination and EHT breakage. In addition, the dimensions of the brace match the upper opening of the posts. If EHTs remodel, i.e., decrease their length over time of culture, they bend the lower end of the silicone posts towards each other. Insertion of the braces therefore tend to stretch the EHT, and the extent of this stretch depends on the degree of remodeling. Multi-cell-type EHTs are shorter and thus, their mechanical stretching is more pronounced, leading to more frequent and greater tissue damage in this group. In case of full detachment, the EHTs were excluded from the analysis. However, due to low numbers of EHTs completing the AE interventions without complications, the partially detached EHTs were included in the analysis. These tissues were still loosely attached at least to one post (often only by a thin thread of fibrin) but could continue contracting almost freely during the AE intervention, escaping the applied load in the experiment. This obviously confounds the analysis and has to be taken into account when interpreting this data.

7.5 The effect of FGF-2 in the EHT system

During the initial phase of the project, EHTs were cultured in standard EHT medium supplemented with VEGF, which is known to be a key factor in EC proliferation and survival (Byrne et al. 2005). However, ECs in the EHTs showed a continuous decrease in density over the culture period, suggesting limited ability of VEGF to support EC survival. Another growth factor, FGF-2, has been described to inhibit EC apoptosis and to promote EC proliferation (Sahni et al. 1999). Indeed, addition of FGF-2 to the culture of multi-cell-type EHT improved EC viability and persistence (Figure 50). Therefore, for some further experiments, FGF-2 was added into the EHT medium composition for the initial series of hypertrophic interventions. However, these initial data showed that FGF-2 not only improved EC density, but exerted marked effects on the function of CM-only and multi-cell-type EHTs as such. These effects are discussed in the sections below.

7.5.1 Baseline conditions

FGF-2 is known to regulate various cellular functions, such as proliferation, survival, migration or angiogenesis (Detillieux et al. 2003). Due to its wide range of actions, adding FGF-2 into the EHT medium changed the EHT characteristics, including their functional performance. In the multi-cell-type system addition of FGF-2 resulted in decreased force and $RT_{80\%}$, whereas the beating frequency was increased (Supplementary Figure 9). Furthermore, the force development over time demonstrated different dynamics. In the multi-cell-type tissues cultured without FGF-2, the force was gradually increasing during the course of culture (Figure 35A). In contrast, the multi-cell-type EHTs cultured in the presence of FGF-2 generated low forces at early stages of culture keeping the low-level force until the end of the experiments (Figure 52A). The force development of multi-cell-type EHTs cultured with FGF-2 in the first three weeks of culture resembled the data obtained by T. Werner (2018). In that dataset, four-cell-type EHTs (containing CMs, ECs, SMCs, CFs) were cultured over a period of 39 days and showed an increase in force between days 26 – 30. However, in this thesis, the EHTs were used for hypertrophic experiments after 3 weeks of culture. The modification of culture conditions (change of the culture medium to serum-free medium) disables the comparison of the later time points of EHT experiments with the data set of T. Werner. The differences in force development between multi-cell-type EHTs cultured with or without FGF-2 might be due to an increase in CF content over time of culture. And indeed, the analysis of the cellular composition of multi-cell-type EHTs cultured in presence of FGF-2 showed a 4.8-fold increase in CF number within the first week of culture and 1.42-fold between week 1 and 3 (Supplementary Figure 10A-B). As shown in the PhD thesis of P. Bangfen (2022), EHTs with a high content of CFs generated lower forces compared to tissues without CFs or containing low number of CFs, demonstrating a negative effect of the CFs on EHT contractility. Thus, the increased number of CFs in the multi-cell-type tissues cultured in medium supplemented with FGF-2 could explain the lower forces being generated by these tissues in comparison to multi-cell-type EHTs cultured without FGF-2.

The effect of FGF-2 in CM-only EHTs differed from that observed in multi-cell-type tissues. CM-only EHTs cultured in the presence of FGF-2 exhibited higher contractile forces (in the first 3 – 4 weeks of culture) and beating frequencies compared to EHTs cultured without this factor (Figure 63, Supplementary Figure 9, Supplementary Figure 11). This force-increasing effect was seen with long-term FGF-2 treatment (from day 0 to the end at day 32) and a treatment started at day 21, where FGF-2 markedly increased force compared to the control EHT (+38%). Moreover, the long- and short-term FGF-2 treatment increased the $RT_{80\%}$ of the tissues (Figure 63). However, this effect was not observed in other batches of CM-only EHTs cultured with FGF-2 (Supplementary Figure 9, Supplementary Figure 11). Taken together, in the CM-only system, FGF-2 changed the contractile features of the tissues exhibiting positive inotropic and chronotropic effects, whereas its effect on the relaxation time varied between the EHT batches.

Although CM-only tissues were generated from a purified CM population (>90% $cTnT^+$ cells), the FGF-2 supplementation was shown to promote the proliferation of the remaining non-CMs in the tissues. This coincides with the published literature (Bikfalvi et al. 1997). The EHTs cultured with FGF-2 displayed a higher number of cells expressing CF and SMC markers, such as TE-7, CNN1 and TAGLN (Supplementary Figure 12). This was further supported by flow cytometry data, in which tissues cultured in presence of FGF-2 demonstrated significantly lower relative numbers of $cTnT^+$ cells compared to the unstimulated EHTs (Supplementary Figure 13). While such a decline in CM numbers would be expected to rather lead to decreased force generation, the increase of non-CMs in the EHTs cultured with FGF-2 could stimulate CM in a paracrine fashion and be the reason for the improved remodeling (Supplementary Figure 14; the impact of non-CMs on EHT remodeling was previously described in sections 7.1.2, 7.3.1 and 7.3.2.1).

Moreover, FGF-2 was found to improve the structure of the EHTs. The CMs in tissues cultured with FGF-2 were elongated and aligned along the edges of the EHTs, whereas CMs in the unstimulated EHTs appeared more rounded and dispersed in the matrix (Supplementary Figure 12). Tissues cultured with FGF-2 display a more mature structure, which may explain the higher generated forces by these tissues. Moreover, various publications depict FGF-2 as a cardioprotective agent, suggesting a possible inhibition of CM apoptosis that might occur during the casting procedure or at early stages of culture (Naito et al. 2006). Under those conditions, the EHTs exposed to FGF-2 in the medium, could contain higher numbers of viable CMs and ultimately be able to generate higher contractile force as observed in this thesis. However, to further confirm the pro-survival effect of FGF-2 on CMs, additional studies on CM number and apoptotic marker expression (e.g., caspase-3) in the EHT system would be necessary.

7.5.2 FGF-2 and its implications/interference with hypertrophy in the EHT system

The supplementation of EHT medium with FGF-2 had several important effects on both CM-only and multi-cell-type EHTs, e.g., improved survival of ECs (in multi-cell-type EHTs) or enhanced contractile function and tissue structure (in CM-only EHTs). The effects on contractile function in multi-cell-type EHTs was not systematically investigated. But it can be concluded that FGF-2 was helpful to establish a five-cell-type model, resembling the cellular composition of a human myocardium.

However, the data also show that FGF-2 has a strong effect on EHTs on its own that confounded further effects of classical pro-hypertrophic interventions. Thus, both methods to evoke hypertrophic changes in multi-cell-type and CM-only EHTs did not result in an unambiguous pathological phenotype. In the presence of FGF-2, PE+ET-1 stimulation induced contractile dysfunction exclusively in multi-cell-type EHTs (Figure 58B). Conversely, in CM-only EHTs the only characteristic observed after hypertrophic treatment was elevated NT-proBNP production (Figure 60). The phenotypic changes observed in PE+ET-1 treatment did not align with the ones evoked by AE. In these experiments, the AE did not induce any significant changes in both types of EHTs (Figure 61, Figure 62). These results suggested that FGF-2 induced CM hypertrophy independently from the applied hypertrophic stimuli. Indeed, FGF-2 has been described in the literature as a pro-hypertrophic factor (House et al. 2010; Kardami et al. 2004; Schultz et al. 1999). Therefore, the obtained data suggested a strong hypertrophic effect of FGF-2 in the EHT system that was responsible for blunting the effect of the PE+ET-1 stimulation or AE. This hypothesis was further investigated in this thesis.

The evaluation of a long- and short-term effect of FGF-2 was performed in the CM-only EHTs. Both types of treatment resulted in reactivation of the fetal gene program i.e., upregulation of *NPPA* and *NPPB*, elevated secretion of NT-proBNP (Table 21) and increased glucose consumption and lactate production (Figure 66). Moreover, long-term treatment with FGF-2 led to recapitulation of further hypertrophic features such as downregulation of *ATP2A2* (Figure 64) and CM enlargement (Figure 65). These results are consistent with the published data. First studies on the pro-hypertrophic potential of FGF-2 were published in 1990 by Parker et al. The authors demonstrated upregulation of the fetal contractile proteins α-skeletal actin, β-myosin heavy chain, and downregulation of α-myosin heavy chain under FGF-2 treatment in rat ventricular CMs (Parker et al. 1990). Further studies showed a direct effect of FGF-2 on CM enlargement and upregulation of the hypertrophic marker ANP (Eppenberger-Eberhardt et al. 1997; Kaye et al. 1996). Furthermore, the importance of FGF-2 in hypertrophic response was demonstrated with FGF-2 knock-out mice models which had a decreased ability to establish a hypertrophic phenotype in response to transverse aortic coarctation (Schultz et al. 1999). In the EHT system, FGF-2 could exert its pro-hypertrophic effect through the interaction with FGFR1, an isoform of FGF receptor primarily expressed in the neonatal and adult CMs. The hypertrophy-related signaling cascade activated in CMs by FGF-2 include mitogen-activated protein kinase (MAPK) and PLC pathways. In the MAPK signaling pathway, the activation of Ras protein leads to activation of downstream effectors such as ERK1/2, p38, and JNK. These are further involved in induction of hypertrophic gene transcription in the nucleus by regulating the activity of transcription factors (e.g., GATA4, MEF2). On the other hand, activation of PLC is followed by an increase in cytosolic Ca^{2+} and an activation of calcium-reactive secondary mediators, which are in turn responsible for regulation of hypertrophic gene transcription and dysregulation of Ca^{2+} re-uptake by SERCA2a (Kardami et al. 2004). These actions of FGF-2 are similar to the signaling pathways activated by GPCRs agonists, i.e., PE and ET-1 and are thoroughly described in section 7.4.

In summary, the obtained results show for the first time a pronounced pro-hypertrophic effect of FGF-2 on hiPSC-CMs. This effect appears to be independent of the presence of other supplemented cell types. This contrasts with the hypertrophic effect of PE+ET-1, which was only seen in multi-cell-type EHTs. Another remarkable difference is that the hypertrophic effect of FGF-2 on CM-only EHTs was associated with improved contractile function, while PE+ET-1 had consistent adverse effects on force generation, both in CM-only and multi-cell-type EHTs. As the reduction of contractile force was observed in the absence (CM-only) and presence (multi-cell-type EHTs) of CM enlargement, the detrimental effect of PE+ET-1 on contractile function seems to occur independently of the induction of CM hypertrophy.

7.6 Conclusions and future perspectives

In this thesis, for the first time, five hiPSC-derived cardiac cell populations were generated and integrated into functional multi-cell-type EHTs. This model closely resembles native human myocardium in terms of cellular composition and structural complexity. The multi-cell-type EHTs were characterized by an accelerated development and remodeling compared to CM-only tissues. Moreover, the ultrastructural analysis of multi-cell-type EHTs indicated a more mature state of the CMs in these tissues. Pharmacological treatment with

PE+ET-1 induced a pathological hypertrophic phenotype in multi-cell-type EHTs. This phenotype was characterized by contractile dysfunction, reactivation of the fetal gene program, increased production of NT-proBNP, upregulation of fibrotic markers, and increased CM size. In contrast, the CM-only tissues exhibited only a partial recapitulation of these features, including contractile dysfunction, partial activation of hypertrophic genes, and elevated secretion of NT-proBNP. Interestingly, the hallmarks of pathological hypertrophy, i.e., fibrotic changes and the increase of CM size, were detected exclusively in multi-cell-type tissues. This result demonstrates the importance of non-CMs in recapitulating a more complete pathological phenotype in the *in vitro* cardiac models. Moreover, in the evaluation of different methods of hypertrophy induction in the EHT system, a higher effectiveness of PE+ET-1 treatment was found compared to AE intervention, presumably due to technical limitations of the mechanical challenge. As an important side aspect, this thesis identified a robust hypertrophic effect of FGF-2 on CM-only EHTs that was independent of adding other cell types and was associated with improved tissue structure and organization and improved contractile function.

The analysis of PE+ET-1 treatment and AE in the multi-cell-type and CM-only EHTs by mass-spectrometry and snRNA-seq is currently in progress. These results will allow to determine the hypertrophic effect on the level of protein and gene expression at single-cell resolution. Given that the induction of hypertrophy required the withdrawal of FGF-2, further studies on other non-hypertrophic factors that promote EC survival in the tissues would be of interest.

In conclusion, this thesis describes a successful establishment of protocols to differentiate five cardiac cell types from one hiPSC line and their implementation into the EHT system. These multi-cell-type tissues more closely recapitulate the cellular diversity of a human myocardium and offer multiple possibilities for multilineage cardiac disease modeling. In this project the potential of multi-cell-type tissues to model cardiac pathological conditions was demonstrated in the hypertrophic experiments, where the recapitulation of major hallmarks of pathological hypertrophy could by exclusively observed in the human non-CM containing EHTs. This result shows the importance of non-CMs in the cardiac *in vitro* models and provides diverse possibilities for disease modeling and drug screening studies.

8 Bibliography

Ackermann M, Kempf H, Hetzel M, et al (2018) Bioreactor-based mass production of human iPSC-derived macrophages enables immunotherapies against bacterial airway infections. Nat Commun 9: 1–13. https://doi.org/10.1038/s41467-018-07570-7

Aggarwal P, Turner A, Matter A, et al (2014) RNA expression profiling of human iPSC-derived cardiomyocytes in a cardiac hypertrophy model. PLoS One 9(9):e108051. https://doi.org/10.1371/journal.pone.0108051

Anzai A, Choi JL, He S, et al (2017) The infarcted myocardium solicits GM-CSF for the detrimental oversupply of inflammatory leukocytes. J Exp Med 214:3293–3310. https://doi.org/10.1084/jem.20170689

Bacakova L, Travnickova M, Filova E, et al (2018) The Role of Vascular Smooth Muscle Cells in the Physiology and Pathophysiology of Blood Vessels. In Muscle Cell and Tissue - Current Status of Research Field. InTech. https://doi.org/10.5772/intechopen.77115

Bajpai G, Schneider C, Wong N, et al (2018) The human heart contains distinct macrophage subsets with divergent origins and functions. Nat Med 24:1234–1245. https://doi.org/10.1038/s41591-018-0059-x

Banerjee I, Fuseler JW, Price RL, et al (2007) Determination of cell types and numbers during cardiac development in the neonatal and adult rat and mouse. Am J Physiol Heart Circ Physiol, 293:1883–1891. https://doi.org/10.1152/ajpheart.00514.2007

Bang C, Batkai S, Dangwal S, et al (2014) Cardiac fibroblast-derived microRNA passenger strand-enriched exosomes mediate cardiomyocyte hypertrophy. J Clin Invest 124: 2136–2146. https://doi.org/10.1172/JCI70577DS1

Bangfen P (2022) Atrial Fibrillation Modelling and Targeted DNA Methylation Editing in Human Engineered Heart Tissue-Based Disease Models. Universität Hamburg. https://ediss.sub.uni-hamburg.de/handle/ediss/9989

Baudino TA, Carver W, Giles W, et al (2006) Cardiac fibroblasts: Friend or foe? Am J Physiol Heart Circ Physiol 291:H1015-26. https://doi.org/10.1152/ajpheart.00023.2006

Baum J, Duffy HS (2011). Fibroblasts and myofibroblasts: What are we talking about? J Cardiovasc Pharmacol 57:376–379. https://doi.org/10.1097/FJC.0b013e3182116e39

Bazgir F, Nau J, Nakhaei-Rad S, et al (2023) The Microenvironment of the Pathogenesis of Cardiac Hypertrophy. Cells 12:1–35. https://doi.org/10.3390/cells12131780

Bergmann O, Zdunek S, Felker A, et al (2015) Dynamics of Cell Generation and Turnover in the Human Heart. Cell 161: 1566–1575. https://doi.org/10.1016/j.cell.2015.05.026

Bernardo BC, Weeks KL, Pretorius L, et al (2010) Molecular distinction between physiological and pathological cardiac hypertrophy: Experimental findings and therapeutic strategies. Pharmacol Ther 128:191–227. https://doi.org/10.1016/j.pharmthera.2010.04.005

Beslika E, Leite-Moreira A, De Windt LJ, et al (2024) Large animal models of pressure overload-induced cardiac left ventricular hypertrophy to study remodeling of the human heart with aortic stenosis. Cardiovasc Res 120:461-475. https://doi.org/10.1093/cvr/cvae045

Boucard E, Vidal L, Coulon F, Mota C, Hascoët JY, Halary F (2022) The degradation of gelatin/alginate/fibrin hydrogels is cell type dependent and can be modulated by targeting fibrinolysis. Front Bioeng Biotechnol 10:920929. https://doi.org/10.3389/fbioe.2022.920929

Bogoyevitch MA, Fuller SJ, Sugden PH (1993) cAMP and protein synthesis in isolated adult rat heart preparations. Am J Physiol 265:C1247-57. https://doi.org/10.1152/ajpcell.1993.265.5.C1247

Boluyt MO, Bing OHL, Lakatta EG (1995) The ageing spontaneously hypertensive rat as a model of the transition from stable compensated hypertrophy to heart failure. Eur Heart J 16: 19-30. https://doi.org/10.1093/eurheartj/16.suppl_n.19

Braz JC, Gregory K, Pathak A, et al (2004) PKC-alpha regulates cardiac contractility and propensity toward heart failure. Nat Med 10:248-54. https://doi.org/10.1038/nm1000

Breckwoldt K, Letuffe-Brenière D, Mannhardt I, et al (2017) Differentiation of cardiomyocytes and generation of human engineered heart tissue. Nat Protoc 12:1177–1197. https://doi.org/10.1038/nprot.2017.033

Brutsaert DL (2003) Cardiac endothelial-myocardial signaling: Its role in cardiac growth, contractile performance, and rhythmicity. Physiol Rev 83:59–115. https://doi.org/10.1152/physrev.00017.2002

Byrne AM, Bouchier-Hayes DJ, Harmey JH (2005) Angiogenic and cell survival functions of Vascular Endothelial Growth Factor (VEGF) Angiogenesis Review Series. J Cell Mol Med 9:777-94. https://doi.org/10.1111/j.1582-4934.2005.tb00379.x

Cao G, Xuan X, Hu J, et al (2022) How vascular smooth muscle cell phenotype switching contributes to vascular disease. Cell Commun Signal 20:180. https://doi.org/10.1186/s12964-022-00993-2

Cartledge JE, Kane C, Dias P, et al (2015) Functional crosstalk between cardiac fibroblasts and adult cardiomyocytes by soluble mediators. Cardiovasc Res 105:260–270. https://doi.org/10.1093/cvr/cvu264

Chaturvedi RR, Herron T, Simmons R, et al (2010) Passive stiffness of myocardium from congenital heart disease and implications for diastole. Circulation 121:979–988. https://doi.org/10.1161/CIRCULATIONAHA.109.850677

Chen MM, Lam A, Abraham JA, et al (2000) CTGF expression is induced by TGF-β in cardiac fibroblasts and cardiac myocytes: A potential role in heart fibrosis. J Mol Cell Cardiol 32:1805–1819. https://doi.org/10.1006/jmcc.2000.1215

Chuva de Sousa Lopes SM, Hassink RJ, et al (2006) Patterning the heart, a template for human cardiomyocyte development. Dev Dyn 235:1994-2002. https://doi.org/10.1002/dvdy.20830.

Conrad CH, Brooks WW, Hayes JA, et al (1995) Myocardial fibrosis and stiffness with hypertrophy and heart failure in the spontaneously hypertensive rat. Circulation 91:161–170. https://doi.org/10.1161/01.cir.91.1.161

Cui Y, Zheng Y, Liu X, et al (2019) Single-Cell Transcriptome Analysis Maps the Developmental Track of the Human Heart. Cell Rep 26:1934-1950.e5. https://doi.org/10.1016/j.celrep.2019.01.079

Dämmrich J, Pfeifer U (1983) Cardiac hypertrophy in rats after supravalvular aortic constriction. Virchows Archiv B Cell Pathol Incl Mol Pathol 43:287–307. https://doi.org/10.1007/bf02932962

Dash BC, Levi K, Schwan J, et al (2016) Tissue-Engineered Vascular Rings from Human iPSC-Derived Smooth Muscle Cells. Stem Cell Reports 7:19–28. https://doi.org/10.1016/j.stemcr.2016.05.004

deAlmeida AC, van Oort RJ, Wehrens XHT (2010) Transverse aortic constriction in mice. J Vis Exp 38:1729. https://doi.org/10.3791/1729

Dewing JM, Saunders V, O'Kelly I, et al (2022) Defining cardiac cell populations and relative cellular composition of the early fetal human heart. PLoS ONE, 17:e0259477. https://doi.org/10.1371/journal.pone.0259477

Drawnel FM, Archer CR, Roderick HL, et al (2012) The role of the paracrine/autocrine mediator endothelin-1 in regulation of cardiac contractility and growth. Br J Pharmacol 168:296-317. https://doi.org/10.1111/bph.2013.168.issue-1

Dun W, Boyden PA (2008) The Purkinje cell; 2008 style. J Mol Cell Cardiol 45:617-24. https://doi.org/10.1016/j.yjmcc.2008.08.001

Dunn ME, Manfredi TG, Agostinucci K, et al (2017) Serum Natriuretic Peptides as Differential Biomarkers Allowing for the Distinction between Physiologic and Pathologic Left Ventricular Hypertrophy. Toxicologic Pathology 45:344–352. https://doi.org/10.1177/0192623316634231

Epelman S, Lavine KJ, Beaudin AE, et al (2014) Embryonic and adult-derived resident cardiac macrophages are maintained through distinct mechanisms at steady state and during inflammation. Immunity 40:91–104. https://doi.org/10.1016/j.immuni.2013.11.019

Eppenberger-Eberhardt M, Aigner S, Donath MY, et al (1997) IGF-I and bFGF differentially influence atrial natriuretic factor and alpha-smooth muscle actin expression in cultured atrial compared to ventricular adult rat cardiomyocytes. J Mol Cell Cardiol 29:2027-39. https://doi.org/10.1006/jmcc.1997.0408

Eschenhagen T, Fink C, Remmers U, et al (1997) Three-dimensional reconstitution of embryonic cardiomyocytes in a collagen matrix: a new heart muscle model system. FASEB J. 11:683-94. https://10.1096/fasebj.11.8.9240969

Gabbiani G, Hirschel BJ, Ryan GB, et al (1972) Granulation tissue as a contractile organ. A study of structure and function. J Exp Med 135:719–734. https://doi.org/doi: 10.1084/jem.135.4.719

Gabbiani G (2003) The myofibroblast in wound healing and fibrocontractive diseases. J Pathol 200:500-3. https://doi.org/10.1002/path.1427

Gaborit N, Le Bouter S, Szuts V, et al (2007) Regional and tissue specific transcript signatures of ion channel genes in the non-diseased human heart. J Physiol, 582:675–693. https://doi.org/10.1113/jphysiol.2006.126714

Giacomelli E, Bellin M, Sala L, et al (2017) Three-dimensional cardiac microtissues composed of cardiomyocytes and endothelial cells co-differentiated from human pluripotent stem cells. Development 144:1008–1017. https://doi.org/10.1242/dev.143438

Grassam-Rowe A, Ou X, Lei M (2020) Novel cardiac cell subpopulations: Pnmt-derived cardiomyocytes. Open Biol 10:200095. https://doi.org/10.1098/rsob.200095

Gu M (2018) Efficient Differentiation of Human Pluripotent Stem Cells to Endothelial Cells. Curr Protoc Hum Genet 98:e64. https://doi.org/10.1002/cphg.64

Guo NN, Liu LP, Zheng YW, et al (2020) Inducing human induced pluripotent stem cell differentiation through embryoid bodies: A practical and stable approach. World J Stem Cells 12:25-34. https://doi.org/10.4252/wjsc.v12.i1.25

Hafen BB, Burns B (2023) Physiology, Smooth Muscle. In: StatPearls. Treasure Island (FL): StatPearls Publishing. Available at: https://www.ncbi.nlm.nih.gov/books/NBK526125/ (Accessed: 23 June 2024)

Hall C, Gehmlich, K, Denning C, et al (2021) Complex relationship between cardiac fibroblasts and cardiomyocytes in health and disease. J Am Heart Assoc 10:e019338. https://doi.org/10.1161/JAHA.120.019338

Hansen A, Eder A, Bönstrup M, et al (2010) Development of a drug screening platform based on engineered heart tissue. Circ Res 107:35–44. https://doi.org/10.1161/CIRCRESAHA.109.211458

Hao H, Ropraz P, Verin V, et al (2002) Heterogeneity of smooth muscle cell populations cultured from pig coronary artery. Arterioscler Thromb Vasc Biol 22:1093–1099. https://doi.org/10.1161/01.ATV.0000022407.91111.E4

Hautmann MB, Madsen CS, Owens GK (1997) A transforming growth factor β (TGFβ) control element drives TGFβ- induced stimulation of smooth muscle α-actin gene expression in concert with two CArG elements. J Biol Chem 272:10948–10956. https://doi.org/10.1074/jbc.272.16.10948

He K, Shi X, Zhang X, et al (2011) Long-distance intercellular connectivity between cardiomyocytes and cardiofibroblasts mediated by membrane nanotubes. Cardiovasc Res 92:39–47. https://doi.org/10.1093/cvr/cvr189

Hecker L, Jagirdar R, Jin T, et al (2011) Reversible differentiation of myofibroblasts by MyoD. Exp Cell Res 317:1914–1921. https://doi.org/10.1016/j.yexcr.2011.03.016

Heijman J, Christ T (2023) Mind the gap: leak currents and induced pluripotent stem cell-derived cardiomyocytes in translational cardiac electrophysiology. Europace. 25:euad236. https://doi.org/10.1093/europace/euad236

Hertig CM, Kubalak SW, Wang Y, et al (1999) Synergistic roles of neuregulin-1 and insulin-like growth factor-I in activation of the phosphatidylinositol 3-kinase pathway and cardiac chamber morphogenesis. J Biol Chem 274:37362–37369. https://doi.org/10.1074/jbc.274.52.37362

Heymans S, Corsten MF, Verhesen W, et al (2013) Macrophage MicroRNA-155 promotes cardiac hypertrophy and failure. Circulation 128:1420–1432. https://doi.org/10.1161/CIRCULATIONAHA.112.001357

Hirt MN, Boeddinghaus J, Mitchell A, et al (2014) Functional improvement and maturation of rat and human engineered heart tissue by chronic electrical stimulation. J Mol Cell Cardiol 74:151–161. https://doi.org/10.1016/j.yjmcc.2014.05.009

Hirt MN, Sörensen NA, Bartholdt LM, et al (2012). Increased afterload induces pathological cardiac hypertrophy: A new in vitro model. Basic Res Cardiol 107:307. https://doi.org/10.1007/s00395-012-0307-z

House SL, House BE, Glascock B, et al (2010) Fibroblast growth factor 2 mediates isoproterenol-induced cardiac hypertrophy through activation of the extracellular regulated kinase. Mol Cell Pharmacol 2:143–154. https://doi.org/10.4255/mcpharmacol.10.20

Hsieh PCH, Davis ME, Lisowski L K, et al (2006) Endothelial-cardiomyocyte interactions in cardiac development and repair. Annu Rev Physiol 68:51–66. https://doi.org/10.1146/annurev.physiol.68.040104.124629

Hu S, Lavinghousez P, Li Z, et al (2011) Differentiation of Endothelial Cells from Human Embryonic Stem Cells and Induced Pluripotent Stem Cells. Springer Protocols Handbooks. 311–320. https://doi.org/10.1007/978-1-61779-267-0_22

Hulsmans M, Clauss S, Xiao L, et al (2017) Macrophages Facilitate Electrical Conduction in the Heart. Cell 169:510-522.e20. https://doi.org/10.1016/j.cell.2017.03.050

Iemitsu M, Miyauchi T, Maeda S, et al (2001) Physiological and pathological cardiac hypertrophy induce different molecular phenotypes in the rat. Am J Physiol Regul Integr Comp Physiol 281:R2029-36. https://doi.org/10.1152/ajpregu.2001.281.6.R2029

Ismaili D, Schulz C, Horváth A, et al (2023) Human induced pluripotent stem cell-derived cardiomyocytes as an electrophysiological model: Opportunities and challenges-The Hamburg perspective. Front Physiol 14:1132165. https://doi.org/10.3389/fphys.2023.1132165

Jaba IM, Zhuang ZW, Li N, et al (2013) No triggers rgs4 degradation to coordinate angiogenesis and cardiomyocyte growth. J Clin Invest 123:1718–1731. https://doi.org/10.1172/JCI65112

Jacquemet V, Henriquez CS (2008) Loading effect of fibroblast-myocyte coupling on resting potential, impulse propagation, and repolarization: insights from a microstructure model. Am J Physiol Heart Circ Physiol 294:H2040-52. https://10.1152/ajpheart.01298.2007

Jalili T, Takeishi Y, Walsh RA (1999) Signal transduction during cardiac hypertrophy: the role of Gαq, PLC βI, and PKC, Cardiovasc Res 44:5–9. https://doi.org/10.1016/S0008-6363(99)00211-4

James TN, Sherf L, Fine G, Morales AR (1966) Comparative ultrastructure of the sinus node in man and dog. Circulation 34:139-63. https://doi.org/doi: 10.1161/01.cir.34.1.139.

Jaminon A, Reesink K, Kroon A, et al (2019) The role of vascular smooth muscle cells in arterial remodeling: Focus on calcification-related processes. Int J Mol Sci 20:5694. https://doi.org/10.3390/ijms20225694

Jiao X, Yu H, Du Z, et al (2023) Vascular smooth muscle cells specific deletion of angiopoietin-like protein 8 prevents angiotensin II-promoted hypertension and cardiovascular hypertrophy. Cardiovasc Res 119:1856–1868. https://doi.org/10.1093/cvr/cvad089

Johansson M, Ulfenborg B, Andersson CX, et al (2020) Cardiac hypertrophy in a dish: A human stem cell based model. Biol Open 9:bio052381. https://doi.org/10.1242/bio.052381

Johansson M, Ulfenborg B, Andersson CX, et al (2022) Multi-Omics Characterization of a Human Stem Cell-Based Model of Cardiac Hypertrophy. Life (Basel) 12:293. https://doi.org/10.3390/life12020293

Kadota S, Pabon L, Reinecke H, et al (2017) In Vivo Maturation of Human Induced Pluripotent Stem Cell-Derived Cardiomyocytes in Neonatal and Adult Rat Hearts. Stem Cell Reports 8:278–289. https://doi.org/10.1016/j.stemcr.2016.10.009

Kane C, Terracciano CMN (2017) Concise Review: Criteria for Chamber-Specific Categorization of Human Cardiac Myocytes Derived from Pluripotent Stem Cells. Stem Cells 35:1881-1897.https://doi.org/10.1002/stem.2649

Karbassi E, Fenix A, Marchiano S, et al (2020) Cardiomyocyte maturation: advances in knowledge and implications for regenerative medicine. Nat Rev Cardiol 17:341-359. https://doi.org/10.1038/s41569-019-0331-x

Kardami E, Jiang ZS, Jimenez SK, et al (2004) Fibroblast growth factor 2 isoforms and cardiac hypertrophy. Cardiovasc Res 63:458-66. https://doi.org/10.1016/j.cardiores.2004.04.024

Kawano H, Do YS, Kawano Y, et al (2000) Angiotensin II Has Multiple Profibrotic Effects in Human Cardiac Fibroblasts. Circulation 101:1130-7. https://doi.org/10.1161/01.cir.101.10.1130

Kaye D, Pimental D, Prasad S, et al (1996) Role of transiently altered sarcolemmal membrane permeability and basic fibroblast growth factor release in the hypertrophic response of adult rat ventricular myocytes to increased mechanical activity in vitro. J Clin Invest 97:281–291. https://doi.org/10.1172/JCI118414

King J, Lowery DR (2023) Physiology, Cardiac Output. In: StatPearls. Treasure Island (FL): StatPearls Publishing. Available at https://www.ncbi.nlm.nih.gov/books/NBK470455/ (Accessed: 23 June 2024)

Knight WE, Cao Y, Lin YH, et al (2021) Maturation of Pluripotent Stem Cell-Derived Cardiomyocytes Enables Modeling of Human Hypertrophic Cardiomyopathy. Stem Cell Reports 16:519–533. https://doi.org/10.1016/j.stemcr.2021.01.018

Krüger-Genge A, Blocki A, Franke RP, et al (2019) Vascular endothelial cell biology: An update. Int J Mol Sci 20:4411. https://doi.org/10.3390/ijms20184411

Kuwahara F, Kai H, Tokuda K, et al (2003) Roles of intercellular adhesion molecule-1 in hypertensive cardiac remodeling. Hypertension 41:819–823. https://doi.org/10.1161/01.HYP.0000056108.73219.0A

Kuwahara F, Kai H, Tokuda K, et al (2004) Hypertensive Myocardial Fibrosis and Diastolic Dysfunction: Another Model of Inflammation? Hypertension 43:739–745. https://doi.org/10.1161/01.HYP.0000118584.33350.7d

Laframboise WA, Scalise D, Stoodley P, et al (2007) Cardiac fibroblasts influence cardiomyocyte phenotype in vitro. Am J Physiol Cell Physiol 292:1799–1808. https://doi.org/10.1152/ajpcell.00166.2006.-Cardiac

Laghmouchi A, Hoogstraten C, Falkenburg JHF, et al (2020) Long-term in vitro persistence of magnetic properties after magnetic bead-based cell separation of T cells. Scand J Immunol 92:e12924. https://doi.org/10.1111/sji.12924

Leid J, Carrelha J, Boukarabila H, et al (2016) Primitive Embryonic Macrophages are Required for Coronary Development and Maturation. Circ Res 118:1498–1511. https://doi.org/10.1161/CIRCRESAHA.115.308270

Lemoine MD, Mannhardt I, Breckwoldt K, et al (2017) Human iPSC-derived cardiomyocytes cultured in 3D engineered heart tissue show physiological upstroke velocity and sodium current density. Sci Rep.7(1):5464. https://doi.org/10.1038/s41598-017-05600-w

Lemoine MD, Krause T, Koivumäki JT, et al (2018) Human Induced Pluripotent Stem Cell-Derived Engineered Heart Tissue as a Sensitive Test System for QT Prolongation and Arrhythmic Triggers. Circ Arrhythm Electrophysiol. 11(7):e006035. https://doi.org/10.1161/CIRCEP.117.006035

Leopold B, Strutz J, Weiß E, et al (2019) Outgrowth, proliferation, viability, angiogenesis and phenotype of primary human endothelial cells in different purchasable endothelial culture media: feed wisely. Histochem Cell Biol 152:377–390. https://doi.org/10.1007/s00418-019-01815-2

Li N, Edel M, Liu K, et al (2023) Human induced pluripotent stem cell-derived cardiac myocytes and sympathetic neurons in disease modelling. Philos Trans R Soc B Biol Sci 378(1879):20220173. https://doi.org/10.1098/rstb.2022.0173

Li X, Van Putten V, Zarinetchi F, et al (1997). Suppression of smooth-muscle α-actin expression by platelet-derived growth factor in vascular smooth-muscle cells involves Ras and cytosolic phospholipase A2. Biochem. J 327:709-16. https://doi.org/10.1042/bj3270709.

Li Y, Li Q, Fan GC (2021) Macrophage efferocytosis in cardiac pathophysiology and repair. Shock 55:177-188. https://doi.org/10.1097/SHK.0000000000001625

Liao X, Shen Y, Zhang R, et al (2018) Distinct roles of resident and nonresident macrophages in nonischemic cardiomyopathy. Proc Natl Acad Sci U S A 115:E4661–E4669. https://doi.org/10.1073/pnas.1720065115

Lincoln TM, Cornwell TL, Komalavilas P, et al (1996) Cyclic GMP-Dependent Protein Kinase in Nitric Oxide Signaling. Methods Enzymol 269:149-66. https://doi.org/10.1016/s0076-6879(96)69017-x

Litviňuková M, Talavera-López C, Maatz H, et al (2020) Cells of the adult human heart. Nature 588:466–472. https://doi.org/10.1038/s41586-020-2797-4

Liu Y, Leri A, Li B, et al (1998) Angiotensin II Stimulation In Vitro Induces Hypertrophy of Normal and Postinfarcted Ventricular Myocytes. Circ Res 82:1145-59. https://doi.org/10.1161/01.res.82.11.1145

Lopez-Yrigoyen M, May A, Ventura T, et al (2020) Production and Characterization of Human Macrophages from Pluripotent Stem Cells. J Vis Exp 158. https://doi.org/.3791/61038.

Madsen A, Krause J, Höppner G, et al (2021) Hypertrophic signaling compensates for contractile and metabolic consequences of DNA methyltransferase 3A loss in human cardiomyocytes. J Mol Cell Cardiol 154:115–123. https://doi.org/10.1016/j.yjmcc.2021.02.002

Magga J, Marttila M, Mäntymaa P, et al (1994) Brain natriuretic peptide in plasma, atria, and ventricles of vasopressin- and phenylephrine-infused conscious rats. Endocrinology. 134:2505-15. https://doi.org/10.1210/endo.134.6.8194476

Maillet M, Van Berlo JH, Molkentin JD (2013) Molecular basis of physiological heart growth: Fundamental concepts and new players. Nat Rev Mol Cell Biol 14:38–48. https://doi.org/10.1038/nrm3495

Mannhardt I, Breckwoldt K, Letuffe-Brenière D, et al (2016) Human Engineered Heart Tissue: Analysis of Contractile Force. Stem Cell Reports 7:29–42. https://doi.org/10.1016/j.stemcr.2016.04.011

Masumoto H, Nakane T, Tinney J. et al. (2016) The myocardial regenerative potential of three-dimensional engineered cardiac tissues composed of multiple human iPS cell-derived cardiovascular cell lineages. Sci Rep 6:29933. https://doi.org/10.1038/srep29933

McKinsey TA, Zhang CL, Olson EN (2000) Activation of the myocyte enhancer factor-2 transcription factor by calcium/calmodulin-dependent protein kinase-stimulated binding of 14-3-3 to histone deacetylase 5. Proc Natl Acad Sci U S A 97:14400-5. https://doi.org/10.1073/pnas.260501497

Milani-Nejad N, Janssen PML (2014) Small and large animal models in cardiac contraction research: Advantages and disadvantages. Pharmacol Ther 141:235-49. https://doi.org/10.1016/j.pharmthera.2013.10.007

Miller CL, Oikawa M, Cai Y, et al (2009) Role of Ca2+/calmodulin-stimulated cyclic nucleotide phosphodiesterase 1 in mediating cardiomyocyte hypertrophy. Circ Res 105:956–964. https://doi.org/10.1161/CIRCRESAHA.109.198515

Minamisawa S, Wang Y, Chen J, et al (2003) Atrial chamber-specific expression of sarcolipin is regulated during development and hypertrophic remodeling. J Biol Chem 278:9570–9575. https://doi.org/10.1074/jbc.M213132200

Mitchell JA, Ali F, Bailey L, et al (2008) Role of nitric oxide and prostacyclin as vasoactive hormones released by the endothelium. Exp Physiol 93:141–147. https://doi.org/10.1113/expphysiol.2007.038588

Mohan P, Brutsaert DL, Paulus WJ, et al (1996) Myocardial contractile response to nitric oxide and cGMP. Circulation 93:1223-9. https://doi.org/10.1161/01.cir.93.6.1223.

Molawi K, Wolf Y, Kandalla PK, et al (2014) Progressive replacement of embryo-derived cardiac macrophages with age. J Exp Med 211:2151–2158. https://doi.org/10.1084/jem.20140639

Molkentin JD (2004) Calcineurin-NFAT signaling regulates the cardiac hypertrophic response in coordination with the MAPKs. Cardiovasc Res 63:467-75. https://doi.org/10.1016/j.cardiores.2004.01.021

Moore L, Fan D, Basu R, et al (2012) Tissue inhibitor of metalloproteinases (TIMPs) in heart failure. Heart Fail Rev 17:693-706. https://doi.org/10.1007/s10741-011-9266-y

Moravec CS, Reynolds EE, Stewart RW, et al (1989) Endothelin is a positive inotropic agent in human and rat heart in vitro. Biochem Biophys Res Commun 159:14-8. https://doi.org/10.1016/0006-291x(89)92397-8

Motley MP, Madsen DH, JHJ, Spencer DE, et al (2016). A CCR2 macrophage endocytic pathway mediates extravascular fibrin clearance in vivo. Blood 127:1085-96. https://doi.org/10.1182/blood-2015-05-644260

Müller P, Gaebel R, Lemcke H, et al (2017) Data on the fate of MACS® MicroBeads intramyocardially co-injected with stem cell products. Data Brief 13:569–574. https://doi.org/10.1016/j.dib.2017.06.035

Nag AC (1980) Study of non-muscle cells of the adult mammalian heart: a fine structural analysis and distribution. Cytobios 28:41-61

Nakamura M, Sadoshima J (2018) Mechanisms of physiological and pathological cardiac hypertrophy. Nat Rev Cardiol 15:387-407. https://doi.org/10.1038/s41569-018-0007-y

Ng SY, Wong CK, Tsang SY (2010) Differential gene expressions in atrial and ventricular myocytes: Insights into the road of applying embryonic stem cell-derived cardiomyocytes for future therapies. Am J Physiol Cell Physiol 299:C1234-49. https://doi.org/10.1152/ajpcell.00402.2009

Nicolás-Ávila JA, Lechuga-Vieco AV, Esteban-Martínez L, et al (2020) A Network of Macrophages Supports Mitochondrial Homeostasis in the Heart. Cell 183:94-109.e23. https://doi.org/10.1016/j.cell.2020.08.031

Ono N, Yamaguchi T, Ishikawa H, (2009) Morphological varieties of the Purkinje fiber network in mammalian hearts, as revealed by light and electron microscopy. Arch Histol Cytol 72:139-49. https://doi.org/10.1679/aohc.72.139

Okamoto K, Aoki K (1963) Development of a strain of spontaneously hypertensive rats. Jpn Circ J 27:282–293. https://doi.org/10.1253/jcj.27.282

Orecchioni M, Ghosheh Y, Pramod AB, et al (2019) Macrophage polarization: Different gene signatures in M1(Lps+) vs. Classically and M2(LPS-) vs. Alternatively activated macrophages. Front Immunol 10:1084. https://doi.org/10.3389/fimmu.2019.01084

Orlova VV, Van Den Hil FE, Petrus-Reurer S, et al (2014) Generation, expansion and functional analysis of endothelial cells and pericytes derived from human pluripotent stem cells. Nat Protoc 9:1514–1531. https://doi.org/10.1038/nprot.2014.102

Owens GK (1995) Regulation of Differentiation of Vascular Smooth Muscle Cells. Physiol Rev 75:487-517. https://doi.org/10.1152/physrev.1995.75.3.487.

Palpant NJ, Pabon L, Friedman CE, et al (2017) Generating high-purity cardiac and endothelial derivatives from patterned mesoderm using human pluripotent stem cells. Nat Protoc 12:15–31. https://doi.org/10.1038/nprot.2016.153

Parker TG, Packer SE, Schneider MO (1990) Peptide growth factors can provoke “fetal” contractile protein gene expression in rat cardiac myocytes. J Clin Invest 85:507–514. https://doi.org/10.1172/JCI114466

Pedrotty DM, Klinger RY, Kirkton RD, et al (2009) Cardiac fibroblast paracrine factors alter impulse conduction and ion channel expression of neonatal rat cardiomyocytes. Cardiovasc Res 83:688–697. https://doi.org/10.1093/cvr/cvp164

Pinto AR, Ilinykh A, Ivey MJ, et al (2016) Revisiting cardiac cellular composition. Circ Res 118:400–409. https://doi.org/10.1161/CIRCRESAHA.115.307778

Pinto AR, Paolicelli R, Salimova E, et al (2012) An abundant tissue macrophage population in the adult murine heart with a distinct alternatively-activated macrophage profile. PLoS ONE 7:e36814. https://doi.org/10.1371/journal.pone.0036814

Pohjolainen L, Ruskoaho H, Talman V (2022) Transcriptomics reveal stretched human pluripotent stem cell-derived cardiomyocytes as an advantageous hypertrophy model. J Mol Cell Cardiol Plus 2:100020. https://doi.org/10.1016/j.jmccpl.2022.100020

Prondzynski M, Krämer E, Laufer SD, et al (2017) Evaluation of MYBPC3 trans-Splicing and Gene Replacement as Therapeutic Options in Human iPSC-Derived Cardiomyocytes. Mol Ther Nucleic Acids 7:475–486. https://doi.org/10.1016/j.omtn.2017.05.008

Rabkin SW, Sunga P, Myrdal S (1987) The effect of epidermal growth factor on chronotropic response in cardiac cells in culture. Biochem Biophys Res Commun 146:889-97. https://doi.org/10.1016/0006-291x(87)90614-0

Ravenscroft SM, Pointon A, Williams AW, et al (2016) Cardiac non-myocyte cells show enhanced pharmacological function suggestive of contractile maturity in stem cell derived cardiomyocyte microtissues. Toxicol Sci 152:99–112. https://doi.org/10.1093/toxsci/kfw069

Rensen SS, Doevendans PA, van Eys GJ (2007) Regulation and characteristics of vascular smooth muscle cell phenotypic diversity. Neth Heart J 15:100–108. https://doi.org/10.1007/BF03085963

Revelo XS, Parthiban P, Chen C, et al (2021) Cardiac resident macrophages prevent fibrosis and stimulate angiogenesis. Circ Res 129:1086–1101. https://doi.org/10.1161/CIRCRESAHA.121.319737

Richards MA, Clarke JD, Saravanan P, et al (2011) Transverse tubules are a common feature in large mammalian atrial myocytes including human. Am J Physiol Heart Circ Physiol 301:H1996-2005. https://doi.org/10.1152/ajpheart.00284.2011

Rockman HA, Ross RS, Harris AN, et al (1991) Medical Sciences Segregation of atrial-specific and inducible expression of an atrial natriuretic factor transgene in an in vivo murine model of cardiac hypertrophy. Proc Natl Acad Sci U S A 88:8277-81. https://doi.org/10.1073/pnas.88.18.8277

Russell WMS, Burch R., Hume CW (1959) The principles of humane experimental technique, London: Methuen 238

Sabbah HN, Sharov VG, Lesch M, et al (1995) Progression of heart failure: A role for interstitial fibrosis. Mol Cell Biochem 147:29-34. https://doi.org/10.1007/BF00944780.

Sadoshima JI, Izumo S (1993) Molecular characterization of angiotensin II--induced hypertrophy of cardiac myocytes and hyperplasia of cardiac fibroblasts. Critical role of the AT1 receptor subtype. Circ Res 73:413-23. https://doi.org/10.1161/01.res.73.3.413

Salvador AM, Nevers T, Velázquez F, et al (2015) Intercellular adhesion molecule 1 regulates left ventricular leukocyte infiltration, cardiac remodeling, and function in pressure overload-induced heart failure. J Am Heart Assoc 5:e003126. https://doi.org/10.1161/JAHA.115.003126

Sansonetti M, Waleczek FJG, Jung M, Thum T, Perbellini F (2020) Resident cardiac macrophages: crucial modulators of cardiac (patho)physiology. Basic Res Cardiol 115:77. https://doi.org /10.1007/s00395-020-00836-6.

Scharhag J, Urhausen A, Herrmann M, et al (2004) No difference in N-terminal pro-brain natriuretic peptide (NT-proBNP) concentrations between endurance athletes with athlete’s heart and healthy untrained controls. Heart 90:1055–1056. https://doi.org/10.1136/hrt.2003.020420

Schmitt-Gräff A, Desmoulière A, Gabbiani G, et al (1994) Heterogeneity of myofibroblast phenotypic features: an example of fibroblastic cell plasticity. Virchows Arch 425:3–24. https://doi.org/10.1007/BF00193944

Schultz JEJ, Witt SA, Nieman ML, et al (1999) Fibroblast growth factor-2 mediates pressure-induced hypertrophic response. J Clin Invest 104:709–719. https://doi.org/10.1172/JCI7315

Segers VFM, Brutsaert DL, De Keulenaer GW (2018) Cardiac remodeling: Endothelial cells have more to say than just NO. Front Physiol 9:382. https://doi.org/10.3389/fphys.2018.00382

Shigeta A, Huang V, Zuo J, et al (2019) Endocardially Derived Macrophages Are Essential for Valvular Remodeling. Dev Cell 48:617-630.e3. https://doi.org/10.1016/j.devcel.2019.01.021

Simões FC, Cahill TJ, Kenyon A, et al (2020) Macrophages directly contribute collagen to scar formation during zebrafish heart regeneration and mouse heart repair. Nat Commun 11:600. https://doi.org/10.1038/s41467-019-14263-2

Simpson P (1985) Stimulation of hypertrophy of cultured neonatal rat heart cells through an alpha 1-adrenergic receptor and induction of beating through an alpha 1- and beta 1-adrenergic receptor interaction. Evidence for independent regulation of growth and beating. Circ Res 56:884-94. https://doi.org/10.1161/01.res.56.6.884

Spach MS, Boineau JP (1997) Microfibrosis produces electrical load variations due to loss of side- to-side cell connections: A major mechanism of structural heart disease arrhythmias. Pacing Clin Electrophysiol 20:397–413. https://doi.org/10.1111/j.1540-8159.1997.tb06199.x

Srivastava RD, Kalitha M, Varma P, Bhatnagar VM (1977) A mechanism of action of phenylephrine on heart. Indian J Physiol Pharmacol 21:167–74

Takahashi K, Ito Y, Morikawa M, et al (2003) Adenoviral-delivered angiopoietin-1 reduces the infarction and attenuates the progression of cardiac dysfunction in the rat model of acute myocardial infarction. Mol Ther 8:584–592. https://doi.org/10.1016/S1525-0016(03)00230-2

Takahashi K, Tanabe K, Ohnuki M, et al (2007) Induction of Pluripotent Stem Cells from Adult Human Fibroblasts by Defined Factors. Cell 131:861–872. https://doi.org/10.1016/j.cell.2007.11.019

Takahashi K, Yamanaka S (2006) Induction of Pluripotent Stem Cells from Mouse Embryonic and Adult Fibroblast Cultures by Defined Factors. Cell 126:663–676. https://doi.org/10.1016/j.cell.2006.07.024

Takahashi T, Allen PD, Izumo S (1992) Expression of A-, B-, and C-type natriuretic peptide genes in failing and developing human ventricles: Correlation with expression of the Ca2+-ATPase gene. Circ Res 71:9–17. https://doi.org/10.1161/01.RES.71.1.9

Tan SH, Ye L (2018) Maturation of pluripotent stem cell-derived cardiomyocytes: A critical step for drug development and cell therapy. J Cardiovasc Transl Res 11:375–392. https://doi.org/10.1007/s12265-018-9801-5

Tanaka A, Yuasa S, Mearini G, et al (2014) Endothelin-1 induces myofibrillar disarray and contractile vector variability in hypertrophic cardiomyopathy-induced pluripotent stem cell-derived cardiomyocytes. J Am Heart Assoc 3(6):e001263. https://doi.org/10.1161/JAHA.114.001263

Tang Y, Nyengaard JR, Andersen JB, et al (2009) The application of stereological methods for estimating structural parameters in the human heart. Anat Rec (Hoboken) 292:1630–1647. https://doi.org/10.1002/ar.20952

Tiburcy M, Hudson JE, Balfanz P, et al (2017) Defined engineered human myocardium with advanced maturation for applications in heart failure modeling and repair. Circulation 135:1832–1847. https://doi.org/10.1161/CIRCULATIONAHA.116.024145

Touyz RM, Alves-Lopes R, Rios FJ, et al (2018) Vascular smooth muscle contraction in hypertension. Cardiovasc Res 114:529-539. https://doi.org/10.1093/cvr/cvy023

Uribe-Querol E, Rosales C (2020) Phagocytosis: Our Current Understanding of a Universal Biological Process. Front Immunol 11:1066. https://doi.org/10.3389/fimmu.2020.01066

van de Schoor FR, Aengevaeren VL, Hopman MTE, et al (2016) Myocardial Fibrosis in Athletes. Mayo Clin Proc 91:1617-1631. https://doi.org/10.1016/j.mayocp.2016.07.012

van Wilgenburg B, Browne C, Vowles J, et al (2013) Efficient, long term production of monocyte-derived macrophages from human pluripotent stem cells under partly-defined and fully-defined conditions. PLoS One 8:e71098. https://doi.org/10.1371/journal.pone.0071098

Vasquez C, Mohandas P, Louie KL, et al (2010) Enhanced fibroblast-myocyte interactions in response to cardiac injury. Circ Res 107:1011–1020. https://doi.org/10.1161/CIRCRESAHA.110.227421

Viola A, Munari F, Sánchez-Rodríguez R, et al (2019) The Metabolic Signature of Macrophage Responses. Front Immunol 10:1462. https://doi.org/10.3389/fimmu.2019.01462

Wagner J, Reinhardt D (1974) Characterization of the adrenoceptors mediating the positive ino- and chronotropic effect of phenylephrine on isolated atria from guinea pigs and rabbits by means of adrenolytic drugs. Naunyn Schmiedebergs Arch Pharmacol. 282:295-306 https://doi.org/10.1007/BF00501237

Wang J, Chen H, Seth A, et al (2003) Mechanical force regulation of myofibroblast differentiation in cardiac fibroblasts. Am J Physiol Heart Circ Physiol 285:1871–1881. https://doi.org/10.1152/ajpheart.00387.2003

Watkins SJ, Borthwick GM, Oakenfull R, et al (2012) Angiotensin II-induced cardiomyocyte hypertrophy in vitro is TAK1-dependent and Smad2/3-independent. Hypertension Research, 35:393–398. https://doi.org/10.1038/hr.2011.196

Webster KA, Discher DJ, Bishopric NH (1993) Induction and nuclear accumulation of Fos and Jun proto-oncogenes in hypoxic cardiac myocytes. J Biol Chem 268:16852–16858. https://doi.org/10.1016/s0021-9258(19)85494-7

Weinberger F, Mannhardt I, Eschenhagen T (2017) Engineering Cardiac Muscle Tissue: A Maturating Field of Research. Circ Res 120:1487-1500. https://10.1161/CIRCRESAHA.117.310738

Werner T (2018) Humanes künstliches Herzgewebe aus mehreren Zelltypen zur Untersuchung kardialer Hypertrophie. Universität Hamburg. http://Ediss.Sub.Uni-Hamburg.de/Volltexte/2018/9072

White MP, Rufaihah AJ, Liu L, et al (2013) Limited gene expression variation in human embryonic stem cell and induced pluripotent stem cell-derived endothelial cells. Stem Cells 31:92–103. https://doi.org/10.1002/stem.1267

Witty AD, Mihic A, Tam RY, et al (2014) Generation of the epicardial lineage from human pluripotent stem cells. Nat Biotechnol 32:1026–1035. https://doi.org/10.1038/nbt.3002

Wollert KC, Fiedler B, Gambaryan S, et al (2002) Gene transfer of cgmp-dependent protein kinase I enhances the antihypertrophic effects of nitric oxide in cardiomyocytes. Hypertension 39:87–92. https://doi.org/10.1161/hy1201.097292

Wu P, Deng G, Sai X, et al (2021) Maturation strategies and limitations of induced pluripotent stem cell-derived cardiomyocytes. Biosci Rep 41:BSR20200833. https://doi.org/10.1042/BSR20200833

Wynn TA, Barron L (2010) Macrophages: Master regulators of inflammation and fibrosis. Semin Liver Dis 30:245-57. https://doi.org/10.1055/s-0030-1255354

Yamazaki T, Komuro I, Kudoh S, et al (1996) Endothelin-1 Is Involved in Mechanical Stress-induced Cardiomyocyte Hypertrophy. J Biol Chem 271:3221-8. https://doi.org/10.1074/jbc.271.6.3221

Yang D, Xi J, Xing Y, et al (2018) A new method for neonatal rat ventricular myocyte purification using superparamagnetic iron oxide particles. Int J Cardiol 270:293–301. https://doi.org/10.1016/j.ijcard.2018.05.133

Yang X, Cheng K, Wang LY, et al (2023) The role of endothelial cell in cardiac hypertrophy: Focusing on angiogenesis and intercellular crosstalk. Biomed Pharmacother 163:114799. https://doi.org/10.1016/j.biopha.2023.114799

Yu J, Vodyanik MA, Smuga-Otto K, et al (2007) Induced pluripotent stem cell lines derived from human somatic cells. Science 318:1917–1920. https://doi.org/10.1126/science.1151526

Zak R (1974). Development and proliferative capacity of cardiac muscle cells. Circ Res 35:17-26

Zeisberg EM, Tarnavski O, Zeisberg M, et al (2007). Endothelial-to-mesenchymal transition contributes to cardiac fibrosis. Nat Med 13:952–961. https://doi.org/10.1038/nm1613

Zhang J, Tao R, Campbell KF, et al (2019) Functional cardiac fibroblasts derived from human pluripotent stem cells via second heart field progenitors. Nat Commun 10:2238. https://doi.org/10.1038/s41467-019-09831-5

Zhou P, Pu WT (2016) Recounting cardiac cellular composition. Circ Res 118:368–370. https://doi.org/10.1161/CIRCRESAHA.116.308139

Zhu H, Kaufman DS (2019) An Improved Method to Produce Clinical-Scale Natural Killer Cells from Human Pluripotent Stem Cells. Methods Mol Biol 2048:107–119. https://doi.org/10.1007/978-1-4939-9728-2_12

Zhuge Y, Zhang J, Qian F, et al (2020) Role of smooth muscle cells in cardiovascular disease. Int J Biol Sci 16:2741–2751. https://doi.org/10.7150/ijbs.49871

9 Appendix

9.1 Supplementary data

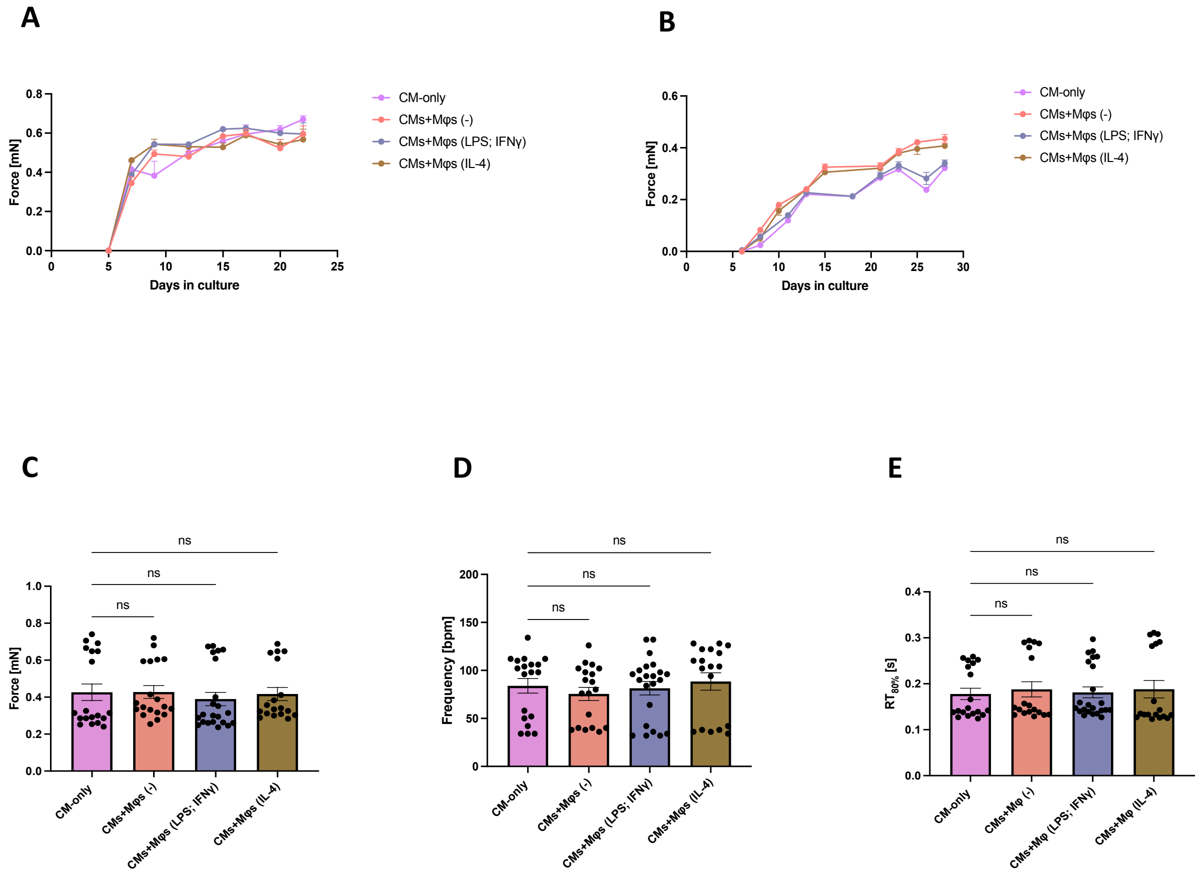

Supplementary Figure 1 Functional analysis of the EHTs containing 90% CMs and 10% Mφs. The Mφs were polarized for 48 hours prior casting the tissues. **(A-B)** Force development of two independent EHT batches. **(C-E)** Analysis of further contractile parameters on day 21 – 22 of culture: **(C)** force, **(D)** frequency, **(E)** $RT_{80\%}$. Data are presented as mean ± SEM; n = 18 – 22 EHTs/group from 2 batches. Statistical analysis: Kruskal-Wallis test, ns $p \geq 0.05$.

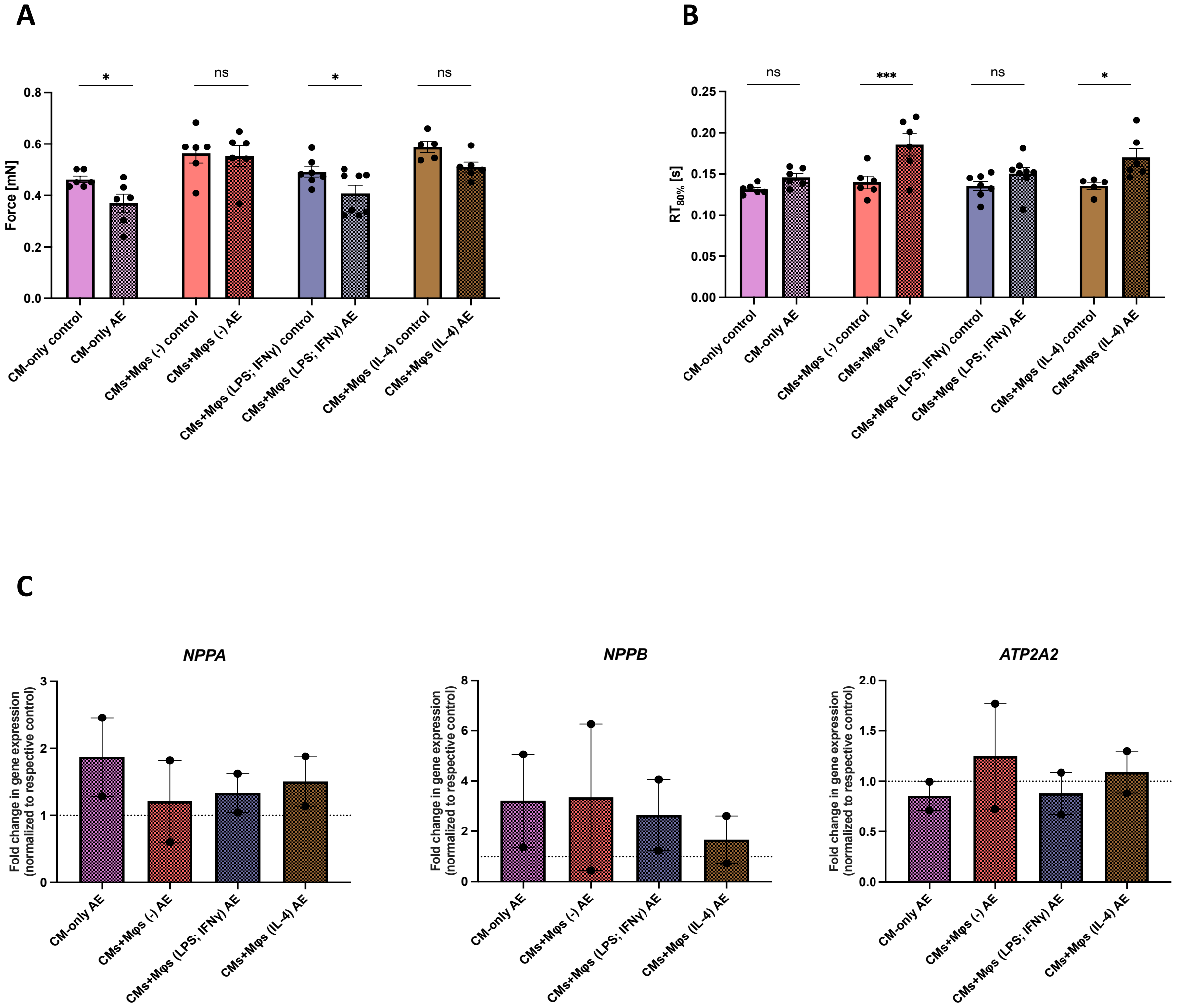

Supplementary Figure 2 Afterload enhancement (AE) in EHTs containing 90% CMs and 10% Mφs. The Mφs were polarized for 48 hours prior casting the tissues. **(A-B)** AE effect on **(A)** force and **(B)** RT$_{80\%}$. Data are presented as mean ± SEM; n = 6 – 8 EHTs/group from 1 batch. Statistical analysis: Two-Way ANOVA with Bonferroni's post-hoc test for multiple comparisons; ns $p \geq 0.05$, *$p < 0.05$, **$p < 0.01$, ***$p < 0.001$. **(C)** Expression of hypertrophic genes. Data are presented as mean ± SEM; n = 2 EHTs/group from 2 batches.

Appendix

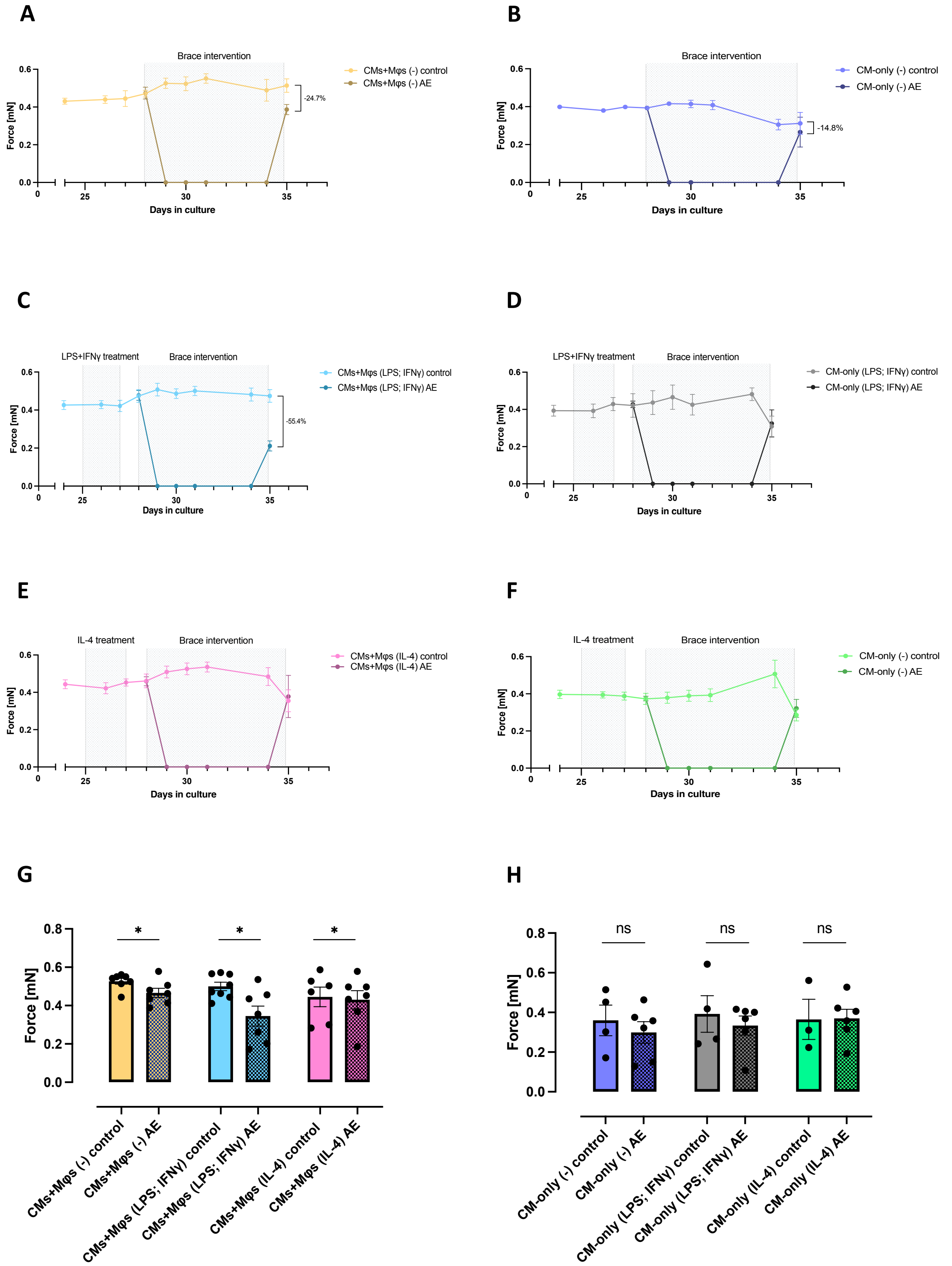
A
Brace intervention
CMs+Mφs (-) control
CMs+Mφs (-) AE
-24.7%
Force [mN]
Days in culture
B
Brace intervention
CM-only (-) control
CM-only (-) AE
-14.8%
Force [mN]
Days in culture
C
LPS+IFNγ treatment
Brace intervention
CMs+Mφs (LPS; IFNγ) control
CMs+Mφs (LPS; IFNγ) AE
-55.4%
Force [mN]
Days in culture
D
LPS+IFNγ treatment
Brace intervention
CM-only (LPS; IFNγ) control
CM-only (LPS; IFNγ) AE
Force [mN]
Days in culture
E
IL-4 treatment
Brace intervention
CMs+Mφs (IL-4) control
CMs+Mφs (IL-4) AE
Force [mN]
Days in culture
F
IL-4 treatment
Brace intervention
CM-only (-) control
CM-only (-) AE
Force [mN]
Days in culture
0.0
0.2
0.4
0.6
0
25
30
35
G
Force [mN]
0.0
0.2
0.4
0.6
0.8
*
*
*
CMs+Mφs (-) control
CMs+Mφs (-) AE
CMs+Mφs (LPS; IFNγ) control
CMs+Mφs (LPS; IFNγ) AE
CMs+Mφs (IL-4) control
CMs+Mφs (IL-4) AE
H
Force [mN]
0.0
0.2
0.4
0.6
0.8
ns
ns
ns
CM-only (-) control
CM-only (-) AE
CM-only (LPS; IFNγ) control
CM-only (LPS; IFNγ) AE
CM-only (IL-4) control
CM-only (IL-4) AE

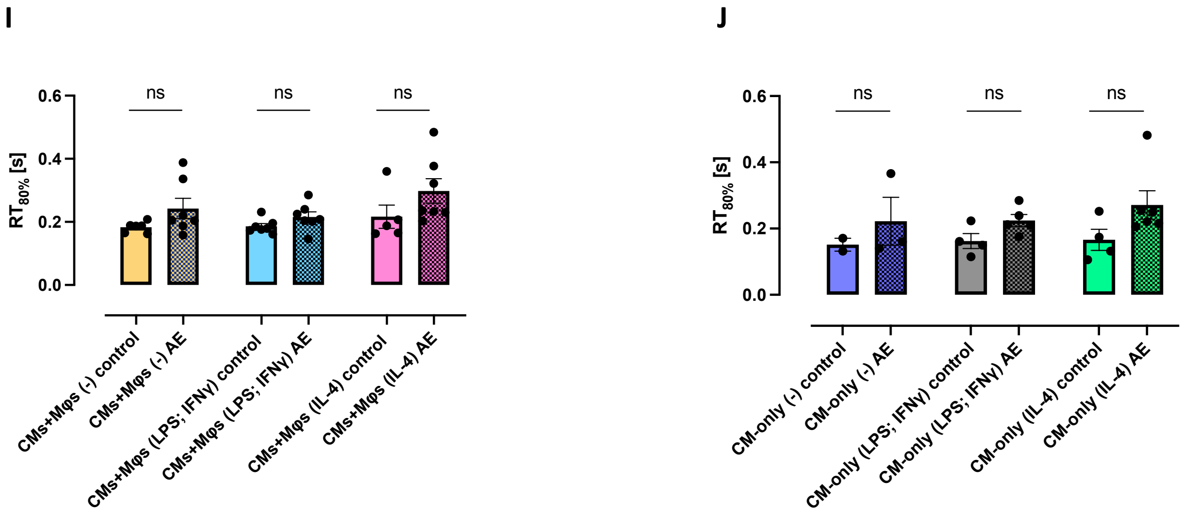

Supplementary Figure 3 The analysis of AE effect on two-cell-type (90% CMs + 10% Mφs) and CM-only tissues. In order to induce different polarization states of the Mφs, after three weeks of culture tissues of each type were assigned to three groups: no treatment (-), 100 ng/mL LPS+20 ng/mL IFNγ (LPS; IFNγ) or 20 ng/mL IL-4 (IL-4). Additionally, corresponding stimulations were performed on CM-only tissues. Afterwards, half of the EHTs from each group underwent 7-day-long mechanical challenge to induce pathological hypertrophy. **(A-F)** The force measurements throughout the experimental procedures. Data are presented as mean ± SEM; n = 8 EHTs/group (days 24 – 27 of culture), n = 3 – 4 EHTs/group (days 28 – 35 of culture) from 1 EHT batch. **(G-J)** The effect of AE on force and RT$_{80\%}$ of (G+I) two-cell-type and (H+J) CM-only tissues. Data are presented as mean ± SEM; n = 2 –8 EHTs/group from 2 EHT batches. Statistical analysis: Two-Way ANOVA with Fisher's LSD test; ns $p \geq 0.05$, *$p < 0.05$.

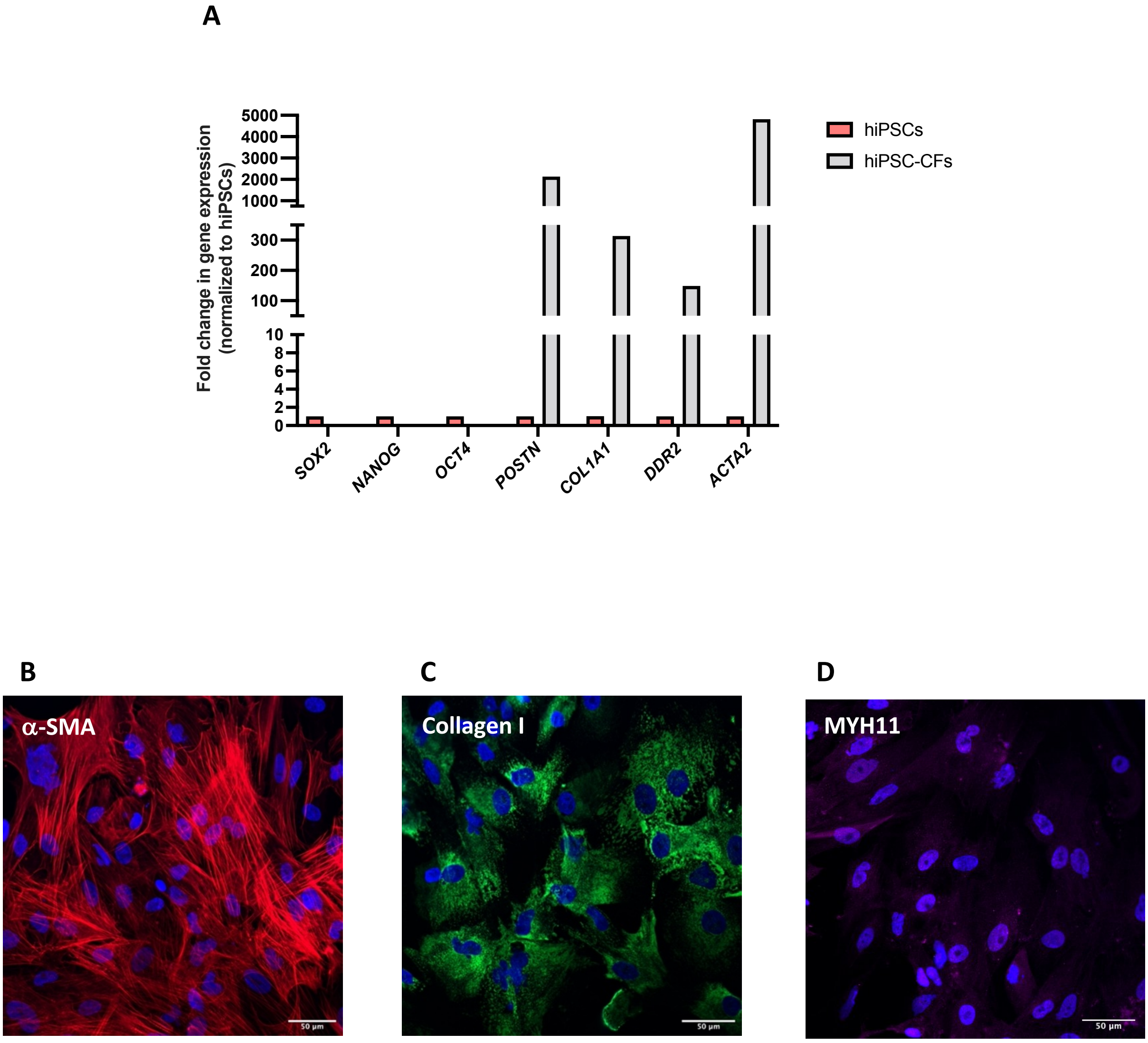

Supplementary Figure 4 Characterization of epicardial hiPSC-CFs generated with a 3D-based differentiation protocol. **(A)** Analysis of stem cell- and fibroblast-related marker expression by RT-qPCR. For the analysis Ct values of target genes were normalized to *GAPDH*. The $2^{-\Delta\Delta Ct}$ values are shown on the graph. Data are presented as mean, n = 3 technical replicates; 1 biological replicate. **(B-D)** Immunofluorescent staining of fibroblast/smooth muscle cell markers. Performed stainings: **(B)** red: α-SMA, blue: DAPI, **(C)** green: collagen I, blue: DAPI, **(D)** magenta: MYH11, blue: DAPI. Scale bar: 50 µm.

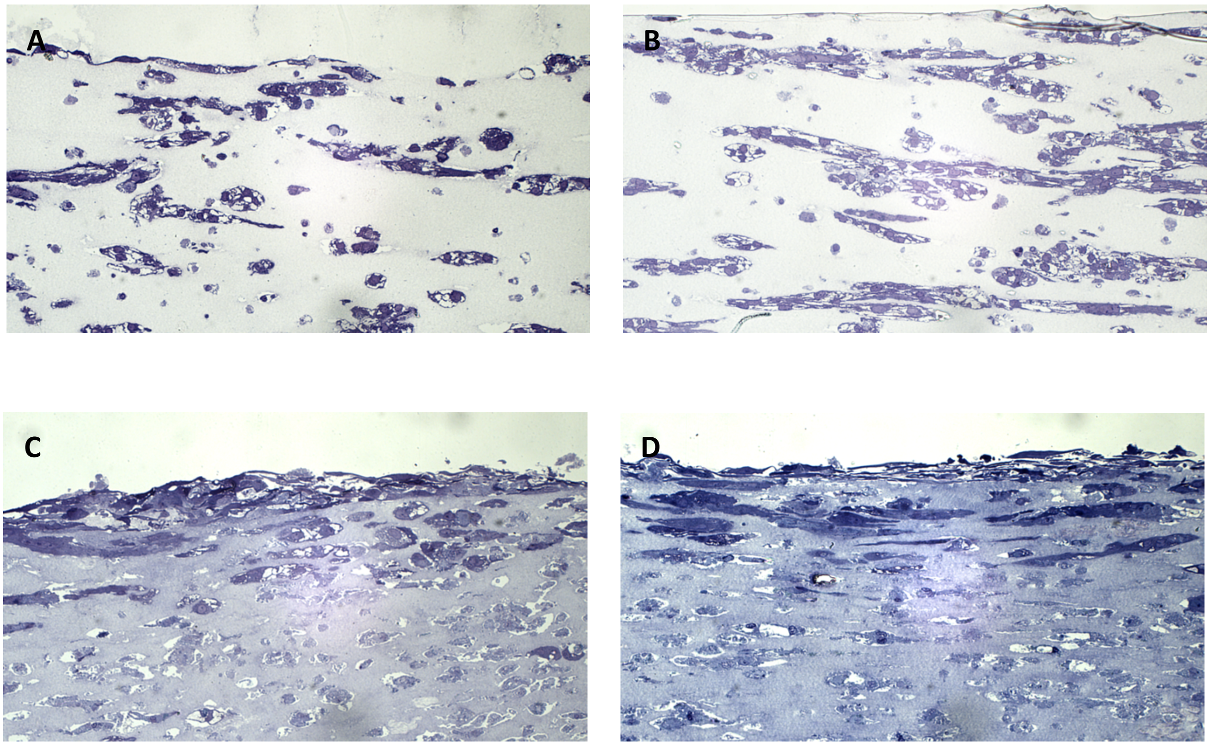

Supplementary Figure 5 Methylene blue staining of 3-week-old **(A-B)** CM-only and **(C-D)** multi-cell-type EHTs.

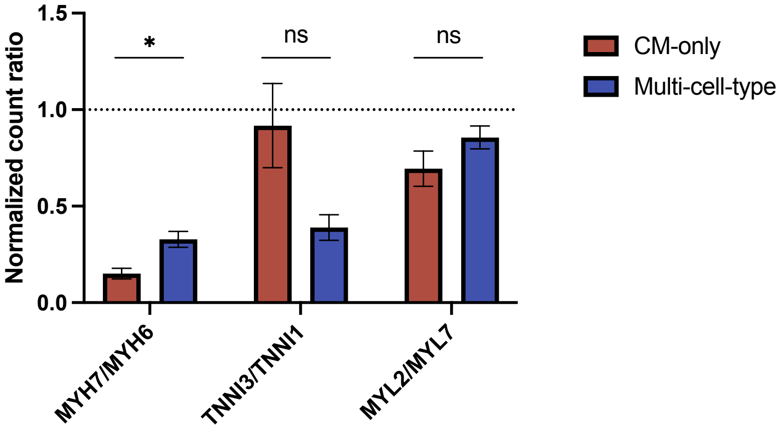

Supplementary Figure 6 Evaluation of CM maturation state in the CM-only and multi-cell-type EHTs. The analysis was performed by calculating ratios between the expression of genes associated with mature CMs to the expression of genes related to CM immaturity. Data are presented as mean ± SEM; n = 3 EHTs/group. Statistical analysis: Unpaired t test; ns $p \geq 0.05$, *$p < 0.05$.

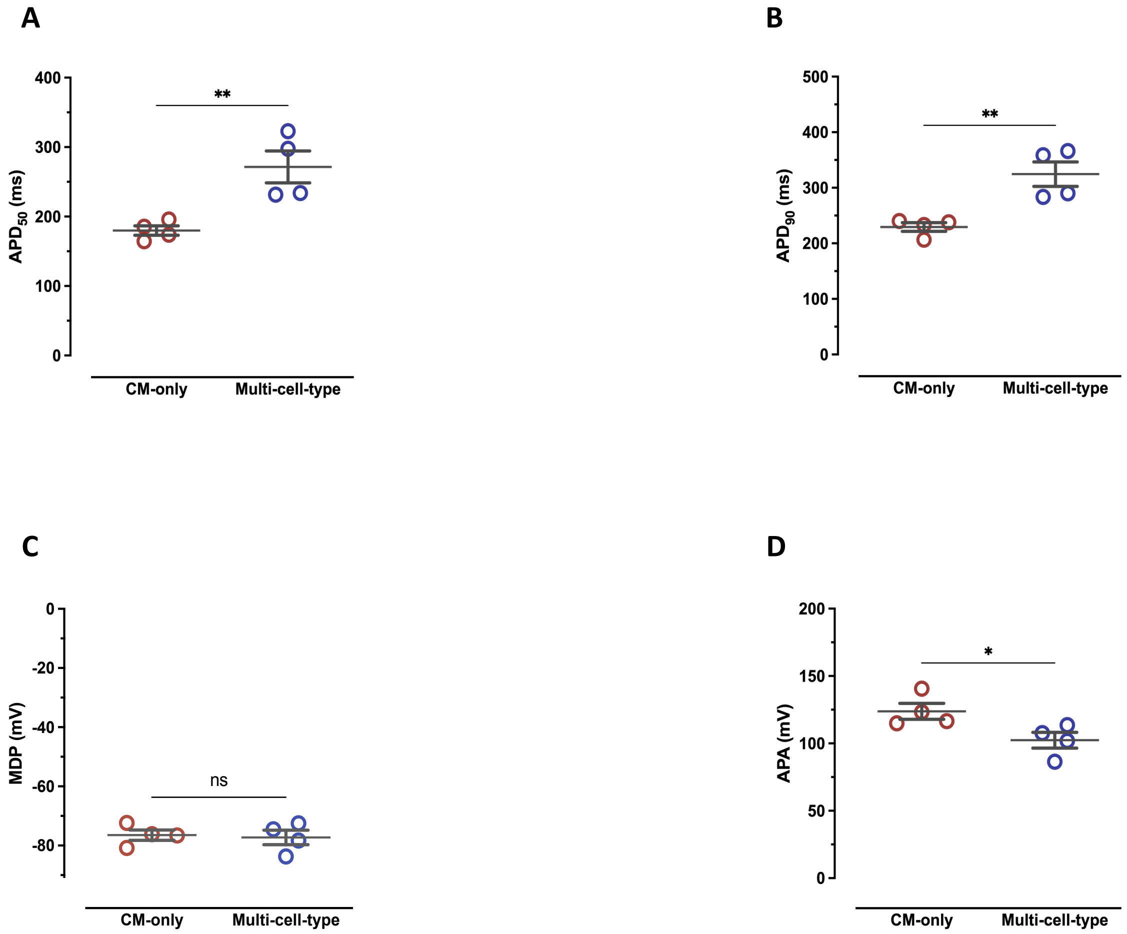

Supplementary Figure 7 Comparison of electrophysiological properties of CM-only and multi-cell-type EHTs recorded by sharp electrode measurements: **(A)** action potential duration at 50% repolarization (APD$_{50}$), **(B)** action potential duration at 90% repolarization (APD$_{90}$), **(C)** maximum diastolic potential (MDP), **(D)** action potential amplitude (APA). Data are presented as mean ± SEM; n = 4 EHTs/group. Statistical analysis: unpaired t test; *$p < 0.05$, **$p \leq 0.01$, ***$p \leq 0.001$.

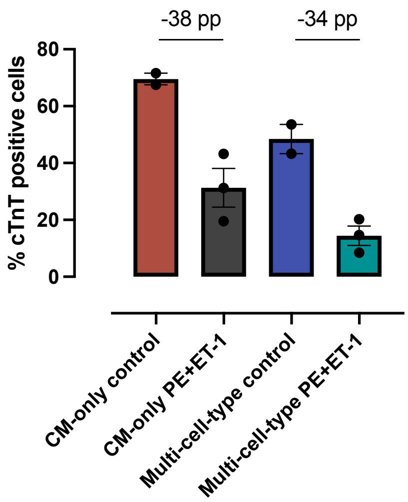

Supplementary Figure 8 Flow cytometry analysis of cTnT expression in CM-only and multi-cell-type EHTs – hypertrophy experiments. On the last day of culture, EHTs were dissociated with papain and single-cell suspension was divided into two samples – one stained with isotype control, the other one with anti-cTnT antibody. The quantification of cTnT positive events was performed with a FACSCanto II Flow Cytometer (BD Biosciences). Data are presented as mean ± SEM; n = 2 – 3 EHTs/group.

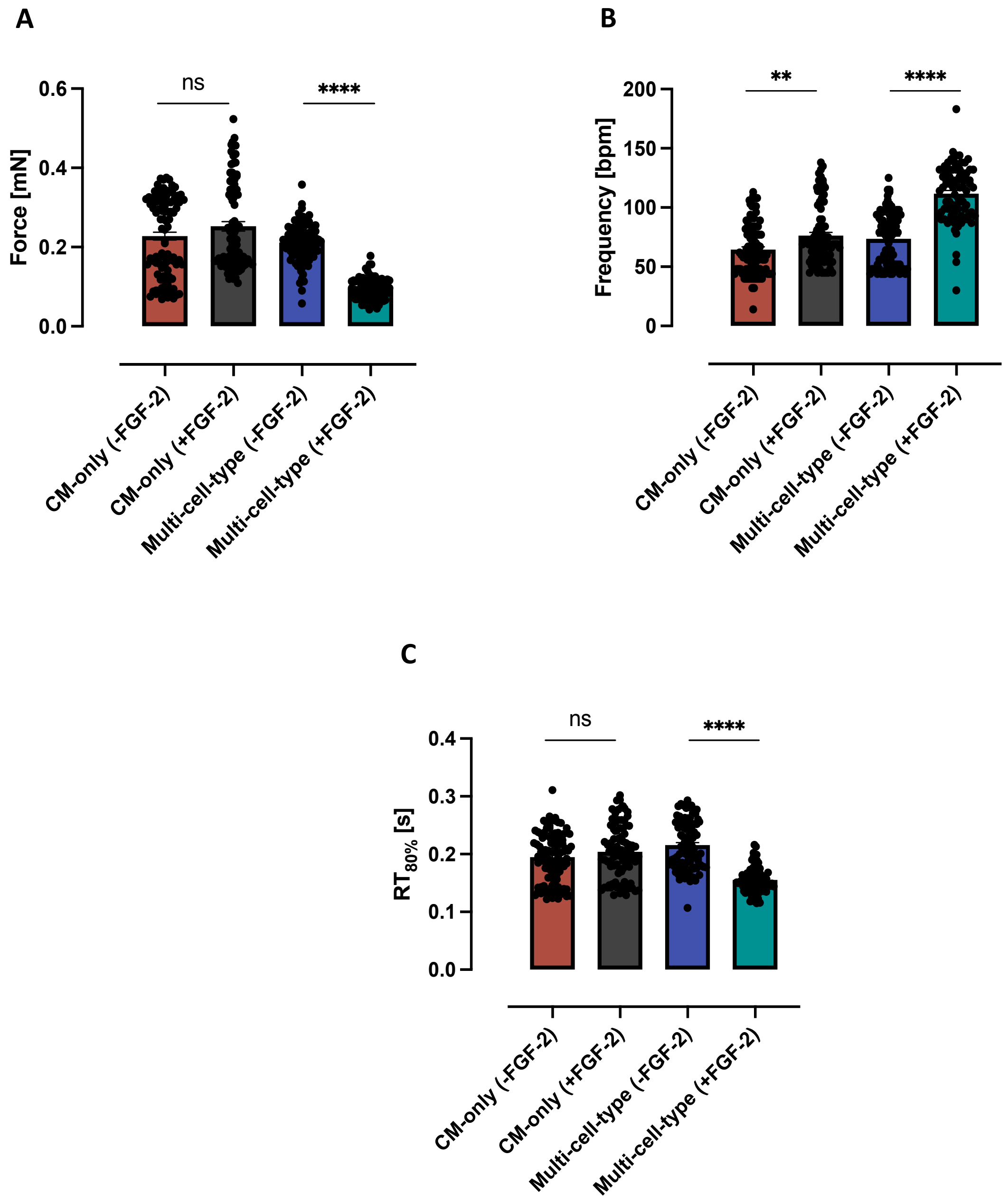

Supplementary Figure 9 Comparison of contractile parameters of CM-only and multi-cell-type EHTs cultured with or without FGF-2: **(A)** force, **(B)** beating frequency, **(C)** RT$_{80\%}$. Values used for analysis were recorded under spontaneous beating conditions on days 21–25 of culture. Data are presented as mean ± SEM; n = 80 – 94 EHTs/group from 3 – 4 EHT batches. Statistical analysis: Two-Way ANOVA with Bonferroni's post-hoc test for multiple comparisons ns $p \geq 0.05$, $**p < 0.01$, $****p < 0.0001$.

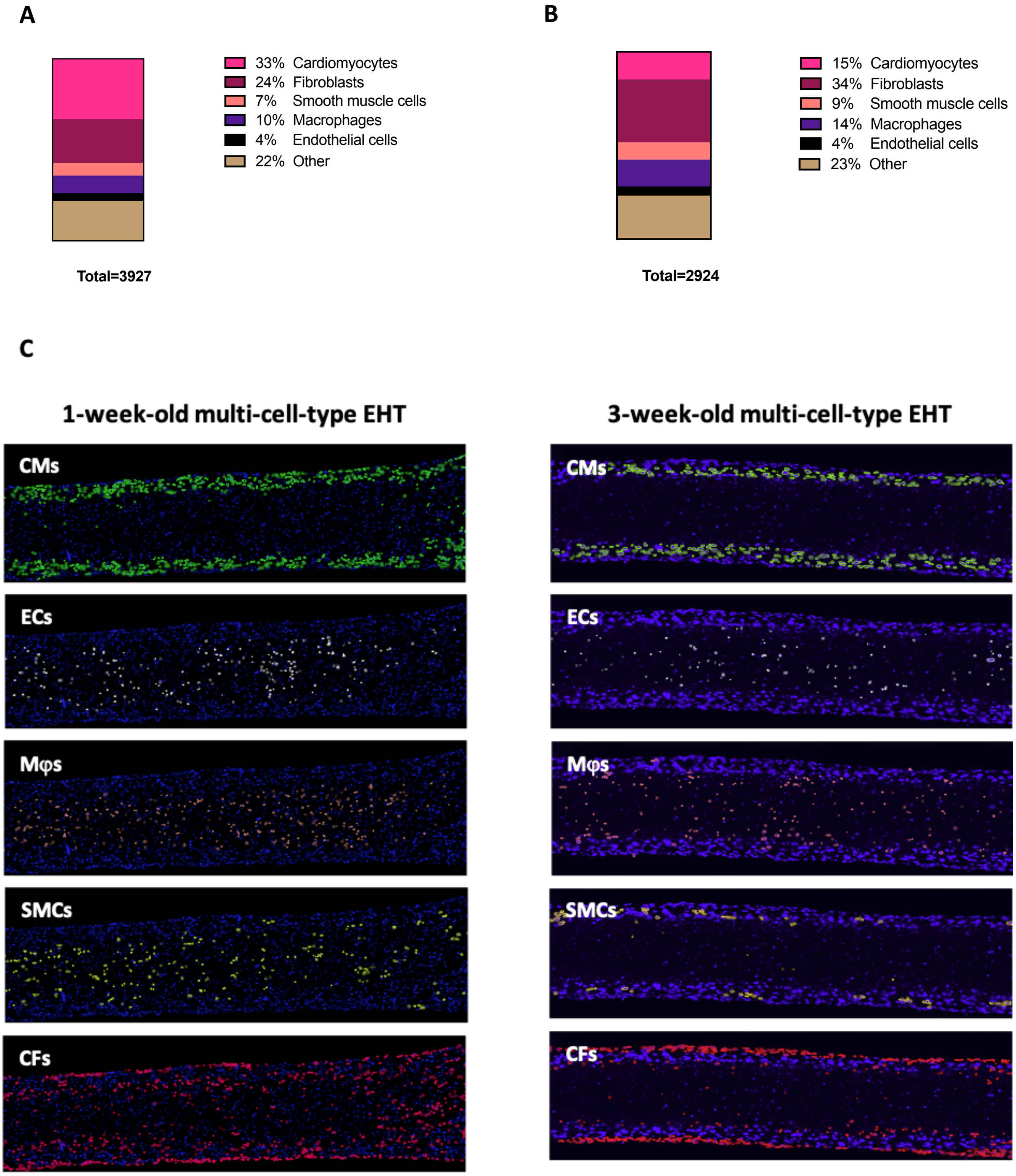

Supplementary Figure 10 Quantification of cell populations in 1-week- **(A)** and 3-week- **(B)** old multi-cell-type EHTs cultured with FGF-2. **(C)** Localization of different cell populations in the 1-week-old (left panel) and 3-week-old (right panel) multi-cell-type EHTs. The analysis was conducted by performing sequential immunofluorescent stainings of cell-type-specific markers with the MICS technology. Obtained imaging data was evaluated (visualization, segmentation, quantification) in the MACS iQ View software. Markers used for identification of different cell types include: cardiomyocytes: α-actinin, fibroblasts: vimentin, smooth muscle cells: MYH11 macrophages: CD68, endothelial cells: CD31. Recognized nuclei not associated with any of the above-listed markers were assigned as “other”. The data are presented as mean from 3 EHTs/group.

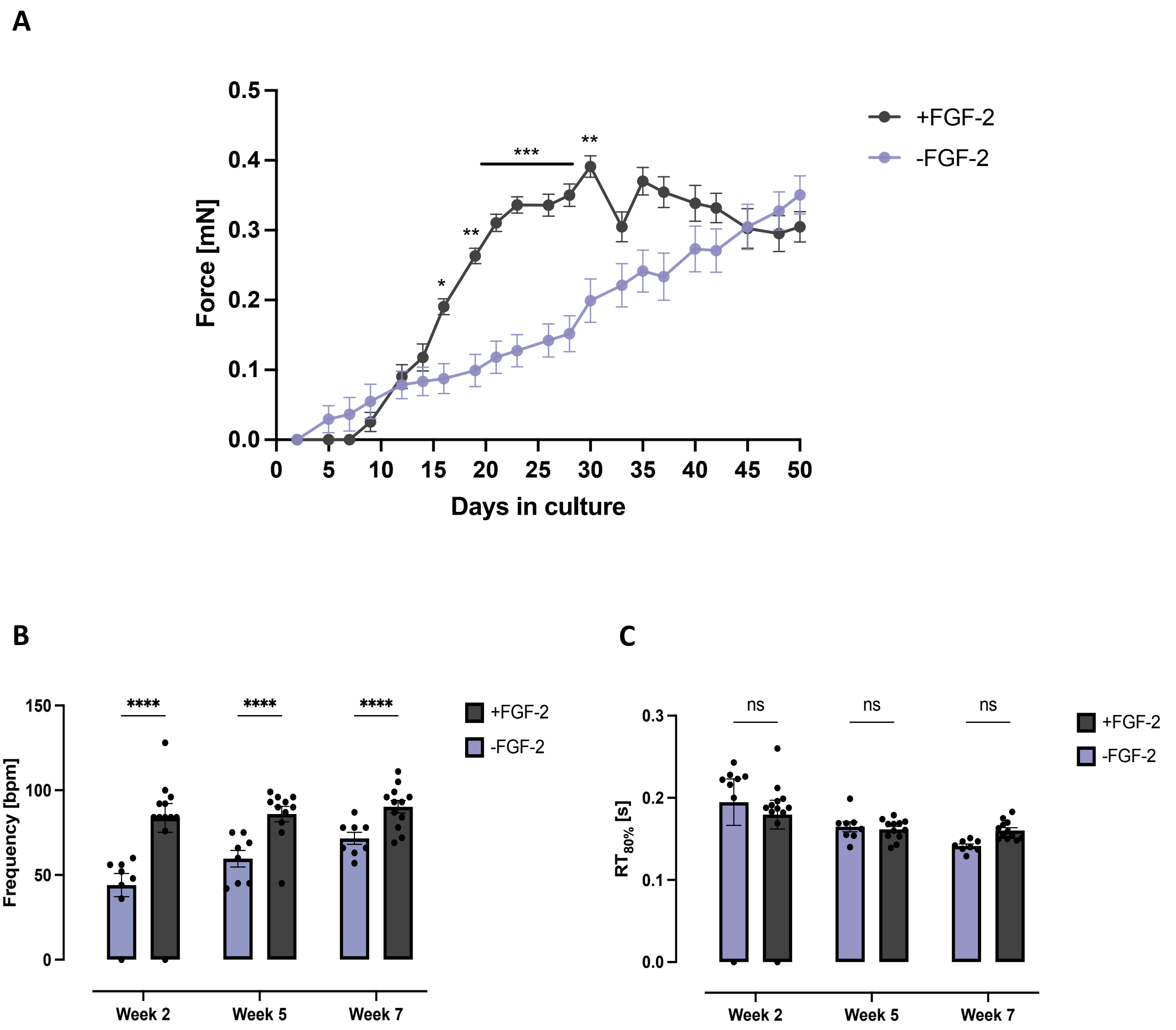

Supplementary Figure 11 Functional characterization of the FGF-2 effects on the CM-only EHTs. **(A)** Force development over 50 days of culture. **(B)** Analysis of spontaneous beating frequencies throughout the culture. **(C)** Analysis of relaxation time on the 2nd, 5th and 7th week of culture under spontaneous beating conditions. Data are displayed as mean ± SEM; n = 8 EHTs cultured without FGF-2 (-FGF); n = 12 EHTs cultured with FGF-2 (+FGF). Statistical analysis: Two-Way ANOVA with Bonferroni's post-hoc test for multiple comparisons; ns $p \geq 0.05$, *$p < 0.05$, **$p \leq 0.01$, ****$p \leq 0.0001$.

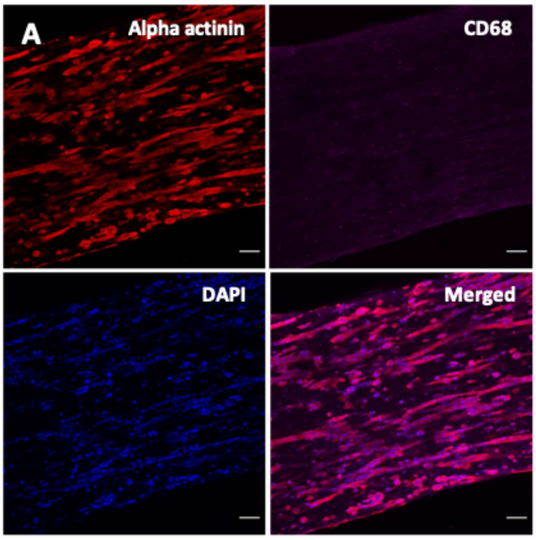
A
Alpha actinin
CD68
DAPI
Merged

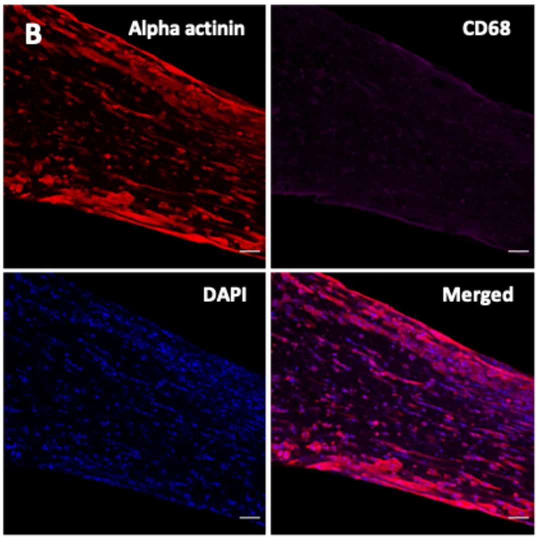
B
Alpha actinin
CD68
DAPI
Merged

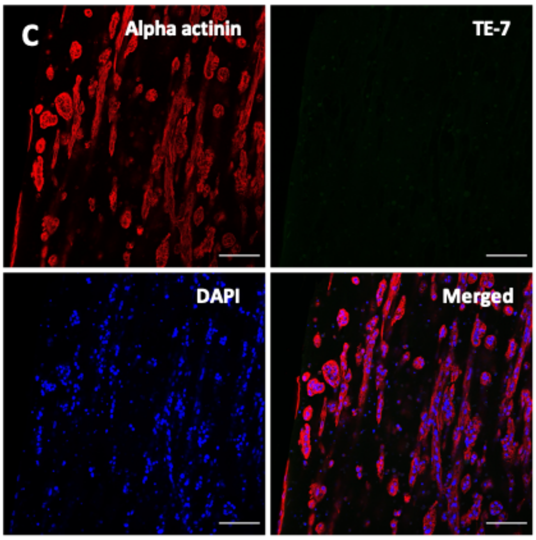
C
Alpha actinin
TE-7
DAPI
Merged

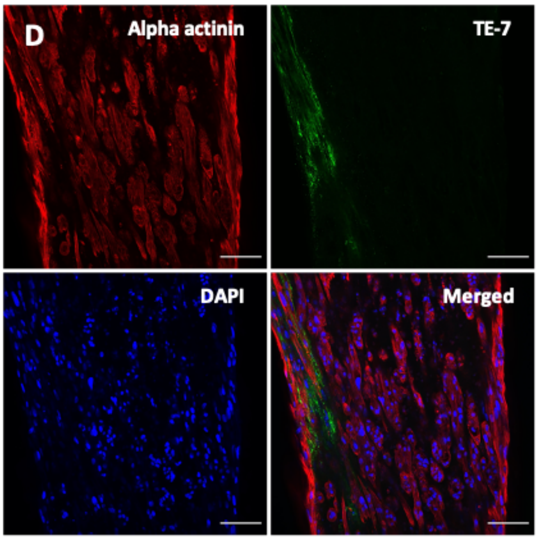
D
Alpha actinin
TE-7
DAPI
Merged

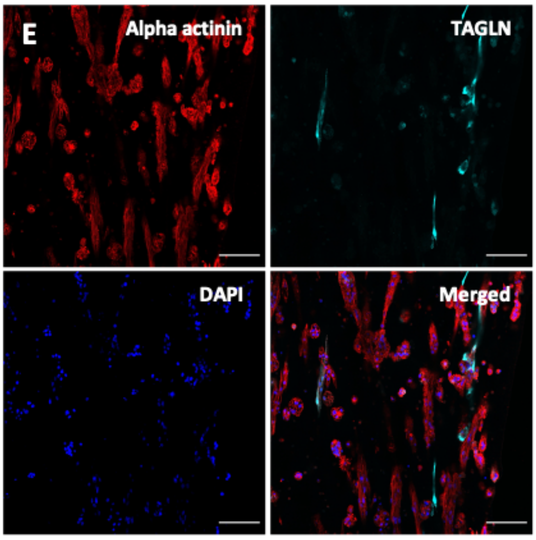
E
Alpha actinin
TAGLN
DAPI
Merged

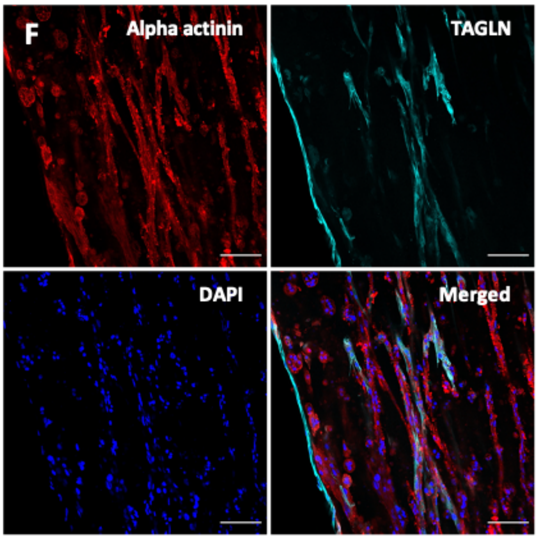
F
Alpha actinin
TAGLN
DAPI
Merged

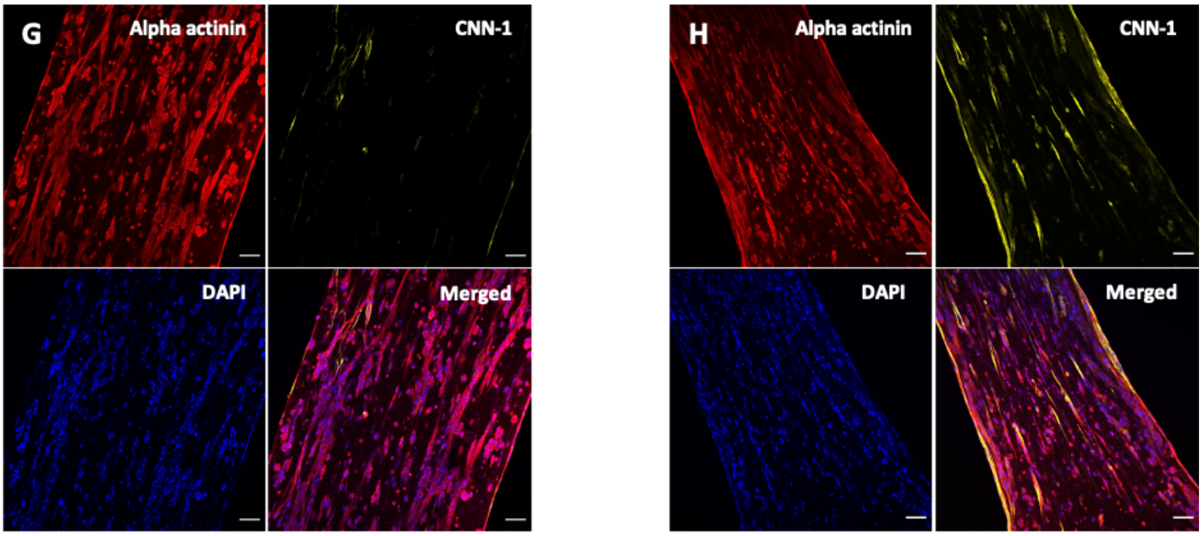

Supplementary Figure 12 Immunofluorescence images of CM-only EHTs cultured without (A, C, E, G) or with FGF-2 (B, D, F, H). Red: alpha actinin, magenta: CD68, TE-7: green, TAGLN: turquoise, CNN-1: yellow, DAPI: blue. Scale bar: 100 µm.

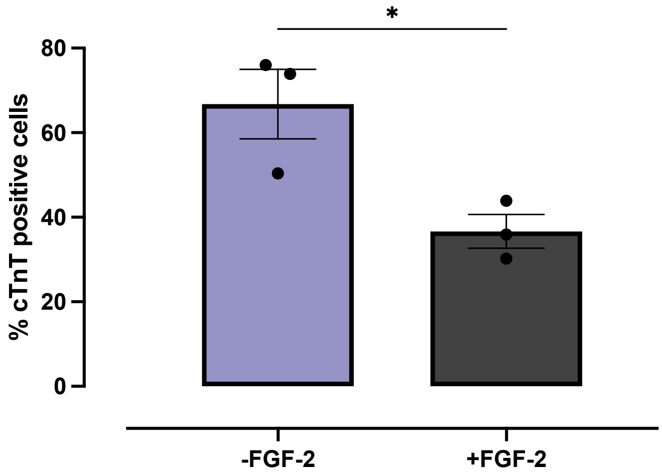

Supplementary Figure 13 Flow cytometry analysis of cTnT in dissociated EHTs on the last day of culture. Data are presented as mean ± SEM; n = 3 EHTs cultured without FGF-2 (-FGF); n = 3 EHTs cultured with FGF-2 (+FGF). Statistical analysis: unpaired t-test; *$p < 0.05$.

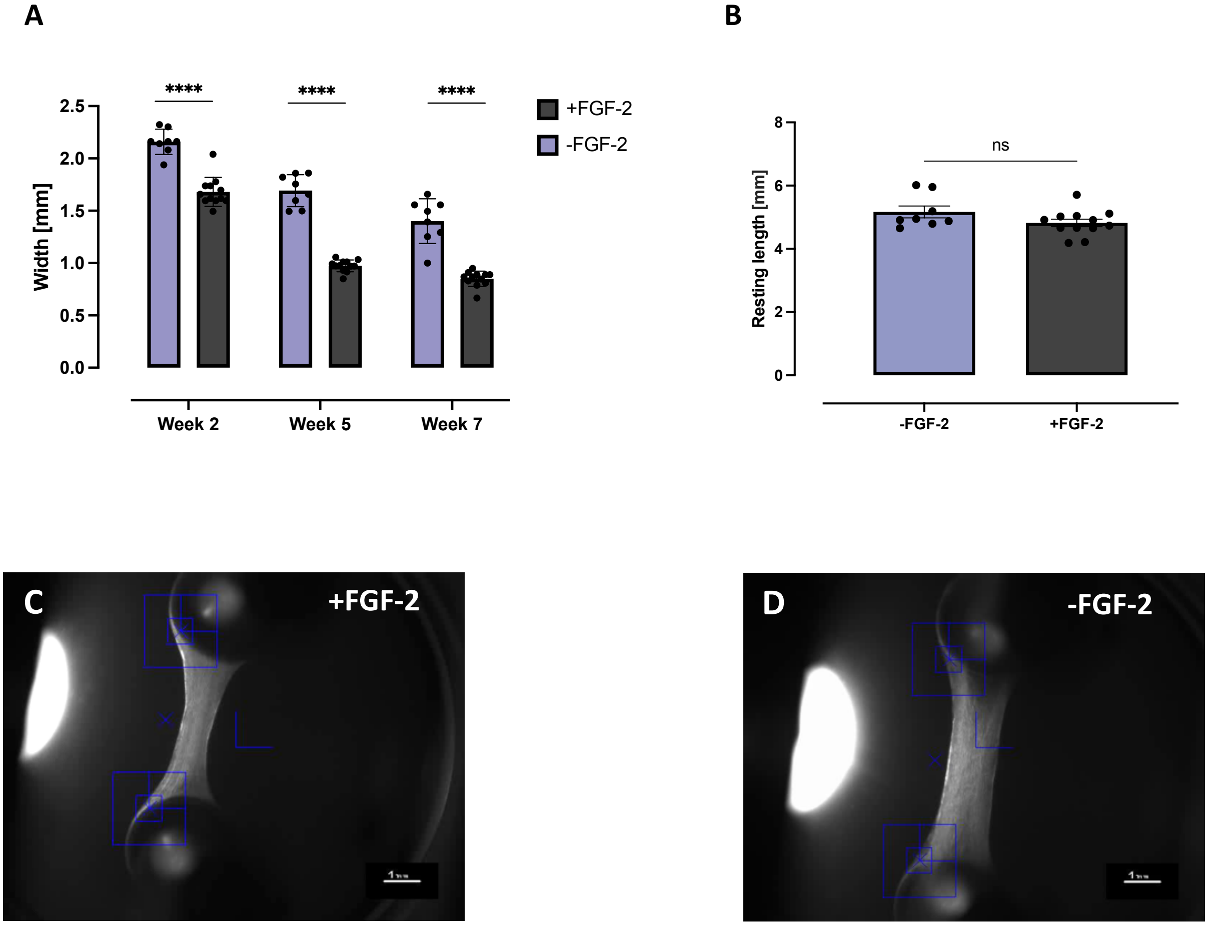

Supplementary Figure 14 Effect of FGF-2 on the remodeling of the tissues. **(A-B)** Supplementation of EHT medium with FGF-2 accelerated the remodeling of the tissues leading to **(A)** decrease in tissues' width but had no effect **(B)** on the resting length – week 7 of culture. **(C-D)** Representative pictures of EHTs on day 40 cultured in medium **(C)** supplemented with FGF-2 and **(D)** without it. Scale bar: 1 mm. Data are presented as mean ± SEM; n = 8 EHTs cultured without FGF-2 (-FGF); n = 12 EHTs cultured with FGF-2 (+FGF). Statistical analysis: (A) Two-Way ANOVA with Bonferroni's post-hoc test for multiple comparisons, (B) Mann-Whitney test; ns $p \geq 0.05$, ****$p \leq 0.0001$.

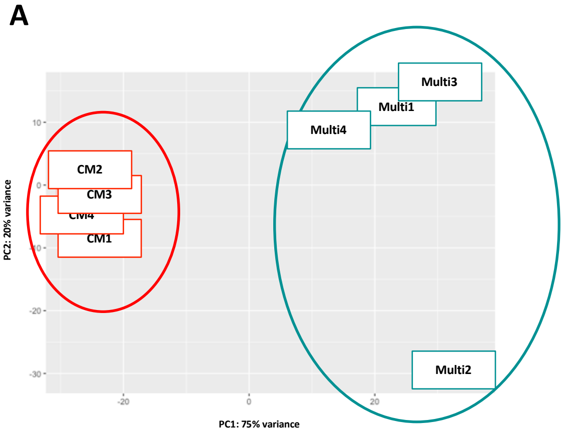
A
Multi3
Multi1
Multi4
CM2
CM3
CM4
CM1
Multi2
10
0
-10
-20
-30
-20
0
20
PC2: 20% variance
PC1: 75% variance

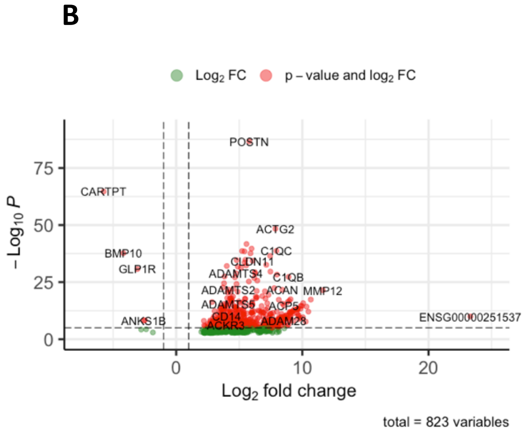
B
Log$_2$ FC
p – value and log$_2$ FC
POSTN
CARTPT
ACTG2
BMP10
GLP1R
C1QC
CLDN11
ADAMTS4
C1QB
ADAMTS2
ACAN
MMP12
ADAMTS5
ACP5
ANKS1B
CD14
ACKR3
ADAM28
ENSG00000251537
75
50
25
0
0
10
20
– Log$_{10}$ P
Log$_2$ fold change
total = 823 variables

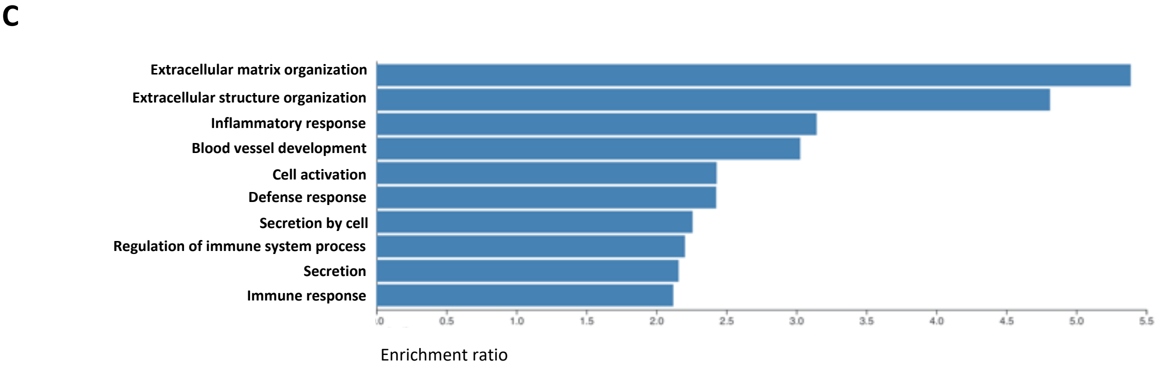
C
Extracellular matrix organization
Extracellular structure organization
Inflammatory response
Blood vessel development
Cell activation
Defense response
Secretion by cell
Regulation of immune system process
Secretion
Immune response
0
0.5
1.0
1.5
2.0
2.5
3.0
3.5
4.0
4.5
5.0
5.5
Enrichment ratio

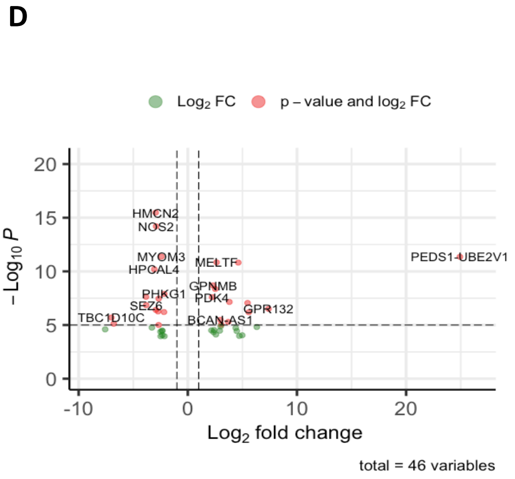
D
Log$_2$ FC
p – value and log$_2$ FC
20
15
10
5
0
HMCN2
NOS2
MYOM3
HPCAL4
MELTF
PEDS1-UBE2V1
GPNMB
PHKG1
PDK4
SEZ6
GPR132
TBC1D10C
BCAN-AS1
-10
0
10
20
– Log$_{10}$ P
Log$_2$ fold change
total = 46 variables

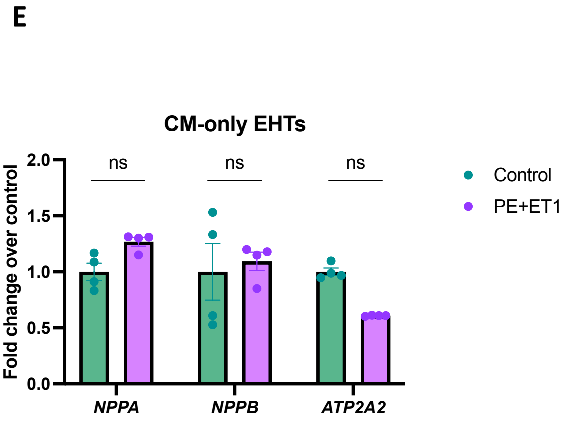
E
CM-only EHTs
ns
ns
ns
Control
PE+ET1
2.0
1.5
1.0
0.5
0.0
Fold change over control
NPPA
NPPB
ATP2A2

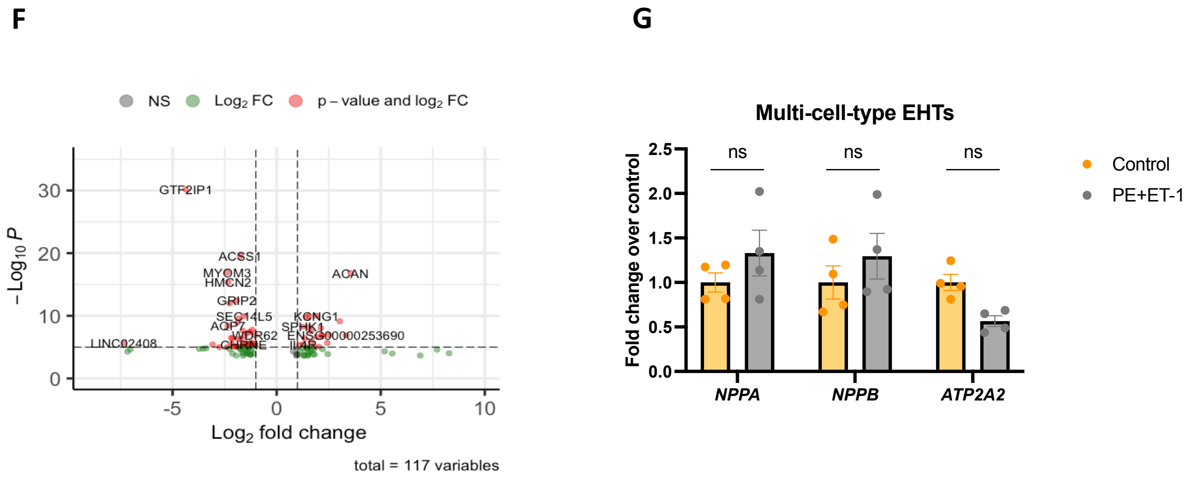

Supplementary Figure 15 Transcriptomic analysis of CM-only and multi-cell-type EHTs cultured with FGF-2. **(A)** PCA plot demonstrating differential clustering between multi-cell-type and CM-only EHTs. **(B)** Volcano plot demonstrating distribution of differentially expressed genes ($\log_2$FC > 0.5 and adjusted p-value <0.05) identified by comparison of multi-cell-type and CM-only EHTs. **(C)** Gene ontology analysis of DEGs – biological process. **(D-G)** Analysis of transcriptomic changes evoked by PE+ET-1 stimulation in **(D-E)** CM-only and **(G-H)** multi-cell-type EHTs cultured with FGF-2. Volcano plots depicting distribution of differentially expressed genes ($\log_2$FC > 0.5 and adjusted p-value <0.05) evoked by PE+ET-1 treatment in the **(D)** CM-only and **(F)** multi-cell-type EHTs. **(E,G)** Analysis of the expression of hypertrophic genes in **(E)** CM-only and **(G)** multi-cell-type EHTs. Fold change for each sample was calculated as a relation of normalized counts of the sample to an average of the normalized counts of control samples. The significance of changes is displayed as adjusted p-value and was determined with the R package DESeq2; ns p ≥ 0.05. Data are presented as mean ± SEM; n = 4 EHTs.

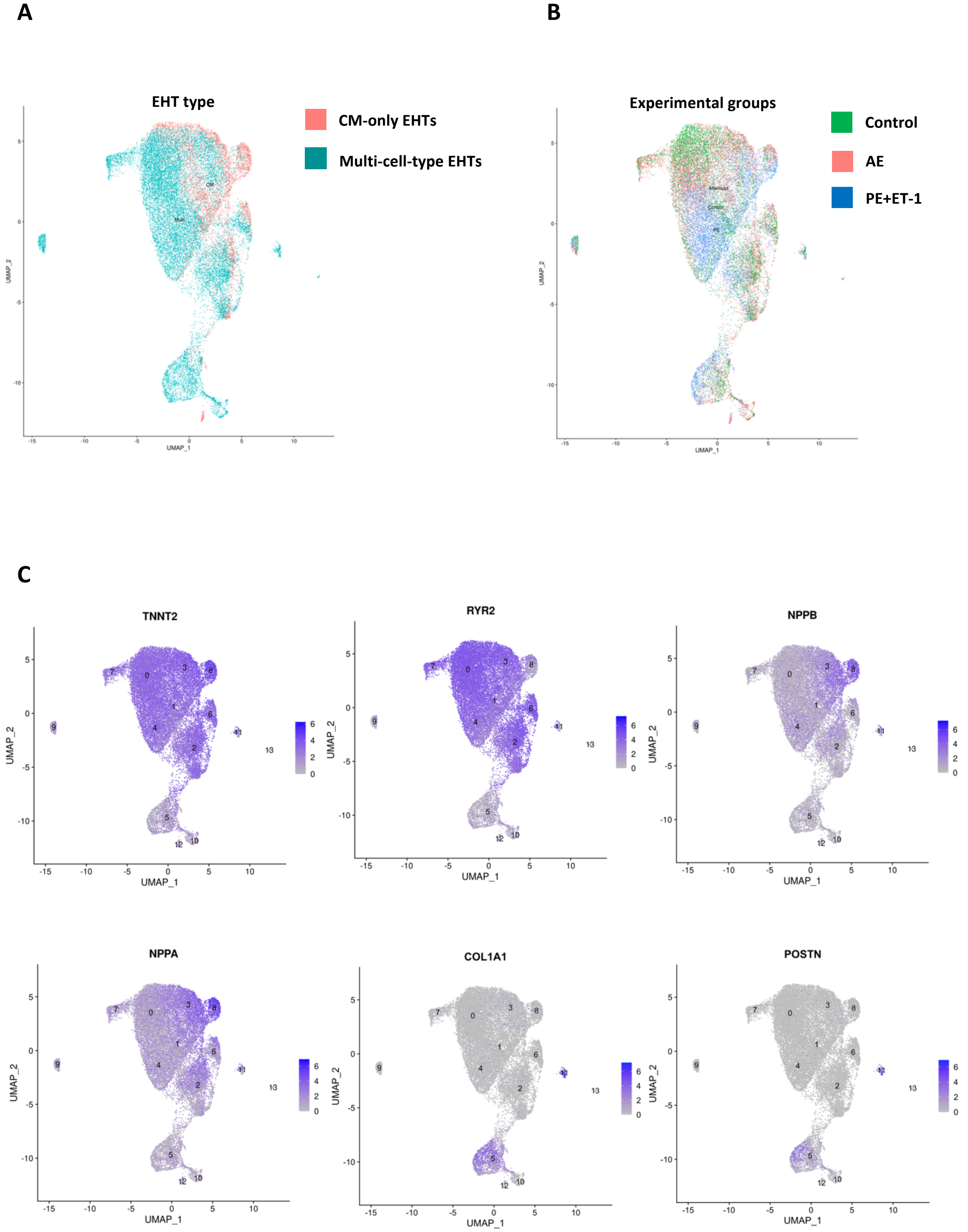

Supplementary Figure 16 Preliminary results of snRNA-seq analysis. **(A-B)** UMAPS representing cell clustering in the obtained dataset with regard to (A) cell type and (B) treatment. **(C)** UMAPS demonstrating expression profile of exemplary genes in the identified cell clusters.

9.2 Composition of media, reagents, buffers and solutions

Table 26 Composition of cell culture media

Application	Medium	Composition
Stem cell culture	FTDA	DMEM/F-12 without glutamine 2 mM L-glutamine 0.1% (v/v) Lipid mix 5 mg/L Transferrin 5 µg/L Selenium 0.1% (v/v) Human serum albumin 5 µg/mL Insulin 2.5 ng/mL Activin-A 30 ng/mL FGF-2 50 nM Dorsomorphin 0.5 ng/mL TGFβ1
	EB formation medium	FTDA 4 mg/mL Polyvinyl alcohol 10 µM Y-27632
CMs, SMCs, CFs (3D diff. protocol)	Mesoderm induction medium	RPMI 1640 4 mg/mL Polyvinyl alcohol 10 mM HEPES 0.05% (v/v) Human serum albumin 250 µM Phosphoascorbate 5 mg/L Transferrin 5 µg/L Selenium 0.1% (v/v) Lipid mix 10 µM Y-27632 3 ng/mL Activin-A 10 ng/mL BMP4 5 ng/mL FGF-2
CMs	Cardiac differentiation medium I	RPMI 1640 0.5% (v/v) Penicillin/streptomycin 10 mM HEPES (pH 7.4) 0.05% (v/v) Human serum albumin 5 mg/L Transferrin 6.6 µg/L Natrium selenite 0.1% (v/v) Lipid mix 1 µM Y-27632 250 µM Phosphoascorbate 1 µM XAV-939

CMs	Cardiac differentiation medium II	RPMI 1640 2% (v/v) B27 plus insulin 0.5% (v/v) Penicillin/streptomycin 10 mM HEPES (pH 7.4) 1 µM Y-27632 500 µM 1-Thioglycerol 1 µM XAV-939
	Cardiac differentiation medium III	RPMI 1640 2% (v/v) B27 plus insulin 0.5% (v/v) Penicillin/streptomycin 10 mM HEPES (pH 7.4) 1 µM Y-27632 500 µM 1-Thioglycerol
SMCs, CFs (3D diff. protocol)	Epi medium	RPMI 1640 0.5% Penicillin/streptomycin 0.1% Lipid mix 250 µM Phosphoascorbate 0.01% Transferrin-selenium 1 µM Y-27632
CFs (2D diff. protocol)	Cardiac fibroblast differentiation basal medium (CFBM)	DMEM, high glucose (4.5g/L) 500 µg/mL Human serum albumin 0.6 µM Linoleic cid 0.6 µg/mL Lecithin 50 µg/mL Phosphoascorbate 7.5 mM GutaMAX 1.0 µg/mL Hydrocortisone 5 ug/mL Insulin
ECs (2D diff. protocol)	Mesoderm induction medium I	RPMI 1640 100 ng/mL Activin A 2% B27 without insulin 1× Matrigel
	Mesoderm induction medium II	RPMI 1640 5 ng/mL BMP4 1 µM CHIR-99021 1x B27 without insulin
	Endothelial cell differentiation medium I	StemPro-34 + Supplement 0.4 mM MTG 2 mM L-glutamine 50 µg/mL Phosphoascorbate 20 ng/mL BMP4 5 ng/mL FGF-2 300 ng/mL VEGF

	Endothelial cell differentiation medium II	EGM 20 ng/mL VEGF 20 ng/mL FGF-2 1 μM CHIR-99021
ECs (3D diff. protocol)	Stage 1 medium	StemPro-34 + Supplement 4mg/mL Polyvinyl alcohol 5 mg/L Transferrin-Selenium 20 μM Y-27632 1x Lipid mix 20 mM HEPES 250 μM Phosphoascorbate 400 μM 1-Thioglycerol 2 mM L-glutamine 3 ng/mL Activin A 20 ng/mL BMP4 5 ng/mL FGF-2
	Stage 2 medium	StemPro-34 + Supplement 4mg/mL Polyvinyl alcohol 5 mg/L Transferrin-selenium 20 μM Y-27632 1x Lipid mix 20 mM HEPES 250 μM Phosphoascorbate 400 μM 1-Thioglycerol 2 mM L-glutamin 100 ng/mL VEGF 10 ng/mL FGF-2
	Expansion medium	EGM-2 30 ng/mL VEGF 20 ng/mL FGF-2
Mφs	Mesoderm/HE induction medium	STEMdiff™ APEL™ 2 40 ng/mL BMP4 20 ng/mL VEGF 20 ng/mL SCF 10 μM Y-27632
	Macrophage differentiation medium	X-VIVO 15 0.05 mM 2-Mercaptoethanol 25 ng/mL IL-3 50 ng/mL M-CSF

Mφs	Macrophage terminal differentiation medium	RPMI 1640 10% Heat inactivated FCS 1% (v/v) Penicillin/streptomycin 1% (v/v) L-glutamine 50 ng/mL M-CSF
EHTs	NKM (EHT casting medium)	DMEM-low glucose 1% (v/v) Penicillin/streptomycin 10% (v/v) Heat inactivated horse serum 1% (v/v) GlutaMAX
	EHT culture medium	DMEM-low glucose 1% (v/v) Penicillin/streptomycin 10% (v/v) Heat inactivated horse serum 10 µg/mL Insulin 33 µg/mL Aprotinin 0.2 mM Tranexamic acid 30 ng/mL VEGF
	Serum-free EHT medium	DMEM-low glucose 1% (v/v) Penicillin/streptomycin 10 mg/L Insulin 33 mg/L Aprotinin 50 ng/mL Hydrocortisone 0.5 ng/mL T_3 30 ng/mL VEGF
CMs, CFs, SMC, ECs	Freezing medium	90% FCS 10% DMSO

Table 27 Composition of reagents, buffers and solutions

Reagent/Buffer/Solution	Composition
Agarose for EHT casting	2% (w/v) Agarose 300 mL DPBS Sterilized by autoclaving and stored at 60 °C
Antibody solution (IF EHTs)	1% BSA 0.5% Triton X-100 in TBS pH 7.5
Antibody solution (IF endothelial cells)	1% BSA 0.3% Triton X-100 in DPBS
Antibody solution (IF cardiomyocytes)	3% milk powder 0.1% Triton X-100 in DPBS
Antibody solution/IF buffer (IF smooth muscle cells/ fibroblasts)	1% (w/v) BSA 155 mM NaCl 2 mM EDTA 2 mM $MgCl_2$ 10 mM Tris, pH 7.5
Aprotinin	33 mg/mL Aprotinin Aqua ad iniectabilia
B27	Basal Medium (Neurobasal) 0.125 mg/mL Catalase 50 µg/mL Glutathione 0.25 mg/mL Human Holo-Transferin 0.1 µg/mL T_3 0.1 mg/mL L-carnitine 0.05 µl/mL Ethanolamine 0.75 mg/mL D+-galactose 0.805 mg/mL Putrescine 0.625 µg/mL Natrium selenite 1 µg/mL Corticosterone 50 µg/mL Linoleic acid 50 µg/mL Linolenic acid 0.315 µg/mL Progesterone 5 µg/mL Retinyl acetate 50 µg/mL DL-alpha tocopherol (vit E) 50 µg/mL DL-alpha tocophercol acetate 0.125 mg/mL Biotin BSA Fraction V IgG free, FA-poor

Blocking buffer (EB dissociation)	RPMI 1640 6 mL/L DNase II type V 1% (v/v) Penicillin/streptomycin
Blocking solution (IF EHTs)	10% goat serum 1% BSA 0.5% Triton X-100 in TBS
BTS solution	30 mM BTS in DMSO
CBFHH (Calcium and Bicarbonat free Hanks with HEPES)	8 g/L NaCl 0.4 g/L KCl 0.2 g/L $MgSO_4 * 7H_2O$ 0.06 g/L KH_2HPO_4 0.0597 g/L $Na_2HPO_4 * H_2O$ 1 g/L Glucose 4.766 g/L HEPES, pH 7.4
Dissociation buffer	HBSS (-) calcium/magnesium 200 U/mL Collagenase II 1 mM HEPES 10 µM Y-27632 30 µM BTS
DNase solution	100 mg DNase II, type V 50 mL DPBS
EDTA	0.5 mM EDTA in DPBS
FACS buffer (surface markers)	DPBS 5% (v/v) FCS
FACS buffer (surface markers, fibroblasts 2D protocol)	DPBS 0.5% BSA
FACS buffer (intracellular markers)	DPBS 5% (v/v) FCS 0.05% (v/v) Sodium azide 0.5% (w/v) Saponin
FACS buffer (intracellular markers, fibroblasts 2D protocol)	DPBS 0.5% BSA 0.1% Triton X-100
Fibrinogen	200 mg/mL Fibrinogen 100 µg/mL Aprotinin 0.9% NaCl solution
HEPES stock solution	1 M HEPES DPBS Sodium hydroxide for pH adjustment to 7.4

Image Stream buffer	DPBS 2% FCS 2 mM EDTA
MACS buffer (neonatal rat CMs)	DPBS 0.5% BSA 2 mM EDTA
MACS buffer (hiPSC-CMs)	DPBS 0.5% FCS 2 mM EDTA
Papain solution	1x HBSS 5 U/mL Papain 1 mM EDTA 5.5 mM L-Cystein-HCl
Phosphoascorbate	1 g Phosphoascorbate dissolved in 12.4 mL PBS
Pluronic F-127 solution	0.1% (v/v) Pluronic F-127 in DPBS
Polyvinyl alcohol (50X)	20 g Polyvinyl alcohol Add H_2O to 100 mL
TBS (10x)	1 M Trizma base or Tris-HCl 1.5 M NaCl H_2O; pH adjusted with 37% HCl to 7.5
TEC buffer (10X)	2.5 g Trizma Base 5.75 g EDTA Disodium salt dihydrate 3.2 g Sodium citrate tribasic dihydrate Disolve in 1 L H_2O, pH adjusted with 10 M NaOH to 9
Thrombin	100 U/mL Thrombin 60% (v/v) PBS 40% (v/v) Aqua ad iniectabilia
Transferrin–selenium	100 mg Transferrin 2 mL Natrium selenite (382 µM)
Tyrode’s solution	127 mM NaCl 4.5 mM KCl 1.5 mM $MgCl_2$ 1.8 mM $CaCl_2$ 10 mM Glucose 22 mM $NaHCO_3$ 0.42 mM Na_2HPO_4 H_2O, pH 7.4

9.3 Devices, Materials and Substances

Table 28 List of devices, materials and substances used in this study and their respective manufacturer

Devices	
AbiPrism7900HT cycler	Applied Biosystems
ABL90 FLEX Analysator	Radiometer
Analytic scale Genius	Sartorius AG
Architect i2000 Immunoassay Analyzer	Abbott
Cell culture incubator CB 220	Binder
Cell culture incubator MCO-19M	Sanyo
Cell culture incubator MCO-20AIC	Sanyo
Cell culture incubators HERAcell 240	Thermo Fisher Scientific
Centrifuge 5415 R	Eppendorf
Centrifuge 5424 R	Eppendorf
Centrifuge 5810 R	Eppendorf
Centrifuge Avanti JXN-26	Beckmann-Coulter
Centrifuge Rotanta/RP	Hettich
Centrifuge Universal 30 RF	Hettich
ChemiDoc Touch Imaging System	Bio-Rad Laboratories
CHIARO nanoindenter system	Optics11
Combispin FVL-2400N with vortex function	PeqLab
FACS Canto II Flow Cytometer	BD Biosciences
FluoroCount Micorplate Reader	Packard
GentleMACS OctoDissociator	Miltenyi Biotec
Heat plate HPL-2	Kunz Instruments
Image Stream	Amnis
Lamp KL-1500	Schott
Leica VT1000 S Vibrating blade microtome	Leica
MACSima Imaging System	Miltenyi Biotec
Magnetic stirring and heating plate IKA Combimag RET	Janke & Kunkel GmbH & Co KG
Magnetic stirring plate Variomag / Cimarec 4 Direct	Thermo Fisher Scientific
Magnetic stirring plate Variomag / Cimarec Direct	Thermo Fisher Scientific
Microscope Axioskop 2 with AxioCam Color	Zeiss
Microscope EVOS FL Cell Imaging System	Thermo Fisher Scientific
Microscope LSM 800 Airyscan	Zeiss
Microscope T1-SM Nikon Eclipse TS100	Nikon
Microtome HM355 S	Thermo Fisher Scientific
Nanodrop ND-1000 Spectrophotometer	Thermo Fisher Scientific

nCounter SPRINT™ Profiler	NanoString
pH meter, digital	Mettler Toledo
Pipette 10/100/1000 µL	Eppendorf, Peqlab
Pipette controller Accu-jet pro	Brand
Pipette controller Pipetus	Hirschmann
Precision Advanced Scale	Ohaus
QuantStudio 5 Real-Time PCR System	Applied Biosystems
S88X dual output square pulse stimulator	Grass
Safety workbench HeraSafe	Heraeus
Safety workbench Safe 2020	Thermo Fisher Scientific
Safire 2 multi-detection plate reader	Tecan
Scale EK-4000H	AND
Spectrophotometer NanoDrop ND-1000	Thermo Fisher Scientific
Thermal cycler Hybaid PCR Sprint	Thermo Fisher Scientific
Thermal cycler vapo.protect	Eppendorf
TissueLyser	QIAGEN
Vibrating blade microtome VT1000S	Leica
Video-optical force analysis system	EHT Technologies GmbH
Vortex Genie	Scientific Industries
Vortex Reax 2000	Heidolph
Vortex VF2	Janke & Kunkel GmbH& Co KG
Warming Cabinet	Custom made at UKE, Hamburg
Water bath	PHOENIX Instrument
Materials and Equipment	
10 mL Wide Tip Stripette	Corning, 4492
12-well plates	Thermo Fisher Scientific, 150628
15 mL tubes	GreinerBio-one, 188271
15 mL tubes red cap	Sarstedt, 62.554.502
24-well plates	Thermo Fisher Scientific, 142475
250 ml Vacuum Filtration "rapid"-Filtermax	TPP, 99250
30 µm MACS SmartStrainer	Miltenyi Biotec, 130-098-458
48-well plates	Thermo Fisher Scientific, 150687
50 mL tubes	GreinerBio-One, 227261
50 mL tubes	Sarstedt
500 mL Vacuum Filtration "rapid"-Filtermax	TPP, 99500
6-well plates	Greiner
6-well plates	Thermo Fisher Scientific, 140675
70 µm MACS SmartStrainer	Miltenyi Biotec, 130-110-916
96-well plates	Thermo Fisher Scientific, 167008
Anti-Nucleus MicroBeads	Miltenyi Biotec, 130-132-997
Aspiration pipette 2 mL	Sarstedt, 86.1252.011
Cell culture tube 12mL, round bottom	GreinerBio One, 163160

Cryovial CryoPure tube 1.6 mL	Sarstedt, 72.379
Dialysis cassettes	Thermo Fisher Scientific, A52961
EHT electrode	EHT Technologies GmbH, P0001
EHT pacing adapter/cable	EHT Technologies GmbH, P0002
EHT PDMS rack (24-well format)	EHT Technologies GmbH, C0001
EHT PTFE spacer 24-well	EHT Technologies GmbH, C0002
Epredia Lab Vision PT-Module	Thermo Fisher Scientific, A80400012
Falcon tube, graduated, 15 mL	Sarstedt, 62.554.502
Flow Cytometry tubes	Sarstedt, 55.1579
GentleMACS C Tubes	Miltenyi Biotec, 130-093-237
GentleMACS Octo Coolers	Miltenyi Biotec, 130-130-533
GentleMACS Octo Dissociator with Heaters	Miltenyi Biotec, 130-096-427
LS columns	Miltenyi Biotec, 130-042-401
MACSima Running buffer	Miltenyi Biotec, 130-121-565
MACSwell^{TM} Deepwell plates	Miltenyi Biotec, 130-126-865
MACSwell^{TM} Four Imaging Frames	Miltenyi Biotec, 130-124-676
Nuclei Extraction Buffer	Miltenyi Biotec, 130-128-024
Nunclon Delta surface Nunc™ EasYFlask™ Cell Culture Flasks 75cm^2	Thermo Fisher Scientific, 156499
Pipette tips	Sarstedt
Pipette tips with filter Biosphere	Sarstedt
QuadroMACS™ separator	Miltenyi Biotec, 130-091-051
SafeSeal tube 1.5 mL	Sarstedt
Serological pipette 10 mL	Sarstedt, 86.1254.001
Serological pipette 2 mL	Sarstedt, 86.1252.001
Serological pipette 25 mL	Sarstedt, 86.1685.001
Serological pipette 5 mL	Sarstedt, 86.1253.001
Serological pipette 50 mL	Sarstedt, 86.1256.001
Spinner flask, 1000 ml	Integra, 182 101
Spinner flask, 500 ml	Integra, 182 051
Superfrost® Plus Slides	VWR, 631-9483
Syringes 1 ml	Braun
T175 suspension cell culture flask	Sarstedt, 83.3912.502
Teflon spacers	EHT technologies GmbH, C0002
TissueLyser steel beads	QIAGEN, 69989
V-shaped sedimentation rack	Custom made at UKE Hamburg
µ-Slide 8 Well	Ibidi, 80826
Media and Serum	
Basal Medium (Neurobasal)	Invitrogen 21103-049
DMEM	Life Technologies, A14430-01
DMEM, high glucose (4.5g/L)	Gibco, 11965092
DMEM/F-12 without Glutamine	Life Technologies, 21331-046

EGM-2	Lonza Bioscience, CC-3162
EGM	Lonza Bioscience, CC-3124
Fetal Calf Serum superior, FCS	Biochrom, S0615
FibroGRO	Milipore, SCMF001
Goat serum	Thermo Fisher Scientific, 16210064
Horse serum	Life Technologies, 26050-088
Human serum albumin	Biological Industries, 05-720-1B
mTeSR1	StemCell Technologies, 05825
RPMI 1640	Life Technologies, 21875-034
StemdiffTM APEL™2	Stemcells Technologies, 05275
StemPro-34 SFM	Life Technologies, 10639011
X-VIVO 15	Lonza Bioscience, 881024
Reagents	
1-Thioglycerol (MTG)	Sigma-Aldrich, M6145
2% gelatin solution	Sigma-Aldrich, 9000-70-8
2-Mercaptoethanol	Gibco, 21985023
2-Propanol	Roth, 9866.6
2-Phospho-L-ascorbic acid trisodium salt	Sigma Aldrich, 49752
2,3-Butanedione monoxime	Sigma Aldrich, 31550
2x DMEM	Gibco, 52100-021
Accutase Cell Dissociation Reagent	Sigma-Aldrich, A6964-100mL
Acetone	Merck, 67-64-1
Activin A	R&D Systems, 338-AC
Agarose	Thermo Fisher Scientific, 15510-027
Anti-Nucleus MicroBeads	Miltenyi Biotec, 130-132-997
Aprotinin	Genaxxon bioscience, M6361.101
Aqua	B. Braun
Biotin	Sigma-Aldrich, B4639-100MG
BMP4	R&D Systems, 314-BP
BSA Fraction V IgG free, FA-poor	Fisher Scientific, 30036578
BTS (N-benzyl-p-toluenesulfonamide)	TCI, B3082-25G
$CaCl_2$ x 2 H_2O	Merck, 1.02382
Catalase	Sigma-Aldrich, C40-100MG
CellMask™ Plasma Membrane Stain	Thermo Fisher Scientific, C10046
CellTiter-Blue® Reagent	Promega, G8080
CHIR-99021	Cayman, 13122
Chloroform	J.T. Baker, 7386
Collagenase II	Worthington, LS004176
Corticosterone	Sigma-Aldrich, C2505-500MG
D(+)-Galactose	Sigma-Aldrich, G0625-100G
D(+)-Glucose anhydrous	Roth, X997.2
D(+)-Saccharose	Roth, 9097.1

DAPI	Biochemica, A1001 0025
DAPI staining solution (for MICS)	Miltenyi Biotec, 130-127-574
Dimethyl sulfoxide (DMSO) for cell culture	Sigma-Aldrich, D4540
DL-alpha tocophercol acetate	Sigma-Aldrich, T3001-10G
DL-alpha tocopherol (vit E)	Sigma-Aldrich, T3251-5G
DNase II, type V	Sigma-Aldrich, D8764
Dorsomorphin dihydrochloride	Tocris, 3093
DPBS	Gibco, 14190250
EDTA disodium salt dihydrate	Roth, X986.2
Endothelin-1	Sigma-Aldrich, E7764
Ethanol 99%	Chemsolute, 2212.5000
Ethanolamine	Sigma-Aldrich E9508-100ML
FcR Blocking Reagent	Miltenyi Biotec, 130-059-901
FGF-2	Peprotech, #100-18B or Miltenyi Biotec,130-104-923
Fibrinogen	Sigma-Aldrich, F8630
Fluoromount-G	Invitrogen, 00-4958-02
Geltrex^{TM}	Gibco, A14133-02
GlutaMAX™ Supplement	Gibco, 35050061
Glutaraldehyde	Science Services, E16222
Glutathione	Sigma-Aldrich, G6013-5G
HBSS w/o Ca^{2+} /Mg^{2+}	Gibco, 14175-053
HEPES	Sigma-Aldrich, 9105.4
Human Holo-Transferin	Sigma-Aldrich, T0665-500MG
Human Serum Albumin	Biological Industries, 05-720-1B
Hydrocortisone	Sigma-Aldrich, H4001
IFNγ	Peprotech, 300-02
IL-3	R&D, 203-IL-100
IL-4	Peprotech, 200-04
Insulin	Sigma-Aldrich, I9278
Laminin	Sigma-Aldrich, L2020
L-Carnitine hydrochloride	Sigma-Aldrich, C0283-1G
L-Cystein hydrochloride	Sigma-Aldrich, C1276
L-Glutamine	Gibco, 25030-081
Linoleic acid	Sigma-Aldrich, L1012-100MG
Linolenic acid	Sigma-Aldrich, L2376-500MG
Lipid Mixture (1000x)	Sigma-Aldrich, L5146
LPS	Thermo Fisher Scientific, 00-4976-93
M-CSF	R&D, 216-MC-100
MACS SmartStrainers (30 µm)	Miltenyi Biotec, 130-098-458
MACS SmartStrainers (70 µm)	Miltenyi Biotec, 130-098-462
MACSima™ Running Buffer	Miltenyi Biotec, 130-121-565

Magnesium chloride hexahydrate ($MgCl_2$ x 6 H_2O)	Sigma Aldrich, M0250
Magnesium sulfate heptahydrat ($MgSO_4$ x 7 H_2O)	Merck, 1.05886
Matrigel® Growth Factor Reduced (GFR) Basement Membrane Matrix	Corning, 354230
Methanol	J. Baker, 8045
Milk powder	Roth, T145.2
Mowiol	Roth, 0713.2
Natrium selenite	Sigma-Aldrich, S5261
NHS-Rhodamine	Thermo Fisher Scientific, 46406
Nitrogen, liquid (N_2)	TMG
Non-essential amino acids	Gibco, 11140
Nuclei Extraction Buffer	Miltenyi Biotec, 130-128-024
Papain from *Carica papaya*	Sigma-Aldrich, 76220
Paraffin	Sigma-Aldrich, 327204
Paraformaldehyde	Merck, 1.04005
Penicillin-Streptomycin	Gibco, 15140
(R)-(−)-Phenylephrine hydrochloride	Sigma-Aldrich, P6126
pHrodo™ Green Zymosan BioParticles™	Thermo Fisher Scientific, P35364
Pluronic F-127	Sigma-Aldrich, P2443-250G
Polyvinyl alcohol (PVA)	Sigma-Aldrich, P8136
Potassium chloride (KCl)	Merck, 104936
Potassium di-hydrogen phosphate (KH_2PO_4)	Merck, 4873
Progesterone	Sigma-Aldrich, P8783-1G
Putrescine dihydrochloride	Sigma-Aldrich, P5780-5G
Retinyl acetate	Sigma-Aldrich, R7882-1G
Roti-Histofix 4%	Roth, P087.3
Saponin	Sigma-Aldrich, 47036 or Merck, 558255
SB-431542 (hydrate)	Cayman, 13031
SCF	R&D, 255-SC-200
Sodium azide	Sigma-Aldrich, 71290
Sodium chloride (NaCl) solution (0.9%)	B. Braun, 3570210
Sodium citrate tribasic dihydrate	Merck, 1064480500
Sodium hydrogen carbonate ($NaHCO_3$)	Merck, 1.06329
Sodium hydrogenphosphate (Na_2HPO_4)	Sigma Aldrich, S0876
Sodium hydroxide	Roth, 6771.1
TGFβ1	Peprotech, 100-21
Thrombin	Sigma-Aldrich, T7513
Tranexamic acid	Sigma 857653-50G
Transferrin	Sigma-Aldrich, T8158
Triiodothyronine	Sigma-Aldrich, T2877-100MG

TRIS-hydrochloride	Roth, 9090.2
Tris-EDTA buffer solution	Sigma-Aldrich, 93283-100ML
Triton X-100	Roth, 3051.3
Trizma base	Sigma-Aldrich, T1503
TRIzol reagent	Life Technologies, 15596026
Trypan blue	Sigma, T8154
TrypLE Select	Gibco, 12563-011
Trypsin-EDTA (0.25%)	Thermo Fisher Scientific, 25200056
VEGF$_{165}$	R&D Systems, 293-VE or Peprotech 100-20
XAV939	Tocris, 3748
Xylene	Carl Roth, 9713.3
Y-27632	Biaffin, PKI-Y27632-010
Kits	
5x HOT FIREPol EvaGreen qPCR Mix Plus ROX	Solis BioDyne, 08-24-00008
CD31 MicroBead Kit, human	Miltenyi Biotec, 130-091-935
DNeasy Blood & Tissue Kit	Qiagen, 69506
High-Capacity cDNA Reverse Transcription Kit	Applied Biosystems, 4368813
iPSC-Derived Cardiomyocyte Isolation Kit, human	Miltenyi Biotec, 130-110-188
Neonatal Cardiomyocyte Isolation Kit, rat	Miltenyi Biotec, 130-105-420
SPLIT RNA Extraction Kit	Lexogen, 008.48
Software	
AxioVision Rel. 4.8.2	Zeiss
BioRender	BioRender
Excel	Microsoft
FACSDiva	BD Biosciences
Fiji	NIH
Flowing software 2.5.1	Turku Bioscience
FlowJo V10	BD Biosciences
IDEAS	Amnis
MACS® iQ View Analysis Software 1.0.0	Miltenyi Biotec
nCounter CNV Collector Tool	Nanostring
Prism 10.0	GraphPad Software
SDS 2.4.1	Applied Biosystem
ZEN 2012	Zeiss

9.4 Antibodies

Table 29 Primary and secondary antibodies used for flow cytometry and Image Stream

Antibody	Dilution/Concentration	Company, cat. number
Anti-cardiac troponin T APC	1:50	Miltenyi Biotec, 130-120-403
REA control antibody APC	1:50	Miltenyi Biotec, 130-120-709
Anti-cardiac troponin-T FITC	1:50	Miltenyi Biotec, 130-119-575
REA control antibody FITC	1:50	Miltenyi Biotec, 130-113-437
Anti-SSEA-3 PE	1:5	BD Pharmingen, 560237
Isotype control PE	1:50	BD Pharmingen, 553943
Anti-TE-7	1:100	Sigma-Aldrich, CBL271
Anti-SMA	1:100	Dako, M0851
Anti-CD68	1:100	Santa Cruz Biotechnology, sc-20060
Anti-CD14 APC	1:20	Thermo Fisher Scientific, 17-0149-42
Anti-CD45 APC	1:20	Biolegend, 304011
Anti-CD31 FITC	1:5	Biolegend, 303104
Anti-CD34 APC	1:20	Biolegend, 343607
Anti-CD309 APC	1:50	Miltenyi Biotec, 130-117-911
Anti-CD144 FITC	1:50	Miltenyi Biotec, 130-123-932
Anti-Vimentin FITC	1:5	R&D, IC105G
Anti-CD90 FITC	1:20	Biolegend, 328107
Macrophage maturation marker	1:100	Thermo Fisher Scientific, 14-0115-80
Goat anti-mouse Alexa Fluor 488	1:200/1:1000	Thermo Fisher Scientific, A11029
Rat IgG2a FITC	0.5mg/mL	Biolegend, 400505
Mouse IgG1 PE	1:20	Biolegend, B150129
CD206 FITC	1:20	Biolegend, 321103
APC Mouse IgG2a	0.2 mg/mL	Biolegend, 400220
APC Mouse IgG1	0.2 mg/mL	Biolegend, 400120
FITC Mouse IgG1	0.2 mg/mL	Biolegend, 981802
PE Mouse IgG2b	0.2 mg/mL	Biolegend, 400313
Purified Mouse IgG1	0.5 mg/mL	Biolegend, 401401

Table 30 Primary and secondary antibodies used for immunofluorescence

Antibody	Dilution	Company, cat. number
Anti-CD31	1:100	Abcam, ab28364
Anti-Collagen I	1:100	Abcam, ab138492
Anti-MYH11	1:100	Abcam, ab133567, ab53219 (discontinued)
Anti-SMA	1:100	Dako, M0851
Anti-alpha-actinin mouse	1:500	Sigma, A2543
Anti-alpha-actinin rabbit	1:500	Sigma, SAB2108642
Anti-cardiac troponin I	1:800	Cell Signaling, 4002
Anti-TAGLN	1:100	Abcam, AB14106
Anti-CNN-1	1:100	Abcam, ab46794
Anti-CD68	1:100	Santa Cruz Biotechnology, sc-20060
Anti-TE-7	1:100	Sigma-Aldrich, CBL271
Alexa Fluor 488 Phalloidin	1:100	Thermo Fisher Scientific, A12379
Goat anti-mouse Alexa Fluor 488	1:200	Thermo Fisher Scientific, A11029
Goat anti-mouse Alexa Fluor 546	1:200	Thermo Fisher Scientific, A11003
Goat anti-rabbit Alexa Fluor 488	1:200	Thermo Fisher Scientific, A11034
Goat anti-rabbit Alexa Fluor 546	1:200	Thermo Fisher Scientific, A11035

Table 31 Antibodies used for MICS

Antibody	Dilution	Company, cat. number
Anti-Collagen I APC	1:50	Miltenyi Biotec, 130-127-017
Anti-MLC2v PE	1:50	Miltenyi Biotec, 130-119-581
Anti-CD14 PE	1:50	Miltenyi Biotec, 130-128-771
Anti-Myosin Smooth Muscle PE	1:50	Miltenyi Biotec, 130-119-314
Anti-CD31 PE	1:50	Miltenyi Biotec 130-128-769
Anti-Ki67 PE	1:50	Miltenyi Biotec, 130-119-356
Anti-Vimentin APC	1:50	Miltenyi Biotec, 130-118-361
Anti-MLC2a PE	1:50	Miltenyi Biotec, 130-117-397

9.5 Primer list

Table 32 Primer sequences used for RT-qPCR

Species	Gene	Primer sequence
Rat	*POSTN*	F: AACCCGGAGTCACCAACATC R: CAACCGGAATGTCTGCTGGA
Rat	*VIM*	F: GCACCCTGCAGTCATTCAGA R: GCAAGGATTCCACTTTACGTTCA
Rat	*ACTA2*	F: CATCCGACCTTGCTAACGGA R: CAGAGTCCAGCACAATACCAG
Rat	*MYH11*	F: ATCGTGAAGACCAGTCCATTCT R: GATGCCACCACAGCCAAATACT
Rat	*PECAM-1*	F: GGACTGCGCCCATCACTTACC R: AACTTCATCCACCGGGGCTATTAC
Rat	*CD45*	F: CCGTTGTACACCAGAGATGA R: TCCCAAAATCAGTCTGCAC
Rat	*CD68*	F: TGTACCTGACCCAGGGTGGAA R: GAATCCAAAGGTAAGCTGTCCGTAA
Rat	*ACTA1*	F: AGGACCTGTACGCCAACAAC R: ACATCTGCTGGAAGGTGGAC
Rat	*TNNT*	F: GCCATCGACCACCTGAATGA R: TTGGCCTTCCCACGAGTTTT
Rat	*GAPDH*	F: CTCATGACCACAGTCCATGC R: TTCAGCTCTGGGATGACCTT
Human	*NPPA*	F: GCTGCTTCGGGGGCAGGATG R: TGCAGCAGAGACCCCAGGGG
Human	*NPPB*	F: TGCAAGGGTCTGGCTGCTTTGG R: CACTTCAAAGGCGGCCACAGGG
Human	*ATP2A2*	F: CCGCAACTACCTGGAACCTG R: TCAGTCATGCACAGGGTTGG
Human	*SOX2*	F: GGGAAATGGGAGGGGTGCAAAAGAGG R: TTGCGTGAGTGTGGATGGGATTGGTG
Human	*NANOG*	F: ACAACTGGCCGAAGAATAGCA R: GGTTCCCAGTCGGGTTCAC
Human	*TBXT*	F: CCTTCAGCAAAGTCAAGCTCACC R: TGAACTGGGTCTCAGGGAAGCA
Human	*PTPRC*	F: CTTCAGTGGTCCCATTGTGGTG R: CCACTTTGTTCTCGGCTTCCAG

Human	*CD14*	F: CGCTCCGAGATGCATGTG R: AGCCCAGCGAACGACAGAT
Human	*CD80*	F: CTCACTTCTGTTCAGGTGTTATCCA R: TCCTTTTGCCAGTAGATGCGA
Human	*TNFA*	F: CTCTTCTGCCTGCTGCACTTTG R: ATGGGCTACAGGCTTGTCACTC
Human	*IL6*	F: GGCACTGGCAGAAAACAACC R: GCAAGTCTCCTCATTGAATCC
Human	*IL10*	F: GCCTAACATGCTTCGAGATC R: GCCTAACATGCTTCGAGATC
Human	*CCL24*	F: CCAGCCTTCTGTTCCTTGGTG R: AACTGCTGGCCCTTCTTGGT
Human	*MRC1*	F: AGCCAACACCAGCTCCTCAAGA R: CAAAACGCTCGCGCATTGTCCA
Human	*ACTA2*	F: TGGAAAAGATCTGGCACCAC R: GGCATAGAGAGACAGCACCG
Human	*POSTN*	F: GAGGCTTGGGACAACTTGGA R: ACAGTGACAACCCATTAGGA
Human	*COL1A1*	F: TGGGATTCCCTGGACCTAAAG R: GGGAGACCCTGGAATCCG
Human	*CNN2*	F: TGTGCATTCTCCAGCCATCA R: GCCACAAGCTGTCCAGTCTA
Human	*GAPDH*	F: CCTCAAGATCATCAGCAATGCC R: ATGTTCTGGAGAGCCCCGC
Human	*GUSB*	F: ACGATTGCAGGGTTTCACCA R: CACTCTCGTCGGTGACTGTT

F: forward primer, R: reverse primer

9.6 Security information

Table 33 List of hazardous substances used in the study according to GHS

Substance	CAS #	H-statements	P-statements
1-Thioglycerol	96-27-5	H: 302, 311+331,315,317	P: 261, 264, 280, 301+312-302+352+312-304+340+P311
2-Mercaptoethanol	60-24-2	H: 317, 361, 402	P: 261, 201, 273, 280, 272, 202, 302+352, 308+313, 333+313, 362+364
2-Propanol	67-63-0	H: 225, 319, 336	P: 210, 233, 305+351+338
Acetone	67-64-1	H: 225, 319, 336	P: 210, 233, 240, 241, 242, 305+351+338, 403+233
BTS (N-benzyl-p-toluenesulfonamide)	1576-37-0	H: 315, 319, 335	P: 302+352, 337+313, 304+340, 312, 280, 332+P313
Calcium chloride dihydrate	10035-04-8	H: 319	P: 280, 305+351+388
Catalase	9001-05-2	H: 334	P: 261-284-501
CHIR-99021	252917-06-9	H: 300, 315, 319, 335	P: 261, 264, 270, 271, 280, 301+310, 321, 330, 302+352, 304+340,305+351+338, 312, 362+364, 332+313, 337+313, 403+233, 405, 501
Chloroform	67-66-3	H: 331, 302, 315, 319, 336, 351, 372, 361d	P: 201, 260, 264, 280, 304+340, 311, 337+313, 308+313, 403+233
Collagenase II	9007-34-5	H: 315, 319, 334, 335	P: 261, 280, 305+351+338, 342+311
DL-alpha tocopherol acetate	58-95-7	H: 413	P: 273, 501
DL-alpha tocopherol	10191-41-0	H: 317	P:261, 272, 280, 302+352, 333+313, 362+364

EDTA disodium salt dihydrate	6381-92-6	H: 332, 373	P: 260, 314
Ethanol, absolute	64-17-5	H: 225, 319	P: 210, 240, 260, 280, 303+361+353, 305+351+338, 501
Ethanolamine	141-43-5	H: 302+312+332, 314, 335, 412	P: 273, 280, 301+312, 303+361+353, 304+340+310, 305+351+338
Glutaraldehyde	111-30-8	H: 317, 302, 314, 331, 334, 400, 411	P: 305+351+338, 310, 405, 501, 285, 303+361+353
Hydrocortisone	50-23-7	H: 360Df, 373	P: 202, 260, 280, 308+313, 405, 501
L-Carnitine hydrochloride	6645-46-1	H: 315, 319, 335	P: 261, 264, 271, 280, 302+353, 305+351+338
Lipid Mixture	64-17-5	H: 225, 319	P210, 233, 240, 241, 242, 305+351+338
Methanol	67-56-1	H: 225, 301+311+331, 370	P: 210, 280, 260, 301+310, 308+310, 403+233
Natrium selenite	10102-18-8	H: 300+330, 315, 317, 319, 411	P: 260, 273, 280, 302+352, 304+340+310, 305+351+338
Nitrogen, liquid (N$_2$)	7727-37-9	H: 281	P: 282, 336+315, 403
Papain from *Carica papaya*	9001-73-4	H: 315, 319, 334, 335	P: 261, 264, 271, 280, 302+352, 305+351+338
Paraformaldehyde	30525-89-4	H: 228, 302+332, 315, 317, 318, 335, 341, 350	P: 210, 280, 301+312, 304+340+312, 305+351+338
Penicillin	61-33-6	H: 317	P: 280
(R)-(-)-Phenylephrine hydrochloride	61-76-7	H: 302, 317	P: 261, 264, 272, 280, 301+312-302+352
Progesterone	57-83-0	H: 351, 360FD, 362	P: 202, 260, 263, 264, 280, 308+313
Putrescine	110-60-1	H: 302, 311, 314, 330	P: 260, 280, 301+312, 303+361+353, 304+340+310, 305+351+338
Retinyl acetate	127-47-9	H: 360D, 413	P: 202, 273, 280, 308+313, 405, 501

Roti-Histofix 4%	50-00-0 67-56-1	H: 302, 317, 341, 350	P: 202, 270, 280, 302+352, 308+313
Saponin	8047-15-2	H: 319, 335	P: 261, 264, 271, 280, 304+340+312, 305+351+338
Sodium azide	26628-22-8	H: 300+310+330, 373, 410	P: 262, 264, 273, 280, 302+352+310, 304+340+310
Sodium hydroxide	1310-73-2	H: 290, 314	P: 233, 280, 303+361+353, 305+351+338, 310
Streptomycin	57-92-1	H: 302	--
Thrombin	9002-04-4	H: 315, 319, 334, 335	P: 261, 264, 271, 280, 302+352, 305+351+338
Tranexamic acid	1197-18-8	H: 315, 319, 335	P: 261, 264, 271, 280, 302+352, 305+351+338
Triiodothyronine	6893-02-3	H: 372	P: 260, 264, 270, 314, 501
Triton X-100	9002-93-1	H: 302, 318, 411	P: 270, 273, 280, 305+351+338, 310
TRIzol reagent	108-95-2 593-84-0 1762-95-4	H: 302+312+332, 314	P: 264, 280, 261, 270, 271, 303+361+353, 301+310, 302+352, 305+351+338, 304+340, 501
Trypan blue	72-57-1	H: 350	P: 201, 202, 280, 308+313, 405, 501
Trypsin-EDTA (0.25%)	9002-07-7	H: 334	P: 261, 284, 342+311, 304+340, 501
Xylene	1330-20-7	H: 226, 304, 312+332, 315, 319, 335, 373	P: 210, 260, 280, 301+310, 303+361+353, 305+351+338
Y-27632	331752-47-7	H: 302-312-332	P: 280

9.7 Financial support

This project has received funding from the European Union’s Horizon 2020 research and innovation programme under the Marie Skłodowska-Curie grant agreement No 813716.

10 Acknowledgements

During my PhD, I met many inspiring professionals who through their scientific support and guidance greatly contributed to this research.

First and foremost, I would like to thank Prof. Thomas Eschenhagen for giving me the opportunity to perform my doctoral project in the IEPT. I always appreciated your great feedback and suggestions during our scientific discussions. I am grateful to Prof. Elke Oetjen for the interest in my project and supervising my thesis on behalf of the Department of Chemistry and to Dr. Marc Hirt for supervising my work and the sweet treats that I could sometimes find on my desk – life-saving at times!

I would like to acknowledge the contribution of my colleagues from the IEPT. Special thanks to Jutta Starbatty for the technical assistance with the molecular biology techniques and to Dr. Tessa Werner for establishing and sharing the differentiation protocols which were the starting point for my project. Furthermore, I would like to thank Dr. Julia Krause and Prof. Friederike Cuello. I could always trust your advice, regardless of whether it was on scientific matters or any other issue. Thank you very much for your support and kindness. I am sincerely thankful to all the collaborators who contributed to this project: Dr. Sandra Hemkemeyer and Prof. Maike Frye for performing the stiffness measurements, June Uebeler for the preparation of neonatal rat cardiac cells and performing the mycoplasma tests together with Anna Steenpaß, Birgit Klampe and Thomas Schulze for the invaluable assistance with stem cell culture, NanoString Core Facility for the karyotyping of stem cells and hiPSC-derivatives, Molecular Cardiology for NT-proBNP assays, Dr. Michaela Schweizer for the TEM data, PD Dr. Torsten Christ and Anna Steenpaß for the electrophysiology analysis, Dr. Artur Ratt for the degradation assay and Dr. Ingke Braren for the help with recording the tube formation assay.

I am sincerely thankful to all my fellow students from the TRAIN-HEART consortium. Special thanks to our collaborators from Miltenyi Biotec, where I had the opportunity do my secondment. Here, I would like to appreciate the great contribution of Dr. Dominik Eckhardt and Alba Albert to the generation and analysis of the MICS data. I am sincerely thankful to our collaborators from the Department of Cardiology at the University of Maastricht in the

Netherlands, Prof. Monika Stoll and Deepak Balamurali, for the RNA-seq and snRNA-seq analysis. TRAIN-HEART facilitated not only the scientific collaborations but also the establishment of friendships. I would like to thank Joana Alves for the great time that we spend together in Hamburg. You are a very talented scientist and my dearest friend. Thank you for all the support, motivation and fun time that we had together in Hamburg as well as on the TRAIN-HEART meetings.

I would like to thank my family and friends for all the unconditional support that I received throughout these years. You always motivated me and assured me that I can achieve any goal. Special thanks to my mother for her sacrifices and all motivational speeches. I am thankful for the patience that you showed when you had to listen to my complaints and all the “You can do it!” and “Remember that you are the best!” messages that I got any time I had a presentation. That always uplifted my spirits!

Lastly, I am truly thankful to my fiancé, Willi. Thank you for all the motivation and support that I received from you. I can’t count the times that you took over dinner preparation or picked me up from the laboratory when I had to stay late. Thank you for your patience, understanding and being by my side at every moment of my life. I am extremely lucky to have you as my partner and share this experience with you.

11 Declaration on Oath

I hereby declare and affirm that this doctoral dissertation is my own work and that I have not used any aids and sources other than those indicated. If electronic resources based on generative artificial intelligence (gAI) were used in the course of writing this dissertation, I confirm that my own work was the main and value- adding contribution and that complete documentation of all resources used is available in accordance with good scientific practice. I am responsible for any erroneous or distorted content, incorrect references, violations of data protection and copyright law or plagiarism that may have been generated by the gAI.

Hamburg, 13.10.2024

Kinga Maria Wrona

Hiermit versichere ich an Eides statt, die vorliegende Dissertationsschrift selbst verfasst und keine anderen als die angegebenen Quellen und Hilfsmittel benutzt zu haben. Sofern im Zuge der Erstellung der vorliegenden Dissertationsschrift generative Künstliche Intelligenz (gKI) basierte elektronische Hilfsmittel verwendet wurden, versichere ich, dass meine eigene Leistung im Vordergrund stand und dass eine vollständige Dokumentation aller verwendeten Hilfsmittel gemäß der Guten wissenschaftlichen Praxis vorliegt. Ich trage die Verantwortung für eventuell durch die gKI generierte fehlerhafte oder verzerrte Inhalte, fehlerhafte Referenzen, Verstöße gegen das Datenschutz- und Urheberrecht oder Plagiate.

Hamburg, 13.10.2024

Kinga Maria Wrona